UNIVERSITÀ DEGLI STUDI DI MILANO

Scuola di Dottorato in Fisica, Astrofisica e Fisica Applicata
Dipartimento di Fisica

Corso di Dottorato in Fisica, Astrofisica e Fisica Applicata
Ciclo XXXI

Search for electroweak production of supersymmetric particles at the LHC Run 2 with the ATLAS detector

Settore Scientifico Disciplinare FIS/01 e FIS/04

Coordinatore: Professor Francesco RAGUSA

Supervisore: Dottor Tommaso LARI

Tesi di Dottorato di:
Sonia Carrà

Anno Accademico 2017/2018

Commission of the final examination:

External Referee:
Prof. Lesya Shchutska - ETH Zurich
Dr. Barbara Mele - INFN Roma

External Member:
Prof. Dan Tovey - University of Sheffield
Prof. Iacopo Vivarelli - University of Sussex
Prof. Andrea Wulzer - Università di Padova

Final examination:

January 8th, 2019

Università degli Studi di Milano, Dipartimento di Fisica, Milano, Italy

Cover illustration:

Galleria Vittorio Emanuele Dome, Milano, Italy

MIUR subjects:

FIS/01 - FIS/04

PACS:

12.60.Jv - 14.80.Ly - 14.80.Nb

Abstract

Two closely related searches for the electroweak production of Supersymmetric particles are presented in this manuscript. The analyses are based on the proton-proton collision data from the Large Hadron Collider Run 2, with a center-of-mass energy of 13 TeV, collected by the ATLAS experiment.

Different Supersymmetric signal models are considered. The first search targets the pair production of either the Supersymmetric partners of the leptons (sleptons) or the W boson and charged Higgs boson super-partners (charginos). In the latter case, the decay of charginos via sleptons is assumed. The search uses data collected by ATLAS between 2015 and 2016, with an integrated luminosity of 36.1 fb^{-1}. The second search targets the direct production of chargino pair with W boson mediated decay. The analysis for the observation of the process was performed using the data collected by ATLAS between 2015 and 2017, reaching an integrated luminosity of 80.5 fb^{-1}.

The signature, common to all the SUSY signal models considered, consists of two charged leptons (electrons or muons) and missing transverse energy. No significant fluctuation above the Standard Model prediction was observed in the analyses. New exclusion limits, tighter than the previously available results, were placed on the masses of the SUSY particles: slepton masses up to 500 GeV are excluded at 95% CL. Chargino masses up to 700 GeV are excluded in the case of the decay mediated by a slepton, while considering the W boson mediated decay the limit on the chargino mass is 410 GeV.

Contents

Introduction

The search for beyond the Standard Model phenomena is one of the fundamental steps in the development of the particle physics and in the comprehension of the Universe.

The Standard Model of particle physics (SM) [1–4] is a quantum field theory describing the interactions of the fundamental particles. The model was formulated between the '60s and '70s and it proved to be highly predictive. Over the decades it was verified by many experiments at the colliders, such as SPS, LEP [5] and Large Hadron Collider (LHC) [6] at CERN and Tevatron [7] at the FermiLab. The last missing piece of the SM was observed in 2012: the CERN ATLAS [8] and CMS [9] experiments announced the discovery of the Higgs Boson [10, 11].

Despite the brilliant experimental observations, the SM is far from being a complete theory, since there are many open questions that are not addressed. The SM can not provide an explanation for dark matter and neutrinos oscillation for example. In order to explain phenomena beyond the Standard Model (BSM) many new theories have been proposed. One of the most motivated is the Supersymmetry theory (SUSY) [12–17]: for each SM particle, a new particle with same quantum numbers, except spin and mass, is introduced. SUSY provides a new set of particles, with a rich phenomenology and many different signatures.

The search of Supersymmetric particles is the object of the work presented in this Thesis. The analyses are based on the proton-proton collision data from the LHC at a center-of-mass energy of 13 TeV, collected by the ATLAS experiment. The particles which are searched for are the Supersymmetric partners of leptons, electroweak gauge and Higgs bosons which are only produced via the electroweak interaction. Despite the relatively low production rate, these particles are a promising avenue for the observation of

Supersymmetry, because very tight limits have been previously set on strongly interacting particles [18–20].

Searches targeting the observation of different Supersymmetric R -parity conserving models are presented in this document. The analyses use different sets of the data collected by the ATLAS experiment, and distinct strategies are exploited for the observation of SUSY particles.

The first analysis was developed in order to observe the direct production of the super-partners of the SM leptons, the sleptons. The sleptons are pair produced and they decay promptly in charged leptons and in the lightest neutralino, a mix of the vector bosons and Higgs super-partners:

$$\tilde{\ell}^+\tilde{\ell}^- \to \ell^+\tilde{\chi}_1^0\ell^-\tilde{\chi}_1^0$$

The neutralino is assumed to be the lightest Supersymmetric particle and to be stable. The direct production of charginos, a mix of the W boson and Higgs super-partners, with a prompt decay mediated by sleptons is also considered. The sleptons then decay in lepton and neutralino:

$$\tilde{\chi}_1^+\tilde{\chi}_1^- \to \tilde{\ell}^+\nu\tilde{\ell}^-\nu \to \ell^+\tilde{\chi}_1^0\nu\ell^-\tilde{\chi}_1^0\nu$$

Both the processes lead to a signature with two charged leptons and weakly interacting particles that escape the detector (the neutrinos and the neutralinos). The data collected by the ATLAS detector between 2015 and 2016 were used, the integrated luminosity is 36.1 fb^{-1}.

The second search discussed in this Thesis considers the direct production of a chargino pair with a prompt decay mediated by a W boson, that decays leptonically:

$$\tilde{\chi}_1^+\tilde{\chi}_1^- \to W^+\tilde{\chi}_1^0W^-\tilde{\chi}_1^0 \to \ell^+\nu\tilde{\chi}_1^0\ell^-\nu\tilde{\chi}_1^0$$

This decay chain is the favorite one in the case of sleptons with masses larger than the chargino's. Since only the W boson leptonic decay is considered, the acceptance of the process is reduced and the observation is more difficult compared to the case of the sleptons mediated decay. Also for this model the signature consists of two charged leptons and invisible particles. The search used the data collected by ATLAS between 2015 and 2017, with an integrated luminosity of 80.5 fb^{-1}.

Summary of the manuscript

This Thesis is structured as follows: Chapter 1 reports a brief introduction to the Standard Model and its limitations, and then it continues with the explanation of the Supersymmetry and the description of the signal models considered in this document. Chapter 2 is dedicated to the description of the Large Hadron Collider and of the ATLAS experimental apparatus. In Chapter 3, the characteristics of the data collected by ATLAS and the quality check performed are illustrated; the computing network, the ATLAS software and the data format are also briefly reported. The data undergo the physics objects reconstruction: the objects of interest for the searches illustrated in this Thesis are reported in Chapter 4.

The general procedure and tools used in the analyses are described in Chapter 5. The signal region strategy, the estimation of the SM background, the Monte Carlo simulation, the study of the uncertainty sources and the statistic interpretation of the result are reported. Chapter 6 illustrates the analysis performed for the observation of the slepton pair production and the chargino pair production with slepton mediated decay: the events selection, the signal regions, the estimation and the validation of the background, the systematic uncertainties and the interpretation of the result are addressed. The structure of Chapter 7 is similar to Chapter 6, but it is dedicated to the search developed for the observation of the chargino pair production with W boson mediated decay and to the obtained result.

Personal contribution

My personal contribution to the SUSY searches presented in this document is reported in the following.

Considering the analysis for the observation of the slepton pair production and the chargino pair production with slepton mediated decay illustrated in Chapter 6, I was in charge of almost all aspects of the analysis. I worked at the analysis software maintenance and I developed the statistical tools for the interpretation. I took care of the sanity checks and of the comparison between data and Monte Carlo simulation. I was in charge of the optimization of the signal regions, I developed the strategy for the SM background estimation and validation and I performed detailed study on the uncertainties and their impact on the search. I provided the statistical interpretation of the final result.

Concerning the chargino pair production with W boson analysis illustrated in Chapter 7, I was one of the the main analyzer of the search. I contributed to the software framework and to the statistical tools, I processed common data and Monte Carlo samples for the analysis team. I performed sanity checks and comparison between data and Monte Carlo simulation. I provided detailed studies on the systematic effects and the final uncertainty estimate.

CHAPTER 1

Physics beyond the Standard Model

This Chapter presents a theoretical introduction of the Supersymmetric models that are relevant for this Thesis. Section 1.1 will provide a brief introduction to the Standard Model and Section 1.2 will illustrate the SM limitations. Section 1.3 will present the Supersymmetry theory and Section 1.4 will focus on electroweak production of SUSY particles and on the simplified models considered in this document.

1.1 The Standard Model

The Standard Model [1–4] is a quantum field theory describing the fundamental particles and their interactions, it includes three of the four fundamental forces (weak, electromagnetic and strong). The SM is a non-abelian gauge theory and it is invariant under the symmetry group $SU(3)_C \otimes SU(2)_L \otimes U(1)_Y$, where C is the color charge, L means left handed and Y is the hypercharge [22].

The Standard Model particles are summarized in Figure 1.1 and they can be classified in two groups: matter fields, which are fermions, and mediators of the interactions, which are gauge bosons:

- the fermions are elementary particles which constitute matter, with spin 1/2. According to their properties under $SU(3)_C$ transformation, fermions are divided into quarks (carrying color charge) and leptons (colorless). Fermions are classified in three generations of increasing mass. The first generation corresponds to what exists in common matter, while the second and third generations are accessible at higher energy. Fermions are further divided into left and right handed helicity eigenstates: left handed states (LH) transform as doublets under the weak interaction

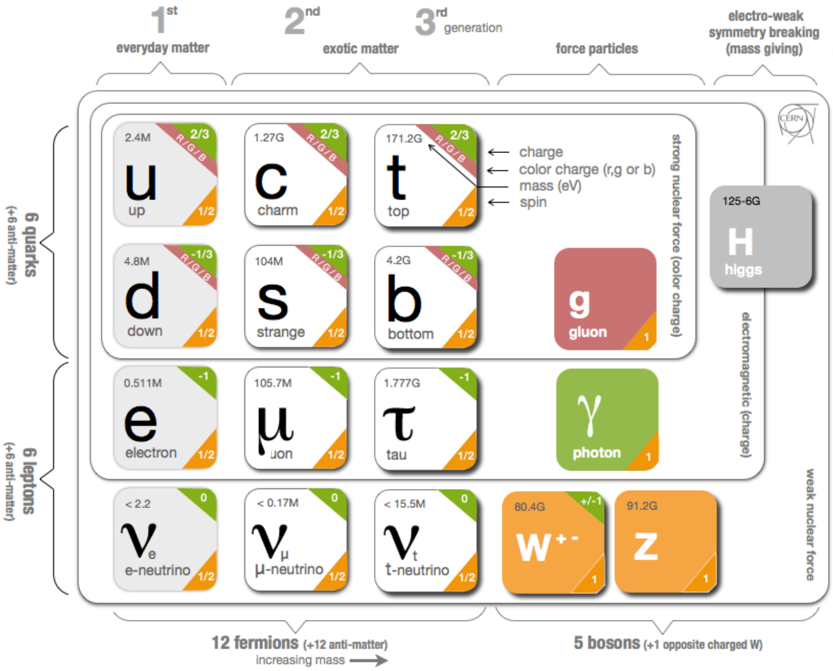

Figure 1.1: Illustration of the fundamental particles of the Standard Model [21]

$SU(2)_L$, right handed states (RH) as singlets. SM fermions are summarized here:

$$\begin{array}{cccccc}
\begin{pmatrix} u_L \\ d_L \end{pmatrix} & \begin{pmatrix} c_L \\ s_L \end{pmatrix} & \begin{pmatrix} t_L \\ b_L \end{pmatrix} & \begin{pmatrix} \nu_{eL} \\ e_L \end{pmatrix} & \begin{pmatrix} \nu_{\mu L} \\ \mu_L \end{pmatrix} & \begin{pmatrix} \nu_{\tau L} \\ \tau_L \end{pmatrix} \\
u_R, d_R & c_R, s_R & t_R, b_R & e_R & \mu_R & \tau_R
\end{array} \tag{1.1}$$

Standard Model neutrinos are assumed to be purely left handed and massless, but the experimental results have shown that neutrinos have masses.

- the gauge bosons are the mediators of the fundamental interactions, with spin 1. The gluons g are the carriers of the strong force, the particle is massless and carries color charge. Electroweak gauge bosons W^i ($i = 1,2,3$) and B are the mediators of the electroweak interaction. Their mass eigenstates are Z and $W^{\pm}$, mediators of the weak interaction, and the photon γ, mediator of the electromagnetic interaction.

Considering the SM as described until this point, any particle mass term in the SM Lagrangian is forbidden by the gauge symmetry. An additional scalar field with an associated boson is needed- The Higgs mechanism will be described in the next Section.

1.1.1 Higgs mechanism

The Higgs mechanism was theorized in the work by Higgs, Englert and Brout [23, 24], in 1964. Later it was used by Weinberg in order to provide the mass terms of the weak

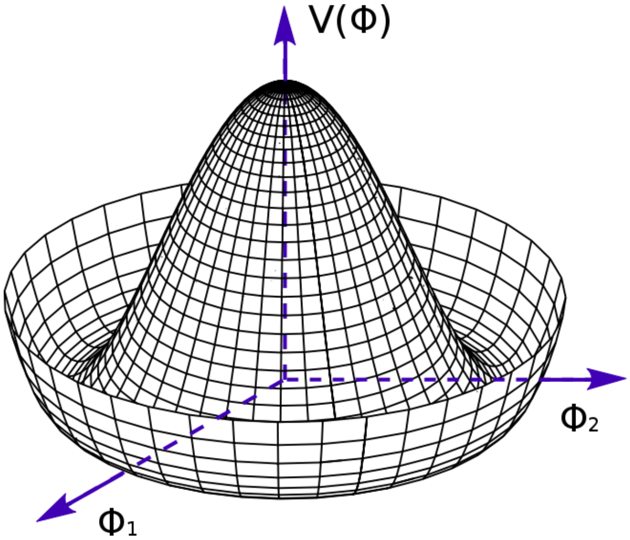

Figure 1.2: Shape of the potential $V(\Phi)$ in the case $\mu^2 < 0$, as a function of the components Φ_1 and Φ_2.

bosons and of the fermions in a gauge-invariant way. The Higgs mechanism is based on the idea of *spontaneous symmetry breaking* (SSB): the theory does not contain an explicit breaking of the gauge symmetry, but mass terms arise from the choice of a minimal configuration of the potential of a new *ad hoc* field, called Higgs field.

The starting point is the SM Lagrangian, only the electroweak interaction is considered:

$$\mathcal{L}_0 = \mathcal{L}_{lepton} + \mathcal{L}_{gauge} \tag{1.2}$$

where the $\mathcal{L}_{lepton}$ is the massless Lagrangian describing leptons, invariant under $SU(2)_L \otimes U(1)_Y$ transformation, and it is defined as follows:

$$\begin{aligned} \mathcal{L}_{lepton} =& \bar{\psi}_L i\gamma_\mu \mathcal{D}^\mu_L \bar{\psi}_L + \bar{\psi}_R i\gamma_\mu \mathcal{D}^\mu_R \bar{\psi}_R \\ \mathcal{D}^\mu_L =& \partial^\mu + ig\frac{\bar{\sigma}\cdot\bar{W}^\mu}{2} + i\frac{g'}{2}Y_L B^\mu \\ \mathcal{D}^\mu_R =& \partial^\mu + i\frac{g'}{2}Y_R B^\mu \end{aligned} \tag{1.3}$$

with ψ_L and ψ_R being the LH and RH components of the fermionic field. The term $\mathcal{L}_{gauge}$ in Eq. (1.2) represents the gauge boson Lagrangian term.

With the aim of realizing the SSB and giving mass to the SM particles, a new complex scalar field Φ is introduced in the SM Lagrangian:

$$\mathcal{L}_{\mathcal{H}} = (\mathcal{D}^\mu\Phi)^\dagger(\mathcal{D}_\mu\Phi) - V(\Phi^\dagger\Phi) \tag{1.4}$$

where $V(\Phi)$ is the potential of the Φ field. The field Φ has to couple to $W^\pm$ bosons in order to give them mass, so Φ must be an isospin doublet: the minimal requirement for the field is to be an isospin doublet of complex scalar fields. Furthermore Φ must not couple to the photon field and this implies $Q = 0$. Considering the relation between isospin and charge ($Y = 2(Q - T^3)$), it implies one of the Φ component musts be zero:

$$\Phi = \left(\begin{array}{c} \phi_1 \\ \phi_2 \end{array} \right) = \left(\begin{array}{c} 0 \\ \phi \end{array} \right) \tag{1.5}$$

The potential $V(\Phi)$ is required to have the form:

$$V(\Phi) = \lambda(\Phi^\dagger\Phi)^2 + \mu^2(\Phi^\dagger\Phi) \tag{1.6}$$

with $\lambda > 0$, to guarantee the existence of a ground state. Depending on the μ^2 sign, the ground state can be unique or degenerate. If $\mu^2 > 0$ the potential presents a minimum at zero, while for $\mu^2 < 0$ there is contour of minima at $\mu^2/\lambda^2 \equiv \frac{1}{2}v^2$, as illustrated in Figure 1.2. The $\mu^2 < 0$ case is the one allowing the SSB, due to the choice of a specific ground state. The field acquires a vacuum expectation value:

$$\langle 0|\Phi|0\rangle = \frac{v}{\sqrt{2}} \tag{1.7}$$

The field Φ can be written as expansion around the ground state:

$$\Phi = \frac{1}{\sqrt{2}} \begin{pmatrix} 0 \\ v + h(x) \end{pmatrix} \tag{1.8}$$

In order to give mass to fermions, an interaction term between the scalar field Φ and the fermionic field is needed:

$$\mathcal{L}_{Yukawa} = -G_{lep}[\bar{\psi}_R(\Phi^\dagger\psi_L) + (\bar{\psi}_L\Phi)\psi_R] \tag{1.9}$$

The Standard Model Lagrangian from Equation (1.2) becomes:

$$\mathcal{L} = \mathcal{L}_{lepton} + \mathcal{L}_{gauge} + \mathcal{L}_H + \mathcal{L}_{Yukawa} \tag{1.10}$$

An important consequence of the introduction of the Higgs field and of the SSB is the mixing between the B e W^i boson, that gives $W^\pm$, Z and A (the photon field):

$$\begin{gathered} W^\pm_\mu = \frac{1}{\sqrt{2}}(W^1_\mu \mp iW^2_\mu) \\ \left(\begin{array}{c} A_\mu \\ Z_\mu \end{array} \right) = \left(\begin{array}{cc} \cos\theta_W & \sin\theta_W \\ sin\theta_W & \cos\theta_W \end{array} \right) \left(\begin{array}{c} B_\mu \\ W^3_\mu \end{array} \right) \end{gathered} \tag{1.11}$$

where the Weinberg angle θ_W is defined as:

$$\begin{cases} \frac{g}{\sqrt{(g')^2+g^2}} = \cos\theta_W \\ \frac{g'}{\sqrt{(g')^2+g^2}} = \sin\theta_W \end{cases} \tag{1.12}$$

The Standard Model particles masses, obtained with the Higgs mechanism, are the following:

$$
\begin{aligned}
m_W &= \frac{1}{2}vg && \text{for} \quad W^{\pm}_{\mu} = \frac{1}{\sqrt{2}}(W^1_{\mu} \mp iW^2_{\mu}) \\
m_Z &= \frac{1}{2}v\sqrt{g^2 + g'^2} && \text{for} \quad Z_{\mu} = \frac{gW^3_{\mu} - g'B_{\mu}}{\sqrt{g^2 + g'^2}} \\
m_{\gamma} &= 0 && \text{for} \quad A_{\mu} = \frac{g'W^3_{\mu} - gB_{\mu}}{\sqrt{g^2 + g'^2}} \\
m_f &= \frac{vY_f}{\sqrt{2}} \quad \text{for the fermions,} && m_H = v\sqrt{2\lambda} \quad \text{for the Higgs boson}
\end{aligned}
\tag{1.13}
$$

The masses of the vector bosons are proportional to the Higgs vacuum expectation value v, while the the masses of the fermions are proportional both to the vacuum expectation value and to the Higgs Yukawa coupling constant Y_f.

1.2 The limitations of Standard Model

The Standard Model provides a successful description of many known phenomena. However, there are some critical points that arise from theoretical considerations and also from experimental results that can not fit in the SM. These issues seem to suggest that SM is a low energy effective version of a more general theory. Some of the particle physics open questions are described in this section.

1.2.1 Dark matter

From many experimental observations [25,26], a small fraction of the Universe is formed by luminous matter, while most part of it remains unknown. Only the 5% of the Universe is composed by barionic matter, 27% by dark matter and 68% is dark energy [27].

Many possible explanations for the Dark Matter were proposed, as example Massive Compact Halo Objects (MACHOs) [28,29], axions [30,31] and weakly interacting massive particles (WIMP) [32]. MACHOs consist of small astronomical objects that do not emit light, such as black holes, planets, brown dwarfs or neutron stars, but this Dark Matter candidate is in contrast with gravitational lenses observation.

Axions are neutral pseudo-scalar particles with very small mass that are introduced to explain CP conservation in the strong interaction, but they can also be a good Dark Matter candidate. Axions are supposed to be relativistic particles, but this hypothesis is in contrast with the model of galaxy formation. Mass agglomeration is possible only in the case of non-relativistic Dark Matter.

Concerning the WIMP, a neutral massive particle with cross section of the order of the weak interaction can be a good Dark Matter candidate, since it is not in contrast with the current observations and, if it has a mass between 10 GeV and 10 TeV, the WIMP density is consistent with the production at the thermal equilibrium. Assuming that the Dark Matter consists of WIMP, the SM does not provide any suitable candidate [33].

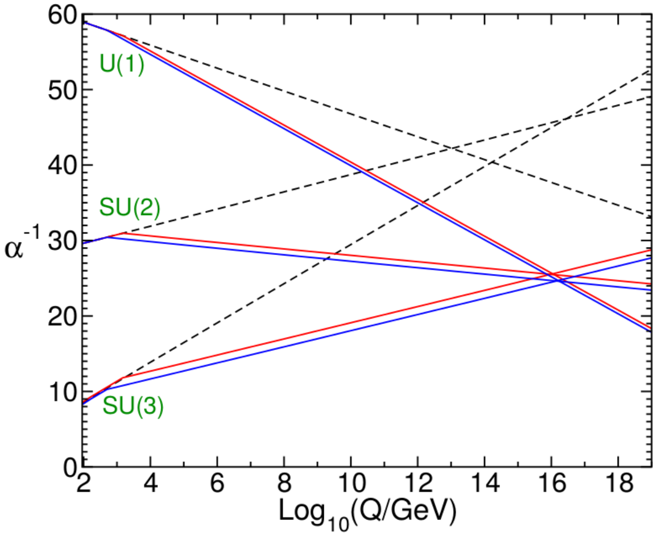

Figure 1.3: Evolution of the inverse gauge couplings α of electromagnetic, weak and strong interaction, as a function of the energy scale in the Standard Model scenario (dashed lines) and considering Minimal Supersymmetric SM (red and blue lines) [35].

1.2.2 Matter-antimatter asymmetry

The Big Bang should have created an equal amount of matter and anti-matter, but the Universe today consist mainly of matter over the anti-matter counterpart [34]. From the cosmological point of view, it is not easy to provide a convincing explanation about how from the thermal equilibrium established after the the Big Bang, most of the anti-matter disappeared.

1.2.3 Gravity

The gravitational interaction is not included in the SM. This unification would require the quantization of the gravity. Since the gravity coupling constant is much smaller compared to other forces, the effect in particle interactions is negligible at the energy accessible today. Quantum gravitational effects are expected to become important only at the Planck scale (10^{19} GeV).

1.2.4 Grand unified theory

The object of Grand Unified Theory (GUT) is the unification of three of the Standard Model fundamental interactions. Considering the electromagnetic, weak and strong interaction coupling constant α extrapolation at large energy scale (Figure 1.3), an unification of the three forces seems not to be possible, since the three constants do not meet each other in one point. But in Minimal Supersymmetric SM scenario (that will be illustrated in Section 1.3.1), the coupling constants of the fundamental forces converge together at a scale of 10^{16} GeV.

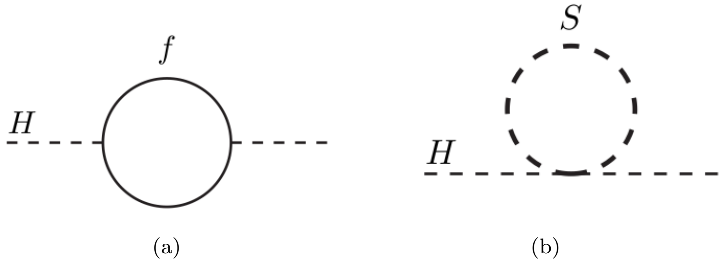

Figure 1.4: One-loop radiative correction to Higgs boson mass due to a fermion f (a) or a scalar particle S (b) [35].

1.2.5 Hierarchy problem

This argument against the Standard Model is more theoretical than practical and it concerns the Higgs boson mass radiative corrections [35–37]. The Higgs potential in Eq. (1.6), considering that $\mu^2/\lambda^2 = \frac{1}{2}v^2$ and $m_H = v\sqrt{2\lambda}$, can be written as:

$$V(\Phi) = m_H^2|\Phi|^2 + \lambda|\Phi|^4 \tag{1.14}$$

Experimentally the Higgs boson mass was proven to be $m_H = 125$ GeV [10, 11]. But m_H receive large corrections due to the Higgs field coupling with the other particles. Considering Figure 1.4(a), the fermion f couples to the Higgs field, with a Lagrangian term $-\lambda_f\Phi\bar{f}f$, giving the Higgs boson mass a correction:

$$\Delta m_H^2 = -\frac{|\lambda_f|^2}{8\pi^2}\Lambda_{\rm UV}^2 + ... \tag{1.15}$$

where $\Lambda_{\rm UV}^2$ is an ultraviolet momentum cutoff, used to regulate the loop integral and it can be interpreted as the scale at which new physics can alter the theory. Fermion f represents each SM lepton or quark (in the latter case a factor 3 should be added to take into account the color). The largest correction comes from the top quark, since in this case $\lambda_f \approx 1$. The issue is that if $\Lambda_{\rm UV}^2$ is of the order the Planck scale, the quantum correction Δm_H is about 15 orders of magnitude larger than the Higgs boson mass. The SM fermions are less affected by the $\Lambda_{\rm UV}^2$ cutoff, since the dependency on $\Lambda_{\rm UV}^2$ is logarithmic and not quadratical.

A solution to this problem is not possible considering only the SM, but it can be found through a new scalar particle S, with mass m_S and a Higgs coupling Lagrangian term $-\lambda_S|\Phi|^2|S|^2$. The interaction diagram is represented in Figure 1.4(b) and the correction is:

$$\Delta m_H^2 = \frac{\lambda_S}{16\pi^2}\left[\Lambda_{\rm UV}^2 - 2m_S^2\log\bigl(\Lambda_{\rm UV}^2/m_S\bigr) + ...\right] \tag{1.16}$$

From the comparison between the fermionic correction to the Higgs mass in Eq. (1.15) and the hypothetical scalar field correction in Eq. (1.16), it seems possible to have a cancellation between the two contributions. The systematic cancellation of the divergent contribution to the Higgs boson mass at all the energy scales can only performed through a symmetry. The previous considerations seems to suggest a symmetry between fermions and bosons, since if each SM fermion has a doublet of corresponding bosons with $\lambda_S = |\lambda_f|^2$, the λ_{UV}^2 contributions can be canceled.

1.3 Supersymmetry

As illustrated in Section 1.2.5, in order to solve the Standard Model hierarchy problem, it is possible to consider a symmetry between fermions and bosons: for each SM fermion, a bosonic partner can be introduced and *vice versa.* This theory is called Supersymmetry [12–17].

A Supersymmetry transformation turns a fermionic state into a bosonic state, and a bosonic state into a fermionic one. The transformation is generated by the operator $\hat{\mathrm{Q}}$, that must be an anticommuting spinor:

$$\hat{\mathrm{Q}}\,|\mathrm{fermion}\rangle = |\mathrm{boson}\rangle \quad \hat{\mathrm{Q}}\,|\mathrm{boson}\rangle = |\mathrm{fermion}\rangle \tag{1.17}$$

Operators $\hat{\mathrm{Q}}$ and $\hat{\mathrm{Q}}^\dagger$ (hermitian conjugate) are fermionic operators and they carry spin angular momentum 1/2, as consequence Supersymmetry must be a space-time symmetry. The operator satisfies the following commutation and anticommutation relations:

$$\begin{aligned} \left\{\hat{\mathrm{Q}},\hat{\mathrm{Q}}^\dagger\right\} &= P^\mu \\ \left\{\hat{\mathrm{Q}},\hat{\mathrm{Q}}\right\} = \left\{\hat{\mathrm{Q}}^\dagger,\hat{\mathrm{Q}}^\dagger\right\} &= 0 \\ \left[P^\mu,\hat{\mathrm{Q}}\right] = \left[P^\mu,\hat{\mathrm{Q}}^\dagger\right] &= 0 \end{aligned} \tag{1.18}$$

where P^μ is the four-momentum generator of space-time translations.

The single particle states of a supersymmetric theory fall into irreducible representations of the supersymmetry algebra, called *supermultiplets.* Each supermultiplet contains fermionic and bosonic states, which are superpartners to each other. Since supersymmetry generators $\hat{\mathrm{Q}}$ and $\hat{\mathrm{Q}}^\dagger$ commute with the generators of gauge transformations, particles in the same supermultiplet must also be in the same representation of the gauge group: electric charges, weak isospin, and color degrees of freedom must be the same.

Each supermultiplet contains an equal number of fermionic and bosonic degrees of freedom:

$$n_B = n_F \tag{1.19}$$

The simplest supermultiplet possible is formed by a single fermion (with two spin helicity states, $n_F = 2$) and two real scalars (each one with $n_B = 1$), and the two scalar degrees of freedom are arranged in a complex scalar field. The combination of a two-component fermion and a complex scalar field is called a *chiral* or *scalar* supermultiplet.

The next-simplest possible supermultiplet contains a spin-1 vector boson. In order to have a renormalizable theory, the particles must be gauge bosons with two helicity states, so $n_B = 2$. The superpartner is a fermion with spin 1/2, with two helicity states ($n_F = 2$), and it is called *gaugino.* The combination of gaugino and gauge bosons is called a *gauge* or *vector* supermultiplet.

1.3.1 Minimal Supersymmetric Standard Model

The Minimal Supersymmetric Standard Model (MSSM) [35] is the SM extension with the minimal number of additional particles. Each fundamental particle is included in a chiral or in a gauge supermultiplet, together with the superpartner with spin differing by 1/2 unit. Standard Model fermions LH and RH parts transform differently under the gauge group, so each component must have its own scalar partner.

The new set of supersymmetric particles is named as follows: bosonic partners of quark and leptons get an *s-* as prefix in the name, as scalar (*squarks* and *sleptons*, or also *sfermions*), while fermionic partners of bosons get a *-ino* suffix. The symbols for the superpartner are the same as for the corresponding Standard Model particle, but with a tilde.

The particles necessary to construct the supersymmetric version of the Standard Model are shown in Tables 1.1 and 1.2 in terms of the superfields. The supersymmetric particles considered in the MSSM are briefly illustrated in the following:

- concerning the sfermion, the u and d quark-squark supermultiplets is presented as example. The superfield consists of an $SU(2)_L$ doublet of quarks:

  $$Q = \begin{pmatrix} u_L \\ d_L \end{pmatrix} \tag{1.20}$$

  and their scalar partners which are also in an $SU(2)_L$ doublet:

  $$\tilde{Q} = \begin{pmatrix} \tilde{u}_L \\ \tilde{d}_L \end{pmatrix} \tag{1.21}$$

  In a similar way, $\bar{u}$ ($\bar{d}$) contains the RH up (down) anti-quark $\bar{u}_R$ ($\bar{d}_R$) and the scalar partner $\tilde{u}^*_R$ ($\tilde{d}^*_R$). Supermultiplets for other quark and leptons are built in similar way.

- concerning the gauge boson, gluino $\tilde{g}$ is the SM gluon superpartner, while winos $\tilde{\omega}^i$ and bino b are the fermionic partners of W^i and B respectively.

- in the case of the Higgs boson, just one chiral supermultiplet is not enough. If there were only one Higgs chiral supermultiplet, the electroweak gauge symmetry would suffer a gauge anomaly, and would be inconsistent as a quantum theory. In the MSSM at least two Higgs doublet fields are required: $H_1 = \left(H_1^+, H_1^0\right)$ and $H_2 = \left(H_2^0, H_2^-\right)$, with the corresponding superpartners.

1.3.2 Supersymmetry breaking

Supersymmetry must be a broken symmetry, otherwise SUSY particles should have the same mass of their SM partners (but this was proven to be false since SUSY particles were not observed yet) [38]. The mechanism of Supersymmetry breaking is not well understood, but it is assumed that the breaking happens due to the interactions of Supersymmetric particle with an unknown sector, that can be associated with the GUT or the gravity, for

Chiral supermultiplets						
Particles		spin 0	spin 1/2	$SU(3)_C$	$SU(2)_L$	$U(1)_Y$
squark - quarks	Q	$\begin{pmatrix}\tilde{u}_L & \tilde{d}_L\end{pmatrix}$	$\begin{pmatrix}u_L & d_L\end{pmatrix}$	3	2	1/6
(3 families)	$\bar{u}$	$\tilde{u}_R^*$	$\bar{u}_R$	$\bar{3}$	1	-2/3
	$\bar{d}$	$\tilde{d}_R^*$	$\bar{d}_R$	$\bar{3}$	1	1/3
sleptons - leptons	l	$\begin{pmatrix}\tilde{\nu} & \tilde{e}_L\end{pmatrix}$	$\begin{pmatrix}\nu & e_L\end{pmatrix}$	1	2	-1/2
(3 families)	$\bar{e}$	$\tilde{e}_R^*$	$\bar{e}_R$	1	1	1
Higgs - higgsinos	H_1	$\begin{pmatrix}H_1^+ & H_1^0\end{pmatrix}$	$\begin{pmatrix}\tilde{H}_1^+ & \tilde{H}_1^0\end{pmatrix}$	1	2	1/2
	H_2	$\begin{pmatrix}H_2^0 & H_2^-\end{pmatrix}$	$\begin{pmatrix}\tilde{H}_2^0 & \tilde{H}_2^-\end{pmatrix}$	1	2	-1/2

Table 1.1: Chiral supermultiplets in the Minimal Supersymmetric Standard Model.

Gauge supermultiplets					
Particles	spin 1/2	spin 1	$SU(3)_C$	$SU(2)_L$	$U(1)_Y$
gluino - gluon	$\tilde{g}$	g	8	1	0
winos - W bosons	$\tilde{\omega}^\pm\ \tilde{\omega}^0$	$W^\pm\ W^0$	1	3	0
bino - B boson	$\tilde{b}^0$	B^0	1	1	0

Table 1.2: Gauge supermultiplets in the Minimal Supersymmetric Standard Model.

example [39]. Many Supersymmetry breaking theories were proposed, but usually these models are valid only under strong assumptions, so the most common approach is to assume that the MSSM is an effective low energy theory (at the electroweak scale) [40–42].

The Supersymmetry breaking is obtained including explicit *soft* mass terms, called soft because they do not introduce any quadratic divergences, for the scalar members of the chiral multiplets and for the gaugino members of the vector supermultiplets in the Lagrangian:

$$\mathcal{L}_{\text{MSSM}} = \mathcal{L}_{\text{SUSY}} + \mathcal{L}_{\text{soft}} \tag{1.22}$$

where the first term consists of the dynamics terms of the superfields and their interactions and the second is the soft Supersymmetry breaking terms. Considering only the first fermions generation, the Lagrangian becomes:

$$\begin{aligned}
-\mathcal{L}_{\text{soft}} =& m_1^2|H_1|^2 + m_2^2|H_2|^2 - \mathcal{B}\mu\epsilon_{ij}(H_1^i H_2^j + \text{h.c.}) \\
&+ \tilde{M}_Q^2(\tilde{u}_L^*\tilde{u}_L + \tilde{d}_L^*\tilde{d}_L) + \tilde{M}_u^2\tilde{u}_R^*\tilde{u}_R + \tilde{M}_d^2\tilde{d}_R^*\tilde{d}_R + \tilde{M}_L^2(\tilde{e}_L^*\tilde{e}_L + \tilde{\nu}_L^*\tilde{\nu}_L) + \tilde{M}_e^2\tilde{e}_R^*\tilde{e}_R \\
&+ \frac{1}{2}\left[M_3\bar{\tilde{g}}\tilde{g} + M_2\bar{\tilde{\omega}}_i\tilde{\omega}_i + M_1\bar{\tilde{b}}\tilde{b}\right] \\
&+ \frac{g}{\sqrt{2}M_W}\epsilon_{ij}\left[\frac{M_d}{\cos\beta}\mathcal{A}_d H_1^i\tilde{Q}^j\tilde{d}_R^* + \frac{M_u}{\sin\beta}\mathcal{A}_u H_2^j\tilde{Q}^i\tilde{u}_R^* + \frac{M_e}{\cos\beta}\mathcal{A}_e H_1^i\tilde{L}^j\tilde{e}_R^* + \text{h.c.}\right]
\end{aligned} \tag{1.23}$$

The first line of Eq. (1.23) is the Higgs boson squared mass terms, where $\mathcal{B}$ is the soft SUSY-breaking Higgs boson mass term, the second line is composed by the squared mass terms for the squarks and the sleptons, the third line gives masses to the MSSM gauginos, and the last line consists in trilinear scalar interactions.

After the introduction of the Lagrangian soft terms, the MSSM is characterized by 124 independent physical parameters. The large number of parameters is a consequence of the missing information about the Suspersymmetry breaking mechanism. However, thanks to experimental and phenomenological considerations, the number of free parameters can be reduced. Measurements of flavor changing neutral currents, leptons flavor violation and CP violation phenomena give stringent limitations on those parameters [43–50], so the effects would be negligible in any observation of direct production of SUSY particles. The parameters are furthermore reduced after imposing the R-parity conservation, that will be illustrated in Section 1.3.3.

In this way the numbers of parameters is reduced down to 19 terms in the phenomenological MSSM model (pMSSM). The parameters that will be relevant to understand the phenomenology and assumptions of the models considered in the following are:

- μ is the coefficient in the Higgs super-potential that gives the mass terms for the Higgs bosons and their partners and is therefore called the *Higgs mass term*;
- M_a (a = 1, 2, 3) are the soft Supersymmetry breaking gaugino mass parameters;
- $\tan\beta$ is the ratio of the Higgs vacuum expectation values of the two Higgs doublets, $\tan\beta = v_1/v_2$;
- the squark and slepton mass matrices that appear in $\mathcal{L}_{\text{soft}}$: $\tilde{M}_Q$ for LH squarks, $\tilde{M}_u$ and $\tilde{M}_d$ for RH squark, $\tilde{M}_L$ and $\tilde{M}_e$ for sleptons.

Particles listed in Tables 1.1 and 1.2, which are gauge eigenstates, are not necessarily mass eigenstates. After the electroweak symmetry and the soft Supersymmetry breaking, the particles with the same quantum number can mix together. The mass eigenstates that are relevant for this thesis will be described in the following.

Sleptons

SM leptons superparner are $\tilde{e}_L$, $\tilde{e}_R$, $\tilde{\mu}_L$, $\tilde{\mu}_R$, $\tilde{\tau}_L$, $\tilde{\tau}_R$, $\tilde{\nu}_e$, $\tilde{\nu}_\mu$ and $\tilde{\nu}_\tau$. In principle any scalars with the same electric charge and color quantum numbers can mix with each other, but most of the mixing angles are very small due to the assumption of no lepton flavor violating processes.

The third generation sleptons can have very different masses compared to the first and second generation, because of the effects of large Yukawa coupling and soft Supersymmetry breaking terms. Tau sleptons mass matrix is:

$$M^2_{\tilde{\tau}} = \begin{pmatrix} m^2_{L_3} + \Delta_{\tilde{e}_L} & v(\mathcal{A}^*_\tau \cos\beta - \mu y_\tau \sin\beta) \\ v(\mathcal{A}_\tau \cos\beta - \mu^* y_\tau \sin\beta) & m^2_{\bar{e}3} + \Delta_{\tilde{e}_R} \end{pmatrix} \tag{1.24}$$

where y_τ is the Yukawa coupling and Δ terms come from quadratic interaction with Higgs field. The pair ($\tilde{\tau}_L$, $\tilde{\tau}_R$) can have an important mixing and the stau mass eigenstates are indicated as $\tilde{\tau}_1$ and $\tilde{\tau}_2$. The first and second generation have small Yukawa coupling and they end up in nearly degenerated and unmixed pairs ($\tilde{e}_R$, $\tilde{\mu}_R$), ($\tilde{e}_L$, $\tilde{\mu}_L$) and ($\tilde{\nu}_e$, $\tilde{\nu}_\mu$).

Higgs sector

The Higgs scalar fields in the MSSM consist of two complex $SU(2)_L$ doublets, H_1 and H_2, with eight degrees of freedom. After the electroweak symmetry breaking, three of them become Nambu-Goldstone bosons, which are the longitudinal modes of the Z and $W^\pm$ bosons.

The remaining five degrees of freedom produce physical observable states, that are the the five Higgs bosons of the MSSM model [51]:

- $H^\pm$, a charged Higgs boson pair;
- A^0, a CP-odd neutral Higgs boson;
- H^0 and h^0, CP-even neutral Higgs bosons (with h^0 being lighter by convention).

The h^0 particle has proprieties similar to the SM Higgs boson and it is supposed to be the lightest of the five Higgs bosons. In the contest of the SUSY models, the particle observed by the ATLAS and CMS collaborations with a mass of 125 GeV is identified with h^0. The measurements of the h^0 coupling with the SM particles place a lower limit of about 400 GeV on the mass of $H^\pm$, A^0 and H^0.

Charginos

Charginos are fermions with spin 1/2 and charge 1, obtained by the combination of wino $\tilde{\omega}^\pm$ and charged higgsinos $\tilde{H}^\pm$, and indicated with $\tilde{\chi}^\pm_{1,2}$. In the $\tilde{\omega}^\pm$-$\tilde{H}^\pm$ basis the chargino mass matrix is:

$$\tilde{\chi}^{\pm} = \begin{pmatrix} M_2 & \sqrt{2}M_W \sin\beta \\ \sqrt{2}M_W \cos\beta & -\mu \end{pmatrix} \tag{1.25}$$

The mass eigenstates are:

$$\begin{aligned} M^2_{\tilde{\chi}^{\pm}_{1,2}} =& \frac{1}{2}M_2^2 + M_W^2 + \frac{1}{2}M_2^2\mu^2 \\ &\mp \frac{1}{2}M_2^2\left[(M_2^2-\mu^2)^2 + 4M_W^4\cos^2 2\beta + 4M_W^2(M_2^2+\mu^2 - 2M_2\mu\sin^2\beta\right]^{\frac{1}{2}} \end{aligned} \tag{1.26}$$

Conventionally $\tilde{\chi}^{\pm}_1$ is the lightest chargino.

Neutralinos

Bino $\tilde{b}$ and wino $\tilde{\omega}^3$ can mix with the neutral higgsinos H^0 and h^0, generating neutral spin 1/2 particles, neutralinos. The mass matrix, in $\tilde{b}$-$\tilde{\omega}^3$-H^0-h^0 basis, is:

$$M^2_{\tilde{\chi}^0_i} = \begin{pmatrix} M_1 & 0 & -M_Z\cos\beta\sin\theta_W & M_Z\sin\beta\sin\theta_W \\ 0 & M_2 & M_Z\cos\beta\cos\theta_W & -M_Z\sin\beta\cos\theta_W \\ -M_Z\cos\beta\sin\theta_W & M_Z\cos\beta\sin\theta_W & 0 & \mu \\ M_Z\sin\beta\sin\theta_W & -M_Z\sin\beta\cos\theta_W & \mu & 0 \end{pmatrix} \tag{1.27}$$

The four mass follow the convention $M_{\tilde{\chi}^0_1} < M_{\tilde{\chi}^0_2} < M_{\tilde{\chi}^0_3} < M_{\tilde{\chi}^0_4}$.

1.3.3 R-parity

Supersymmetry as described until this point does not prevent lepton and baryon number violating interactions and can allow the proton decay. Since these processes are restricted by many experimental results [52–54], a new symmetry is introduce in order to avoid lepton and baryon numbers violation.

The R-parity is a multiplicative quantum number defined as [55]

$$R = (-1)^{3(B-L)S} \tag{1.28}$$

where S is the spin. Standard Model particles have R-parity +1, while their SUSY partners have R-parity equal to -1.

The assumption of R-parity conservation has many important experimental consequences. SUSY particles can only be pair produced from SM particles and then they decay in a chain until the lightest SUSY particle is produced (LSP). The LSP must be stable and neutral, since there are stringent cosmological constrains on charged and colored particles which are stable [32]: this makes the particle a good Dark Matter candidate. In all the scenarios considered in this thesis, the lightest neutralino $\tilde{\chi}^0_1$ is assumed to be the LSP.

Since the LSP is neutral and colorless, only weak interaction with ordinary matter is possible. Such as neutrinos, the LSP escapes detectors, giving a missing transverse energy signature at experiments at colliders. This point is further explained in Section 4.5.

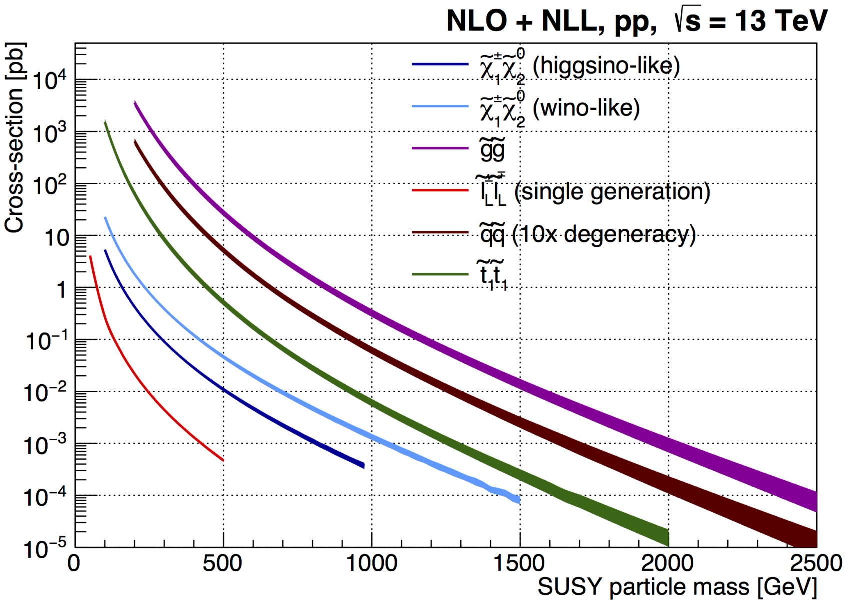

Figure 1.5: SUSY cross section for the production of gluino, squark,stop, chargino-neutralino and slepton pair, at $\sqrt{s}$ = 13 TeV [56].

1.4 Electroweak production of SUSY particles

In this section the SUSY models considered in the analyses addressed in Chapter 6 and Chapter 7 are illustrated. The production cross section of Supersymmetric particles depends on the type of interaction involved and on the masses of the particles themselves. Squarks and gluinos would be produced in strong interactions with significantly larger cross sections than non-colored SUSY particles of equal masses, such as the sleptons and charginos. The cross section for these processes, in the $\sqrt{s}$ = 13 TeV case, are reported in Figure 1.5.

The direct electroweak production can dominate SUSY production at the LHC if the masses of the gluinos and the squarks are significantly larger. With searches performed by the ATLAS and CMS experiments during LHC Run 2, the exclusion limits on squark and gluinos masses extend to up to approximately 2 TeV [18–20], making electroweak production an increasingly promising probe for SUSY signals at the LHC.

The Feynman production diagrams at the leading order for the processes of interest in this Thesis are reported in Figure 1.6. In the proton-proton collision, sleptons, charginos and neutralinos can be produced from quark in a t-channel diagram with the mediation of a squark, or in a s-channel diagram, with the interaction mediated by photon or Z-$W^\pm$ bosons. Since in this work squarks are supposed to be very heavy compared to sleptons, charginos and neutralinos, the production is dominated by the s-channel diagrams.

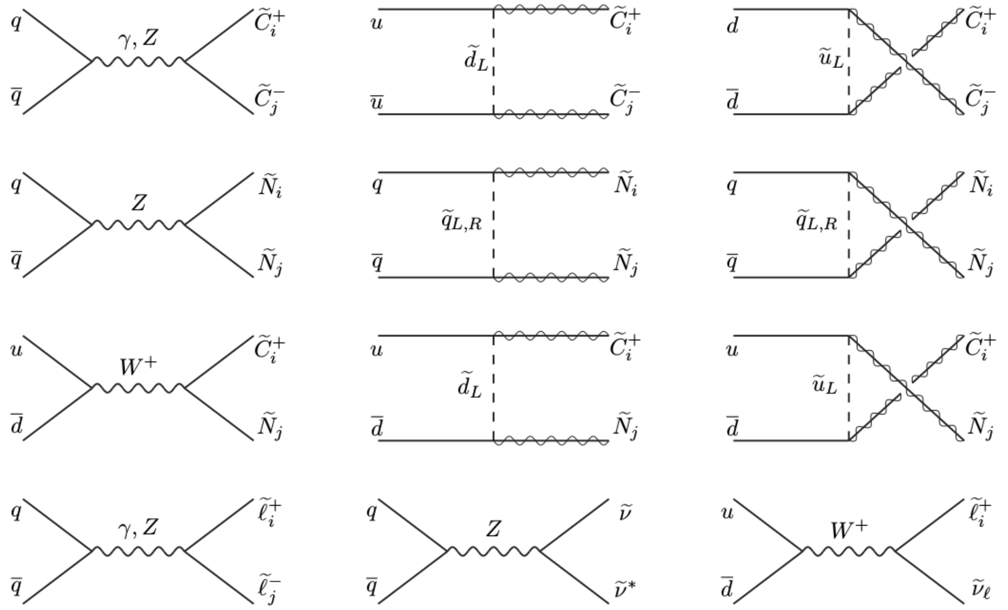

Figure 1.6: Feynman production diagrams for slepton, chargino and neutralino pairs. The t-channel production is supposed to be negligible, since squark are assumed to be very heavy compared to sleptons, charginos and neutralinos. The s-channel mediated by photon, Z or $W^\pm$ is the relevant production channel for this work [35].

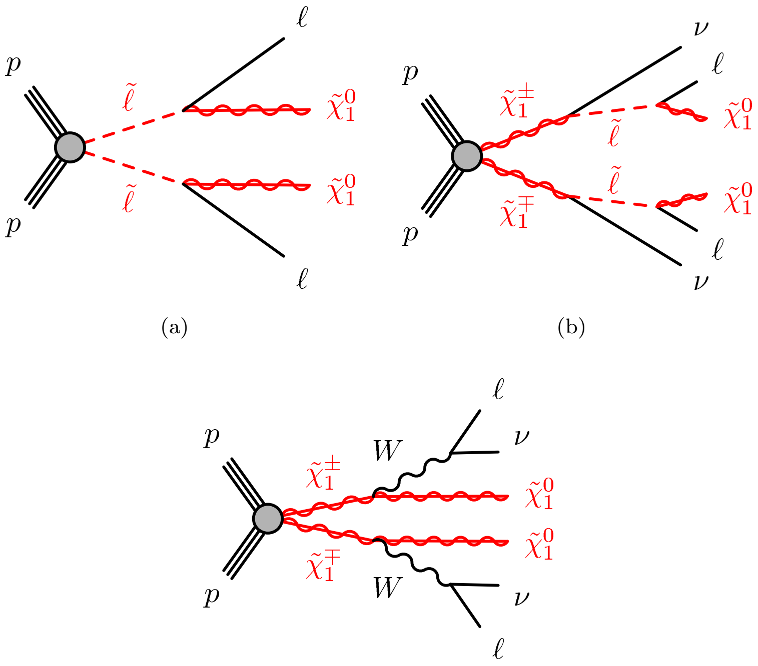

(a) (b)

(c)

Figure 1.7: SUSY models considered in this work: (a) sleptons direct production, (b) charginos direct production with slepton mediated decay, (c) charginos direct production with W boson mediated decay [58, 59].

1.4.1 Simplified Models

Simplified Models [57] are considered in this work. Depending on the hypothesis on the SUSY mass spectrum, many production processes and decay chains can occur. The possible phenomena are classified according to the signature (for example a final state with two leptons and no hadronic activity). All the possible signatures are considered independently and a specific search is optimized for only one signature. The masses of the Supersymmetric particles directly involved are considered as free parameters and the other s-particles are assumed to have significantly larger masses and to be decoupled. The results obtained correspond to the particular production channel, but it is possible to have an interpretation for a different model scaling the cross sections.

The SUSY processes of interest are illustrated in Figure 1.7 and described in the following.

Sleptons direct production

The production diagram of a slepton pair is shown in Figure 1.7(a). The considered sleptons are a *selectron* or a *smuon*, with the same mass (*mass degenerate*) and decaying respectively into an electron or a muon and a neutralino, with a 100% branching ratio.

Sleptons production cross section		
Mass [GeV]	$\tilde{l}_L$ [fb]	$\tilde{l}_R$ [fb]
100	534 ± 18	190 ± 7
200	43.2 ± 1.9	16.2 ± 0.8
300	8.80 ± 0.48	3.34 ± 0.19
400	2.60 ± 0.17	1.00 ± 0.07
500	0.94 ± 0.07	0.36 ± 0.03

Table 1.3: Slepton production cross section at NLO+NLL for selectron and smuons, considered to be mass degenerate, in the LH and RH helicity cases [60, 61].

Direct production of a *stau*, decaying into tau lepton, is also possible, but it is not considered, since tau leptons decay hadronically with a 68% branching ratio and the the analysis developed in Chapter 6 does not include hadronic signature. Furthermore the branching ratio of the tau decaying in an electron or a muon is too small to provide any sensitivity for the stau observation using this decay channel.

The production cross section for LH and RH sleptons are reported in Table 1.3, for slepton masses of 100, 200, 300, 400 and 500 GeV.

The signature of this process is two leptons with same flavor, muons or electrons, and missing transverse energy. No hadronic activity is expected to rise directly from the SUSY process, but it is possible to have initial state radiation.

Charginos direct production with slepton mediated decay

The diagram of the process is reported in Figure 1.7(b). The chargino is supposed to be pure wino state. The charginos are pair produced and then decay into a neutrino and a LH charged or neutral slepton (with 50% branching ratio in each case), the sleptons (charged or neutral) then decay in neutralinos and leptons.

The production cross sections for different chargino masses are reported in Table 1.4: the production cross sections of the chargino as pure higgsino state are also reported for comparison. Comparing the pure wino state cross section with the slepton ones (Table 1.3), the sleptons production cross section is almost fifty times smaller, considering the same mass.

The signature of this process is similar to the sleptons direct production one, with two leptons and missing transverse energy, but in this case leptons can have the same flavor or different flavor.

Charginos direct production with W boson mediated decay

The charginos, considered as pure wino state, are pair produced as illustrated in Figure 1.7(c). Charginos then decay in a W boson and a neutralino, with 100% branching ratio. The leptonic decay of the W boson is then considered, with a 10.8% branching ratio for each leptonic flavor. The production cross section are the same considered in the

Charginos production cross section		
Mass [GeV]	wino [fb]	higgsino [fb]
100	11 611 ± 519	2 884 ± 127
200	903 ± 54	244 ± 14
300	190 ± 13	52.6 ± 3.6
400	58.6 ± 4.7	16.3 ± 1.3
500	22.1 ± 2.0	6.22 ± 0.54
600	9.50 ± 0.91	2.69 ± 0.26
700	4.44 ± 0.46	1.26 ± 0.13

Table 1.4: Chargino production cross sections, considered as a pure wino state or as pure higgsino state [60, 62]: in the pure wino status case the cross section are about four time larger.

previous case (Table 1.4), but due to the W boson decay branching ratio the acceptance is reduced.

As in the previous cases, the signature of the process consists of two leptons and missing transverse energy.

1.4.2 Lifetime and decay width of the SUSY particles

Two important assumptions are considered in the SUSY searches presented in this Thesis: the mean lifetime and the decay width of the slepton and the chargino are both small enough to be negligible from the detection point of view. These hypotheses are discussed in the following.

The sleptons and the charginos are assumed to be much heavier than the SM particles and a large mass split with the neutralino is assumed. As consequence the sleptons and the charginos decay rapidly due to the large number of available final states [63]. In particular, if the mean life time is lower than $\sim$ 100 fs, the SUSY particle will not be able to travel more than $\sim$ 10 μm, that is lower that the detector resolution. As consequence, is possible to observe directly only the decay products and not the primary particles.

Searches for long-living particles, that can travel a considerable distance inside the detector before decaying [64] are also considered by the ATLAS Collaboration and dedicated analyses are developed for these models, but the topic is beyond the scope of this work.

Concerning the decay width of sleptons and charginos, it is assumed to be lower of the energy resolution of the detector, therefore no significant effects are present in the SUSY signal. It is possible to compute the sparticles width with the `SUSYHits` software [65] for the models of interest for this document, since the width range from 70 MeV for a slepton with a 100 GeV mass, to 7 GeV in the case of pure wino state chargino with mass 700 GeV.

Chapter 2

Experimental apparatus

In this Chapter the experimental apparatus is described. A brief introduction on particles collider is given in Section 2.1 and the Large Hadron Collider is presented in Section 2.2. The ATLAS experiment is described in Section 2.3.

2.1 Particle colliders

Particle accelerators and colliders can be linear or circular. Linear accelerators present less technical complication, since no beam steering system is necessary, but the energy is limited by the product of the length and the electric field strength of accelerating cavities, since a long linear accelerator is needed and the beam is used only once. In circular colliders only a short section provides the acceleration to the particles, since the beam travels around the ring multiple times before reaching the designed energy. Furthermore in circular colliders the beam can be used for several collisions. However the beams stability in a circular collider is a crucial point, dipoles and quadrupoles magnets are needed to bend and focus the beam over a long period [66].

Another important point is the particles to be used. In a circular collider using an electron-positron beam (such as LEP), a large amount of energy is loss due to synchrotron radiation:

$$\frac{dE}{dt} \propto \frac{E^4}{m^4 R^2} \tag{2.1}$$

where E and m are the particle energy and mass, and R is the orbit radius. Since the proton mass is very large compared to the electron's, the synchrotron radiation for an hadronic machine is smaller. In particular to reach the same energy with the same orbit, the accelerator need to compensate for a synchrotron radiation loss of the order of $(m_p/m_e)^4 \sim 10^{13}$.

On the other hand, hadrons are not elementary particles, but composed by quarks and gluons. In this case two kinds of interaction are possible [67]

- soft collisions, that are long distance collisions in which the protons behave as elementary particles. Usually the transferred momentum is low, therefore the particles in the final state have small transverse momentum.
- hard collisions, that are short distance collisions, protons interact revealing their inner structure. A large momentum is exchanged and there is a chance to generate new particles. The cross section for hard collisions, which are important for the discovery of new physics, is much smaller than the one for soft collisions.

In the search for new particles, the hard collisions are the ones of interest, but in this case the interaction is between gluons and quarks from the incoming protons and the energy of the parton is just a fraction of the proton energy:

$$\sqrt{\hat{s}} = \sqrt{x_a x_b s} \tag{2.2}$$

where x_a and x_b is the fraction of the proton momentum carried by the partons. The proton-proton hard scattering cross section can be described in terms of a partonic cross section convoluted with the Parton Distribution Functions (PDF) of the partons inside the protons [68]:

$$\sigma_{pp\to X} = \sum_{a,b} \int_0^1 dx_a \int_0^1 dx_b f_a(x_a, Q^2, \mu_F^2) f_b(x_b, Q^2, \mu_F^2) \hat{\sigma}_{ab\to X}(\hat{s}, \mu_F^2, \mu_R^2) \tag{2.3}$$

where Q is the transferred momentum and f_a and f_b are the PDFs. The factorization scale μ_F is the scale at which the PDFs are evaluated. The cross section of the elementary interaction between partons is indicated as $\hat{\sigma}_{ab\to X}$, it is a function of the partonic center of mass energy and of the factorization and renormalization scale μ_R, that is the scale at which the strong coupling constant α_S is evaluated. Parton PDFs for $Q^2 = 10$ GeV^2 and $Q^2 = 10^4$ GeV^2 are reported in Figure 2.1.

2.2 The Large Hadron Collider

The Large Hadron Collider (LHC) [6] is the world's largest particle accelerator and collider, located at CERN, Geneva. The idea of a *hadron collider in the LEP tunnel* was proposed for the first time in 1984, during a CERN and European Committee for Future Accelerators workshop. The CERN council approved the construction of the LHC in 1994 and the collider was built between 1998 and 2008. The collider is hosted in the LEP tunnel, 27 km long and 100 m underground. LHC is designed to accelerate protons and heavy ions, the maximum center-of-mass energy being 14 TeV and the maximum instantaneous luminosity of 10^{34} cm^{-2} s^{-1}. LHC successfully operated between 2009 and 2012, with a center-of-mass energy of 7 and then 8 TeV (Run 1). After a 2 year maintenance shut down, a second data taking period started in 2015, with 13 TeV energy.

2.2.1 CERN accelerators and experiments complex

LHC is the latest stage of the accelerator complex, shown in Figure 2.2. Other machines are used to achieve the energy necessary for the injection to the LHC:

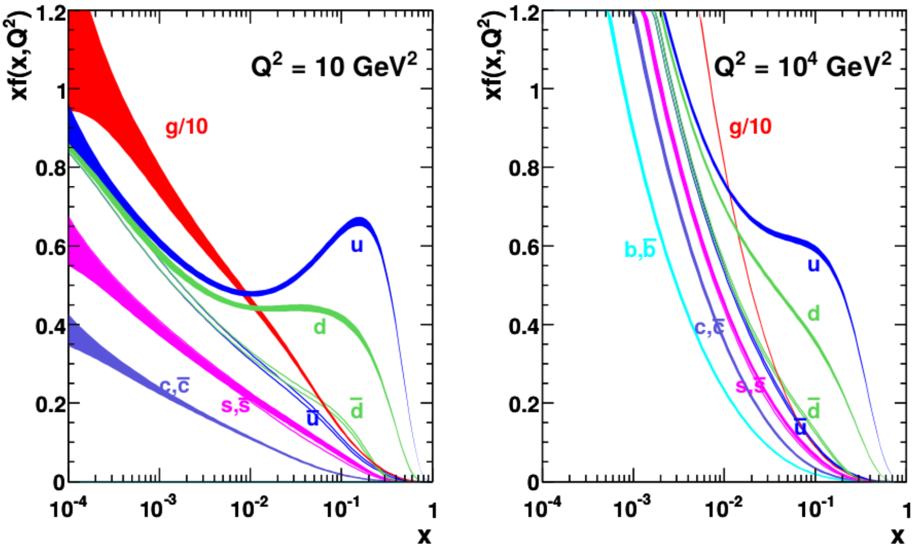

Figure 2.1: Parton distribution function evaluated with MSTW 2008 NLO, at $Q^2 = 10$ GeV^2 and $Q^2 = 10^4$ GeV ^{2} [69]. The band width correspond to the uncertainty.

- the first step is to generate the protons, hydrogen ionized by electric field is used as proton source;
- the first accelerating machine is Linac 2, the proton energy is increased to 50 MeV;
- the next step is the Proton Synchrotron Booster (PSB), where protons reach 1.4 GeV;
- proton beam is then injected in the Proton Synchrotron (PS), the final energy is 25 GeV;
- the last step is Super Proton Synchrotron (SPS), protons are accelerated up to 450 GeV, since this is the proper energy to be injected in the LHC rings.

The LHC provides protons and ions collisions to four main experiments at the interaction points: ATLAS [8] and CMS [9], the two multipurpose detectors, LHCb [70], dedicated to b-physics, and ALICE [71], focusing on heavy-ion physics.

2.2.2 LHC luminosity and pile-up

One of the goals of physics at particles colliders is the discovery of rare processes. Considering a process, the production rate at a collider is given by

$$R = \sigma\left(\sqrt{s}\right)\mathfrak{L} \tag{2.4}$$

$\sigma\left(\sqrt{s}\right)$ is the production cross section, that is a function of the machine center of mass energy. A collider with larger energy is going to increse the discovery opportunity. $\mathfrak{L}$ is

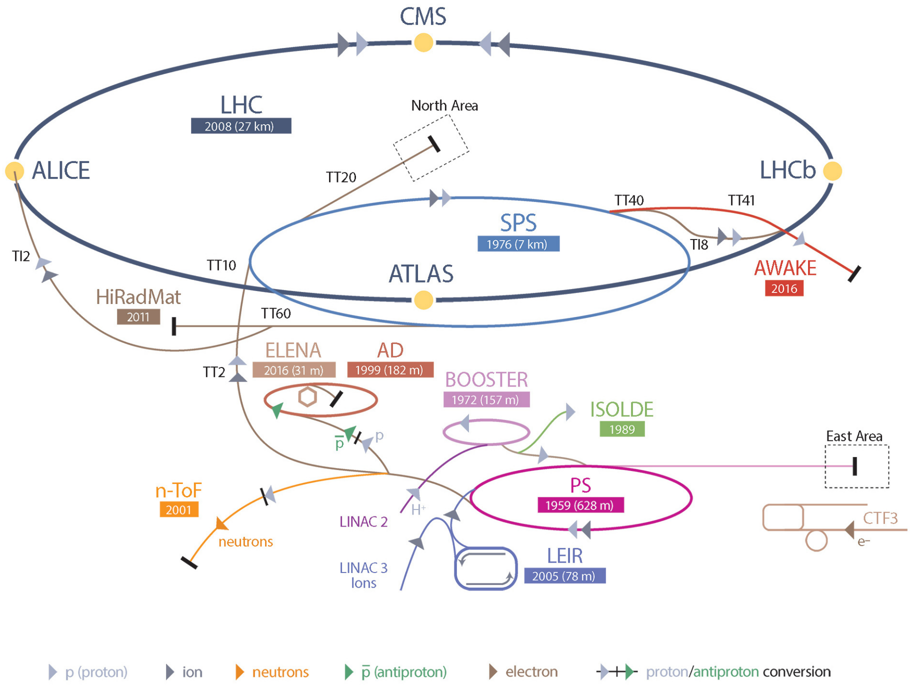

Figure 2.2: Schematic of the CERN accelerators complex and of the experiments that utilizing the beams [72].

the instantaneous luminosity, that depends on many machine parameters:

$$\mathfrak{L} = \frac{N_b^2 n_b f_r \gamma}{4\pi \epsilon_n \beta^*} F \tag{2.5}$$

where:

- N_b is the numbers of particles in each bunch;
- n_b is the number of bunches in each beam;
- f_r is the revolution frequency;
- γ is the relativistic Lorentz factor;
- ϵ_n is the transverse beam emittance, normalized to the beam momentum;
- β^* is the focusing function at the collision point;
- F is the geometric luminosity reduction factor due to the crossing angle at the interaction point.

In the LHC, the spacing between bunches is 25 ns. After completing the injection of all the bunches, the beams are accelerated up to 6.5 TeV and then focused. The collisions can start and once the *stable beam* status is declared, the experiments can begin the data taking. The LHC beams luminosity is not constant during the data taking period because of the beam degradation, beams collision being one of the first causes of degradation. The time available for data taking after stable beam declaration is called *physics run*. Once the beams luminosity is too low, it is convenient to dump the beams and start a new injection. The LHC cycle is summarized in Figure 2.3.

Another important parameter is the integrated luminosity, defined as:

$$L = \int_0^T \mathfrak{L} dt \tag{2.6}$$

where T correspond to the data taking period. The integrated luminosity delivered by the LHC per year is reported in Figure 2.4. Due to the improved luminosity, each year is possible to have more data in a shorter time. The integrated luminosity collected by ATLAS, after data quality requirement (illustrated in Section 3.2), during 2015 was 3.2 fb^{-1}, during 2016 32.9 fb^{-1} and 44.3 fb^{-1} in 2017.

Increasing the instantaneous luminosity, the mean number of inelastic interactions per bunch crossing is increasing too: these collision are called *pile-up events.* These events are originated mainly from soft collisions, so they are not interesting for the new physics searches, they represent a source of background. Large pile-up deteriorates the energy resolution for object measurement and makes the identification of vertices and the reconstruction of tracks more difficult due to the larger number of hits in the tracker. The amount of pile-up is parametrized in terms of the mean number of interactions per bunch crossing $< \mu >$. During 2015 $< \mu >$ was 13.4, it increased to 25.1 during 2016 and then to 37.8 in 2017 data taking. Pile-up distribution per year are reported in Figure 2.5.

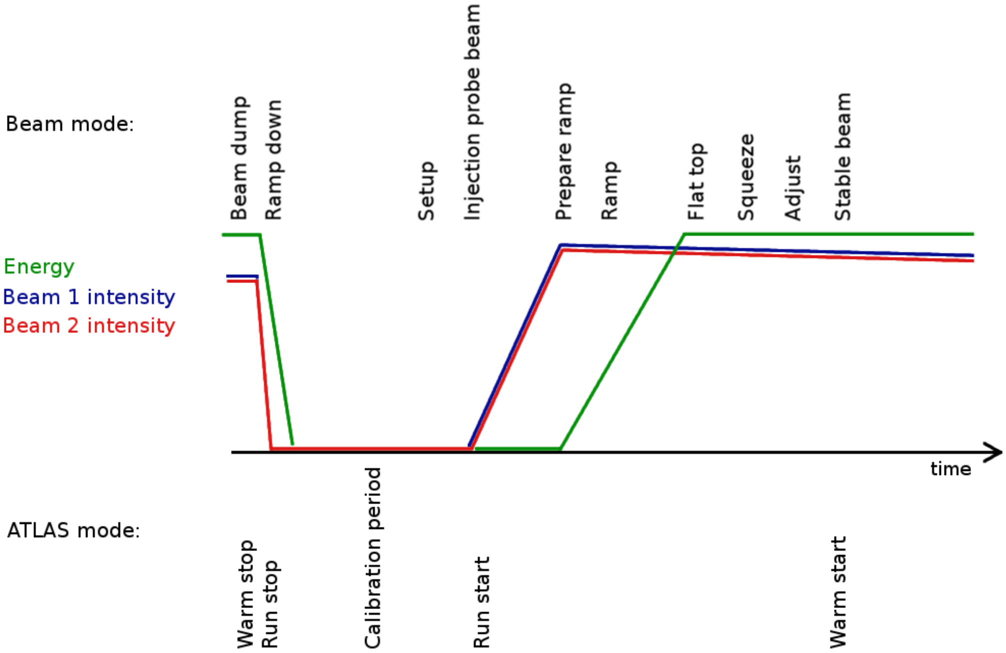

Figure 2.3: Summary of the LHC beam modes, as function of the intensity and the energy of the beams. The ATLAS operations are also reported.

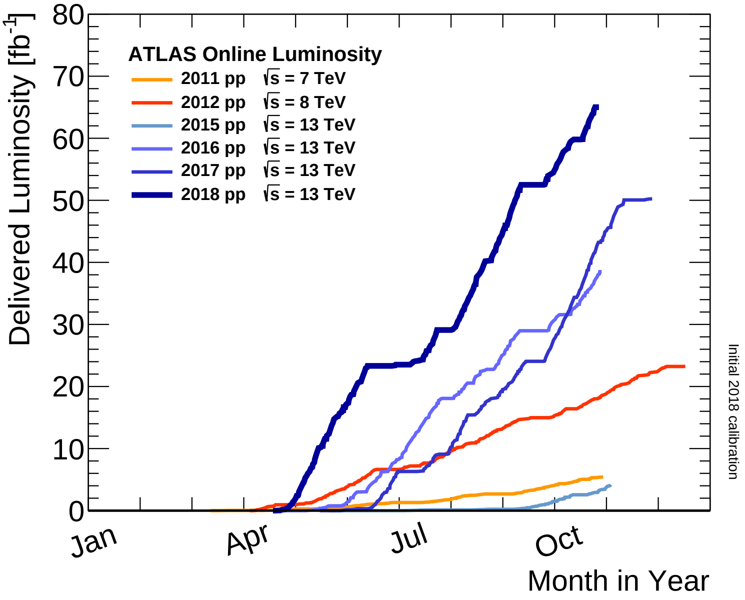

Figure 2.4: Cumulative luminosity delivered to ATLAS during stable beams, for p-p collisions, as a function of time [73].

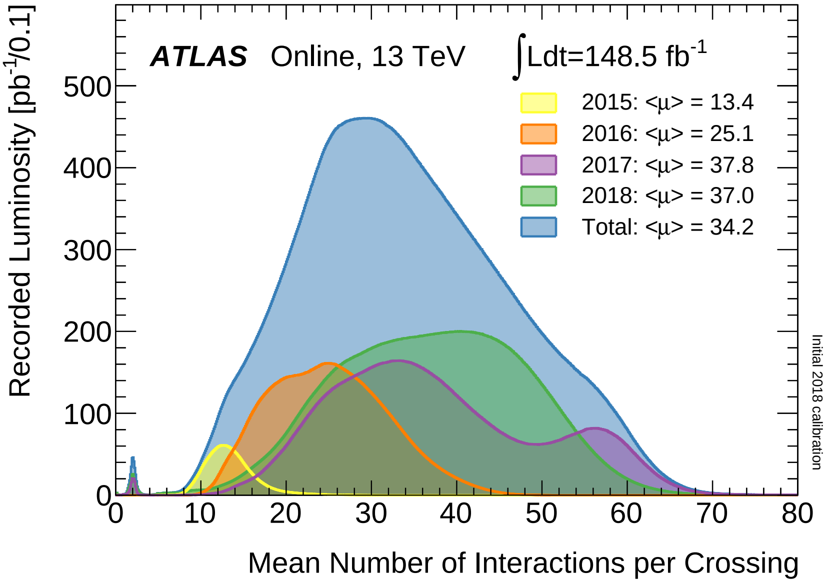

Figure 2.5: Luminosity-weighted distribution of the number of interactions per crossing during 2015, 2016, 2017 and 2018 data taking [73].

2.3 The ATLAS experiment

The ATLAS detector (*A Toroidal LHC ApparatuS*) is a general purpose experiment, designed to explore a wide range of physical processes [8]. The ATLAS collaboration proposed to built the detector in 1992, in order to take advantage of the discovery potential of the upcoming Large Hadron Collider. The technical proposal was submitted to the LHC Experiments Committee in 1994 and approved in 1996.

ATLAS is located in an underground cavern, 100 m deep, that was built expressly to host the experiment, since ATLAS is larger then any LEP experiment. The cavern was completed in 2003 and the installation of the detector began soon after. The detector was completed in 2008 and the first LHC collisions were recorded in 2009.

The ATLAS detector (Figure 2.6) has a cylindrical layout, providing an almost full coverage of the solid angle around the interaction point. The cylinder diameter is 25 m and the lenght is 44 m, with a weight of 7000 tons. A cartesian coordinate system originates from the interaction point (Figure 2.7). The z-axis points in the direction of the beam clockwise, the x-axis points at the center of LHC ring. Transverse quantities (like transverse momentum) are defined in the $x-y$ plane. Due to the cylindrical symmetry, a cylindrical coordinate system is also used, ϕ being the azimutal angle (around the beam axis), θ the polar angle (from the beam axis). Pseudo-rapidity is often used instead of the polar angle:

$$\eta = -\log\tan\frac{\theta}{2} \tag{2.7}$$

The angular distance using η and ϕ is defined as:

$$\Delta R = \sqrt{(\Delta\eta)^2 + (\Delta\phi)^2} \tag{2.8}$$

The ATLAS detector is composed by many sub detectors:

- *Inner Detector*: the most internal part is dedicated to tracking charged particles and vertex reconstruction. High-resolution semiconductor detectors and straw-tube tracking detectors are used. The Inner Detector is placed inside a solenoid which provides a 2 T magnetic field.

- *Calorimeters*: placed outside the solenoid, calorimeters are composed of sampling electromagnetic and hadronic calorimeters with either liquid Argon (LAr) or scintillating tiles as active medium. The main goal is the electrons, photons and hadrons energy measurement.

- *Muon Spectrometer*: the muon system surrounds the calorimeter. A combination of high precision tracking chambers and fast triggering chambers is used. An air-core toroid system generates the magnetic field and gives strong bending power.

2.3.1 Magnet system

A schematic view of the ATLAS magnetic system is shown in Figure 2.8, it is composed of:

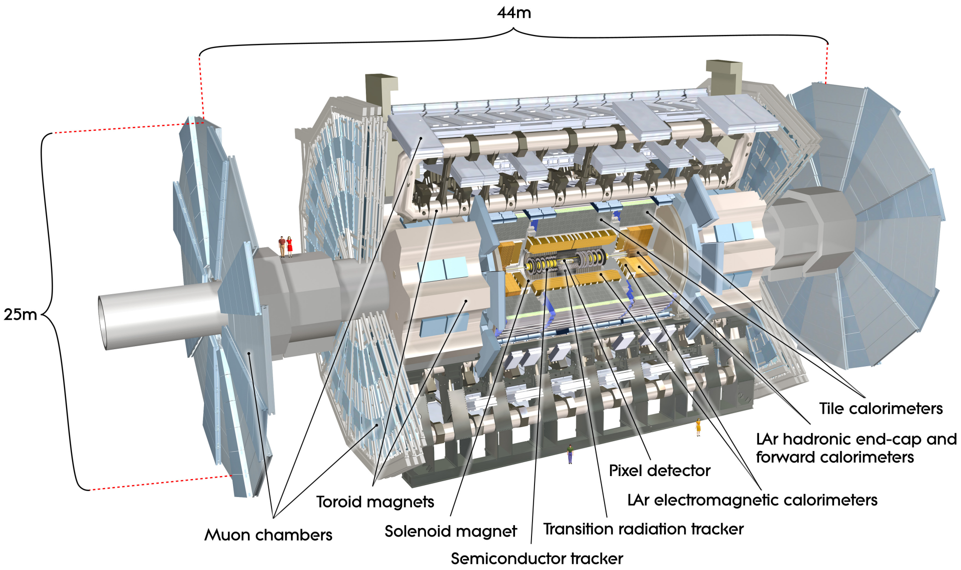

Figure 2.6: Representation of the ATLAS detector [8].

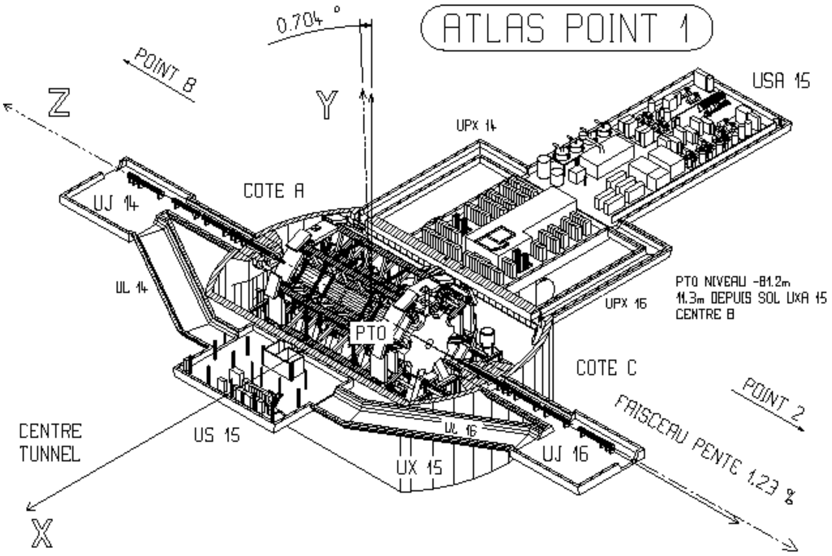

Figure 2.7: ATLAS cartesian coordinate system [8].

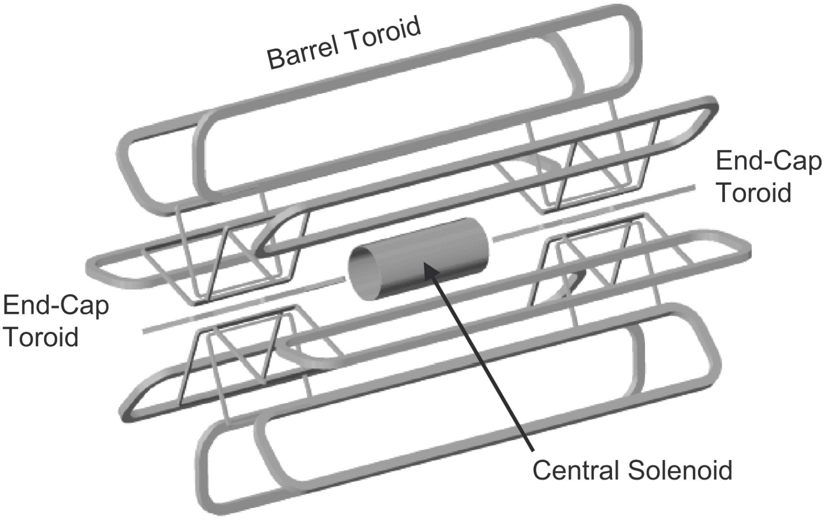

Figure 2.8: Schematic view of of the four ATLAS magnets [8].

- the central solenoid [74], a superconducting material coil with 2.3 m diameter and 5.3 m long. It is located between the Inner Detector and the Calorimeters and provides a 2 T magnetic field to the Inner Detector, in the direction of the beam. Since the solenoid is in front of the Calorimeters, it has to be as thin as possible in order to minimize the amount of material. The thickness is only 5 cm, corresponding to 0.66 radiation lengths. It is placed inside the Calorimeters cryostat and cooled down to a temperature of 4.5 K.

- the toroids, the magnetic field needed for the Muon Spectrometer is provided by a barrel toroid [75] and two end-cap toroids [76] with eight separates coils each. They provide a 0.5 T magnetic field in the barrel region and 1 T for the end-caps. The barrel toroid has an inner diameter of 9.4 m, an outer diameter of 20.1 m, and it is 25.3 m long. The end-cap toroids are 5.0 m axial long, with a 10.7 m outer diameter The system is air-core and is able to generate a strong bending power in a large volume, while minimizing multiple scattering effects.

2.3.2 Inner detector

The Inner Detector [77, 78] is the inner-most ATLAS sub-detector, with a cylindrical shape around the beam pipe. The diameter is 2.1 m and the length 6.2 m, the η coverage is up to 2.5. The detector is designed to provide pattern recognition, excellent momentum resolution of charged particles and vertex reconstruction capability. Due to the proximity to the interaction point, radiation hardening to high flux of radiation is required for all the components. The subdetector structure (Figure 2.9) is the following:

- the Pixel Detector [79], constituted by silicon sensors, is the closest to the beam pipe. It is arranged in 4 cylindrical layers placed at 33, 51, 89 and 123 mm from the interaction point and in three disk for each end-cap. The first cylindrical layer is called Insertable B-Layer (IBL) [80], it was installed during the fist long shutdown after LHC Run 1. The IBL pixel dimensions are 50×250 μm^2, all the other pixels are 50×400 μm^2. The Pixel Detector, due to its closeness to the interaction point, is the one with the highest granularity and spacial resolution. These features allow an excellent discrimination between close tracks and to reconstruct the vertices of the decay the B and D meson and tau leptons. The pixel intrinsic hit position resolution is 12 μm in the transverse plane (R-ϕ) and 72 μm in the first layer and 115 μm for the other three layers along the z direction. The Pixel Detector provides generally four points for each particle crossing the detector.

- the Semiconductor Tracker (SCT) is a silicon microstrip detector [81,82]. The strips are arranged in four cylindrical layers outside the Pixel Detector and in nine disks for each end-cap. Each layer and disk has two set of sensor, mounted with different angle, to provide the measurement of the two coordinates. The layers distance from the interaction point is 299, 371, 443 and 514 mm. The nine layers in the end-cap are located at distance of 854, 934, 1092, 1300, 1400, 1771, 2115, 2505 and 2720 mm from the interaction point. The intrinsic resolutions is 17 μm in the transverse plane (R-ϕ) and 580 μm along the z direction.
- the Transition Radiation Tracker (TRT) [83,84] is the outer part of the Inner Detector and consists of 4 mm straw tubes with a 0.03 mm diameter gold-plated tungsten wire and filled with Xenon and Argon based gas mixture. The space between the straws is filled with polymer fibers in order to create transition radiation. There are 50 000 straws in the barrel and 250 000 for each end-cap. The TRT extension is from 0.55 m to 1.08 m from the interaction point. The TRT provides around 36 space-points for each track, with an intrinsic hit resolution of 130 μm in the transverse plane (R-ϕ). The TRT purpose is not only to provide additional hits for the tracks reconstruction and momentum measurement, but also to help in discriminating electrons from pions.

The Inner Detector expected resolution for different track parameters is reported in Table 2.1, where d_0 and z_0 are respectively the distance to the beam axis in the transverse and longitudinal planes, p_{T} is the particle momentum in the transverse plane.

2.3.3 Calorimeters

The main purpose of calorimeters is measuring the energy and direction of hadrons, electrons and photons, and giving a fundamental contribution in the measurement of the missing transverse energy. ATLAS calorimetric system, shown in Figure 2.10, consists of three different calorimeter types: the Electromagnetic Calorimeter (EM) that covers the pseudo-rapidity region $|\eta| < 3.2$, the Hadronic Calorimeter (Had) covering the region $|\eta| < 3.9$ and the Forward Calorimeter (FCal) which covers the region $3.1 < |\eta| < 4.9$.

A brief description of the different calorimeters is provided in the following:

- Electromagnetic Calorimeters, extend up to a radius of 2.25 m and are 6.65 m long [86]. They cover the pseudo-rapidity region of $|\eta| < 3.2$, divided into a barrel

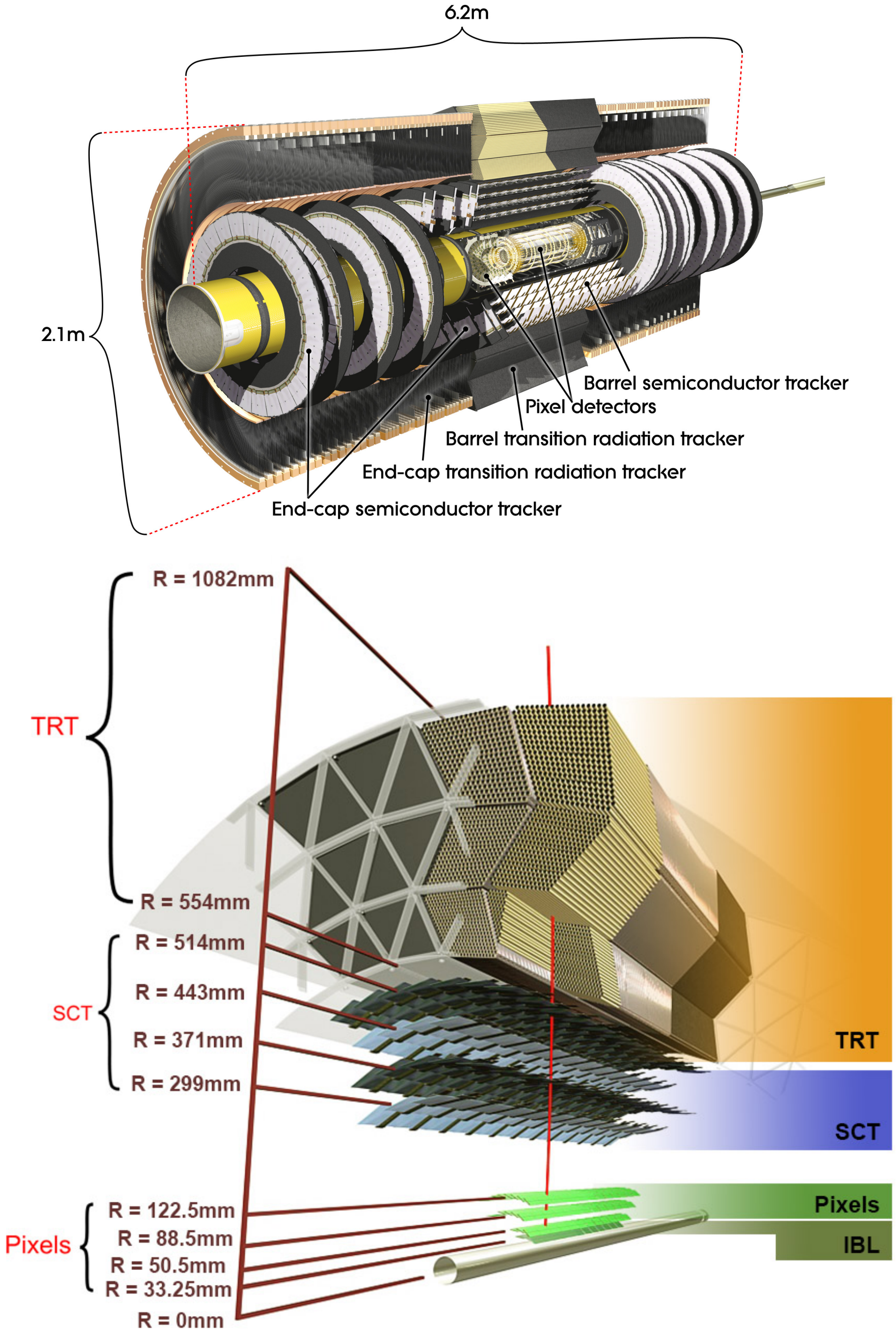

Figure 2.9: Illustrations of the ATLAS Inner Detector [8].

Inner Detector resolution		
Track parameter	Resolution	Units
Transverse impact parameter	$\sigma(d_0) \simeq 11 \oplus 73/(p_\mathrm{T}\sqrt{\sin\theta})$	μm
Longitudinal impact parameter	$\sigma(z_0) \simeq 87 \oplus 115/(p_\mathrm{T}\sqrt{\sin^3\theta})$	μm
Inverse transverse momentum	$\sigma\left(\frac{1}{p_\mathrm{T}}\right) \simeq 0.36 \oplus 13/(p_\mathrm{T}\sqrt{\sin\theta})$	TeV^{-1}
Azimuthal angle	$\sigma(\phi) \simeq 0.075 \oplus 1.8/(p_\mathrm{T}\sqrt{\sin\theta})$	mrad
Cotangent polar angle	$\sigma(\cot\theta) \simeq 0.70 \oplus 2.0/(p_\mathrm{T}\sqrt{\sin^3\theta})$	10^{-3}

Table 2.1: Inner Detector resolution for different track parameters [85].

part ($|\eta| < 1.5$, EMB) and two end-cap components ($1.4 < |\eta| < 3.2$, EMEC), each one placed in its own cryostat. EM is a sampling calorimeter, using lead as absorber and Liquid Argon (LAr) as the sensitive medium. The layers of electrodes and absorbers are bent with accordion shape and immersed in a LAr vessel: using this structure the full azimuthal angle ϕ is covered without non-sensitive regions from the outgoing readout cables. The calorimeters are also segmented in 3 longitudinal layers in the $0 < |\eta| < 2.5$ region and two in the higher η region ($2.5 < |\eta| < 3.2$). An additional layer of LAr in front of the calorimeter in the regions up to $|\eta| < 1.8$ is also present. It is called pre-sampler and its purpose is to measure the energy deposits from electromagnetic showers starting before reaching the calorimeter. The total EM calorimeter depth is approximately 25 radiation lengths for all the η regions. The EM energy resolution is

$$\frac{\sigma}{E} \simeq \frac{10-17\%}{\sqrt{E}} \oplus 0.7\% \tag{2.9}$$

where the energy is expressed in GeV and the first term depends on η.

- Hadronic Calorimeter, extend up to a radius of 4.25 m radius and is 6.10 meters long, it covers the pseudo-rapidity region of $|\eta| < 3.2$, in the central part with $|\eta| < 1.7$. A sampling calorimeter (TileCal) with scintillating tiles and steel as passive medium is used in the barrel [87]. The end-cap sections of the hadronic calorimeter (HEC) use LAr as active material and copper as absorber and it is placed in separate cryostat together with the forward calorimeters. The thickness of the calorimeter is 11 interaction lengths in the $\eta = 0$ region. The energy resolution for hadronic jets, combined with electromagnetic calorimeter, is

$$\frac{\sigma}{E} \simeq \frac{50\%}{\sqrt{E}} \oplus 3\% \tag{2.10}$$

- Forward Calorimeters [88], covering the pseudo-rapidity region $3.1 < |\eta| < 4.9$. This region of the detector is exposed to extremely high fluxes of particles; the ability of coping with these conditions drives the design of this component. The FCal is located at 4.7 m from the interaction point and consists of three longitudinal

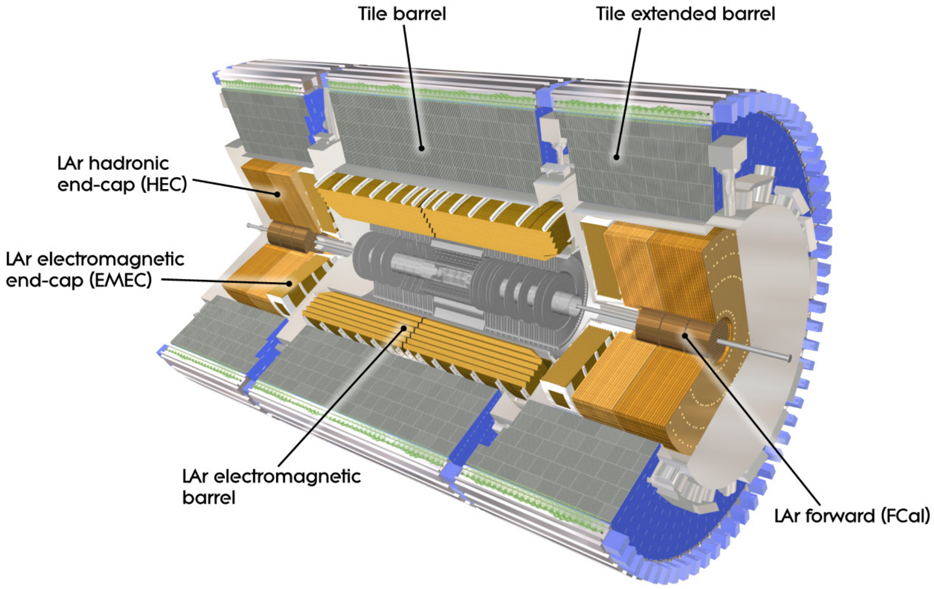

Figure 2.10: Illustration of ATLAS Calorimeters system [8].

layers: an electromagnetic calorimeter and two hadronic calorimeters. The active medium for all of them is LAr, while copper is employed as passive medium in the electromagnetic part and tungsten is used in the hadronic parts. The thickness of all the calorimeters is 10 interaction lengths. The energy resolution of the FCal is:

$$\frac{\sigma}{E} \simeq \frac{100\%}{\sqrt{E}} \oplus 10\% \tag{2.11}$$

A summary of the calorimeter geometry is reported in Table 2.2: coverage, granularity and longitudinal segmentation are reported for each sub-system.

2.3.4 Muon spectrometer

The Muon Spectrometer (MS) is the outer part of ATLAS experiment [89]. All the particles produced in the proton-proton collision are absorbed by the calorimeters (except for neutrinos), only muons are able to reach the Spectrometer. The purpose is the high precision measurement of the muon momentum, track reconstruction and trigger, using the magnetic field generated by toroid magnets. The MS is composed by a central barrel, with three layer at radii of approximately 5 m, 8 m, and 10 m, and four wheels for each end-cap, at 7 m, 11 m, 15 m and 22 m from the interaction point. The detector design is reported in Figure 2.11. The MS chambers can operate at room temperature and four different technologies are used according to the requirements of momentum precise measurement (covering the pseudo-rapidity region $|\eta| < 2.7$) and timing for trigger purpose (region $|\eta| < 2.4$):

Calorimeters geometry			
EM calorimeter	Barrel	End-cap	
Coverage	$\|\eta\| < 1.475$	$1.375 < \|\eta\| < 3.2$	
Longitudinal segmentation	3 samplings	3 samplings	$1.5 < \|\eta\| < 2.5$
		2 samplings	$1.375 < \|\eta\| < 1.5$
			$2.5 < \|\eta\| < 3.2$
Granularity ($\Delta\eta \times \Delta\phi$)			
Sampling 1	0.003×0.1	0.025×0.1	$1.375 < \|\eta\| < 1.5$
		0.003×0.1	$1.5 < \|\eta\| < 1.8$
		0.004×0.1	$1.8 < \|\eta\| < 2.0$
		0.006×0.1	$2.0 < \|\eta\| < 2.5$
		0.1×0.1	$2.5 < \|\eta\| < 3.2$
Sampling 2	0.025×0.025	0.025×0.025	$1.375 < \|\eta\| < 2.5$
		0.1×0.1	$2.5 < \|\eta\| < 3.2$
Sampling 3	0.05×0.025	0.05×0.025	$1.5 < \|\eta\| < 2.5$
Presampler	Barrel	End-cap	
Coverage	$\|\eta\| < 1.52$	$1.5 < \|\eta\| < 1.8$	
Longitudinal segmentation	1 sampling	1 sampling	
Granularity ($\Delta\eta \times \Delta\phi$)	0.025×0.1	0.025×0.1	
Hadronic Tile	Barrel	End-cap	
Coverage	$\|\eta\| < 1.0$	$0.8 < \|\eta\| < 1.7$	
Longitudinal segmentation	3 samplings	3 samplings	
Granularity ($\Delta\eta \times \Delta\phi$)			
Sampling 1 and 2	0.1×0.1	0.1×0.1	
Sampling 3	0.2×0.1	0.2×0.1	
Hadronic Lar		End-cap	
Coverage		$1.5 < \|\eta\| < 3.2$	
Longitudinal segmentation		4 samplings	
Granularity ($\Delta\eta \times \Delta\phi$)		0.1×0.1	$1.5 < \|\eta\| < 2.5$
		0.2×0.2	$2.5 < \|\eta\| < 3.2$
Forward calorimeters		Forward	
Coverage		$3.1 < \|\eta\| < 4.9$	
Longitudinal segmentation		3 samplings	
Granularity ($\Delta\eta \times \Delta\phi$)		0.2×0.2	

Table 2.2: Pseudo-rapidity coverage, granularity and longitudinal segmentation of the ATLAS Calorimeters [85].

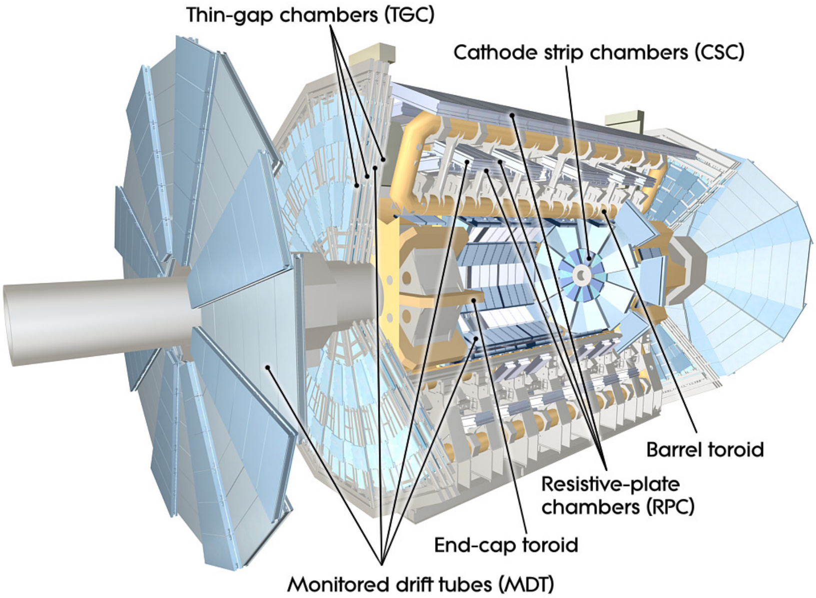

Figure 2.11: Illustration of ATLAS Muon Spectrometer [8].

- Monitored Drift Tube (MDT) chambers provide a precise momentum measurement in the bending plane in the region with $|\eta| < 2.7$. The chambers are built of cylindrical aluminum drift tubes, with 30 mm radius and filled with a Ar/CO_2 mixture of gases, and a central wire at high potential. These chambers consist of three to eight layers of drift tubes, providing an intrinsic resolution of 35 μm per chamber.

- Cathode-strip chambers (CSC) are multi-wire proportional chambers with high rate capability and time resolution, used for the muon momenta measurement in the forward region ($2 < |\eta| < 2.7$). The cathode planes of these chambers are segmented into strips in orthogonal directions, in order to measurement both coordinates. The intrinsic resolution in the bending plane is 40 μm and approximately 5 mm in the transverse plane.

- additional fast chamber are used for trigger purpose: Resistive Plate Chambers (RPC) in the barrel region ($|\eta| < 1.05$) and Thin Gap Chambers (TGC) in the end-caps ($1.05 < |\eta| < 2.4$). The intrinsic time resolution is 1.5 ns for RPC and 4 ns for TGC.

The overall transverse momentum resolution for the Muon Spectrometer is:

$$\frac{\sigma}{p_{\mathrm{T}}} \simeq \frac{0.29\ \mathrm{GeV}}{p_{\mathrm{T}}} \oplus 0.043 \oplus 4.1 \times 10^{-4}\mathrm{GeV}^{-1} \times p_{\mathrm{T}} \tag{2.12}$$

2.3.5 Data acquisition and trigger system

The LHC provides to the experiments collisions with really high rate: a bunch crossing every 25 ns, with 33 proton-proton collisions per bunch crossing (average value for the full Run 2). Since it is not possible to save the full amount of information, a trigger system is used [90, 91]. The event rate is decreased from the nominal bunch crossing rate of 40 MHz to about 1 kHz, that is the maximum rate at which data can be saved. The ATLAS trigger and data acquisition system (TDAQ) is summarized in Figure 2.12. The trigger consists of two separated steps:

- Level 1 Trigger (L1), hardware-based. The decision is formed by the Central Trigger Processor (CTP), using inputs from the Calorimeters and the Muon Spectrometer, as well as several other subsystems (Minimum Bias Trigger Scintillators, LUCID Cherenkov counter and Zero-Degree Calorimeter), in order to find objects with large transverse momentum. One or more Regions-of-Interest (RoI) are defined by L1 trigger for each event. The L1 decision is taken in less then 2.5 μs and it reduces the event rate to about 100 kHz.

- High-Level Trigger (HLT), software-based. After L1 acceptance, events are buffered in the Read-Out System (ROS) and then processed by the HLT. RoI information is reconstructed by trigger algorithms. Accepted events are transferred as RAW data to local storage at the ATLAS site and then to the Tier-0 facility at CERN Computing Center.

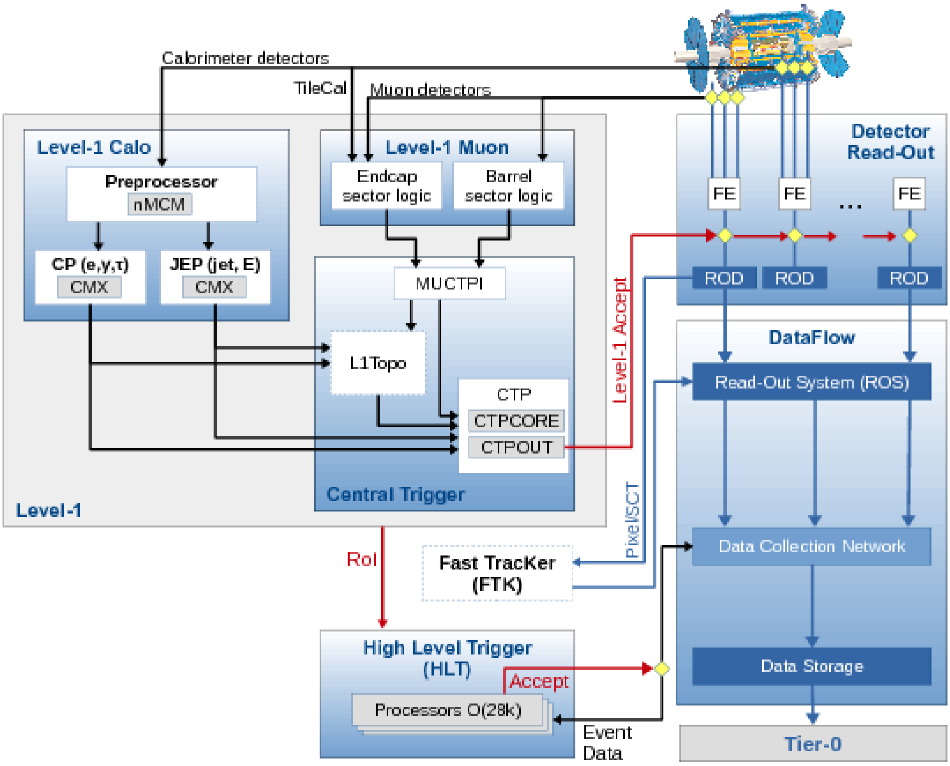

Figure 2.12: ATLAS trigger and data acquisition system [91].

Chapter 3

ATLAS data set

This Chapter provides a brief description of the data collected by the ATLAS detector. Section 3.1 specifies the set of data used in analyses presented in this Thesis. Section 3.2 and Section 3.3 describe the calibration procedure and data quality requirement. The computing network, the ATLAS software and the data format are presented in Section 3.4.

3.1 Data set

The analyses presented in Chapter 6 and Chapter 7 use the data collected by the ATLAS detector during the LHC proton-proton collisions, between 2015 and 2017. The amount of data collected by ATLAS in the period of interest is presented in Figure 3.1, as a cumulative luminosity function of the time: the plot reports the total luminosity delivered by LHC, the amount of data recorded by ATLAS [92] and the data passing the quality requirements necessary to be used in physics analyses.

3.2 Data preparation

Before being used for physics analyses, the data undergo several step. Events passing the HLT selection are assigned to one or more *streams*, depending on which class of triggers they fired: physics, express and calibration [94]. The same event can end up in different streams, since the express stream has a subset of the events in the physics stream. Physics stream contains the data to be used in physics analyses, while events in the express and calibration streams are used for quality check and calibration.

Data are stored at the Tier-0 Facility at CERN Computing Centre and then undergo the *Propt Calibration Loop* [93]. The various steps are summarized in Figure 3.2 and described in the following:

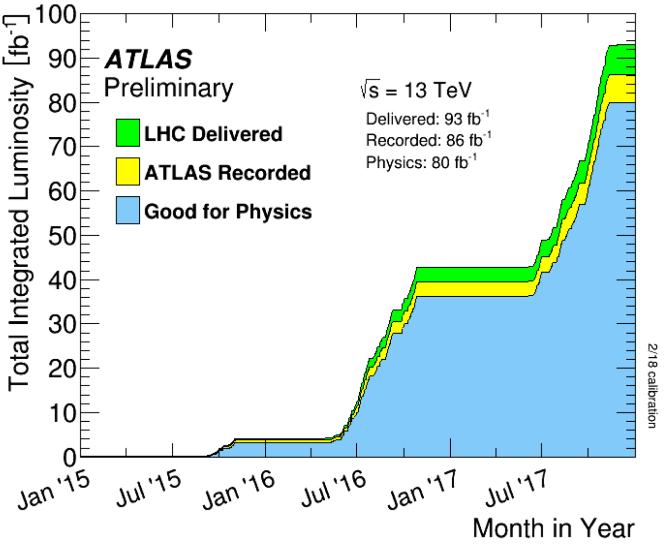

Figure 3.1: Cumulative luminosity, as a function of time: delivered to ATLAS in green, recorded by ATLAS in yellow, and certified to be good quality data in blue (entering GRL), for the 2015-2017 data taking [73].

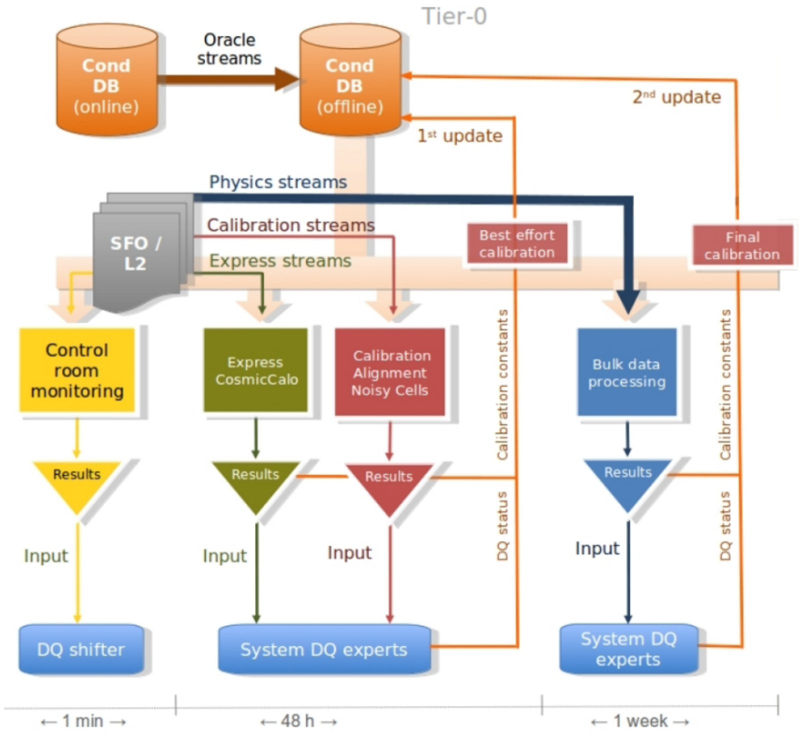

Figure 3.2: Scheme of the ATLAS data preparation Prompt Calibration Loop [93].

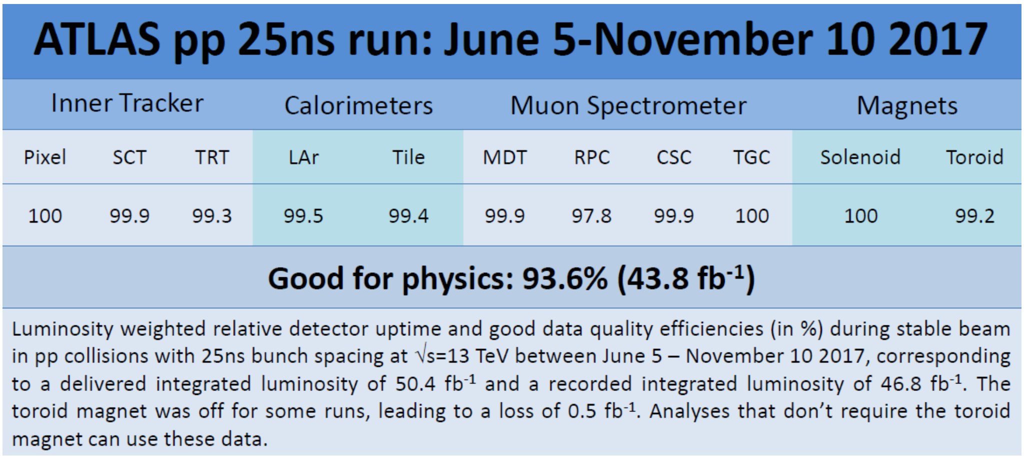

ATLAS pp 25ns run: June 5-November 10 2017

Inner Tracker			Calorimeters		Muon Spectrometer				Magnets	
Pixel	SCT	TRT	LAr	Tile	MDT	RPC	CSC	TGC	Solenoid	Toroid
100	99.9	99.3	99.5	99.4	99.9	97.8	99.9	100	100	99.2

Good for physics: 93.6% (43.8 fb^{-1})

Luminosity weighted relative detector uptime and good data quality efficiencies (in %) during stable beam in pp collisions with 25ns bunch spacing at $\sqrt{s}$=13 TeV between June 5 – November 10 2017, corresponding to a delivered integrated luminosity of 50.4 fb^{-1} and a recorded integrated luminosity of 46.8 fb^{-1}. The toroid magnet was off for some runs, leading to a loss of 0.5 fb^{-1}. Analyses that don't require the toroid magnet can use these data.

Figure 3.3: Fraction of the integrated luminosity good for physics, after all the data quality requirement, for the 2017 data taking. For each subsystem, the percentage of good quality data provided is reported [95].

- a preliminary step is the online monitoring from the ATLAS control room. A fraction of events from the express stream is reconstructed in order to produce monitoring histograms within minutes of the data being recorded. The data quality shifter provides a fast feedback and minimizes the data losses;
- the second data quality check is done using the express stream, in particular the CosmicCalo subset. Cosmic ray events provide a broad coverage for potential problems and it is possible to give an early warning to the data preparation team that will perform the further steps;
- the data calibration is performed (third column of Figure 3.2). Many dedicated calibrations needed to maximize the detector and physics performance, as example correcting detector mis-alignments and determining the beamspot position.

After the Calibration Loop, the data can be reconstructed. From the sub-detectors informations, physical objects as electrons, muons, jets, photon and missing energy are identified and their properties are measured. The detail about the procedure are described in Chapter 4.

3.3 Good run list

Events passing all the data quality assessment enter in the Good Run List (GRL), that indicates the sub set of data that are suitable for physics analysis. The GRL removes luminosity blocks (1-2 minutes of data-taking) affected by detector problems, for example issues concerning liquid Argon system and SCT from Inner Detector, or also incomplete events. Events passing the GRL requirement enter in the integrated luminosity computation. The GRL for the 2015 data taking provides an integrated luminosity of 3.2 fb^{-1}; in

2016, 32.9 fb^{-1} of good quality data were collected; the 2017 data in the latest available GRL have a 44.3 fb^{-1} integrated luminosity.

Figure 3.3 reports the luminosity weighted relative fraction of good quality data delivery by the various components of the ATLAS detector subsystems during the 2017 data taking. The data refer to a older GRL, so the integrated luminosity is 43.8 fb^{-1} , while the luminosity used in the analysis for 2017 data set is 44.3 fb^{-1}.

3.4 Computing network, software framework and data format

The ATLAS experiment produces a huge amount of data, that are used by thousand collaborators all over the world. Adequate computing network and common analysis framework and data format are needed.

The Worldwide LHC Computer Grid is a global network of computer centers, that provides resources to store, distribute and process the data collected by the LHC experiments. The Grid consist of 170 centers across 41 countries. These computer centers are group together in four levels of Tiers, Tier-0 being the CERN Computing Center, while Tier-1, 2 and 3 are localized around the world and provides a different set of services.

`ATHENA` is the ATLAS software framework [96] and it used to reconstruct data, perform Monte Carlo simulation and physics analyses. `ATHENA` consist of many packages, written in `C++` language, and they can be executed by Python script (*jobOptions*). Two different `ATHENA` release were used in the work presented in this thesis: release 20.7, in used from 2015 to 2016, and release 21.0, in used since 2017.

The common data format currently used by the Collaboration are:

- RAW data: after being accepted by the HLT, ATLAS data are stored at the Tier-0;
- xAOD (Analysis Object Data) are the reconstructed and calibrated data;
- xAOD derivation (DAOD), performed through the Derivation Frameworks, are xAOD with a reduced set of information, in order to be more analysis-specific;
- Ntuples, each analysis group produce private samples starting from the derivation. `ATHENA` or `root` based framework can be used.

CHAPTER 4

ATLAS physics objects reconstruction

The particles produced by the LHC proton-proton collisions or in the decays of other particles are stored in term of the electric signals acquired in the various ATLAS sub-detectors. The combined information collected from the sub-detectors is used for the particles identification and the precise measurement of their properties. This procedure is referred to as objects reconstruction.

The physic objects used in SUSY analyses considered in this work are described in this Chapter. Section 4.1 describes items that are used in the definition for electrons (Section 4.2), muons (Section 4.3), jets (Section 4.4) and missing transverse energy (Section 4.5).

4.1 Tracks, vertices and clusters

This section presents the definition of items that are used in the following to build the objects:

- *Hits* are the space points where charged particles cross the detector, measured by Pixel, SCT and TRT and they are the inputs to the tracks reconstruction.

- *Tracks* in the Inner Detector are obtained by fitting sets of hits in the various layers of the detector. The first algorithm searches for a set of three hits compatible with a helicoidal track. The three hits are then the *seed* for the Kalman filter [97] this algorithm is used to build complete track candidates by incorporating additional hits to the track seeds. A second fit is performed on the obtained track candidates and an ambiguity solving procedure is applied for the tracks that have hits in common.

- *Vertices* are reconstructed with an iterative vertex finding algorithm from at least two selected tracks [98]; the primary vertex is selected among the reconstructed vertices as the one with the largest sum of squared of transverse momenta of the tracks associated to it.

- *Impact parameters* are defined respect to the interaction point, d_0 is the transverse impact parameter and z_0 denotes the longitudinal one. $\sigma(d_0)$ and $\sigma(z_0)$ are the corresponding uncertainties.

- *Energy clusters* are obtained by grouping calorimeters cells around a seed cell with an energy deposition above a certain threshold. Two methods are used in ATLAS to form energy clusters: the sliding window algorithm is used for the reconstruction of electrons and photons and the topological clustering [99] is used for the reconstruction of jets.

4.2 Electrons

Electrons are characterized by an energy deposition in the Electromagnetic Calorimeter and by a track in the Inner Detector. In the following, descriptions of reconstruction, identification and isolation are reported [100].

4.2.1 Reconstruction

The first step is the identification of *seed-clusters* inside the EM calorimeter with an energy deposit of at least 2.5 GeV using the sliding window algorithm, then clusters are formed around the seeds using a clustering algorithm and their kinematic is reconstructed. The efficiency of the cluster search is 95% for a energy deposit of $E_{\mathrm{T}} = 7$ GeV and 99% with $E_{\mathrm{T}} = 15$ GeV. The tracks reconstruction is then performed and they are matched to EM clusters using the distance in η and ϕ between the position of the track in the calorimeter, after extrapolation, and the cluster barycentre.

The four-momentum of the electrons is computed using information from both the energy cluster and the track. The electron are also required to be compatible with a primary interaction vertex of the hard collision, in order to reduce the background from conversions and secondary particles.

4.2.2 Identification

In order to discriminate the electron candidates from other ojects such as hadronic jets or converted photons, algorithms for electron identification (ID) are applied. The ID algorithms use quantities related to the electron cluster and track measurements, such as calorimeter shower shapes, information from the transition radiation tracker, track-cluster matching related quantities, track properties, bremsstrahlung effects.

The baseline ID algorithm used for Run-2 data analyses is the likelihood-based method. Three operating points are provided for electron ID: these are referred to, in order of increasing background rejection, as *Loose*, *Medium*, and *Tight*. The same variables are use to define the electron operating points, with different selections. The identification efficiency as a function of E_{T} from Monte Carlo simulation is reported in Figure 4.1.

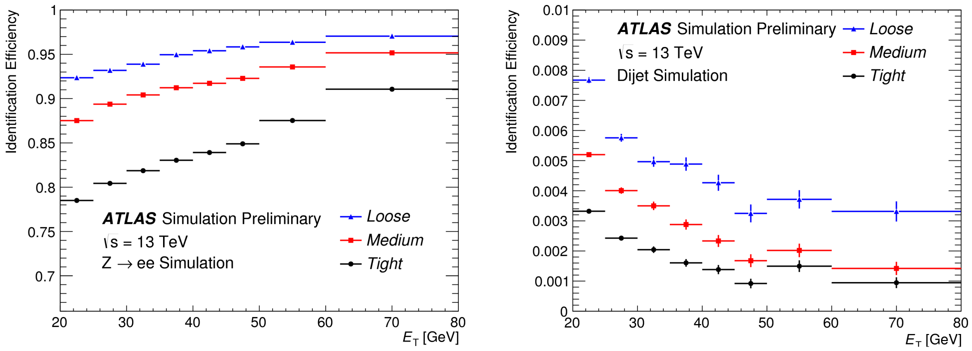

Figure 4.1: Efficiency to identify electrons from $Z \to ee$ Monte Carlo sample (left) and misidentification probability to identify hadrons as electrons (background rejection, right) estimated using dijet Monte Carlo sample, for the operating points *Loose*, *Medium*, and *Tight* [100].

4.2.3 Isolation

Isolation requirements for electrons are also used, in order to reject non-isolated electron candidates like electrons originating from converted photons produced in hadron decays, electrons from heavy flavor hadron decays and light hadrons misidentified as electrons. Both calorimeter and tracking information are used, two discriminating variables have been designed:

- calorimetric isolation energy $E_{\mathrm{T}}^{\mathrm{cone0.2}}$, defined as the sum of transverse energies of topological clusters, within a cone of $\Delta R = 0.2$ around the candidate electron cluster.

- track isolation $p_{\mathrm{T}}^{\mathrm{varcone0.2}}$, defined as the sum of transverse momenta of all tracks, satisfying quality requirements, within a cone of $\Delta R = \min(0.2,\ 10\ \mathrm{GeV}/E_{\mathrm{T}}\ )$ around the candidate electron track and originating from the reconstructed primary vertex.

Different requirement are applied to the quantity $E_{\mathrm{T}}^{\mathrm{cone0.2}}/E_{\mathrm{T}}$ and $p_{\mathrm{T}}^{\mathrm{varcone0.2}}/E_{\mathrm{T}}$. The resulting operating points are divided into two classes: *efficiency targeted operating points*, where varying requirements are used in order to obtain a given isolation efficiency; *fixed requirement operating points*, if the upper thresholds on the isolation variables are constant.

The efficiency targeted operating points are the one used in final states with large E_{T} in order to maintain high signal efficiency. The available working point are listed in Table 4.1, the efficiency is also reported.

4.2.4 Calibration of the Monte Carlo simulations

The accuracy of the Monte Carlo simulation to model the electron measurement efficiency is a crucial point for precision measurements and searches for new physics. In order to

Electron isolation operating points	
Operatin point	Efficiency
LooseTrackOnly	99%
Loose	98%
Tight	95%
Gradient	90/99% at 25/60 GeV
GradientLoose	95/99% at 25/60 GeV

Table 4.1: Efficiency targeted operating points for electrons isolation [100].

achieve reliable predictions, the Monte Carlo samples are corrected to reproduce the efficiencies measured with data.

The measured identification efficiency in data is compared to those computed in Monte Carlo simulations: the data over MC simulation ratios (*scale factors*) are applied to correct the MC for the residual differences. Scale factor are generally close to unity.

In the electron case, the identification efficiency is evaluated using the *tag-and-probe* method. Monte Carlo simulation for $J/\psi \to ee$ and $Z \to ee$ are scaled to data in order to reconstruct the J/ψ and Z boson mass peaks. The scale factors are a function of the electrons energy and η. Similar methods are developed to account also for the data over Monte Carlo discrepancy due to reconstruction, isolation and trigger selection efficiency, using only $Z \to ee$ events.

4.3 Muons

Muons are able to reach the outer part of the ATLAS experiment, the Muon Spectrometer, so these particles give a signal in all the ATLAS sub-detectors: ID, Calorimeters and then MS. The reconstruction is performed using information from all the parts of the detector. Reconstruction, identification and isolation of muons will be described in this section [101].

4.3.1 Reconstruction

Muon reconstruction is first performed independently in the ID and MS. The information from individual sub-detectors is then combined. The reconstruction procedure for ID tracks is addressed in Section 4.1. Muon reconstruction in the MS starts with a search for hit patterns inside each muon chamber to form segments. Muon track candidates are then built by fitting together hits in different layers using the initial segment as seed.

The combined muon reconstruction is performed according to various algorithms based on the information provided by the ID, Calorimeters and MS. Depending on which sub-detectors are used in reconstruction, four different types of muons are defined:

- *combined muons*: track reconstruction is performed independently in the ID and MS, then a combined track is formed with a global refit that uses all the hits from ID and MS sub-detectors;

- *segment-tagged muons*: a track in the ID is classified as a muon if, once extrapolated to the Muon Spectrometer, it is associated with at least one track segment. Segment-tagged muons are used when a muon crosses only one layer of MS chambers;

- *calorimeter-tagged muons*: a track in the ID is identified as a muon if it can be matched to an energy deposit in the calorimeter compatible with a minimum-ionizing particle. This selection has low efficiency, but it is needed in order recovers acceptance in the region where the ATLAS MS is only partially instrumented to allow for cabling and services to the calorimeters and ID;

- *extrapolated muons*: the muon trajectory is reconstructed based only on the MS track and a loose requirement on compatibility with the interaction point. Extrapolated muons are mainly used to extend the muon acceptance into the region $2.5 < |\eta| < 2.7$, which is not covered by the ID.

The overlap between different muon categories is resolved before producing the collection of muons used in physics analyses. If two muons have the same Inner Detector track, preference is given to combined muons, then to segment-tagged muon, and finally to calorimeter tagged muons. The overlap with extrapolated muons in the muon system is resolved by analyzing the track hits and selecting the track with better fit quality and larger number of hits.

4.3.2 Identification

In order to select prompt muons over the background (mainly muon from pion and kaon decays) muon identification is performed by applying quality requirements. Non-prompt muons originated from decay usually present a deviation in the track. Variables that ensure a good track quality are used:

- *q/p significance*: defined as the absolute value of the difference between the ratio of the charge and momentum of the muons measured in the ID and MS divided by the sum in quadrature of the corresponding uncertainties;

- ρ' is the absolute value of the difference between the transverse momentum measurements in the ID and MS, divided by the p_{T} of the combined track;

- χ^2 of the combined track fit.

Specific selections on the number of hits in the ID and MS are also required, in order to provide a robust momentum measurement.

Four operating points for the muon identification are available:

- *loose* is optimized for reconstructing Higgs boson candidates in the four leptons final state, in order to maximize the selection efficiency. All muon types are used.

- *medium* is the default identification, only combined and extrapolated muons are used. Hits criteria are applied and q/p significance is required to be less than seven;

Muon reconstruction operating points				
	$4 < p_{\mathrm{T}} < 20$ GeV		$20 < p_{\mathrm{T}} < 100$ GeV	
Selection	μ efficiency [%]	Misidentification [%]	μ efficiency [%]	Misidentification [%]
Loose	96.7	0.53	98.1	0.76
Medium	95.5	0.38	96.1	0.17
Tight	89.9	0.19	91.8	0.11
High-p_{T}	78.1	0.26	80.4	0.13

Table 4.2: Reconstruction efficiency for prompt muons and misidentification rate for hadrons, in two different p_{T} ranges, for the muon identification operating points. The efficiency are computed using $t\bar{t}$ Monte Carlo simulation [101].

- *tight* operating point use only combined muon, $\chi^2 < 8$ is required. Further selection on ρ' and q/p significance are also applied.
- *hight-p_{T}* is a selection that aims to maximize the momentum resolution for tracks with p_{T} >100 GeV. The selection is optimized for searches for high-mass Z' and W' resonances

Reconstruction efficiency for prompt muons and misidentification rate for hadrons are computed using $t\bar{t}$ Monte Carlo simulation, the result for each operating point is reported in Table 4.2.

4.3.3 Isolation

The isolation of the muon candidate inside the detector is a powerful tool for background rejection. Two variables are defined to perform muon isolation:

- calorimetric isolation $E_{\mathrm{T}}^{\mathrm{topcone20}}$ is the sum of the transverse energy of topological clusters in a cone size $\Delta R = 0.2$ around the candidate muon;
- track isolation $p_{\mathrm{T}}^{\mathrm{varcone30}}$ is defined as the scalar sum of transverse momenta from tracks with $p_{\mathrm{T}} > 1$ GeV, inside a cone with $\Delta R = \min(0.3,\, 10\,\mathrm{GeV}/p_{\mathrm{T}}^{\mu})$.

Selections on the relative variables $p_{\mathrm{T}}^{\mathrm{varcone30}}/p_{\mathrm{T}}$ and $E_{\mathrm{T}}^{\mathrm{topcone20}}/E_{\mathrm{T}}$ are performed and different operating points are provided. Fixed cut and efficiency targeted isolation points are both available, the description is reported in Table 4.3.

4.3.4 Calibration of the Monte Carlo simulations

Similarly to the electron case, scale factors for the optimal data and Monte Carlo simulation agreement are computed. The tag-and-probe method is used to evaluate the identification efficiency. Monte Carlo simulation for $J/\psi \rightarrow \mu\mu$ and $Z \rightarrow \mu\mu$ are scaled to data in order to reconstruct the J/ψ and Z boson mass peaks. Using a similar procedure, a set of corrections is applied to the Monte Carlo muon momentum, and scale factors for the reconstruction, isolation and trigger efficiency are used.

Muon isolation operating points			
Operating point	Track Iso	Calo Iso	Definition
LooseTrackOnly	✓	✗	99% efficiency constant in η and p_{T}
Loose	✓	✓	99% efficiency constant in η and p_{T}
Tight	✓	✓	96% efficiency constant in η and p_{T}
Gradient	✓	✓	$\geq$ 90(99)% efficiency at 25 (60) GeV
GradientLoose	✓	✓	$\geq$ 90(99)% efficiency at 25 (60) GeV
FixedCutTightTrackOnly	✓	✗	$p_{\mathrm{T}}^{\mathrm{varcone30}}/p_{\mathrm{T}} < 0.06$
FixedCutLoose	✓	✓	$p_{\mathrm{T}}^{\mathrm{varcone30}}/p_{\mathrm{T}} < 0.15$, $E_{\mathrm{T}}^{\mathrm{topcone20}}/E_{\mathrm{T}} < 0.30$

Table 4.3: Definition of the muons isolation operating point. [101].

4.4 Jets

Partons coming from the proton-proton interaction can never be observed directly because of the properties of the strong interaction. After the production, quarks and gluons are subjected to fragmentation and hadronization and the result is a spray of collimated hadrons, conserving the direction of the initial parton. The hadrons coming from the hadronization of a parton are called jet.

4.4.1 Reconstruction

Hadronic particles crossing the ATLAS detector deposit their energy mainly in the calorimeter system, and in particular they are able to reach the hadronic calorimeter. Jets are reconstructed in the ATLAS detector using the anti-k_t algorithm [102]. The initial seed is the deposit inside the calorimeter, found using the topological clustering algorithm. For each pair of clusters i and j the following quantities are defined:

$$\begin{aligned} d_{ij} &= \min\left(\frac{1}{p_{\mathrm{T}i}^2}, \frac{1}{p_{\mathrm{T}j}^2}\right)\frac{\Delta R_{ij}^2}{R^2} \\ d_{iB} &= \frac{1}{p_{\mathrm{T}i}^2} \end{aligned} \tag{4.1}$$

The d_{ij} variable is the distance between two objects and d_{iB} is the distance between the object and the beam. The variable R is a parameter that sets the resolution at which jets are resolved from each other. The typical value used by ATLAS Collaboration is 0.4. The minimum d_{min} between all the d_{ij}, d_{iB} is defined. If d_{min} is a d_{ij}, cluster i and j are merged. If it is a d_{iB}, cluster i is declared to be a final jet. This procedure is iterated until no clusters are left.

4.4.2 Energy calibration

The jet energy calibration relates the energy measured with the ATLAS calorimeter to the true energy of the corresponding jet of stable particles. To achieve this, Monte Carlo

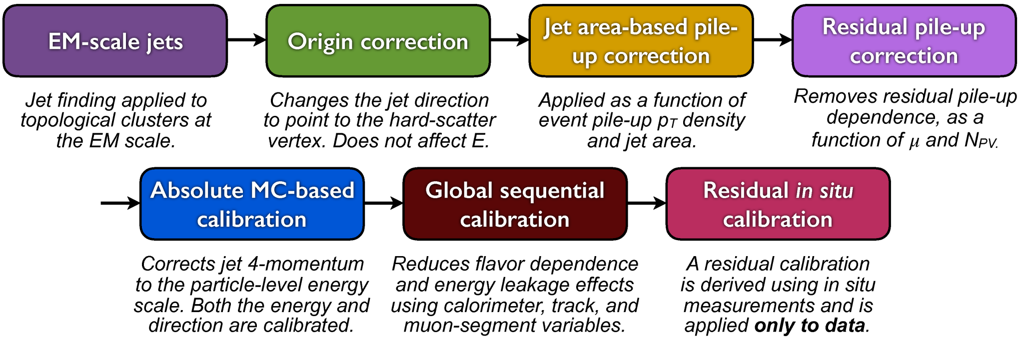

Figure 4.2: Calibration stage for jets [103].

simulations, that use the same algorithms used on data, are used. The different steps of the calibration procedure are [103]:

- origin correction: the jet direction is changed in order to match the position of the primary vertex of the interaction. This improves the η resolution and does not affect the energy;
- pile-up correction: the residual pile-up dependency is removed;
- absolute Monte Carlo based calibration: the reconstructed jet four-momentum and the jet η are corrected using the absolute jet energy scale and η calibration, obtained from Monte Carlo simulation. Biases are mainly due to transition between different calorimeter technologies and sudden changes in calorimeter granularity;
- global sequential calibration: the calorimeter response and the jet reconstruction are sensitive to fluctuations in the jet particle composition and the distribution of energy within the jet. Jets initiated by quark or gluon show different particle composition and shower shape. These effects are reduced at this stage using not only information from the calorimeters but also tracking variables from Inner Detector and Muon Spectrometer;
- residual *in situ* calibration: jet response in data and in Monte Carlo simulation can still show small differences, due to the inaccuracy in the detector response and material description in the simulation. Differences between data and simulation are quantified by balancing jet p_{T} against other well-measured reference objects, and the correction is applied to data.

Figure 4.2 summarizes the jet calibration steps.

4.4.3 Jet vertex fraction and jet vertex tagging

In order to suppress jets from pile-up events, further techniques based on the track associated to the jets are used [104].

Requirements on the Jet Vertex Fraction (JVF) is applied: the variable is used to identify the vertex from which the jet originated and a cut on JVF helps to remove jets which are not associated to the primary vertex. The JVF is defined for each jet with respect to each primary vertex (PV) as the sum of the scalar transverse momentum of the tracks that are associated with the jet and originated from the PV, divided by the scalar p_{T} sum of all the tracks associated to the jet:

$$\mathrm{JVF}(\mathrm{jet}_i, \mathrm{PV}_j) = \frac{\sum_m p_{\mathrm{T}}(\mathrm{track}_m^{\mathrm{jet}_i}, \mathrm{PV}_j)}{\sum_n \sum_l p_{\mathrm{T}}(\mathrm{track}_l^{\mathrm{jet}_i}, \mathrm{PV}_n)} \tag{4.2}$$

where m runs over all tracks originating from PV_j matched to jet_i, n over all primary vertices in the event and l over all tracks originating from PV_n matched to jet_i.

Applying a lower cut on JVF rejects the majority of pile-up jets, but leads to a jet efficiencies that depend on the number of reconstructed primary vertices in the event. In order to avoid this effect, a multivariate combination of JVF and N_{PV} is used: such variable is called *Jet Vertex Tagger* (JVT) [105]. A lower limit on JVT is used instead of JVF for pile-up jets suppression.

Scale factors to ensure a good data-simulation agreement for the JVT variable are applied to the Monte Carlo.

4.4.4 B-tagging

The identification of jets originating from a b quark is called b-tagging and it is possible due to the presence of displaced vertices. The multivariate b-tagging algorithm `MV2c10` [106] is used, and it is based on boosted decision trees (BDT) [107].The input variables for the BDT are the following:

- a likelihood-based combination of the transverse and longitudinal impact parameter significances;
- the presence of a secondary vertex and related properties;
- jets p_{T} and η are also included, in order to take advantage of correlations with other variables.

The BDT is performed using a subset of events from a $t\bar{t}$ Monte Carlo simulation and by assigning b-jets as signal, and c-jets and light-flavor jets as background. The `MV2c10` output distribution is shown in Figure 4.3. Different working points can be defined depending on the desired tagging efficiency and background mistagging rate. The available working points are listed in Table 4.4.

Scale factors to account for the different tagging efficiency in data and Monte Carlo simulation are computed, dependencies on momentum, η or number of vertices were not observed.

4.5 Missing transverse energy

As discussed in Section 2.1, in a proton-proton collider the momentum of the colliding partons is not known, but the transverse momentum is close to zero. Therefore the momentum conservation implies that the vector sum of the transverse momenta of the

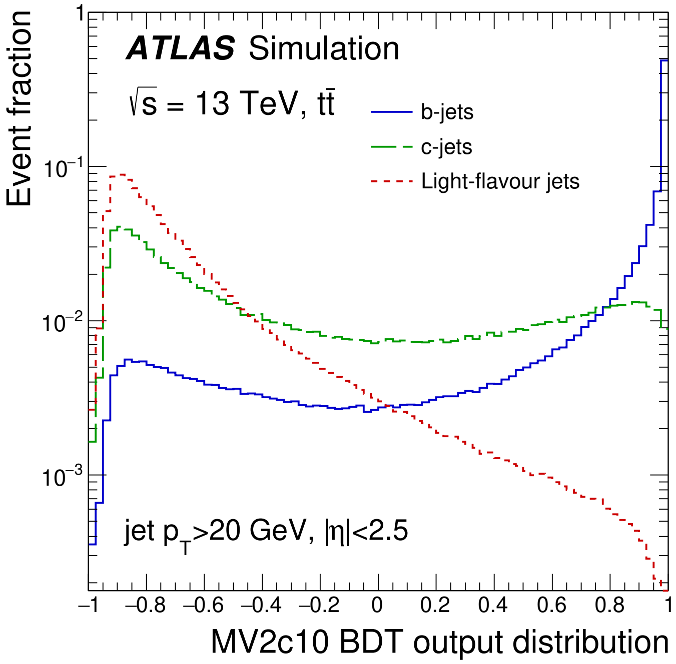

Figure 4.3: The `MV2c10` output for b-jets, c-jets and light-flavor jets, considering simulated $t\bar{t}$ Monte Carlo events [107].

b-tag working points				
WP name	Cut value	b-jet efficiency	c-jet mistag rate	LF-jet mistag rate
85%	0.1758	85%	32%	2.9%
77%	0.6459	77%	16%	0.77%
70%	0.8244	70%	8.3%	0.26%
60%	0.9349	60%	2.9%	0.065%
50%	0.9769	50%	0.94%	0.017%

Table 4.4: b-tag working point with the associated cut on the `MV2c10` output, b-tag efficiency and background mistagging rate [108].

collision products should be zero. An imbalance in the total visible transverse momenta can indicate the presence of neutral, weakly interacting, stable particles in the final state escaping the detector. This is the case of the Standard Model neutrinos, but also Beyond the Standard Model particles are expected to show the same behavior: this makes the unbalanced transverse momentum a crucial signature in the search of new physics phenomena.

4.5.1 E_{T}^{miss} reconstruction

E_{T}^{miss} is built as the negative sum of the transverse momenta of all objects in the considered event. Two contributions are usually identified in the E_{T}^{miss} reconstruction algorithms:

- hard object, fully reconstructed and calibrated particles and jets;
- soft items, reconstructed charged-particle tracks, associated with the hard-scatter vertex but not with an hard object.

The missing momentum transverse components $E_{x(y)}^{miss}$ are given by [109]:

$$E_{x(y)}^{miss} = - \sum_{i \in [\text{hard objects}]} p_{x(y),i} - \sum_{i \in [\text{soft items}]} p_{x(y),i} \tag{4.3}$$

A set of observables is constructed from $E_{x(y)}^{miss}$. The vector $\mathbf{E}_{\mathrm{T}}^{miss}$, the magnitude E_{T}^{miss} and the azimuthal angle $\phi(\mathbf{E}_{\mathrm{T}}^{miss})$ are defined as follows:

$$\begin{aligned} \mathbf{E}_{\mathrm{T}}^{miss} &= \left(E_{\mathrm{x}}^{miss}, E_{\mathrm{y}}^{miss}\right) \\ E_{\mathrm{T}}^{miss} &= |\mathbf{E}_{\mathrm{T}}^{miss}| = \sqrt{(E_{\mathrm{x}}^{miss})^2 + (E_{\mathrm{y}}^{miss})^2} \\ \phi(\mathbf{E}_{\mathrm{T}}^{miss}) &= \arctan\left(E_{\mathrm{y}}^{miss}/E_{\mathrm{x}}^{miss}\right) \end{aligned} \tag{4.4}$$

4.5.2 E_{T}^{miss} significance

Event with E_{T}^{miss} can indicate the presence of a weakly interacting particle in the final state, but it is also possible to have fake E_{T}^{miss}: it can arise from particles escaping the acceptance of the detector, inaccuracy or failure in objects reconstruction. Since 2017, with the `ATHENA` release 21.0, a new tool to evaluate the E_{T}^{miss} reconstruction quality is available.

The degree to which the reconstructed E_{T}^{miss} is consistent with momentum resolution and particle identification efficiencies can be evaluated with the E_{T}^{miss} significance, indicated as $\mathcal{S}(E_{\mathrm{T}}^{miss})$ [110]. Event-by-event, E_{T}^{miss} significance is determined from the log-likelihood ratio that the reconstructed E_{T}^{miss} is consistent with the null hypothesis of having zero real E_{T}^{miss}, given the full event composition. A high value of $\mathcal{S}(E_{\mathrm{T}}^{miss})$ is an indication that the observed E_{T}^{miss} in the event can not be explained from momentum resolution effects, suggesting that the event can contain undetected particles.

A simple way to evaluate $\mathcal{S}(E_{\mathrm{T}}^{miss})$ is to consider:

$$\mathcal{S}(E_{\mathrm{T}}^{miss}) = \frac{E_{\mathrm{T}}^{miss}}{\sqrt{\sum E_{\mathrm{T}}}} \tag{4.5}$$

The definition is based on the assumption that the E_{T} is calculated using calorimeter signals only. The new approach instead uses the measurements from all the ATLAS subdetectors, in order to improve the performance of the reconstructed objects. An object-based $\mathcal{S}(E_{\mathrm{T}}^{miss})$ variable was developed and it is calculated event by event considering the expected resolutions and likelihood of mismeasurement of all the objects that enter the E_{T} reconstruction. The new $\mathcal{S}(E_{\mathrm{T}}^{miss})$ is defined as:

$$(\mathcal{S}(E_{\mathrm{T}}^{miss}))^2 = \frac{|E_{\mathrm{T}}^{miss}|^2}{\sigma_L^2(1-\rho_{LT}^2)} \tag{4.6}$$

where σ_L^2 is the total variances in the longitudinal direction and ρ_{LT} is the correlation factor of the longitudinal L and transverse T measurements, considering the E_{T}^{miss} direction.

CHAPTER 5

Analysis strategy

The purpose of this Chapter is to illustrate the general strategy for the search of Supersymmetric particles. The techniques and tools here presented are applied in the analyses for the observation of charginos and sleptons direct production, that will be illustrated in Chapters 6 and 7.

The discrimination between the SUSY signal and the SM background is performed with the selection of a signal region (Section 5.1) using suitable kinematic variables (Section 5.2). The procedure to obtain the Monte Carlo simulation used for the signal and background samples is described in Section 5.3. A careful estimate of the SM background (Section 5.4) and a validation of the procedure (Section 5.5) are mandatory. Many uncertainty sources can affect the measurements: experimental and theoretical effects are described in Section 5.6. Finally, the likelihood fit and the interpretation of the result are illustrated in Section 5.7.

5.1 Final state and signal region selection

The first step is to identify the signature of the signal. For example the SUSY models illustrated in Section 1.4.1 have a final state with two leptons, no jets and large missing transverse energy. All the events with the signature of interest, selected by a suitable trigger, are considered. Standard Model processes that have the same signature are called background. Standard Model production cross sections are generally very large compared to the SUSY cross sections.

Considering the kinematic of the events, signal and background are expected to have different features. Kinematic variables built from Monte Carlo simulation both for signal and background can be used to investigate the difference. It is possible to select a specific phase space where the signal/background ratio is larger compared to other regions: this kinematic region is called *signal region* (SR). In order to built the most powerful signal region, many kinematic variables are usually investigated and the cuts on the variables providing the best SRs are selected in an optimization procedure.

The SRs power is quantified using the statistical significance. The statistical tools used in the SUSY searches will be illustrated in detail in Section 5.7, and the definition of the p-value and the significance used for the final interpretation of the results will be explained.

In the scope of this Section, an approximation can be used. The general approach in the search for new physics is to define as null hypothesis $\mathcal{H}_b$ the presence of only background processes, while the alternative hypothesis $\mathcal{H}_{s+b}$ is the presence of the signal, where s and b are the average number of signal and backgrounds events respectively. The frequentist probability value or p-value correspond to the probability, under to assumption of a specific hypothesis, of observing a result as compatible or less with the hypothesis than the one expected [111].

Once a signal region is selected, the number of events entering in the region follows a Poissonian distribution with mean $\mu = s+b$. The number of observed events N is the sum of signal s and background b. If N is large enough ($N \sim 10$), a Gaussian distribution with mean μ and standard deviation $\sigma = \sqrt{s+b}$ is a good approximation of the Poissonian distribution. Assuming as null hypothesis the presence of only background events in the SR ($s = 0$), the p-value is:

$$p_b = 1 - \Phi\left(\frac{x-\mu}{\sigma}\right) = 1 - \Phi\left(\frac{x-b}{\sqrt{b}}\right) \tag{5.1}$$

Φ being the Gaussian cumulative function, and x the number of observed events. Defining the statistical significance as

$$Z = \Phi^{-1}(1-p), \tag{5.2}$$

the following formula can be derived from the comparison of Eq. (5.1) and Eq. (5.2):

$$Z = \frac{x-b}{\sqrt{b}} \tag{5.3}$$

In the case of the observation of a number of events $s + b$, the equation becomes:

$$Z = \frac{s}{\sqrt{b}} \tag{5.4}$$

The prediction on the number of background events is usually affected by systematic uncertainties, so the denominator is modified to account for the background absolute error δb:

$$Z = \frac{s}{\sqrt{b + \delta b^2}} \tag{5.5}$$

Since the hypothesis of the presence of only background events was assumed, for increasing value of Z (corresponding to a small p-value) the hypothesis becomes less probable. For a p-value lower then a certain threshold chosen before the experiment, the background-only hypothesis should be rejected. The object of the search is to claim the discovery of new phenomena and to exclude the background-only hypothesis, so a signal region with the best possible significance is selected.

Using the kinematic variables that show different features between signal and background, possible signal regions are defined performing kinematic cuts on a set of kinematic variables. A measure of the significance as defined in Eq. (5.5) is computed for each SR candidate. Different combination of the kinematic variables are tested and a scan on the kinematic cut is performed. The SR definition that gives the better significance is chosen.

Some clarifications are needed at this point:

- the procedure of optimization for the SR selection as presented is in this Section is a simplified view, since the formula reported in Eq. (5.5) is an approximation that is effective only in the presence of a large number of events;
- the obtained SR are optimized to maximize the discovery probability. But it is also possible to built regions optimized for having the strongest possible exclusion limits, in the case of non observation of the SUSY signal. This point will be addressed in Section 5.7.5;
- in a typical SUSY search, it is not considered a unique signal, but a set of MC signal samples with different parameters (usually the masses of the SUSY particles) is used. The number of signal events s observed in the SR will be different depending on the peculiar signal considered, so the optimal SR definition can be different for different signal samples. For these reason, the searches usually includes more then one SR;
- the signal regions selection is performed using only Monte Carlo simulation. The comparison between data and the expected background is performed only after the finalization of the background estimation methods, complete of all the experimental and theoretical uncertainties, and after the validation procedure;
- the characteristic of the kinematic variables used for the SR selection are not provided in this Section, but a concrete example of is described in the next Section.

5.2 The *stransverse mass* $m_{\mathbf{T2}}$

In the case of a SUSY production channel with two visible objects and missing transverse energy in the final state, one of the most powerful discriminating variables is the *stransverse mass* m_{T2} [112–114].

The concept behind this variable is based on the transverse mass. Considering the W boson mass measurement in an experiment such as ATLAS in the case of the decay in charged lepton and neutrino, the neutrino goes undetected and it is not possible to directly reconstruct the W boson mass. Instead the transverse mass variable can be used to achieve this information:

$$m_{\mathrm{T}}^2 = 2(E_{\mathrm{T}}^{\ell} E_{\mathrm{T}}^{miss} - \mathbf{p}_{\mathrm{T}}^{\ell} \cdot \mathbf{p}_{\mathrm{T}}^{miss}) \tag{5.6}$$

where for the neutrino $E_{\mathrm{T}}^{miss} \equiv \mathbf{p}_{\mathrm{T}}^{miss}$. The variable has the propriety that

$$m_{\mathrm{T}}^2 \leq m_W^2 \tag{5.7}$$

with the equality possible only if the two particles have the same rapidity. One single event provides an upper limit on the W boson mass, but building the m_{T}^2 distribution with a large population in the tail provides a measure of the W boson mass.

The concept can be generalized to the case of missing transverse energy arising from more then one particle. The particles $\mathcal{A}$ and $\mathcal{B}$ are produced from the proton-proton interaction and then decay as $\mathcal{A} \rightarrow \alpha\chi$ and $\mathcal{B} \rightarrow \beta\chi$, where α and β are visible particles and χ is invisible. This is the case of the SUSY diagram considered in Figure 1.7(a), where the final state consist of two leptons and the missing transverse energy is given by two neutralinos, but it is also the case of the Standard Model diboson production, with two W boson both decaying into leptons.

The splitting of the missing energy between the two invisible particles is unknown, so the missing transverse momentum $\mathbf{p}_{\mathrm{T}}^{miss}$ is splitted in all the possible combination $\mathbf{q}_{\mathrm{T}}$ and $\mathbf{p}_{\mathrm{T}}^{miss} - \mathbf{q}_{\mathrm{T}}$ between the two invisible particles. The m_{T} variable is computed for each branch and then combined in the m_{T2} variable, defined as:

$$m_{\mathrm{T2}} = \min_{\mathbf{q}_{\mathrm{T}}} \left\{ \max \left[m_{\mathrm{T}}(\mathbf{p}_{\mathrm{T}}^{\alpha}, \mathbf{q}_{\mathrm{T}}; m_{\chi}), m_{\mathrm{T}}(\mathbf{p}_{\mathrm{T}}^{\beta}, \mathbf{p}_{\mathrm{T}}^{miss} - \mathbf{q}_{\mathrm{T}}; m_{\chi}) \right] \right\} \tag{5.8}$$

The mass of the invisible particle is added as explicit parameter, since in the case of SUSY signal the neutralino can have a large mass and affect the shape and the end-point of the m_{T2} variable. Similarly to the m_{T} case, also m_{T2} is upper limited. Considering the diboson production, when $\mathbf{q}_{\mathrm{T}}$ is equal to the transverse momentum of one of the invisible particles, both the m_{T} combinations satisfy the Eq. (5.7), and so does their maximum. Considering the minimum on all the $\mathbf{q}_{\mathrm{T}}$ possible values, the inequality is still verified.The bound on the m_{T2} variable is:

$$m_{\mathrm{T2}}^2 \leq m_W^2 \tag{5.9}$$

Figure 5.1 shows the distribution of m_{T2} in the case of the two Standard Model processes, $t\bar{t}$ and WW production, selecting only events with two leptons. In both the cases, after an initial plateau, the m_{T2} distribution drops around 80 GeV, corresponding to the W boson mass. For the $t\bar{t}$ the decrease is faster and the tail is less populated. The tail of the distribution is due both to events with an off-shell W boson and to detector resolution effects. Considering the WW process, the distribution shows a longer tail, since the W boson mass is not limited from above by the top quark mass as in the previous case. The m_{T2} distributions for $t\bar{t}$ events before and after considering the detector effects are shown in Figure 5.2, lepton and E_{T}^{miss} reconstruction efficiencies and resolutions affect the shape of the distribution.

The m_{T2} variable can be used also in the case of missing transverse energy from more than two particles. Considering the models presented in Figure 1.7(b) and 1.7(c), two neutralinos and two neutrinos are present in the final state. In this case neutralino and neutrino from the same branch are considered together for the $\mathbf{q}_{\mathrm{T}}$ splitting. In the case of the charginos pair production with W boson mediated decay, the m_{χ} value in Eq. (5.8) is unknown and it is usually set to zero. The m_{T2} kinematic limitation becomes:

$$m_{\mathrm{T2}}^2 \leq m_{\chi_1^{\pm}}^2 - m_{\chi_1^0}^2 \tag{5.10}$$

Figure 5.3 illustrates the characteristics of the m_{T2} variable for different signal Monte Carlo simulations. The first plot consider increasing charginos mass (100, 300, 500 GeV)

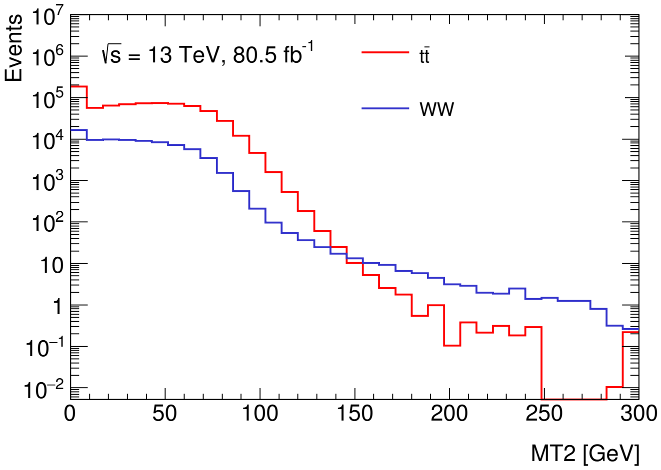

Figure 5.1: Monte Carlo simulation for the m_{T2} variable in the case of the $t\bar{t}$ and diboson WW Standard Model processes. Events used for the plots are required to have two leptons in the final state.

and a fixed neutralino mass (1 GeV): the endpoint of the distribution moves to larger m_{T2} values with the increasing chargino mass, as expected from Eq. 5.10. In the second plot, chargino mass is fixed to 300 GeV and the variation of neutralino mass is considered (1, 50 and 100 GeV). With increasing neutralino masses, the distribution endpoint moves to lower m_{T2} values.

Since the endpoint of the m_{T2} distribution depends on the mass of the parent particles (Standard Model or SUSY) and SUSY particles are expected to be heavier compared to the Standard Model particles, a lower cut on m_{T2} can help to discriminate between the SUSY signal and the background. This analysis strategy is not effective in scenarios with a compressed mass spectrum. If the mass difference between the chargino and the neutralino or between the slepton and the neutralino is small, the second member of the Eq. (5.10) is smaller of m_W^2 and it is not longer possible to select a signal region using a lower cut on the m_{T2} variable.

In SUSY searches with a final state including missing transverse energy, the requirement on the E_{T}^{miss} can be implicit, since the m_{T2} variable is correlated to the missing transverse energy. Figure 5.4 shows the events distribution in the m_{T2}-E_{T}^{miss} plane for diboson and $t\bar{t}$ background: selecting events with $m_{\mathrm{T2}} > 80$ GeV also implies a selection on the E_{T}^{miss} variable.

5.3 The Monte Carlo simulation

As already mentioned in the previous Chapters and in Section 5.1, Monte Carlo simulations are an essential tool in the understanding of the detector and of the data. The object of Monte Carlo simulations is to describe, as accurately as possible, the characteristics of physics processes of interest and the detector response.

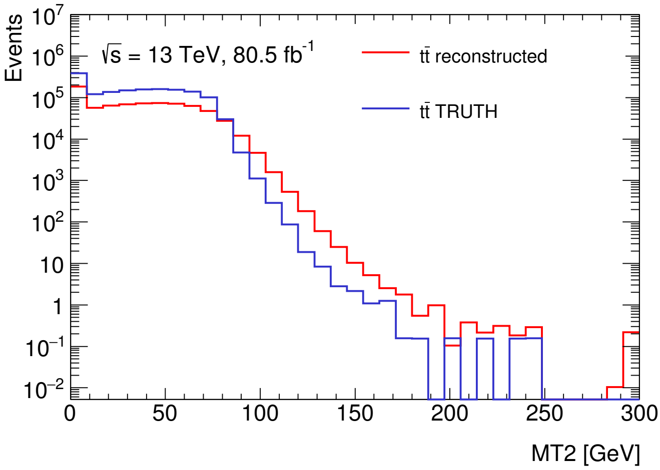

Figure 5.2: Monte Carlo simulation for the m_{T2} variable in the case of the $t\bar{t}$ process, before (*Truth*) and after (*reconstructed*) considering the detector effects. Events used for the plots are required to have two leptons in the final state.

The procedure use by the ATLAS Collaboration, and more in general by the high energy physics community, to produce the Monte Carlo simulation is described in the following. The details about the Monte Carlo simulation used in the searches presented in this Thesis will be described in dedicated Sections in Chapters 6 and 7.

5.3.1 Matrix elements and parton shower

The first step of Monte Carlo simulations is the computation of the protons hard scattering cross section, as reported in Eq. (2.3). The partonic cross section for the production of a final state X from the two incoming partons a and b can be expressed at all orders as [115]:

$$\hat{\sigma}_{ab\to X} = \sum_{k=0}^{\infty} \int d\Phi_{X+k} \left| \sum_{\ell=0}^{\infty} \mathcal{M}_{X+k}^{(\ell)} \right|^{2} \tag{5.11}$$

where the PDFs factors are omitted. The sum over k represent the sum over additional emission of quarks or gluons together with the X final state, that can occur before the hard scattering or in the final state, addressed as *initial state* or *final state radiation* (ISR/FSR). The sum over ℓ runs over additional virtual corrections (the loops). The matrix element $\mathcal{M}_{X+k}^{(\ell)}$ is the probability amplitude to produce the final state $X+k$ with ℓ virtual loops. Since it is not possible to extend the sums up to infinity, the computation is done with a certain number of additional parton and loops. The possible cross section orders are:

- $k = 0$, $\ell = 0$: leading order (LO) for the X production
- $k = n$, $\ell = 0$: leading order for the $X + n$ jets production

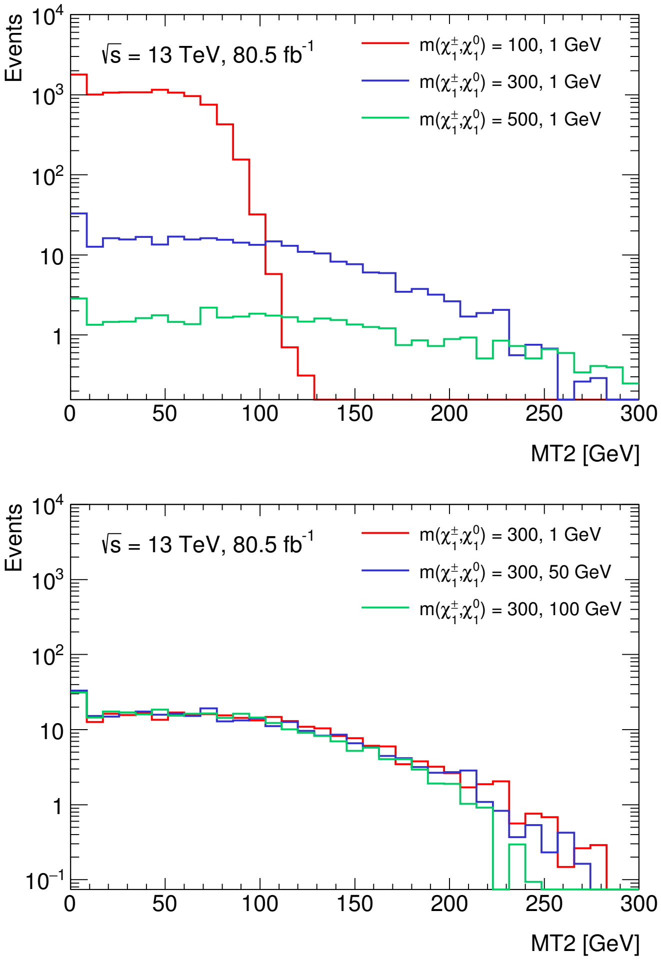

Figure 5.3: m_{T2} distribution from the Monte Carlo simulation of the charginos direct production with W mediated decay, for different SUSY particles masses: in the first plot a fixed neutralino mass is considered (1 GeV), while in the second plot chargino mass is fixed to 300 GeV. Only events with two leptons in the final state are considered.

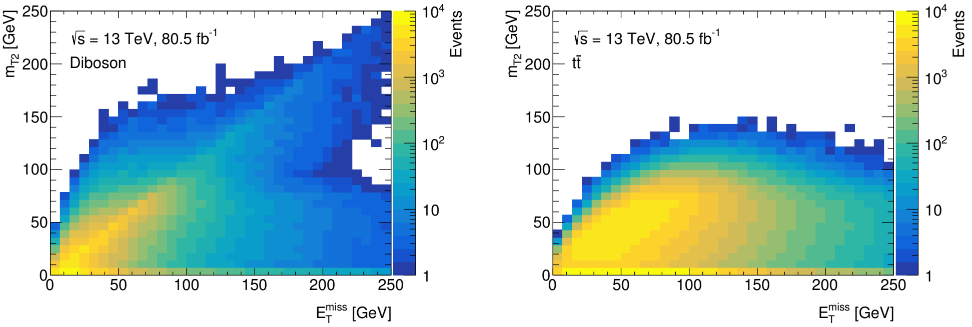

Figure 5.4: Distribution in the $m_{\mathrm{T}2}$-E_{T}^{miss} plane of the diboson (WW, WZ and ZZ, on the left) and $t\bar{t}$ (on the right) events, from Monte Carlo simulation.

- $k + \ell \leq n$: next^n to leading order (N^{n}LO) for the X production, it includes N^{n-1}LO for X + 1 jets, N^{n-2}LO for X + 2 jets, ect.

The computation of the matrix elements implies the choice of a PDFs set and of the factorization and renormalization scale.

The description of matrix elements and the additional radiation can be provided by the same software or a dedicated software can be used in the two cases. In general the high momentum jets are included in the matrix element computation, while additional soft jets are simulated by the *parton shower* software. The matching between the jets produced in the matrix elements simulation and the ones from the parton shower is not trivial, careful matching procedures are applied in order to avoid overestimating or underestimating the amount of radiation.

5.3.2 Underlying events and pile-up

The partons from the colliding protons that do not take part in the hard scattering can undergo interactions as well, in the so-call *underlying events*, originating secondary interactions with low momentum transfer. A dedicated software is usually exploited in the simulation of the underlying events. The pile-up events, from the interacting of other protons in the same buch crossing, are evaluated with the same software used for the underlying events simulation.

5.3.3 Hadronization

After the generation of all the particles produced in the protons interaction, the set of soft and hard QCD objects is transformed in primary hadrons, which may then decay further. In the context of Monte Carlo simulation, this step is denoted as *hadronization*.

5.3.4 Reconstruction

The output of the events simulation described until this point is a set of stable particles (or with a mean life long enough to interact with the detector) with the corresponding four-vector. In order to compare the MC simulation to the data collected by ATLAS, the effect of the detector has to be considered. The response of the experimental apparatus to the particles is simulated through the `Geant4` software [116], that describes each part of the detector. The trigger selection is also emulated. After this step, the simulated events have the same format of the real data collected by the ATLAS detector. Therefore the same algorithms and objects reconstruction procedure used for the data, as described in Chapter 4, are applied to the Monte Carlo simulations.

5.3.5 Monte Carlo calibration

In order to describe the data in the most accurate way possible, the Monte Carlo simulation undergo many calibrations. The *pile-up reweighting* procedure is performed: the MC samples are generated with a specific pile-up configuration, but the pile-up condition can change during the data taking, so weights are applied the simulated events to match the pile-up of the considered data set. Corrections concerning the reconstruction and identification efficiency of the physics objects are also considered, as described in Sections 4.2.4 and 4.3.4.

5.3.6 Truth level samples

The reconstruction and calibration are fundamental steps to obtain a Monte Carlo simulation that describes the data with accuracy. However for studies involving only Monte Carlo samples it is possible to use the output of the simulation after the hadronization step, before considering the effect of the detector. Such samples are called *Truth level* or *particle level* simulations.

The advantage of such samples is that the production is faster and more events are available compared to the reconstructed samples, since no detector inefficiency is considered. As an example, Truth level samples can be used in the estimate of theoretical systematic uncertainties, as will be described in Section 5.6.2.

5.4 Background estimation

After the selection of one or more signal regions for the observation of the SUSY signal of interest, it is fundamental to have a careful background estimation and uncertainties as small as possible.

The Standard Model events entering the selection can be classified as irreducible or reducible background. The events from the first class have real leptons and genuine missing transverse energy, while in the second case at least one lepton is “fake” (particle misidentified as leptons) or not prompt (non-isolated leptons coming from the decay of particles in a jet, and not from the proton-proton interaction); fake missing transverse energy can appear in case of particles escaping the detector or bad objects reconstruction.

Different technique can be used in the background estimation. The methods that will be used in the analyses illustrated in Chapter 6 and 7 are the following:

- considering a Standard Model process, the corresponding Monte Carlo simulation is normalized to data in a *control region* (CR) and then extrapolated to the signal region. The control region is a kinematic selection enriched with the SM process considered, with the highest possible purity. The method is further explained in Section 5.4.1;

- fully data driven method can also be used. The estimate of the background is completely based on the data. For the analyses illustrated in Chapter 6 and 7, this method is only used for fake and non-prompt leptons and the technique will be explained in Section 6.7.3;
- background processes can also be evaluated directly from Monte Carlo simulation. This is generally done only for minor backgrounds.

5.4.1 Control region

In an extreme phase space such as the signal regions, the Monte Carlo simulation might not provide a completely satisfying prediction, so the Monte Carlo simulation normalized in the CR can give a more accurate background prediction. In order to be effective, the method needs a CR close to the SR, in order to have a similar kinematic. The CR need a high purity for the background process of interest, in order to minimize statistic effects, and a low signal contamination, to not bias the estimate.

It is possible to have more then one CR, each one dedicated to a specific background. A simultaneous likelihood fit is performed, a normalization factor is computed for each process and the normalization is then applied to all the regions used in the search.

The scheme of a possible situation is illustrated in Figure 5.5: two kinematic variables (Variable 1 and Variable 2) are used to select the signal regions SR1 and SR2. Two control regions are designed to have a good purity and low signal contamination, but also to be close to the SRs; validation regions, that will be illustrated in Section 5.5, are also present.

5.5 Validation

Before performing the comparison between data and expected background in the signal regions, the background estimation methodology needs to be validated. A set of *validation regions* (VR) is defined for this purpose. The VR should be as close as possible to the signal regions, but with low signal contamination. After ensuring that the data are well described by the background estimation in the VRs, it is possible to look for possible SUSY signal in the SRs.

5.6 Uncertainties

Several sources of experimental, theoretical and statistical uncertainties are considered for the Standard Model background estimate and for the SUSY signal predictions.

The experimental and theoretical uncertainties are reflected in the Monte Carlo samples as the variation of a quantity, such as the particles momentum or the cross section.

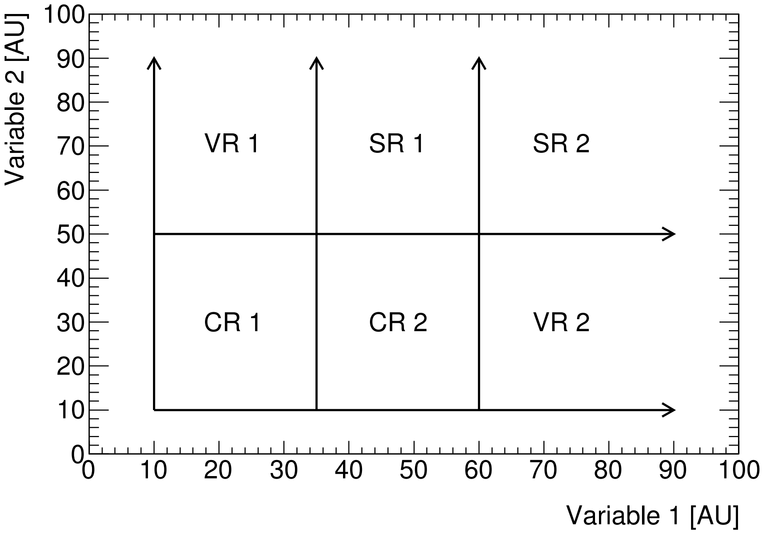

Figure 5.5: Scheme of the typical region configuration for a SUSY search: signal regions SR1 and SR2 are defined using two kinematic variables. Control regions are defined to have a good purity for the process of interest but also to be close to SRs. Validation regions, that provide a verification for the procedure, are in an intermediate position.

The variation due to the systematic effect is then propagated through the full analysis chain, giving a different number of expected events in the regions considered by the analysis.

The impact of a systematic uncertainty in a specific region is given by the the difference in the number of events obtained using the nominal sample and using the sample with the systematic variation:

$$\text{uncertainty [\%]} = \frac{\text{nominal yield - variation yield}}{\text{nominal yield}} \tag{5.12}$$

In the case of a background sample normalized in a dedicated control regions, the yields used in the systematic uncertainty estimate are normalized too, and the formula becomes:

$$\text{uncertainty [\%]} = \left(\frac{\text{nominal yield}}{\text{nominal yield in CR}} - \frac{\text{variation yield}}{\text{variation yield in CR}}\right)\left(\frac{\text{nominal yield}}{\text{nominal yield in CR}}\right)^{-1} \tag{5.13}$$

The background yields computed for the nominal and the variation samples are used as input for the uncertainties description in the likelihood fit, as will be illustrated in Section 5.7.1. Anyway it is also possible to use as input the uncertainties computed with the Eq. (5.12) or (5.13).

The source of uncertainties for the SUSY searches presented in this Thesis are now described.

5.6.1 Experimental systematic uncertainties

Concerning the experimental systematics, the uncertainties arising from the physics objects considered in the analyses are the following:

- in the case of the muons, the uncertainty on the momentum resolution is obtained with a $\pm 1\sigma$ variation in the smearing of the ID and MS track. Muon energy scale uncertainty is calculated from $\pm 1\sigma$ variations in the scale of the muon momentum. Uncertainties on the reconstruction and isolation efficiency are computed using respectively $\pm 1\sigma$ variations in the statistical and systematic error on the reconstruction scale factors and on the muon isolation scale factors;
- considering the electrons, uncertainty on the energy scale are obtained from $\pm 1\sigma$ variations in the scale of the electron momentum. The identification efficiency uncertainty is evaluated with $\pm 1\sigma$ variations in the error on the electron identification scale factors. The uncertainty on the reconstruction efficiency is calculated with a $\pm 1\sigma$ variations in the error on the reconstruction scale factors. The isolation efficiency uncertainty is obtained with a $\pm 1\sigma$ variations in the error on the electron isolation scale factors;
- concerning systematics effects that affects the jets [117], the energy resolution uncertainty is obtained from $\pm 1\sigma$ variations in the smearing of jets, while the energy scale uncertainty is calculate with $\pm 1\sigma$ variations in the scale of the jet momentum. The unceratinty associate to the flavor-tagging efficiency is evaluated with $\pm 1\sigma$ variations in the error on the scale factor that corrects the tagging rate in simulation to match the rate in the data. The JVT uncertainty is estimated from $\pm 1\sigma$ variations which account for the residual contamination from pile-up jets after pile-up suppression;
- missing transverse energy systematics effects are due to the soft term resolution and scale (since hard objects systematics are already included in the previous cases) [118]. The soft term resolution and scale are obtained respectively from the $\pm 1\sigma$ variations in the missing transverse energy resolution and scale, derived from comparisons of data to Monte Carlo simulation.

As described in Section 5.3.5, Monte Carlo simulations undergo a pile-up reweighting procedure to match the data pile-up distribution and an uncertainty is associated to the method. An uncertainty associated to the measurement of the integrated luminosity collected by ATLAS is also considered.

5.6.2 Theoretical systematic uncertainties

A general description of the theoretical systematic effects affecting the Monte Carlo samples is provided in this section. However, since some uncertainties can be negligible or not present depending on the specific MC sample considered, a detailed description of the systematic effects will be provided for each search illustrated in this Thesis.

The following systematic uncertainties may affect the MC simulations, obtained as described in Section 5.3:

- *factorization and renormalization of the QCD scales*: the computation of the proton-proton cross section for the production of certain final states depends on the factorization and renormalization scales and it is possible to have different choices for these parameters;

- *matching between the matrix element and the parton shower*: as mentioned in Section 5.3.1, the jets produced by the the matrix elements simulation and the ones from the parton shower need to be matched in order to avoid underestimation or double counting of the radiation. Different matching procedures are available, leading to possible different results;

- *PDF*: the PDFs used in the Monte Carlo simulation are obtained by fitting experimental data. Many PDFs are available, provided by different research groups. It is also possible to use many different parametrizations in the fit, leading to different PDF distributions;

- *cross section*: the cross section for the simulated samples can be computed by the same program taking care of the production of the events or by a dedicated software, but in any case the estimate is affected by uncertainty. In the case of MC samples normalized in a CRs, this uncertainty is erased;

- *choice of a specific software*: many programs are available for each step of the simulation chain and in some cases different softwares can give different predictions, as for example the choice of peculiar parton shower. In these cases a systematic uncertainty due to the choice of a specific software is applied.

5.6.3 Other uncertainties

Other uncertainties that can affect the results are:

- *Monte Carlo statistic*: due to the finite number of Monte Carlo events generated, the MC statistical uncertainties can affect the final result. Monte Carlo simulation are produced with an equivalent integrated luminosity that is larger compared to the data, but in tight selections as the signal regions the statistical effect can be significant;

- *control region statistic*: selecting the CR, the kinematic cut should be tight enough to have a good purity for the process of interest, but also loose enough to allow for a large number of events, since the normalization factor obtained is affected by the statistical error of the CR. The normalization factor with its uncertainty is then propagated to the SR;

- *data driven method uncertainties*: the estimate of the fake and non-prompt leptons is affected by the uncertainties associate to the Matrix Method used in the evaluation. The method and the associated systematic uncertainties will be illustrated in Section 6.7.3.

5.6.4 Uncertainties for the signal samples

The experimental, theoretical and statistical uncertainties described in the previous Sections affect all the type of Monte Carlo simulation, also the signal samples. The signal experimental systematic uncertainties are treated in the same as the background MC samples. The theoretical systematics instead are usually grouped together under the cross section uncertainty.

For the signal samples considered in the searches presented in this work, the cross sections are computed with a dedicated software, RESUMMINO [60], and the production cross section with the uncertainties for sleptons and charginos are reported in Tables 1.3 and 1.4 respectively [61, 62]. The theoretical systematic uncertainties affecting the cross section are the factorization and renormalization scale and the PDF uncertainties, as described in Section 5.6.2. The uncertainties are combined together in the values reported in Tables 1.3 and 1.4.

5.7 Statistical interpretation of the result

The description of the likelihood function, the statistical tools and the interpretation of the result of a SUSY search are presented in this Section. The likelihood fit and the result interpretation is performed using the HistFitter software [119].

5.7.1 Likelihood fit

The result of a SUSY search is extracted by an hypothesis test peformed using the likelihood function that has as input the Monte Carlo simulation yields and the observed number of events in the CRs and SRs and the systematic uncertainties, as described in Sections 5.1, 5.4.1, 5.5 and 5.6. The likelihood function L is built as the product of Poisson probability density functions describing the observed number of events in the SR and CRs and a distribution representing the systematic uncertainties:

$$\begin{aligned} L(\boldsymbol{n}, \boldsymbol{\theta}^0 | \mu_{sig}, \boldsymbol{b}, \boldsymbol{\theta}) &= P_{\mathrm{SR}} \times P_{\mathrm{CR}} \times C_{\mathrm{syst}} \\ &= P(n_S | \lambda_S(\mu_{sig}, \boldsymbol{b}, \boldsymbol{\theta})) \times \prod_{i \in \mathrm{CR}} P(n_i | \lambda_i(\mu_{sig}, \mu_{\mathrm{NF}}, \boldsymbol{b}, \boldsymbol{\theta})) \times C_{\mathrm{syst}}(\boldsymbol{\theta}^0, \boldsymbol{\theta}) \end{aligned} \tag{5.14}$$

P_{SR} and P_{CR} are the Poissonian probability associated to SR and CRs, when the numbers of observed events are n_S and n_i respectively. The expected values λ_S and λ_i are functions that depends on the background predictions $\boldsymbol{b}$, the nuisance parameters that parametrize the systematic uncertainties $\boldsymbol{\theta}$, the background normalization factor μ_{NF} and the signal strength parameter μ_{sig}. The signal strength is a normalization factor for the signal, that is used to test different hypothesis: the signal can be turned off considering $\mu_{sig} = 0$, while $\mu_{sig} = 1$ corresponds to the value predicted by the model under consideration.

The systematic uncertainties are described with Gaussian distributions C_{syst}, where $\boldsymbol{\theta}^0$ is the central value around which $\boldsymbol{\theta}$ is varied in the likelihood maximization. The variation of $\boldsymbol{\theta}$ impact on the expected value, as described by λ_S and λ_i. If the nuisance parameter are independent, C_{syst} is the product of the probability distributions corresponding to the different systematic uncertainties sources:

$$C_{\text{syst}}(\boldsymbol{\theta}^0, \boldsymbol{\theta}) = \prod_{j \in \text{S}} G(\theta_j^0 - \theta_j) \tag{5.15}$$

with S being the set of uncertainties considered.

The likelihood function is maximized over the following parameters: $\boldsymbol{\theta}$, μ_{sig} and μ_{NF}. The values obtained in the maximization will be labeled as $\hat{\boldsymbol{\theta}}$, $\hat{\mu}_{sig}$ and $\hat{\mu}_{\text{NF}}$.

5.7.2 Hypothesis test

As already mentioned in Section 5.1, in the search of new phenomena the null hypothesis $\mathcal{H}_b$ is the presence of only background processes, while the alternative hypothesis $\mathcal{H}_{s+b}$ is the presence of the beyond the SM physics signal.

In order to test a possible value of the signal strength μ_{sig}, the profile log likelihood ratio is used [120]. The test statistic, fixing μ_{sig}, is defined as:

$$q_{\mu_{sig}} = -2 \log \left(\frac{L(\mu_{sig}, \hat{\hat{\boldsymbol{\theta}}})}{L(\hat{\mu}_{sig}, \hat{\boldsymbol{\theta}})} \right) \tag{5.16}$$

where $\hat{\hat{\boldsymbol{\theta}}}$ is the value maximizing the likelihood for the specific μ_{sig}. The distribution of the statistic test is indicated as $f(q_{\mu_{sig}}|\mu_{sig}, \boldsymbol{\theta})$. The f distribution can be determined using many pseudo experiments (*toys*), obtained randomizing the number of observed events. In the case of a large statistic sample, the f distribution is known to be a χ^2 distribution with one degree of freedom, due to the Wilk's theorem. The case of large statistics is called *asymptotic regime* [121].

The p-value assigned by an hypothesis test is calculated using the distribution of the statistic test, and in the case of the alternative hypothesis $\mathcal{H}_{s+b}$ is:

$$p_{\mu_{sig}} = \int_{q_{\mu_{sig}}^{obs}}^{\infty} f(q_{\mu_{sig}}|\mu_{sig}, \boldsymbol{\theta}) dq_{\mu_{sig}} \tag{5.17}$$

When the p-value for the alternative hypothesis $\mathcal{H}_{s+b}$ is lower then a certain predefined threshold, the alternative hypothesis is excluded. The convention followed in the high energy physics experiments is to use a threshold equals to 0.05, that correspond to a 95% CL.

Instead, considering the null hypothesis $\mathcal{H}_b$, the p-value becomes:

$$p_b = \int_0^{q_{\mu_{sig}}^{obs}} f(q_{\mu_{sig}}|0, \boldsymbol{\theta}) dq_{\mu_{sig}} \tag{5.18}$$

If the p-value for the null hypothesis is lower than the threshold, the background-only hypothesis is excluded. Conventionally, the threshold to declare evidence for new physics is $1.3\ 10^{-3}$, while the discovery is claimed in the case of $p_b \leq 2.87\ 10^{-7}$.

The statistical significance Z can be used instead of p-value. The p-value is converted in the equivalent number of standard deviation of a normal Gaussian distribution needed to the integral of the upper tail equal to the p-value itself:

$$Z = \Phi^{-1}(1-p) \tag{5.19}$$

where Φ indicate the Gaussian cumulative function. The p-value threshold used to claim an evidence corresponds to $Z = 3\sigma$, while the threshold for the discovery is equivalent to $Z = 5\sigma$.

5.7.3 The CL_s method

In the case of a non-significant excess of the data above the SM prediction in the SRs, the CL_s method is used to determine exclusion intervals [122–124].

The CL_s is a modified definition of the usual confidence level, used in searches for new physics where a small number of signal events is expected. In this case the statistic distribution f for the null hypothesis $\mathcal{H}_b$ and alternative one $\mathcal{H}_{s+b}$ are close to each other. An under-fluctuation in the data can bring to the exclusion of the alternative hypothesis $\mathcal{H}_{s+b}$, even if it is almost indistinguishable from the null hypothesis $\mathcal{H}_b$.

The CL_s method prevents this situation, by defining:

$$CL_s = \frac{CL_{s+b}}{CL_b} = \frac{p_{\mu_{sig}}}{1-p_b} \tag{5.20}$$

Using the CL_s method, the alternative hypothesis is excluded at 95% CL if $CL_s < 0.05$.

5.7.4 Likelihood fit strategy

Different strategies for the likelihood fit are used:

- *background-only fit*: the purpose is the estimate of the total SM background in the VRs and SRs, without any assumption on the signal model. Only the background Monte Carlo simulation are used. The signal contamination in the CRs is assumed to be negligible and μ_{sig} is assumed to be zero. The dominant background processes are simultaneously normalized to data in the CRs in order to compute the normalization factor μ_{NF}, the fit result is used to predict the VRs and SRs background: the result is independent on the VRs and SRs observed data, since the CRs data are the only constrain;

- *model-dependent fit*: the object is to study a specific signal model. If after performing the background-only fit no significant excess is observed in the SRs, exclusion limits can be set on the signal model considered. Together with the background MC samples, also a signal samples is included in all the regions, in order to account for possible signal contamination in the CRs. The μ_{sig} is assumed to be one. Observed data in the CRs and SRs are used as constrains. Many non-overlapping SRs can be combined together in the exclusion fit, giving better exclusion sensitivity compared to a single SR (see Section 5.7.6). Since a grid of signal samples with different parameter is used, the model-dependent fit is performed for each signal sample. Signals having a $CL_s < 0.05$ are excluded: and an exclusion contour at 95% CL in the parameters phase space is obtained;

- *model-independent fit*: the purpose is to provide an upper limit, independent from the specific signal model for which the search was designed for, on the number of events beyond the expected number in the SRs. In this way is possible to interpret the result of a search for other different signal models. For this fit strategy, observed data in the CRs and SRs are used as constrains and a dummy signal value is assumed for the SR, but no signal contamination is considered in the CRs. Only one SR is considered in the fit and the procedure is repeated for each SR of interest. A crucial difference between the background-only and the model-independent fit is that in the first case the μ_{sig} is set to zero in the numerator of the likelihood fuction in Eq. (5.16) , while in the second case μ_{sig} is set to one.

The build of likelihood function and the three type of differents fit are performed using the HistFitter package.

5.7.5 Signal regions optimization strategy

A simplified view of the strategy used in the SRs selection and optimization was described in Section 5.1, but a more complete explanation is provided in this Section.

The optimization of the SRs can be done in two different ways:

- *optimization for the discovery*: as in the procedure illustrated in Section 5.1, the p-value and the significance are built for the background-only hypothesis $\mathcal{H}_b$. The p-value is computed as reported in Eq. (5.18), and not with approximated significance reported in Eq. (5.5). The object is to selected the SRs with the largest possible significance, in order to be able to reject the $\mathcal{H}_b$ hypothesis;

- *optimization for the exclusion*: the SRs are defined to have the largest possible coverage for the exclusion limits in the considered phase space. The alternative hypothesis $\mathcal{H}_{s+b}$ is assumed and the CL_s is computed as in Eq. (5.20). The regions providing the smallest CL_s, corresponding to a large probability of rejecting the hypothesis $\mathcal{H}_{s+b}$, are selected.

Since both the discovery of new phenomena and the exclusion of a phase space portion are fundamental parts of the search for beyond the Standard Model physics, the analyses usually include two set of signal regions, one optimized for the discovery ad one optimized for the exclusion.

5.7.6 Signal regions combination and shape fit

In the case of the model-dependent fit used to compute the exclusion limits, stronger limits can be obtained combining together orthogonal SRs. The SRs defined in order to maximize the exclusion probability can be divided into bins using suitable kinematic variables. The likelihood function reported in Eq. (5.7.1) is modified to account for the combination of the multiple SRs used.

This procedure provides more information to the likelihood, compared to the use of only the integrated signal region. The analysis is sensitive to the different shape of signal and background and a better rejection of signal non compatible with the observed data is possible. This technique is called *shape fit*.

CHAPTER 6

Search for sleptons direct production

The search presented in this Chapter was developed in order to observe the direct production of slepton pairs and the chargino pair with slepton mediated decay. The analysis uses proton-proton collision data collected by ATLAS in 2015 and 2016, with a total integrated luminosity of 36.1 fb^{-1} [58].

The models and the signature are described in Section 6.1 and the Monte Carlo simulation used is reported in Section 6.2. Section 6.3 illustrates the triggers and the data quality requirements. The objects definition is reported in Section 6.4, while Section 6.5 presents the preliminary selection common to all the regions. The signal regions definition, the background estimate strategy and the validation of the analysis are reported respectively in Section 6.6, 6.7 and 6.8. The uncertainties are addressed in Section 6.9 and the result is finally reported in Section 6.10. The results obtained by the CMS Collaboration considering the same signal models are discussed in Section 6.11.

6.1 Models and signature

The SUSY models considered in this search are the direct production of sleptons and the direct production of charginos with slepton mediated decay, as described in Section 1.4.1. The search was initially developed to target the sleptons observation, since the process had not yet been explored with the ATLAS Run 2 data, and then extended to the chargino model.

The two processes have a similar signature: the final state consists of two opposite sign leptons (electron or muon) and missing energy due to neutralinos and neutrinos, without hadronic activity arising directly from the SUSY process. In the sleptons production case, the two leptons need to have the same flavor, in order to avoid leptonic number violation, while in the charginos case also e-μ events are possible.

The mass spectra of the Supersymmetryc particles are illustrated in Figure 6.1. In the case of the charginos direct production, the mass of the intermediated slepton is assumed to be in the middle point between the charginos and the neutralino mass:

$$m(\tilde{l}_{\mathrm{LH}}) = \frac{1}{2}\left[m(\tilde{\chi}_1^{\pm}) + m(\tilde{\chi}_1^0)\right] \tag{6.1}$$

The dependence of the search sensitivity on the assumption of the slepton mass was investigated in the ATLAS Run 1 result for the same analysis [125]. The final result is not strongly affected by the slepton mass, unless it is very close to the neutralino's: in this case the momentum of the leptons in the final state would be low and the selection performed in the search would no longer be effective. For this reason, only the case of slepton mass in the middle point between the chargino and the neutralino is considered in this Thesis.

Depending on the mass differences between the particles involved, the spectra can be compressed or not. In case of a compressed spectrum, the leptons in the final state would have low momentum. The analysis here presented is based on the assumption of a large mass difference between the slepton or chargino and the neutralino. The compressed spectrum case is not considered, therefore leptons with large momentum are used in the search.

Searches with the aim of observe the same SUSY processes were already performed with the data collected by the ATLAS detector during LHC Run 1, with $\sqrt{s} = 8$ TeV [125]. The result of the slepton search is shown in Figure 6.2, in the form of *exclusion limits* in the sleptons-neutralino mass plane, corresponding to the two free parameters of the model. The non-observation of the signal is converted in a lower limit on the masses of the SUSY particles considered in the model. Two set of curves are present in the plots, the area circumscribed by the blue dashed line (*expected limit*) would be excluded at 95% of confidence level (CL) in the case of the observation in the SRs of a number of events matching the SM prediction. The yellow band correspond to the $\pm 1\sigma$ variation on the expected limit, including all the uncertainties except the one on the the signal cross-section. The set of red curves corresponds to the exclusion limit for the observed data, at 95% CL. The observed limit can be weaker or stronger compared to the expected one, depending on the fact that data can respectively over-fluctuate or under-fluctuate compared to the SM prediction. The dotted red lines correspond to $\pm 1\sigma$ variation on the observed limit due to the signal cross-section uncertainty. Figure 6.2(a) reports the limit in the case of LH sleptons, while Figure 6.2(b) shows the limit in the RH case. Combining together the two cases (Figure 6.2(c)), slepton with mass up to 330 GeV is excluded.

Considering the chargino production, the Run 1 analysis provided the exclusion limit shown in Figure 6.3: in a chargino-neutralino mass plane, chargino with mass up to 480 GeV is excluded with 95% confidence level. The result obtained using data with $\sqrt{s} = 7$ TeV is also shown with a continuous blue line. A preliminary result using Run 2 data (2015 and part of the 2016 data sets) was also produced [126]. The Run 1 exclusion limit was extended to 640 GeV, as shown in Figure 6.4. The same plot also shows a Run 1 exclusion limit obtained with a search sensitive to the compressed spectrum scenario, the contour being the one close to the diagonal (continuous blue line).

The search presented in this Chapter uses an integrated luminosity of 36.1 fb^{-1}, corresponding to the data collected by ATLAS between 2015 and 2016 (see Section 3.3). Compared to Run 1, the increased center of mass energy and the larger amount of data collected provide a great occasion for the SUSY particles discovery, allowing to cover a wider phase space. Moreover, in case of non-observation of the signal, it is possible to have a significant improvement of the Run 1 exclusion limits.

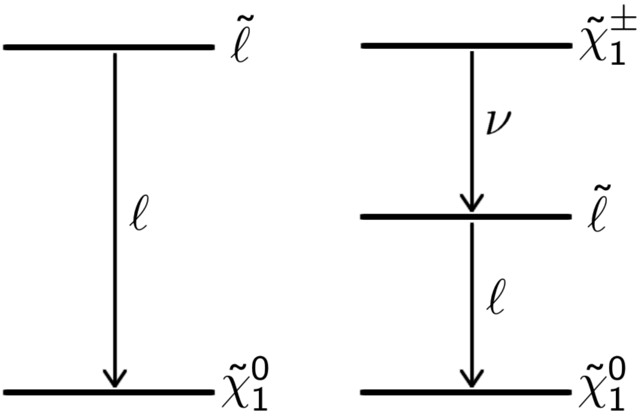

(a) (b)

Figure 6.1: Mass spectrum in the case of the (a) sleptons direct production, where the slepton decays in neutralino emitting a lepton and (b) charginos direct production, where the chargino decays in slepton emitting a neutrino, and then the slepton decays in neutralino emitting a lepton.

6.2 Monte Carlo samples

A general description of the Monte Carlo samples used by the ATLAS Collaboration was reported in Section 5.3. The simulated samples used in the specific analysis illustrated in this Chapter, both for the SUSY signal and for the background processes, are described in this Section.

6.2.1 Signal samples

The Monte Carlo signal samples, both for sleptons and charginos production, are generated using MadGraph5_aMC@NLO [127], that provides leading-order matrix elements with up to two extra partons, and interfaced with Pythia8 [128], with the A14 tune for the modeling of the SUSY particles decay chain, parton showering and hadronization. The NNPDF2.3 LO set is used as parton distribution function.

Cross sections are computed at the next-to-leading-order (NLO), with soft gluon emission effects added at next-to-leading-logarithm (NLL) accuracy [60–62]. The uncertainty

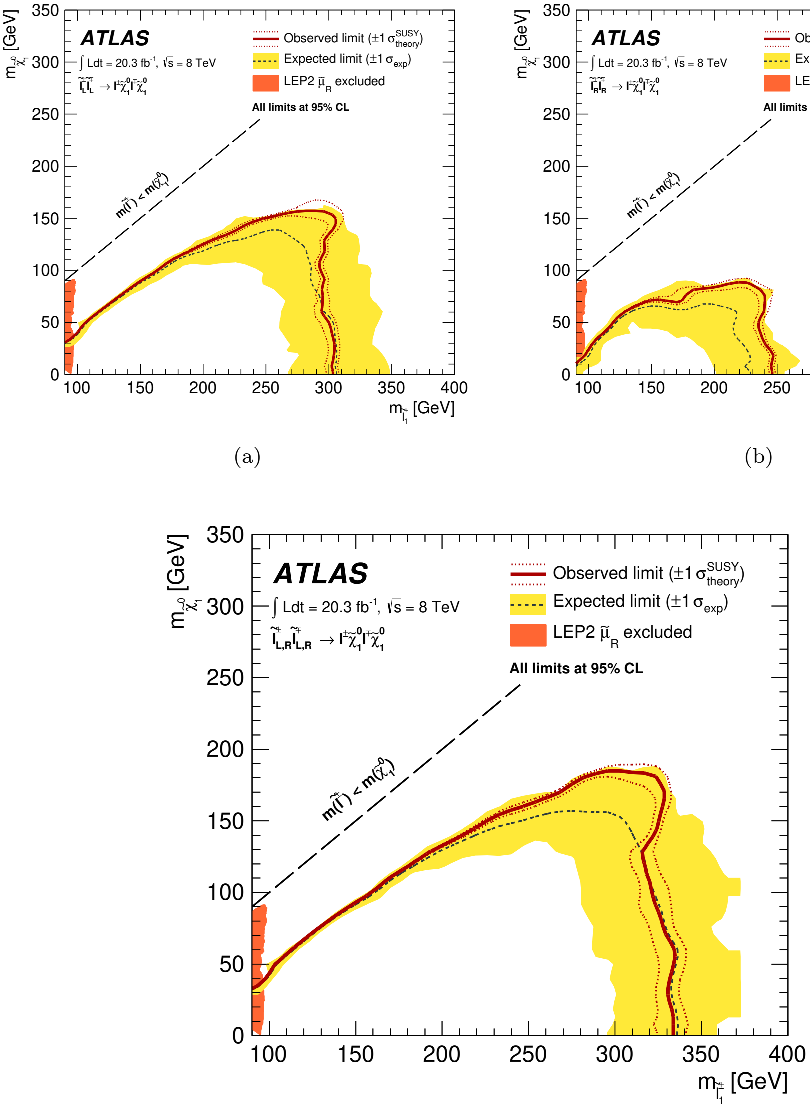

(a)

(b)

(c)

Figure 6.2: Exclusion limits at the 95% confidence level in the slepton-neutralino masses plane, in the case of (a) RH, (b) LH and (c) both RH and LH sleptons. The blue dashed line represents the expected exclusion limit, with the yellow band corresponding to the $\pm 1\sigma$ variation due to all the uncertainties sources except the one on the the signal cross-section. The red line correspond to the observed exclusion limit, with a $\pm 1\sigma$ variation due to the signal cross-section uncertainty (red dotted lines). The result is obtained using the data collected by ATLAS at the LHC Run 1, with $\sqrt{s}$ = 8 TeV and an integrated luminosity of 20.3 fb^{-1} [125].

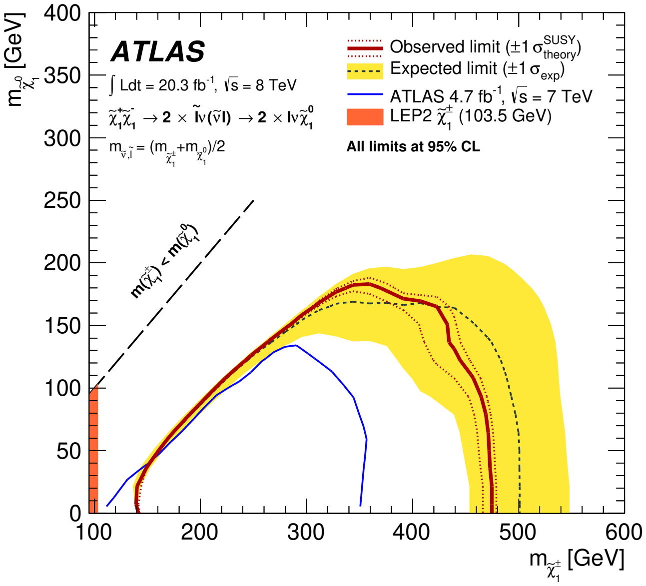

Figure 6.3: Exclusion limits at the 95% confidence level in the chargino-neutralino masses plane for the chargino pair production with slepton mediated decay model. The blue dashed line represents the expected exclusion limit, with the yellow band corresponding to the $\pm 1\sigma$ variation due to all the uncertainties sources except the one on the the signal cross-section. The red line correspond to the observed exclusion limit, with a $\pm 1\sigma$ variation due to the signal cross-section uncertainty (red dotted lines). The result is obtained using the data collected by ATLAS at the LHC Run 1, with $\sqrt{s} = 8$ TeV and an integrated luminosity of 20.3 fb^{-1} [125]. The observed limit of a search performed using data with $\sqrt{s} = 7$ TeV is also reported (blue continuous line).

on the cross section is taken from an envelope of predictions that use different PDF sets and different factorization and renormalization scales. The production cross sections for slepton and chargino pair for various mass values are reported in Tables 1.3 and 1.4 respectively, the uncertainty ranges from 3% to 10%.

Many samples with different SUSY particles masses are generated. The samples grid for the sleptons search is reported in Figure 6.5: the slepton mass range is between 100 and 700 GeV, with 50 GeV step; a neutralino mass between 1 GeV and 400 GeV, with 50 GeV step, is considered. A finer granularity is used in the region close to the diagonal, in order to have a better precision in the computation of the exclusion contour.

The signal grid generated for the charginos with slepton mediated decay is shown in Figure 6.6: charginos mass between 150 and 900 GeV with 100 GeV step and neutralino mass from 1 GeV to 400 GeV with 50 GeV spacing are considered. The grid granularity however is not constant, lower granularity is used in the region already excluded by the results of previous searches, while a finer granularity is used in the region close to the diagonal.

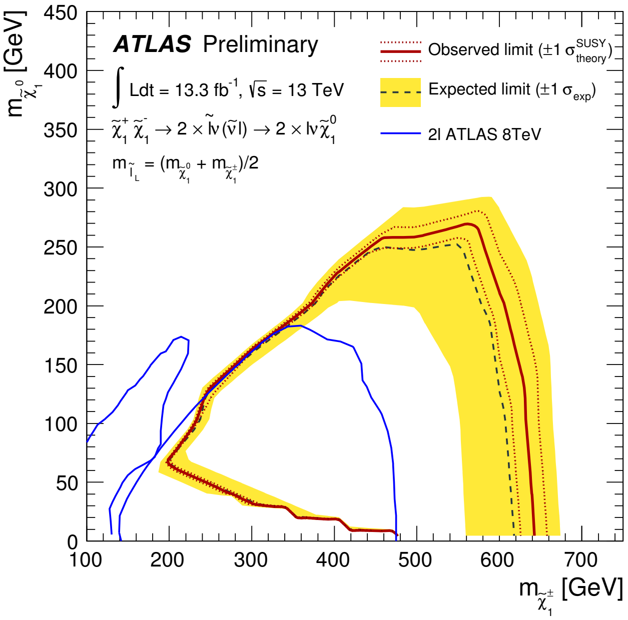

Figure 6.4: Exclusion limits at the 95% confidence level in the chargino-neutralino masses plane. for the chargino pair production with slepton mediated decay model. The blue dashed line represents the expected exclusion limit, with the yellow band corresponding to the $\pm 1\sigma$ variation due to all the uncertainties sources except the one on the the signal cross-section. The red line correspond to the observed exclusion limit, with a $\pm 1\sigma$ variation due to the signal cross-section uncertainty (red dotted lines). The result is obtained using the data collected by ATLAS at the LHC Run 2, between 2015 and July 2016, with $\sqrt{s} = 13$ TeV and an integrated luminosity of 13.3 fb^{-1} [126]. The observed limit of the Run 1 searches, for compressed (curve near the diagonal) and non compressed mass spectrum, are also reported (blue continuous lines).

6.2.2 Background samples

The background samples used in the analysis are:

- diboson (VV): this category include WW, WZ and ZZ processes [129]. Events can have two charged leptons and two neutrinos, three charged leptons and a neutrino or four charged leptons. The Sherpa v2.2.1 generator is used [130]. The matrix elements for diagrams with four electroweak vertices with additional hard parton emissions are calculated with Comix [131] and virtual QCD corrections are computed with OpenLoops [132]. The NNPDF3.0 NNLO PDF [133] set is used, together with a dedicated parton shower tuning developed by the Sherpa authors. Cross sections at the next-to-leading-order are used.

- $t\bar{t}$ and Wt [134, 135] the events are generated using Powheg [136, 137], considering the CT10 as PDF set [138]. Pythia 6 [139] is used for the parton shower and

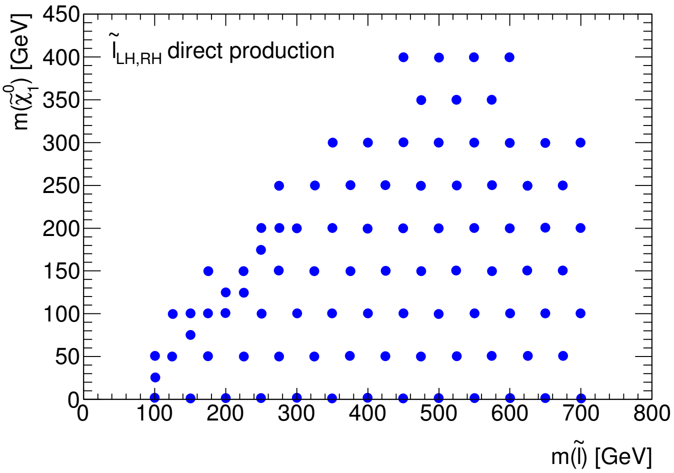

Figure 6.5: Points of the Monte Carlo simulation of the signal grid used in the search for sleptons direct production.

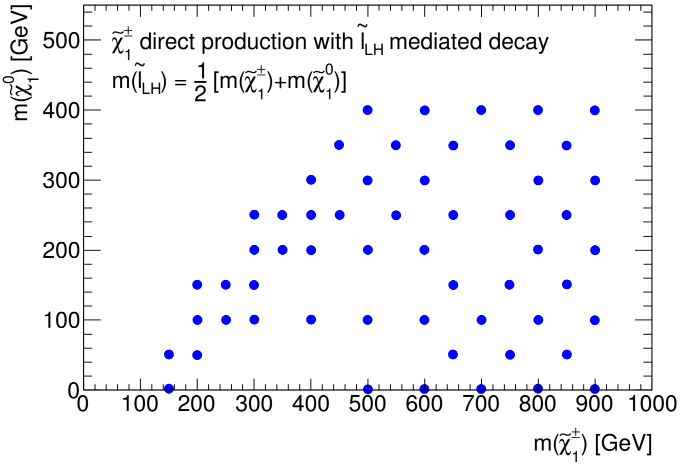

Figure 6.6: Points of the Monte Carlo simulation of the signal grid used in the search for charginos direct production with slepton mediated decay.

Monte Carlo samples				
Sample	Generator	Parton shower	PDF	Cross section
SUSY signal	MadGraph5	Pythia8	NNPDF2.3 NNLO	NLO+NNLL
Diboson	Sherpa	Sherpa	NNPDF3.0 NNLO	NLO
$t\bar{t}$	Powheg	Pythia6	CT10	NNLO+NNLL
Wt	Powheg	Pythia6	CT10	NLO
Z/γ^*+jets	Sherpa	Sherpa	CT10	NNLO
Triboson	Sherpa	Sherpa	NNPDF3.0 NNLO	NLO
$t\bar{t}V$	MadGraph5	Pythia8	NNPDF3.0 NNLO	NLO
Higgs	Pythia8	Pythia8	NNPDF3.0 NNLO	NNLO+NNLL
$t\bar{t}H$	MadGraph5	Herwig++	CT10	NLO

Table 6.1: Signal and background samples used in the analysis illustrated in this Chapter. For each process the generator, the parton shower, the PDF set and the order of the cross section are reported.

Perugia 2012 tune [140] is employed for the underlying event. The top quark mass is assumed to be 172.5 GeV. The samples are normalized to NNLO + NNLL (next-to-next-to-leading-logarithm) QCD cross section [141].

- Z/γ^*+jets [142,143] events are produced using Sherpa v2.2.1, with matrix elements calculated using Comix and OpenLoop, for up to two partons at NLO and up to four partons at leading order (LO). The CT10 PDF set and the Sherpa parton shower tuning are used. A K-factor was used to normalize the Z+jets events to the NNLO QCD cross sections [144].

- other minor background processes are also considered: triboson processes (WWW, WWZ, WZZ and ZZZ) with fully leptonic final state are simulated using Sherpa v2.2.1, NNPDF3.0 NNLO PDF and NLO cross section are used. $t\bar{t}$ associated to W or Z boson events [145] are generated with MadGraph5_aMC@NLO and Pythia 8 [128] is used as parton shower, with NNPDF3.0 NNLO PDF and NLO cross section. Higgs boson production processes [146] are generated using Pythia 8 and normalized to NNLO+NNLL cross section. In case of $t\bar{t}$ associated to H boson events, the events generator is MadGraph5_aMC@NLO and Herwig++ is used as parton shower, with NLO cross section.

A summary of the signal and background samples used is reported in Table 6.1.

6.3 Trigger and events quality

This Section illustrates the trigger selection used in the search and the quality checks that data have to undergo to be used in an analysis.

6.3.1 Trigger

Triggers based on the requirement of two leptons (electrons or muons) are used: the two particles can be two muons, two electrons or one electron and one muon. In order to fire the trigger, the two particles need to have a p_{T} larger then a certain threshold. Table 6.2 reports the different thresholds used for events with two electrons, two muons or a electron-muon pair. The thresholds can be different in 2015 and 2016 data, since a tighter selection was used during 2016 in order to account for the increasing LHC instantaneous luminosity.

The leptons transverse momentum used in the trigger selection algorithms (online) does not correspond exactly to the p_{T} evaluated after the objects reconstruction (offline), since in the first case a limited amount of information and quick algorithms are used, while in the second case the momentum is evaluated from objects reconstructed following the procedures illustrated in Chapter 4 and benefits of a precise calibration. As consequence, the selection efficiency of the trigger is a function of the leptons offline momentum, as illustrated in Figure 6.7: part of the 2015 data set is used to compute the efficiency for a single electron trigger with an online selection of $p_{\mathrm{T}} > 12$ GeV, showing that the trigger has low efficiency in the 12-20 GeV interval [147]. This consideration still holds in the case of dileptonic triggers.

The online selection on the leptons p_{T} for the dileptonic triggers used in the search ranges from 12 to 22 GeV, so in order to ensure a good trigger efficiency the leptons are required to have p_{T} larger then 25 GeV.

Trigger online selection		
Trigger type	2015 data	2016 data
ee	$p_{\mathrm{T}}^{e} > 12$ GeV	$p_{\mathrm{T}}^{e} > 17$ GeV
$\mu\mu$	$p_{\mathrm{T}}^{\mu} > 18$ GeV	$p_{\mathrm{T}}^{\mu} > 22$ GeV
$e\mu$	$p_{\mathrm{T}}^{e} > 17$ GeV, $p_{\mathrm{T}}^{\mu} > 14$ GeV	$p_{\mathrm{T}}^{e} > 17$ GeV, $p_{\mathrm{T}}^{\mu} > 14$ GeV

Table 6.2: Online selection on the leptons transverse momentum performed by the dileptonic triggers used in the search. The p_{T} thresholds are different in the case of di-electron, di-muon or electron-muon pairs. The thresholds of the triggers were changed between 2015 and 2016, in order to account for the increasing LHC instantaneous luminosity and pile-up condition.

6.3.2 Events quality

In order to be used in a physics search, events collected by ATLAS must satisfy the following requirement:

- events are required to be part of the Good Run List, as illustrated in Section 3.3;
- events can have an error flag associated to LAr or Tile calorimeter, due to noise bursts or temporary trip in the high voltage. Events affected by such errors are removed;

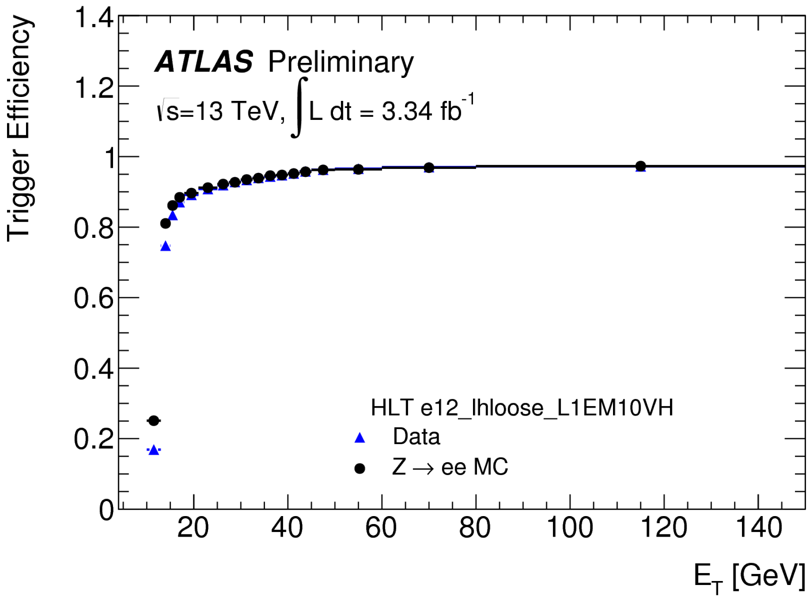

Figure 6.7: Efficiency of a single electron trigger as a function of the offline electron E_T, with an online selection of $p_\mathrm{T} > 12$ GeV, evaluated using ATLAS data collected during 2015. The data are compared to the expectation from $Z \to ee$ simulation. The uncertainty bars, obtained combining statistical and systematic uncertainties, are smaller then the marker dimension [147].

- the SCT modules can go in *busy* status due to large number of signal that need to be recorded. The problematic modules are auto-recovered in few seconds, but events affected by the procedure are removed;

- event must have at least one primary vertex;

- events with jets coming from non-collisional background are removed. Non-collisional background consist of particles that have not been produced in normal collisions of the LHC beams [148].The sources are protons from the beam that are lost in the proximity of the experiment or residual gas inside the beam pipe (*beam-induced background*). Other sources of non-collisional background are the cosmic-ray showers, the particles reaching the ATLAS detector being predominantly muons. Both beam-induced background and cosmic-ray muons can fire a trigger, due to a large energy deposit in the calorimeter or due to an overlap with a collision event. In order to remove non-collisional background, quality criteria for jets selection are applied [149], such as position in the detector, shower shape, and track compatible with the vertex;

- events containing cosmic muons or muons originated from the background in the cavern are removed. These particles are identified due to the non compatibility with the interaction vertex.

Objects definition		
Object	Quantity	Value
Electrons	Acceptance	$\|\eta\| < 2.47$
	Momentum	$p_{\mathrm{T}} > 25$ GeV
	Identification	Medium
	Isolation	GradientLoose
	Impact parameter	$\|z_0 \sin\theta\| < 0.5$ mm
		$\|d_0/\sigma_{d_0}\| < 5$
Muons	Acceptance	$\|\eta\| < 2.4$
	Momentum	$p_{\mathrm{T}} > 25$ GeV
	Identification	Medium
	Isolation	GradientLoose
	Impact parameter	$\|z_0 \sin\theta\| < 0.5$ mm
		$\|d_0/\sigma_{d_0}\| < 3$
Jets	Acceptance	$\|\eta\| < 2.4$
	Momentum	$p_{\mathrm{T}} > 20$ GeV
	Jet vertex tagger	JVT$>$ 0.59 if $p_{\mathrm{T}} < 60$ GeV
	b-tagging	77 % working point

Table 6.3: Requirement for the objects used in the analysis: electrons, muons and jets.

6.4 Physics objects definition and selection

The characteristics of the physics objects used in the ATLAS searches were illustrated in Chapter 4. Among the collections of physics objects available, the most suitable definitions and working points are chosen for each analysis. The objects used for the search reported in this Chapter are described in this section.

6.4.1 Electrons

The geometric acceptance is $|\eta| < 2.47$, that is the Inner Detector coverage, and p_{T} should be larger then 25 GeV, to ensure high trigger efficiency (see previous Section). The operating point for the identification is *Medium*, providing an identification efficiency of 89% and a misidentification rate (evaluated as the probability to identify an hadron as an electron) of 0.4% for electrons with $p_{\mathrm{T}} = 25$ GeV. In order to reject non-prompt electrons, the isolation requirement is *GradientLoose*, an operating point providing an efficiency of 95% for electrons with $p_{\mathrm{T}} = 25$ GeV.

Electrons track also have to be compatible with the primary interaction vertex of the hard collision, in order to reduce electrons from conversions and secondary particles [100]. The following selections are applied: $|z_0 \sin\theta| < 0.5$ mm and $|d_0/\sigma_{d_0}| < 5$, where d_0 is the distance of the track to the beam-line and z_0 is the distance along the beam-line between the point where d_0 is measured and the beam-spot position.

The requirements for the electrons are summarized in Table 6.3.

6.4.2 Muons

Geometric acceptance for muons is $|\eta| < 2.4$ and the momentum selection is $p_{\mathrm{T}} > 25$ GeV. The identification operating point is *Medium* , which provides a flat efficiency of 96% and a misidentification rate of 0.17%. *GradientLoose* isolation is used, providing a 90% efficiency at $p_{\mathrm{T}} = 25$ GeV. Similarly to the electron case, requirements on the impact parameters are applied: $|z_0 \sin\theta| < 0.5$ mm and $|d_0/\sigma_{d_0}| < 3$ [101].

Muons selection criteria are reported in Table 6.3

6.4.3 Jets

Only jets in the barrel region ($|\eta| < 2.4$) are considered, with momentum $p_{\mathrm{T}} > 20$ GeV. The anti-k_t algorithm is used for the reconstruction, with 0.4 as distance parameter. Jets from pile-up events are reduced applying the JVT selection for jets with $p_{\mathrm{T}} < 60$ GeV, the JVT requirement is not applied to jets with larger p_{T} since the pile-up contribution becomes negligible. The b-tagging is provided by the `MV2c10` algorithm, with a 77% efficiency working point. Jets requirements are summarized in Table 6.3.

6.4.4 Overlap removal

During the object reconstruction, ambiguity in the classification of an object in more categories can occur. The overlap is removed following the procedure [150]:

- if a b-tagged jet is close to an electron, with $\Delta R < 0.2$, the electron is removed, since it is likely to be from a semi-leptonic b-hadron decay; if instead the jet is not b-tagged, the jet itself is removed, as it likely originates from a shower induced by the electron;
- a jet close to a muon ($\Delta R < 0.2$) that carry a significant fraction of the jet energy itself (70%) is removed from the jets list, since the jet mostly originate from muon bremsstrahlung;
- an electron and muon close to the remaining jets ($\Delta R < 0.4$) are removed, in order to reject leptons coming from c-hadron and b-hadron semi-leptonic decays;
- electron sharing an Inner Detector track with a muon is removed from the electrons list.

6.5 Preliminary selection

After passing the trigger and the quality requirements, a preliminary selection, that will be in common to all the regions of interest for the analysis, is performed. Only events with exactly two opposite sign leptons, with same flavor or different flavor, $p_{\mathrm{T}} > 25$ GeV and the proper operating points discussed in Section 6.4, are considered. A cut on the leptons invariant mass, $m_{\ell\ell} > 40$ GeV, is applied in order to remove the low mass resonances. The selection is summarized in Table 6.4.

Preliminary selection	
Quantity	Selection
Quality requirement	✓
Trigger	✓
Leptons number	exactly 2
Leptons sign	opposite sign
Leptons flavor	SF or DF
Leptons momentum	$p_\mathrm{T} > 25$ GeV
Leptons invariant mass	$m_{\ell\ell} > 40$ GeV

Table 6.4: Preliminary selection in common to all the regions considered in the analysis.

6.6 Signal regions

The signal regions selection is described in this Section. Two different signal models are considered: in the direct sleptons case the leptons in the final state can only have the same flavor, while in the charginos case the different flavor is also possible. Since the background composition is different in the case of SF or DF leptons in the final state, the SRs definitions will be different.

A large range of possible masses for the SUSY particles is considered. The kinematic variables distributions depends on the mass of the SUSY particles involved (as illustrated in Section 5.2 for the $m_{\mathrm{T}2}$ variable), so the optimal cut for the SR selection is not unique for all the signal samples and more then one SR is considered, in order to have a good sensitivity over a large spectrum of masses.

The SRs used in the analysis are classified as:

- *inclusive signal regions*, that are optimized for the discovery of the SUSY signal and are used in the discovery fit to provide the upper limits on the SUSY cross sections, as illustrated in Section 5.7.5. These regions are called inclusive since they are not orthogonal;

- *exclusive signal regions*, that are obtained splitting the inclusive regions in smaller regions, called *bins*. The binning is optimized to maximize the exclusion limits and the bins are used to perform the shape fit, as illustrated in Section 5.7.6. These regions are called exclusive since they are orthogonal, in order to be combined in the shape fit.

The kinematic selection for the SRs is now described. The requirements common to all the signal regions, inclusive or exclusive, are the following (summarized in Table 6.5):

- *jets multiplicity*: no hadronic activity is expected to originate directly from the signal process, but initial state state radiation is still possible. Jets are classified as b-tagged jets and non-b-tagged jets, that include jets from light quarks and gluons. Applying the zero jets requirement, a scan on different jet momentum threshold was performed. The best cuts combination is to consider as threshold $p_\mathrm{T} > 20$ GeV for b-tagged jets and a more loose requirement of $p_\mathrm{T} > 60$ GeV for non-b-tagged

Signal region common selection	
Quantity	Selection
non-b-tagged jets multiplicity	0 ($p_{\mathrm{T}} > 60$ GeV)
b-tagged jets multiplicity	0 ($p_{\mathrm{T}} > 20$ GeV)
Leptons invariant mass	$m_{\ell\ell} > 111$ GeV
Stransverse mass	$m_{\mathrm{T2}} > 100$ GeV

Table 6.5: Selection common to all the SRs.

jets. The tighter requirement on the b-tagged jets is motivated by the fact that this selection is useful to remove the $t\bar{t}$ process, while the fraction of b-tagged jets (that can rise from gluon splitting into $b\bar{b}$) in the signal events is expected to be small. Since no significant difference was observed upon different signal samples, the cut is the same in all the signal regions;

- *stransverse mass*: the m_{T2} variable was described in Section 5.2. A scan on different cut was performed. A baseline cut of at least $m_{\mathrm{T2}} > 100$ GeV is applied, in order to remove most of the $t\bar{t}$ and diboson backgrounds. Since the m_{T2} distribution endpoint depends strongly on the SUSY particle masses, the optimal cut is different for each signal samples, so different m_{T2} selections are considered;

- *leptons invariant mass*: in case of same flavor leptons, a huge background contribution is due to Z+jets and ZZ events, especially in the leptons invariant mass region in the window between 71 and 111 GeV. Since in general the signal samples have larger $m_{\ell\ell}$ compared to the background, a baseline cut of $m_{\ell\ell} > 111$ GeV is applied. The lower cut on $m_{\ell\ell}$ is convenient also in the case of different flavor leptons: the chargino samples used in the optimization procedure have a large mass, since mass up to 600 GeV are excluded by previous result, giving an harder $m_{\ell\ell}$ distribution compared to the SM background.

6.6.1 Inclusive signal regions

Inclusive signal regions are defined as follows:

- regions with different flavor leptons have the same $m_{\ell\ell}$ cut at 111 GeV. An increasing selection on m_{T2} is used, since it is the variable with the larger variation for different signal samples and for increasing chargino masses the m_{T2} endpoint moves at larger value. The m_{T2} variable is required to be larger then 100, 150, 200 or 300 GeV, the regions are named SR2-DF-100, SR2-DF-150, SR2-DF-200 and SR2-DF-300 respectively;

- regions with same flavor leptons use different $m_{\ell\ell}$ selections, since a large fraction of ZZ events survive the Z veto and it is one of the dominant background for a selction with SF leptons. The ZZ $m_{\ell\ell}$ distribution is anyway softer compared to

Inclusive signal region definitions		
Region	m_{T2} [GeV]	$m_{\ell\ell}$ [GeV]
SR2-SF-loose	> 100	> 111
SR2-SF-tight	> 130	> 300
SR2-DF-100	> 100	> 111
SR2-DF-150	> 150	> 111
SR2-DF-200	> 200	> 111
SR2-DF-300	> 300	> 111

Table 6.6: Definitions of the inclusive signal regions. Label "DF" or "SF" refers respectively to signal regions with different flavor or same flavor lepton pair.

the SUSY signals considered. SR2-SF-loose has $m_{\mathrm{T2}} > 100$ GeV and $m_{\ell\ell} > 111$ GeV, while SR2-SF-tight has $m_{\mathrm{T2}} > 130$ GeV and $m_{\ell\ell} > 300$ GeV.

The definitions of the inclusive signal regions are reported in Table 6.6 and a scheme in the m_{T2}-$m_{\ell\ell}$ plane is shown in Figure 6.8.

The kinematic distributions for the data and expected SM background in inclusive SRs are reported in the Figure 6.9, 6.10 and 6.11. The result after the background-only likelihood fit is shown, the normalization factors extracted from the corresponding CRs are used to rescale the $t\bar{t}$ and VV contributions. The "top" background includes $t\bar{t}$ and Wt, and the "other" backgrounds include Higgs bosons, $t\bar{t}V$ and VVV process. The "reducible" category corresponds to events with FNP leptons estimated with the Matrix Method. The uncertainty bands include all systematic and statistical contributions that will be described in Section 6.9. The final bin in each histogram also contains the events in the overflow bin.

Figures 6.9 and 6.10 show the $m_{\ell\ell}$ and m_{T2} distributions in SR2-SF-loose and SR2-SF-tight, and MC simulation for two signal samples are overlayed for comparison. Slepton pair production with slepton mass of 400 and 500 GeV and neutralino mass of 1 GeV are considered. Both the RH and the LH components of the SUSY signals are considered.

Figure 6.11 reports the $m_{\ell\ell}$ and m_{T2} distributions in SR2-DF-100 and MC simulation for two signal samples are overlayed for comparison: chargino pair production with charginos mass of 750 and 300 GeV and neutralino mass of 150 GeV are considered. The selections $m_{\mathrm{T2}} > 150$ GeV, $m_{\mathrm{T2}} > 200$ GeV and $m_{\mathrm{T2}} > 300$ GeV in Figure 6.11(b) correspond to SR2-DF-150, SR2-DF-200 and SR2-DF-300 respectively.

6.6.2 Exclusive signal regions

The exclusive signal regions are obtained splitting in bins the inclusive signal regions described in the previous Section:

- in the different flavor leptons case, the binning is performed only using the m_{T2} variable: $100 < m_{\mathrm{T2}} < 150$ GeV, $150 < m_{\mathrm{T2}} < 200$ GeV, $200 < m_{\mathrm{T2}} < 300$ GeV and $m_{\mathrm{T2}} > 300$ GeV bins are considered, named respectively SR2-DF-a, SR2-DF-b, SR2-DF-c and SR2-DF-d;

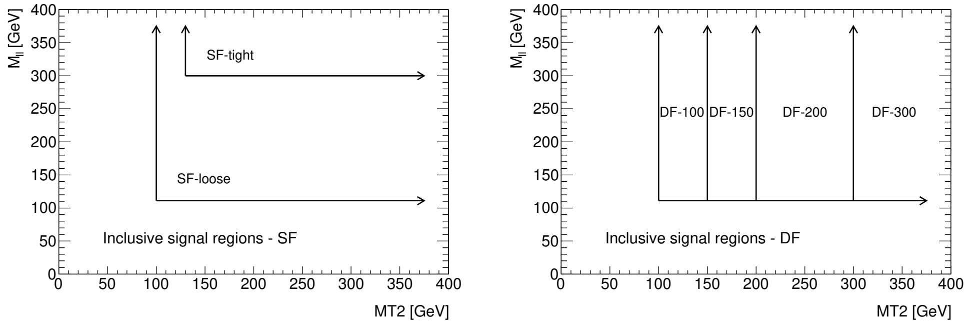

Figure 6.8: Representation of the inclusive signal regions in the m_{T2}-$m_{\ell\ell}$ plane. The plot on the left shows the SF regions, the one on the right the DF regions.

- in the same flavor leptons case, two dimensional orthogonal bins are obtained using both m_{T2} and $m_{\ell\ell}$ variables. The m_{T2} steps are the same of the different flavor leptons case, the $m_{\ell\ell}$ bins are 111-150 GeV, 150-200 GeV, 200-300 GeV and >300 GeV. The 4 m_{T2} intervals and 4 $m_{\ell\ell}$ intervals are combined together and give 13 exclusive regions. In the $m_{\mathrm{T2}} > 300$ GeV case the $m_{\ell\ell}$ division is not applied, due to the low statistic of the region.

In the case of the charginos decaying via sleptons signal, the different flavor selection provides a better sensitivity, due to the smaller contamination of Z+jets and ZZ backgrounds. For this reason the binning in same flavor leptons selection was optimized for the direct slepton signal, that can only have a same flavor leptons final state.

The exclusive signal regions definition, with the naming convention, are summarized in Table 6.7 and in Figure 6.12. The kinematic distribution for the data and expected SM background in exclusive SF SRs are reported in Figure 6.13 and 6.14, showing the m_{T2} distribution for different $m_{\ell\ell}$ selection.

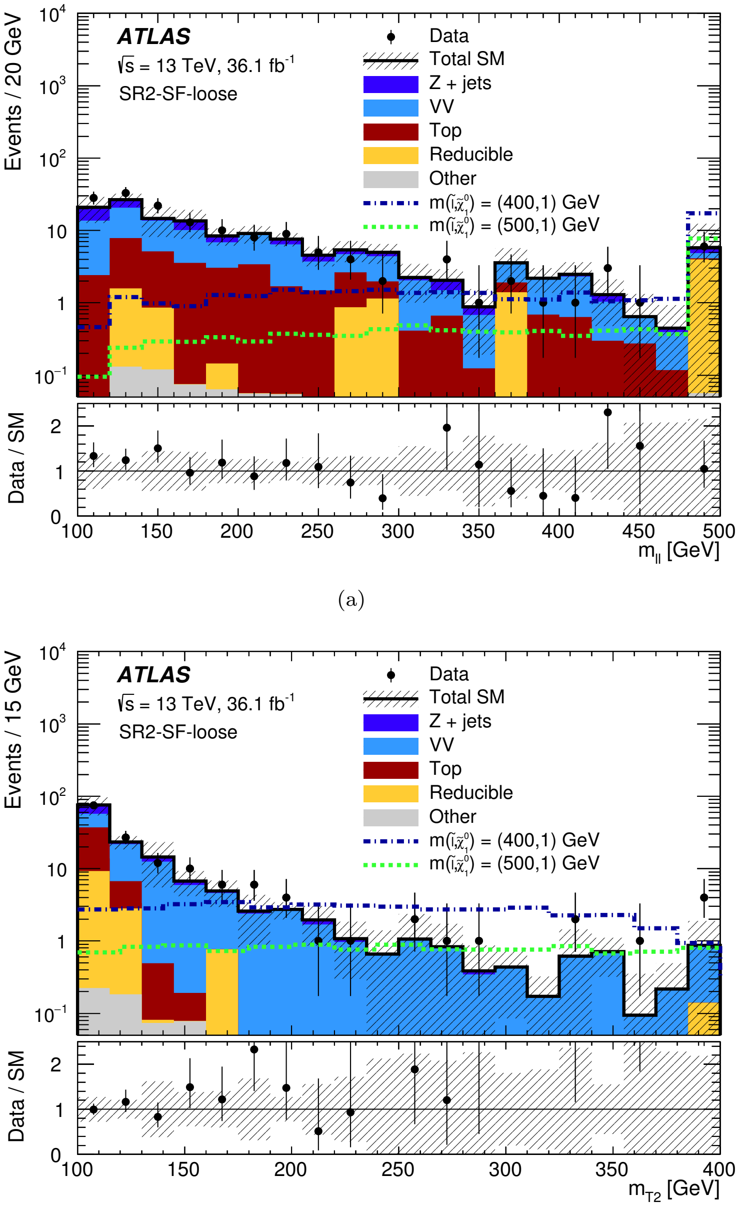

(a)

(b)

Figure 6.9: The (a) $m_{\ell\ell}$ and (b) m_{T2} distributions for data and the estimated SM backgrounds in SR2-SF-loose region, after performing the background-only likelihood fit. The uncertainty bands include all systematic and statistical contributions. Simulated signal samples for slepton pair production are overlayed for comparison: slepton with mass of 400 and 500 GeV and neutralino mass of 1 GeV are considered.

Exclusive signal region definitions			
SF bin	DF bin	m_{T2} [GeV]	$m_{\ell\ell}$ [GeV]
SR2-SF-a	SR2-DF-a	$\in [100, 150]$	$\in [111, 150]$
SR2-SF-b			$\in [150, 200]$
SR2-SF-c			$\in [200, 300]$
SR2-SF-d			> 300
SR2-SF-e	SR2-DF-b	$\in [150, 200]$	$\in [111, 150]$
SR2-SF-f			$\in [150, 200]$
SR2-SF-g			$\in [200, 300]$
SR2-SF-h			> 300
SR2-SF-i	SR2-DF-c	$\in [200, 300]$	$\in [111, 150]$
SR2-SF-j			$\in [150, 200]$
SR2-SF-k			$\in [200, 300]$
SR2-SF-l			> 300
SR2-SF-m	SR2-DF-d	> 300	> 111

Table 6.7: Definitions of the inclusive signal regions. Label “DF” or “SF” refers respectively to signal regions with different flavor or same flavor lepton pair.

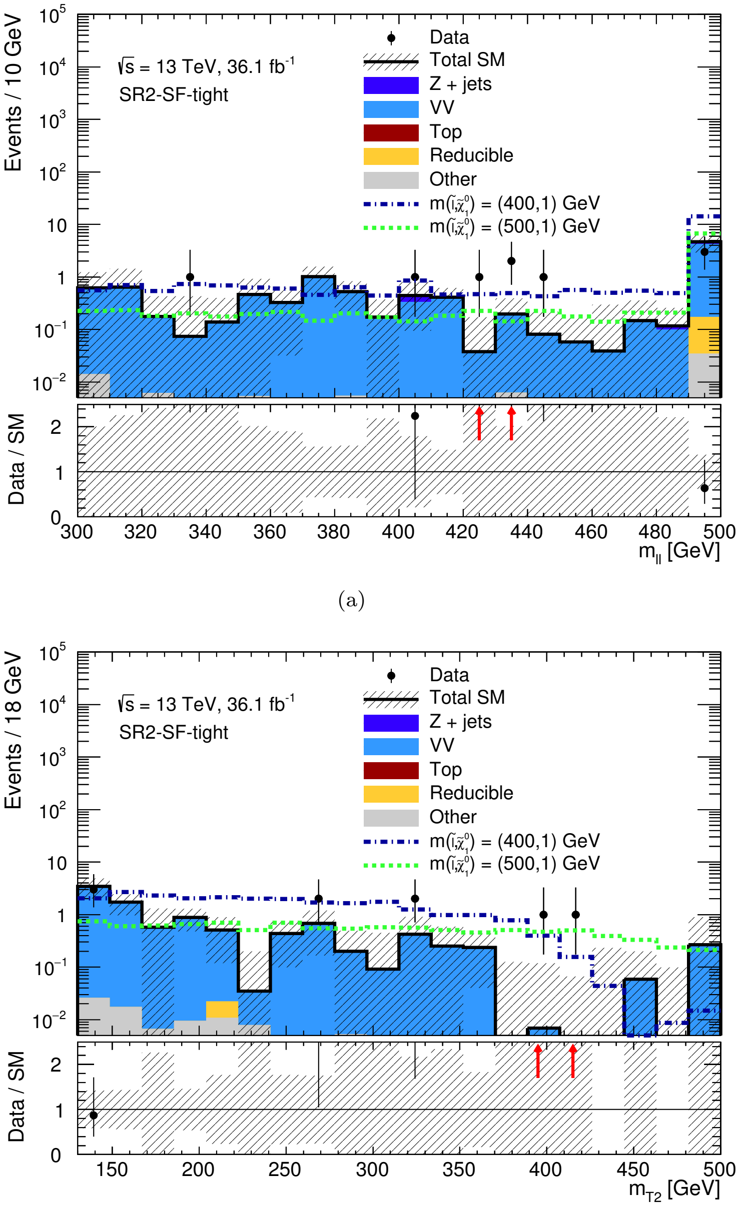

(a)

(b)

Figure 6.10: The (a) $m_{\ell\ell}$ and (b) m_{T2} distributions for data and the estimated SM backgrounds in SR2-SF-tight region, after performing the background-only likelihood fit. The uncertainty bands include all systematic and statistical contributions. Simulated signal samples for slepton pair production are overlayed for comparison: slepton with mass of 400 and 500 GeV and neutralino mass of 1 GeV are considered. The red arrows indicate a bin where the ratio of data to SM background, minus the uncertainty on this quantity, is larger than the y-axis maximum.

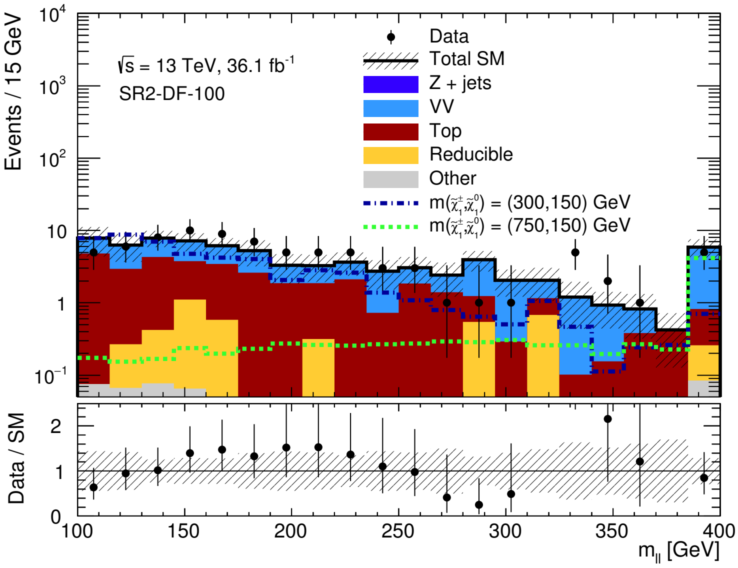

(a)

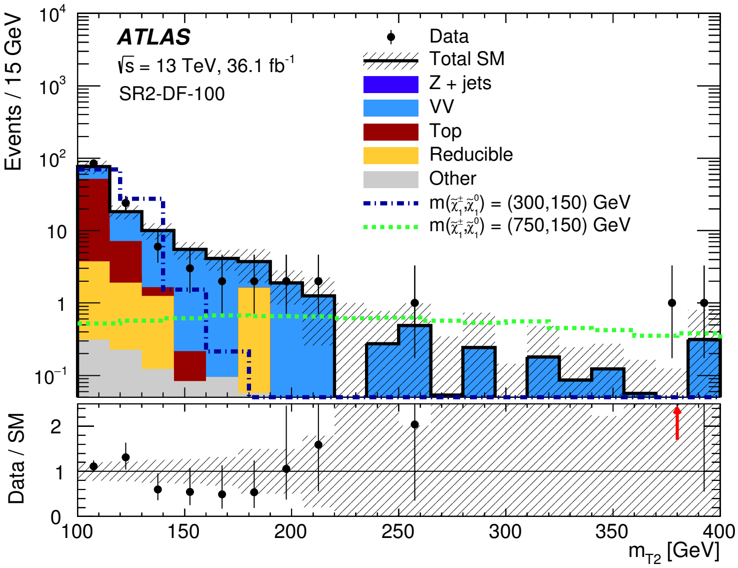

(b)

Figure 6.11: The (a) $m_{\ell\ell}$ and (b) m_{T2} distributions for data and the estimated SM background in the SR2-DF-100 region, after performing the background-only likelihood fit. The uncertainty bands include all systematic and statistical contributions. Simulated signal samples for chargino pair production are overlayed for comparison: chargino with mass of 750 and 300 GeV and neutralino mass of 150 GeV are considered. The red arrows indicate a bin where the ratio of data to SM background, minus the uncertainty on this quantity, is larger than the y-axis maximum.

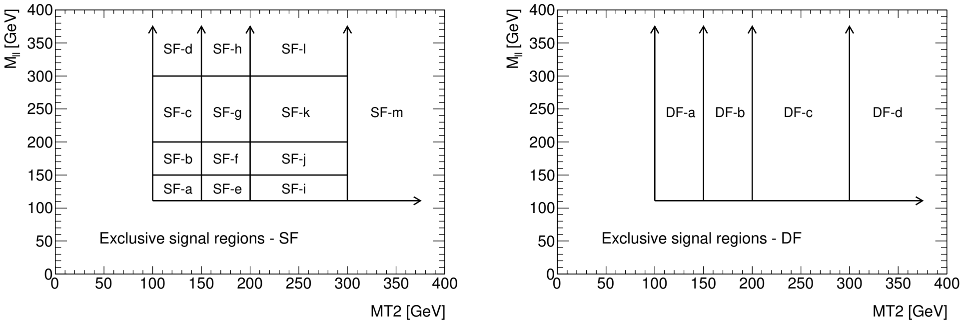

Figure 6.12: Representation of the exclusive signal regions in the m_{T2}-$m_{\ell\ell}$ plane. The plot on the left shows the SF regions, the one on the right the DF regions.

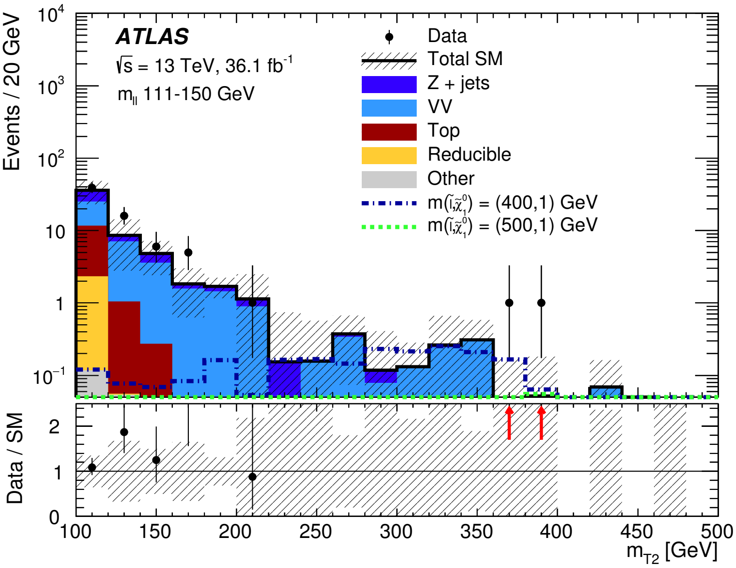

(a)

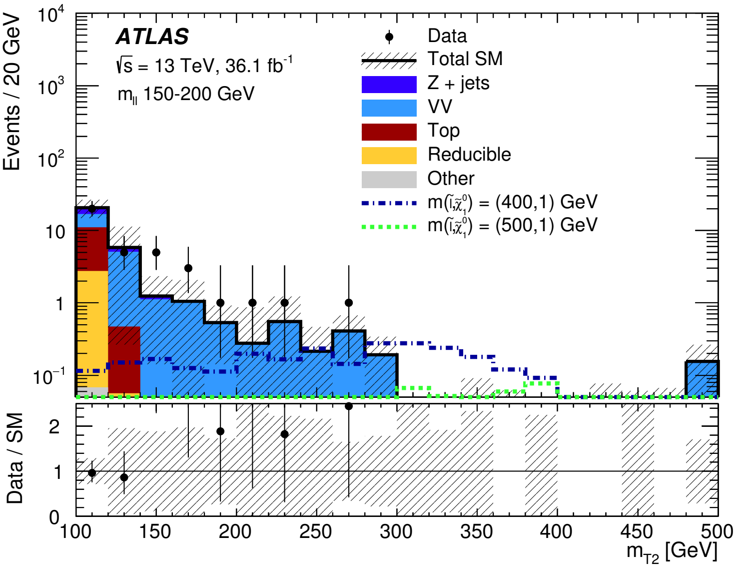

(b)

Figure 6.13: The m_{T2} distributions for data and the estimated SM background in the $111 < m_{\ell\ell} < 150$ region (corresponding to SR2-SF-a,b,c,d) and $150 < m_{\ell\ell} < 200$ GeV (corresponding to SR2-SF-e,f,g,h), after performing the background-only likelihood fit. The uncertainty bands include all systematic and statistical contributions. Simulated signal samples for slepton pair production are overlayed for comparison: slepton with mass of 400 and 500 GeV and neutralino mass of 1 GeV are considered. The red arrows indicate a bin where the ratio of data to SM background, minus the uncertainty on this quantity, is larger than the y-axis maximum.

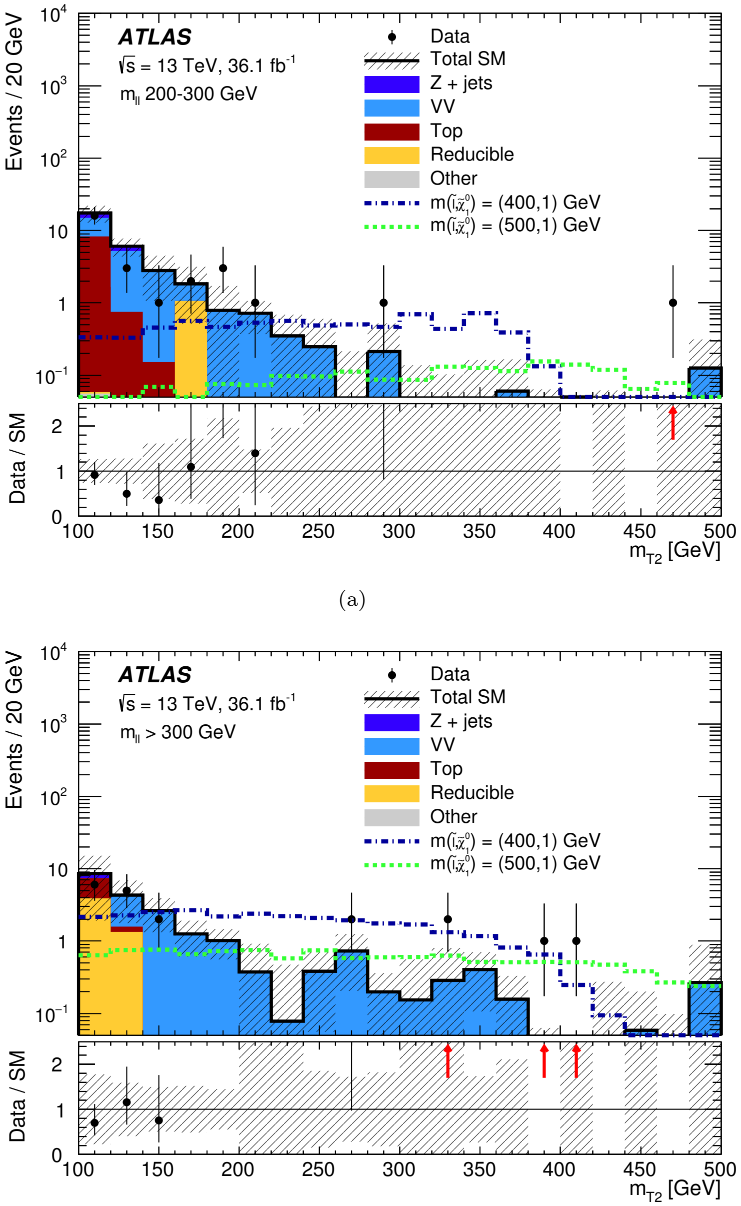

(a)

(b)

Figure 6.14: The $m_{\rm T2}$ distributions for data and the estimated SM background in the $200 < m_{\ell\ell} < 300$ GeV (corresponding to SR2-SF-i,j,k,l) and $m_{\ell\ell} > 300$ GeV (corresponding to SR2-SF-m), after performing the background-only likelihood fit. The uncertainty bands include all systematic and statistical contributions. Simulated signal samples for slepton pair production are overlayed for comparison: slepton with mass of 400 and 500 GeV and neutralino mass of 1 GeV are considered. The red arrows indicate a bin where the ratio of data to SM background, minus the uncertainty on this quantity, is larger than the y-axis maximum.

6.7 Background estimation

The procedure to evaluate the Standard Model background in the designed signal regions is addressed in this Section. The main background are diboson and $t\bar{t}$ processes, normalized to data in dedicated control regions (Section 6.7.1). The minor background processes estimated directly from Monte Carlo simulations are briefly described in Section 6.7.2. Background due to fake or non-prompt leptons is computed using the Matrix Method, as explained in Section 6.7.3.

6.7.1 Control regions

The main backgrounds processes in the signal regions are diboson, that includes WW, WZ and ZZ, and $t\bar{t}$. Dedicated control regions are developed for each background.

WW events pass the "exactly two leptons" requirement only if both the bosons decay leptonically, and the final state can have same flavor or different flavor leptons in equal measure. WZ events pass the selection in case of W hadronic decay and Z decaying in two charged leptons, resulting in a same flavor final state; there is also a small probability, in the case of W leptonic decay, to miss one of the three charge leptons and classify the events as "exactly two leptons". ZZ events enter in the two leptons selection in case of one Z decaying in charged leptons and the second Z decaying in neutrinos or quarks.

The diboson background is evaluated using Sherpa Monte Carlo simulation. This generator takes into account the interference between diboson production diagram decaying in the same final state, as for $WW \to \ell\nu\ell\nu$ and $ZZ \to \ell\ell\nu\nu$. The diagrams producing the same final state are then considered together and the information about the parent particles is not available in this MC generator. As consequence, an event can not be categorized as WW or ZZ using the parent particles information.

In order to have a precise background estimation, diboson events are classified in different flavor and same flavor leptons categories. From studies performed with others Monte Carlo generators (as example Powheg), it was verified that WW process is dominant in the different flavor categories, while in the same flavor case half of the contribution comes from WW and the other half from WZ-ZZ events.

Two control regions are designed for diboson:

- CR2-VV-SF, dedicated to the normalization of diboson events with same flavor leptons. Jets multiplicity is zero for both b-tagged ($p_{\mathrm{T}} > 20$ GeV threshold) and non-b-tagged jets ($p_{\mathrm{T}} > 60$ GeV threshold). Leptons invariant mass is selected close to the Z peak ($|m_{\ell\ell} - m_Z| < 20$ GeV), in order to have events dominated by WZ and ZZ events. A cut on the stransverse mass is also applied ($m_{\mathrm{T2}} > 130$ GeV) in order to have a selection close to the signals regions;

- CR2-VV-DF, dedicated to the normalization of diboson events with different flavor leptons. Also in this case jets multiplicity is zero for both b-tagged and non-b-tagged jets. Selection on the stransverse mass is $50 < m_{\mathrm{T2}} < 75$ GeV to have a selection close to the signal regions. The selection does not reach the signal regions at $m_{\mathrm{T2}} = 100$ GeV in order to have a validation region with intermediate m_{T2} values (see Section 6.8).

Control region definitions			
Region	CR2-VV-SF	CR2-VV-DF	CR2-Top
Leptons flavor	SF	DF	DF
non-b-tagged jets multiplicity	0	0	0
b-tagged jets multiplicity	0	0	≥ 1
$\lvert m_{\ell\ell} - m_Z\rvert$ [GeV]	< 20	–	–
m_{T2} [GeV]	> 130	$\in [50, 75]$	$\in [75, 100]$

Table 6.8: Definition of the control regions for diboson with same flavor leptons (CR2-VV-SF), diboson with different flavor leptons (CR2-VV-DF) and $t\bar{t}$ (CR2-Top) processes. The b-tagged jets momentum threshold is $p_{\mathrm{T}} > 20$ GeV and non-b-tagged jets momentum threshold is $p_{\mathrm{T}} > 60$ GeV, as in the signal regions case.

The $t\bar{t}$ events final state is characterized by two leptons and two b-jets. In case of $t\bar{t}$ events with soft jets, this background can enter in the signal regions. The background is normalized in a dedicated control region. CR2-Top is defined using events with different flavor leptons and at least one b-tagged jet, in order to have a good purity. The requirement on the stransverse mass is $75 < m_{\mathrm{T2}} < 100$ GeV, to improve the purity and to have a selection close to the signal regions. The definitions of the control regions are reported in Table 6.8.

The m_{T2} distribution for the data and expected SM background in the CRs is reported in Figure 6.15, 6.16 and 6.17, together with the corresponding validation regions in the case of CR2-Top and CR2-VV-DF (validation regions will be illustrated in Section 6.8). Signal samples are also overlayed to the background simulation in order to show the signal contamination, that is negligible in all the considered regions. The signal contamination will be further discussed in Section 6.10.1.

6.7.2 Minor background processes

Other Standard Model processes, having a small contribution, can enter the signal regions:

- Wt associated production, in the case of W leptonic decay, has two prompt charged leptons and genuine E_{T}^{miss} from neutrinos;
- Z/γ^*+jets process, with Z/γ^* decaying in charged leptons, can enter the signal regions selection in case of fake E_{T}^{miss};
- the contribution of processes such as triboson, Higgs boson production and $t\bar{t}$ associated to W, Z or H boson is almost negligible. They are group together under the label “Others” in the following.

These minor background processes are estimated directly from the Monte Carlo simulations.

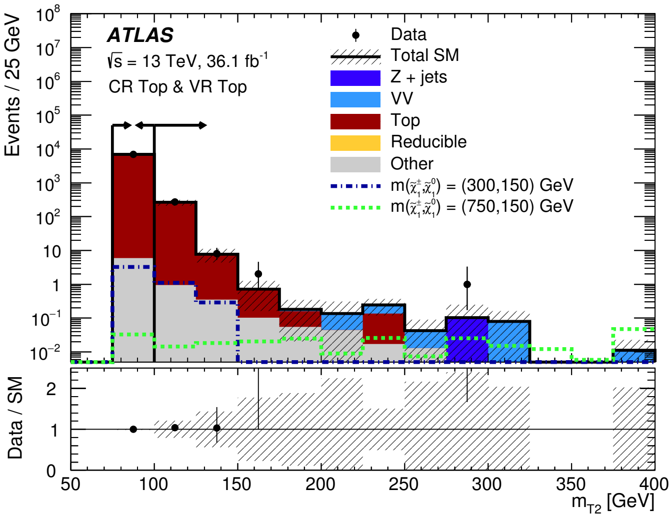

Figure 6.15: $m_{\rm T2}$ distributions for data and the estimated SM backgrounds in CR2-Top and VR2-Top, after performing the background-only likelihood fit. The arrows denote the $m_{\rm T2}$ ranges of the CR and VR. The uncertainty bands include all systematic and statistical contributions. Simulated signal samples for chargino pair production are overlayed to show the signal contamination: chargino with mass of 750 and 300 GeV and neutralino mass of 150 GeV are considered.

6.7.3 Fake and non-prompt leptons estimate using Matrix Method

Events containing at least one fake or non-prompt (FNP) lepton can originate from semi-leptonic decays of b- or c-quarks, misidentification of light flavor jets or photon conversions. The Standard Model processes that enter the analysis selection due to FNP leptons are multijet, W+jets and single-top production events.

Since this background is difficult to evaluate from Monte Carlo simulation, data driven methods are usually used. The Matrix Method [151] uses two set of leptons based on different selection criteria: a *tight* selection (corresponding to leptons passing the full selection reported in Table 6.3) and a *loose* selection (looser identification criteria and no isolation requirement). Leptons passing the tight criteria are denoted with T, while leptons passing the loose selection are L. Lepton passing at least the loose selection are *inclusive loose* and leptons passing loose but not tight are called *exclusive loose* (l).

The following quantities are used in the Matrix Method:

- all the events containing two inclusive leptons are classified and counted: N_{TT}, N_{Tl}, N_{lT}, N_{ll} are the number of events and the first leptons is the one with the higher $p_{\rm T}$;
- the real efficiency r denotes the probability for real leptons that satisfies the loose selection to also satisfy the tight selection. The probability r is estimated in a dedicated region enriched in Z boson process with the tag-and-probe method;
- the fake rate f is the corresponding probabilities for the FNP leptons passing the

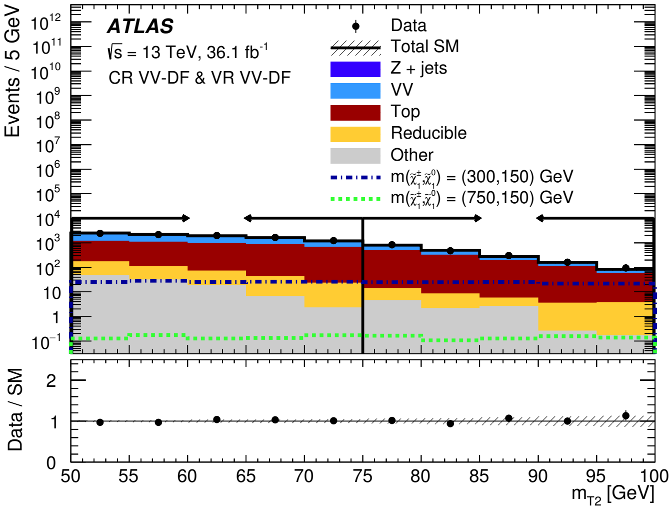

Figure 6.16: m_{T2} distributions for data and the estimated SM backgrounds in CR2-VV-DF and VR2-VV-DF, after performing the background-only likelihood fit. The arrows denote the m_{T2} ranges of the CR and VR. The uncertainty bands include all systematic and statistical contributions. Simulated signal samples for chargino pair production are overlayed to show the signal contamination: chargino with mass of 750 and 300 GeV and neutralino mass of 150 GeV are considered.

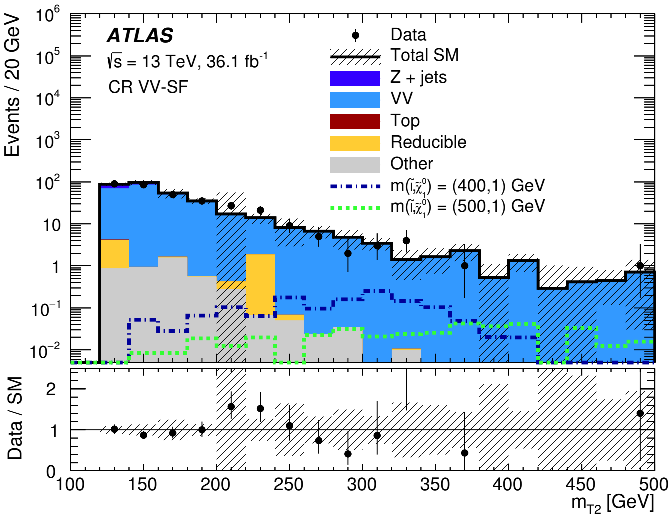

Figure 6.17: m_{T2} distributions for data and the estimated SM backgrounds in CR2-VV-SF, after performing the background-only likelihood fit. The uncertainty bands include all systematic and statistical contributions. Simulated signal samples for slepton pair production are overlayed to show the signal contamination: slepton with mass of 400 and 500 GeV and neutralino mass of 1 GeV are considered.

loose selection to also pass the tight requirement. The fake rate is measured in events dominated by leptons from heavy flavor decays and photon conversions.

The probabilitis r and f are a function of p_{T} and η and in general they are different for electrons and muons and need to be estimated separately.

Using this information, the events with two real (N^{RR}_{LL}), one real and one fake (N^{RF}_{LL} and N^{FR}_{LL}) or two fake (N^{FF}_{LL}) leptons can be estimated inverting the following matrix:

$$\begin{pmatrix} N_{TT} \\ N_{Tl} \\ N_{lT} \\ N_{ll} \end{pmatrix} = \begin{pmatrix} r_1 r_2 & r_1 f_2 & f_1 r_2 & f_1 f_2 \\ r_1(1-r_2) & r_1(1-f_2) & f_1(1-r_2) & f_1(1-f_2) \\ (1-r_1)r_2 & (1-r_1)f_2 & (1-f_1)r_2 & (1-f_1)f_2 \\ (1-r_1)(1-r_2) & (1-r_1)(1-f_2) & (1-f_1)(1-r_2) & (1-f_1)(1-f_2) \end{pmatrix} \begin{pmatrix} N^{RR}_{LL} \\ N^{RF}_{LL} \\ N^{FR}_{LL} \\ N^{FF}_{LL} \end{pmatrix} \tag{6.2}$$

Since the analysis selection consist of two leptons passing the tight requirement, the number of events containing one or two FNP leptons are computed as follow:

$$\begin{aligned} N^{RR}_{TT} =& r_1 r_2 N^{RR}_{LL} \\ N^{RF}_{TT} =& r_1 f_2 N^{RF}_{LL} \\ N^{FR}_{TT} =& f_1 r_2 N^{FR}_{LL} \\ N^{FF}_{TT} =& f_1 f_2 N^{FF}_{LL} \end{aligned} \tag{6.3}$$

The method is then validated in a dedicated region which is known to be dominated by fake leptons. The selection should avoid statistical limitation but also be as close as possible to the SRs of interest and for this purpose events with same sign leptons are used.

Uncertainties arise from the use of the Matrix Method. The limited statistic in the region where the real efficiency and the fake rate are calculated (a $\pm 1\sigma$ variation on the two probabilities is considered to account for the effect) and the uncertainty on the number of events with TT, Tl, lT and ll leptons used in the Matrix are the main systematic effects.

6.8 Validation

In order to ensure a correct background estimation, dedicated validation regions are built. Three validation regions are considered:

- VR2-VV-SF is dedicated to the same flavor diboson background validation. Only events with zero b-tagged and non-b-tagged jets are considered and a veto on the Z invariant mass window ($|m_{\ell\ell} - m_Z| > 20$ GeV) is applied, in order to suppress Z+jets contribution. The m_{T2} selection is between 75 and 100 GeV. In this region the $t\bar{t}$ contribution is significant, but a higher selection is not possible, in order to avoid an overlap with the signal regions. Concerning the background composition, the resulting region is dominated by diboson, $t\bar{t}$ and Z+jets processes;

- VR2-VV-DF selects events with different flavor leptons and zero b-tagged and non-b-tagged jets in order to obtain a large contribution from diboson background. As in previous case, the $75 < m_{\mathrm{T2}} < 100$ GeV selection is used in order to be close to the signal region, but the $t\bar{t}$ gives a large contribution too;

Validation region definitions			
Region	VR2-VV-SF	VR2-VV-DF	VR2-Top
Lepton flavor	SF	DF	DF
non-b-tagged jets multiplicity	0	0	0
b-tagged jets multiplicity	0	0	≥ 1
$\|m_{\ell\ell} - m_Z\|$ [GeV]	> 20	–	–
m_{T2} [GeV]	$\in [75, 100]$	$\in [75, 100]$	> 100

Table 6.9: Definition of the validation regions for diboson with same flavor leptons (VR2-VV-SF), diboson with different flavor leptons (VR2-VV-DF) and $t\bar{t}$ (VR2-Top) processes. The b-tagged jets momentum threshold is $p_{\mathrm{T}} > 20$ GeV and non-b-tagged jets momentum threshold is $p_{\mathrm{T}} > 60$ GeV, as in the signal regions case.

- VR2-Top uses events with different flavor leptons, at least one b-tagged jets and zero non-b-tagged jets. Large m_{T2} is considered ($m_{\mathrm{T2}} > 100$ GeV), in order to have the same signal regions selection.

The definitions of the validation regions are reported in Table 6.9.

Figure 6.15 and 6.16 report the m_{T2} distribution for the data and expected SM background in VR2-Top and VR2-VV-DF respectively (together with the corresponding CRs), after performing the background-only likelihood fit and including all the uncertainties; Figure 6.18 shows the E_{T}^{miss} distribution in VR2-Top and VR2-VV-DF; E_{T}^{miss} and m_{T2} distributions in VR2-VV-SF are illustrated in Figure 6.19. All the plots show a good agreement between the data and the SM background prediction. The simulation for the signal samples is also reported in the plots, overlayed to the estimated background. The signal contamination is small in all the considered VRs and will be further discussed in Section 6.10.1.

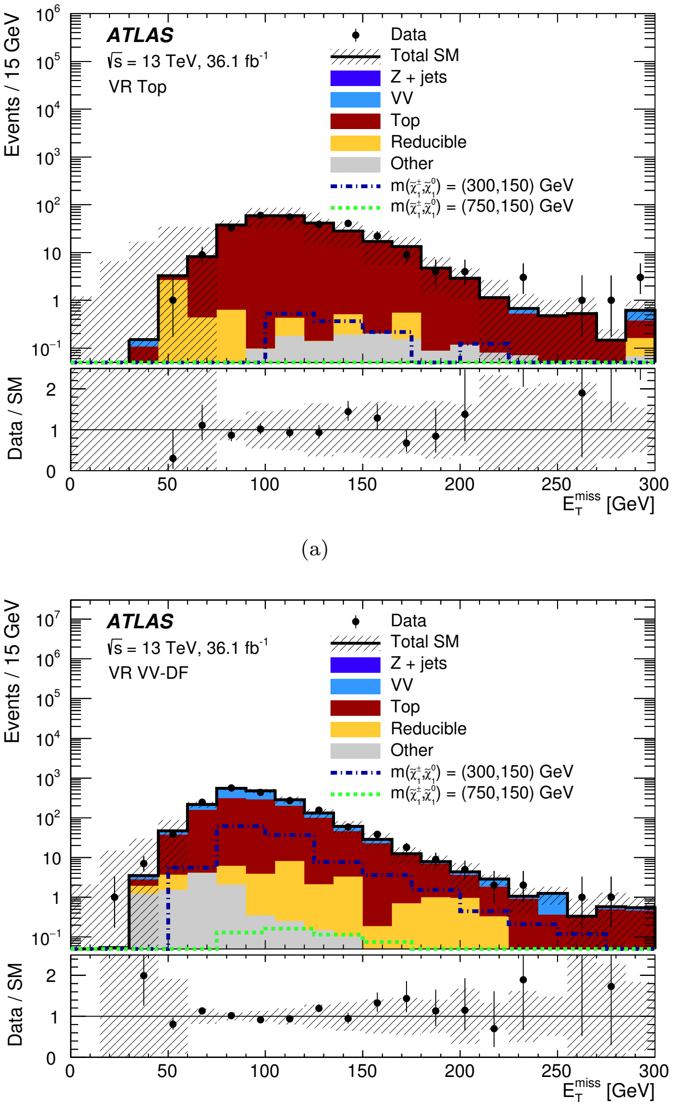

(a)

(b)

Figure 6.18: E_{T}^{miss} distribution for data and the estimated SM backgrounds in VR2-Top and VR2-VV-DF, after performing the background-only likelihood fit. The uncertainty bands include all systematic and statistical contributions. Simulated signal samples for chargino pair production are overlayed to show the signal contamination: chargino with mass of 750 and 300 GeV and neutralino mass of 150 GeV are considered.

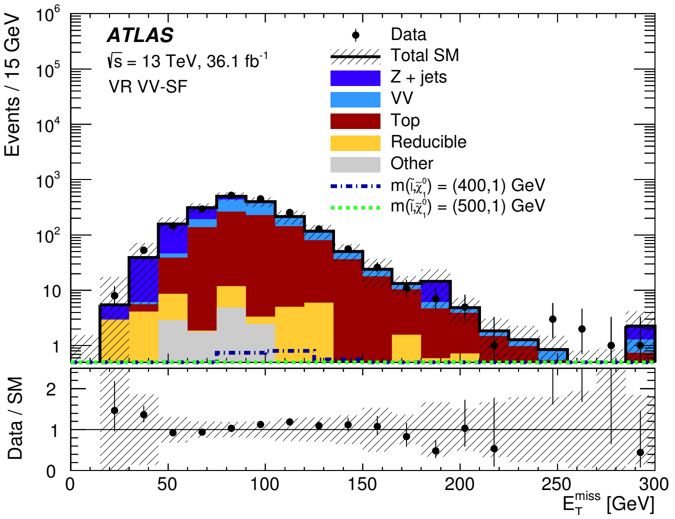

(a)

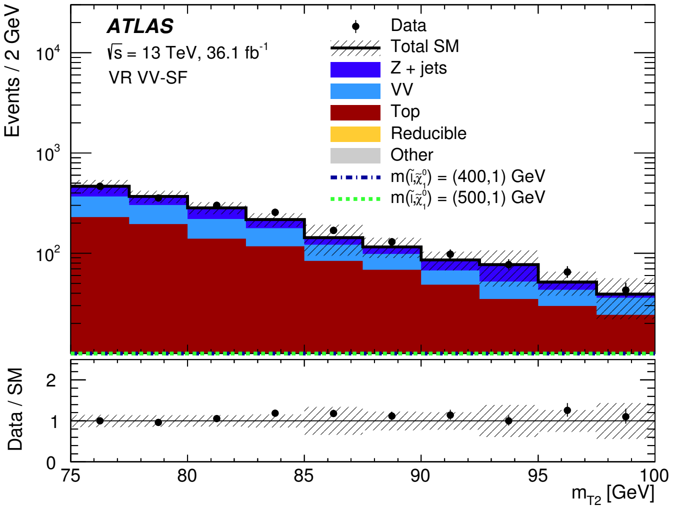

(b)

Figure 6.19: E_{T}^{miss} and m_{T2} distributions for data and the estimated SM backgrounds in VR2-VV-SF, after performing the background-only likelihood fit. The uncertainty bands include all systematic and statistical contributions. Simulated signal samples for chargino pair production are overlayed to show the signal contamination: slepton with mass of 400 and 500 GeV and neutralino mass of 1 GeV are considered.

6.9 Systematic uncertainties

All the experimental systematic uncertainties illustrated in Section 5.6 are included in the likelihood fit. As will be described in Section 6.10, the dominant experimental systematic uncertainties are the ones coming from the E_{T}^{miss} soft term and from the jets energy scale and resolution.

The variation of the m_{T2} distribution due to the E_{T}^{miss} soft term for $t\bar{t}$ and diboson MC samples, for the preliminary selection, is shown in Figure 6.20. Figure 6.21 reports the variation of the m_{T2} distribution due to the jets systematics effects, for $t\bar{t}$ and diboson background samples. The impact of the systematics variation on the diboson samples is quite small. The effects is larger for the $t\bar{t}$ background, in particular the distributions show different behavior in the region corresponding to CR2-Top ($75 < m_{\mathrm{T2}} < 100$ GeV) and to the signal regions ($m_{\mathrm{T2}} > 100$ GeV), providing a motivation for the large uncertainties due to the E_{T}^{miss} soft term and to the jet energy scale and resolution.

The following theoretical systematics, specific of each Monte Carlo simulator, are considered:

- the $t\bar{t}$ background is simulated using the Powheg Monte Carlo generator, and Pythia6 is used for the parton shower. To account for the systematic effects due to the choice of the specific generator and parton shower, the nominal sample is compared to one using the aMC@NLO generator and Pythia8 for the parton shower, and to one using the Powheg generator and Herwig++ for the parton shower. The uncertainty arising from different tuning of the initial state and final state radiation simulation is also considered: samples with lower and higher amount of radiation are used. The variation of the m_{T2} distribution for the different MC samples is illustrated in Figure 6.22;

- when the Wt sample is produced, events from the $t\bar{t}$-Wt interference are produced too and need to be removed following the *diagram removal* method, in order to avoid double counting. The nominal sample is compared to a varied sample that uses the *diagram subtraction* method instead;

- the Sherpa simulation for diboson background is affected by QCD scale uncertainties. The factorization and renormalization are scaled up and down by factors 2.0 and 0.5 with respect to the nominal values used in the MC generation. The matching between the matrix elements and parton shower is performed following the CKKW recommendation, with a scale of 20 GeV. Variation samples using a matching scale of 15 GeV or 30 GeV instead are used to estimate the systematic effect due to the choice of a specific scale. Uncertainty due to the resummation scale (labelled as QSF) is also considered and it is evaluated using samples where the scale is varied by factors 2.0 and 0.5. The variation of the m_{T2} distribution for the different MC samples is illustrated in Figure 6.23;

- in the Z+jets samples case, the QCD scale uncertainties are considered, the factorization and renormalization scale variations are obtained as in the diboson case.

All the theoretical systematic uncertainties are estimated using Truth level samples.

Uncertainties arising from the FNP evaluation with the Matrix Method (as described in Section 6.7.3) and on the SUSY particles production cross section (Section 6.2) are also included.

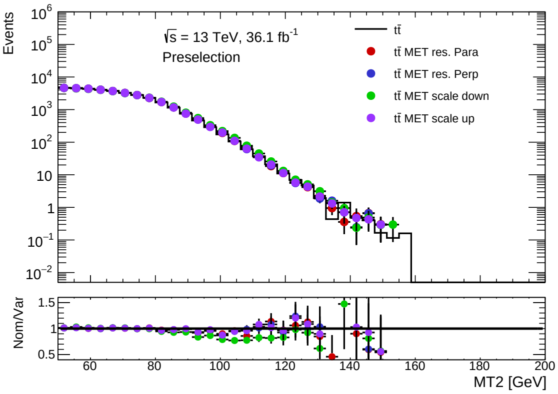

(a) $t\bar{t}$, preliminary selection

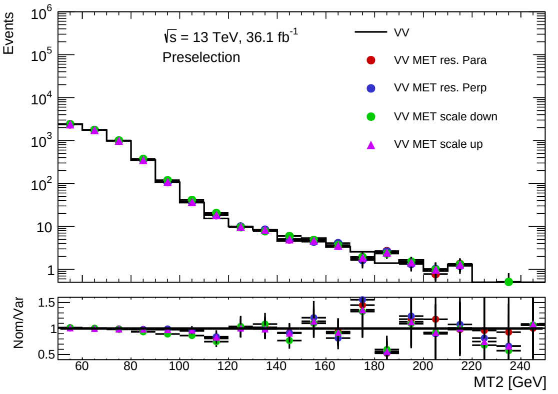

(b) VV DF, preliminary selection

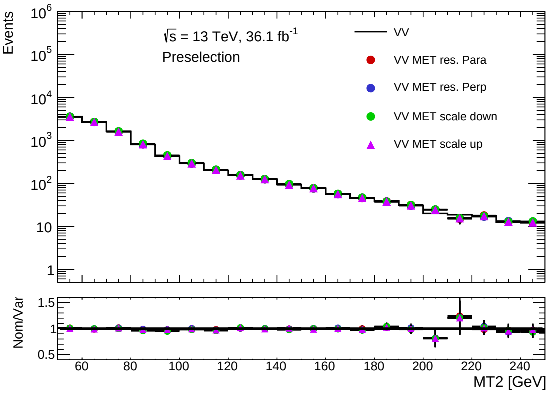

(c) VV SF, preliminary selection

Figure 6.20: m_{T2} distribution for the nominal sample and the experimental systematics variation due to the energy resolution and scale of the E_{T}^{miss} soft term, for $t\bar{t}$ (a), diboson with DF leptons (b) and diboson with SF leptons (c). Preliminary selection is considered.

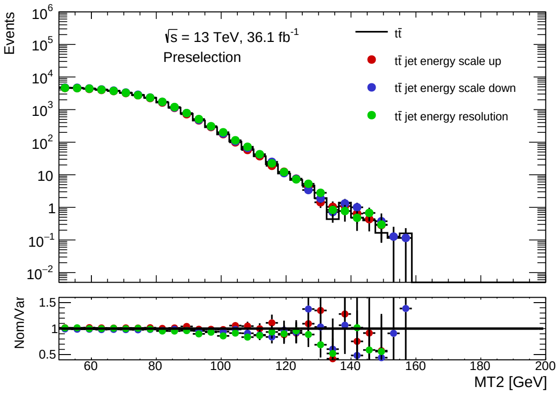

(a) $t\bar{t}$, preliminary selection

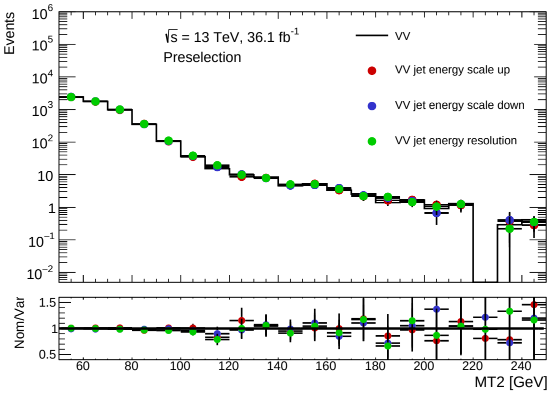

(b) VV DF, preliminary selection

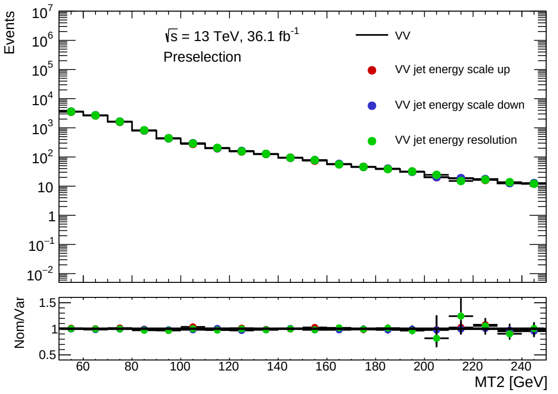

(c) VV SF, preliminary selection

Figure 6.21: m_{T2} distribution for the nominal sample and the experimental systematics variation due to the jets energy resolution and scale, for $t\bar{t}$ (a), diboson with DF leptons (b) and diboson with SF leptons (c). Preliminary selection is considered.

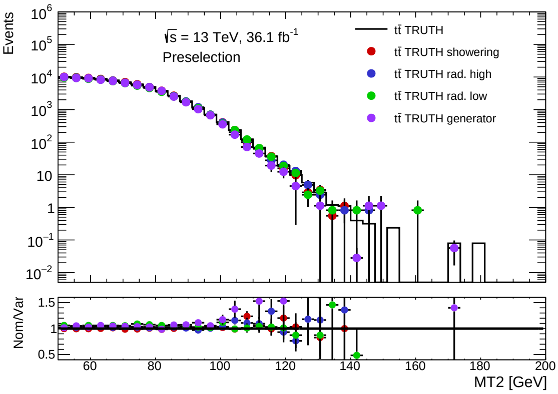

(a) Preliminary selection

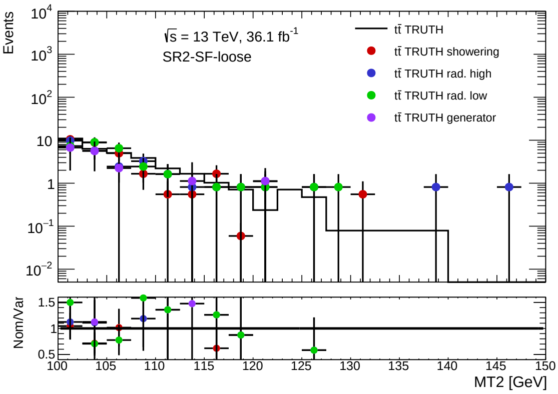

(b) SR2-SF-loose

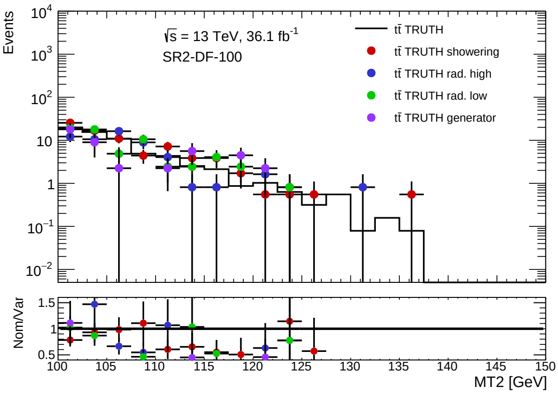

(c) SR2-DF-100

Figure 6.22: m_{T2} distribution for the nominal $t\bar{t}$ sample and the theoretical systematics variation, at the Truth level. Preliminary selection (a), SR2-SF-loose (b) and and SR2-DF-100 (c) are considered.

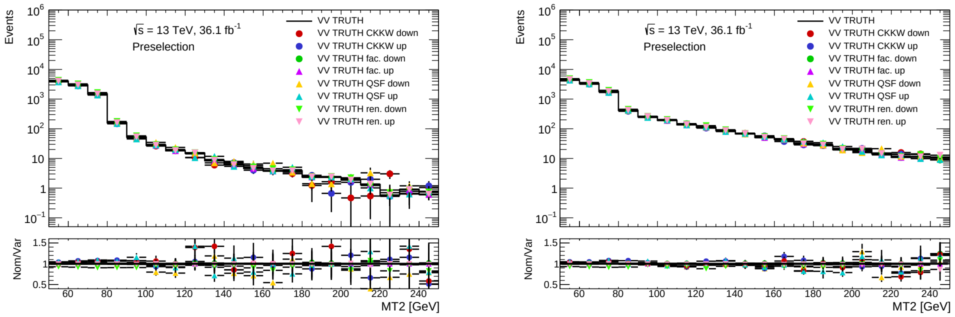

(a) Preliminary selection - DF leptons (b) Preliminary selection - SF leptons

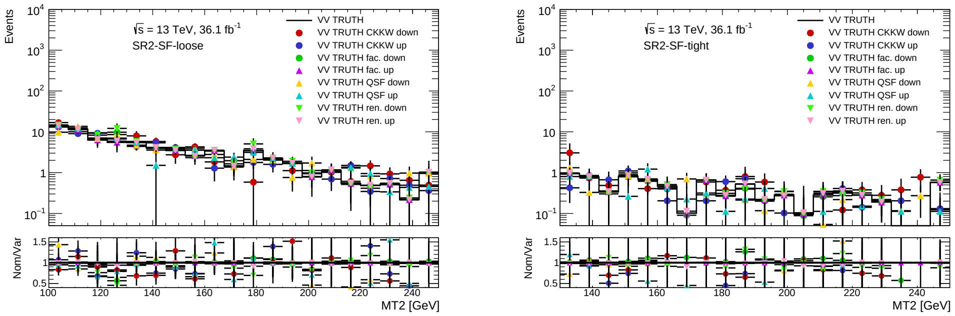

(c) SR2-SF-loose (d) SF2-SF-tight

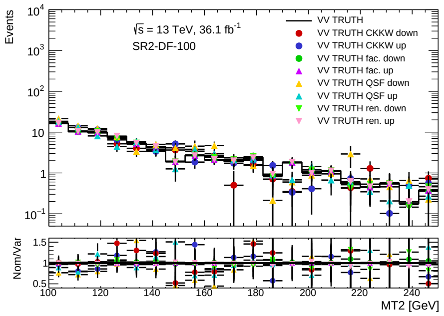

(e) SR2-DF-100

Figure 6.23: m_{T2} distribution for the nominal diboson sample and the theoretical systematics variation, at the Truth level. Preliminary selection with DF leptons (a) or SF leptons (b) and the inclusive SRs (SR2-SF-loose (c), SF2-SF-tight (d) and SR2-DF-100 (e) are considered.

6.10 Result and interpretation

The results obtained in the search for the direct production of slepton pair and the chargino pair with slepton mediated decay are reported in this Section. Three different likelihood fit strategies, as described in Section 5.7.4, are used: the result of the background-only fit is reported in Section 6.10.1, the model-dependent fit with the exclusion limits are illustrated in Section 6.10.2 and the model-independent fit and the upper limits are described in Section 6.10.3.

6.10.1 Background-only likelihood fit

The results illustrated in this Section are obtained performing the background-only likelihood fit as described in Section 5.7.4. The diboson (separated in SF and DF events) and the $t\bar{t}$ MC simulation are normalized simultaneously in the CRs. The three normalization factors for the diboson SF, dibosons DF and $t\bar{t}$ samples are obtained and then transfered to the VRs and SRs. No signal samples is used and the signal strength parameter is set to zero.

Table 6.10 reports the yields of the observed data in the CRs, compared to the total Standard Model events expected, after performing the likelihood fit. The breakdown of the SM background composition, after applying the MC normalization factors, is reported. All the systematic and statistical uncertainties are considered.

The normalization factors obtained in the background-only likelihood fit are:

- $\mu_{NF}^{t\bar{t}} = 0.95 \pm 0.03$
- $\mu_{NF}^{\text{VV-DF}} = 1.06 \pm 0.19$
- $\mu_{NF}^{\text{VV-SF}} = 0.96 \pm 0.11$

The second part of Table 6.10 shows the expected yields for two samples of the sleptons direct production process and two samples of the charginos direct production with slepton mediated decay. In the sleptons direct production sample, both RH and LH particles are considered in the computation. Dividing the signal yields by the total SM background expected in each region, the signal contamination is obtained and the number are reported in the Tables between square brackets. The signal contaminations in all the CRs are negligible, the maximum one being 1.4%.

The normalization factors extracted from the CRs are then propagated to the VRs and SRs. The VRs yields are shown in Table 6.11: data are compared with the SM background prediction, all the uncertainties are included. Data are found well modeled by the SM prediction within the uncertainties. The Table also report the signal contaminations for different SUSY signal. The contaminations are very small, ranging from the 0.04% to the 6%.

The comparison between the expected SM events and the observed data in the inclusive SRs is reported in Table 6.12, where the regions for both SF and DF selection are reported. The background processes that dominate the SR2-SF-loose region are diboson, $t\bar{t}$ and Z+jets, while in the SR2-SF-tight selection the diboson are the main background. In the region selected with DF leptons, the Z+jets process is negligible. The $t\bar{t}$ contribution is important only in DF-100, then it disappears due to the increasing m_{T2} cut and the diboson are the main background component.

The excess of the data compared to the SM prediction is quantified in terms of statistical significance and the obtained numbers are reported in the last row of Table 6.12. The significance is not reported in case of observed data less then the SM prediction. The regions SF-tight and DF-150 show a good agreement between data and SM prediction, while in the region SF-Loose, DF-100 DF-200 and DF-300 the data are over-fluctuating, giving a significance of 1.0σ, 0.77σ, 1.5σ and 1.3σ respectively. The deviation of the data from the prediction are anyway not significant enough to claim the observation of new physics phenomena.

The total systematic uncertainties on the SM prediction in the inclusive SRs are reported in Tables 6.13 and 6.14. All the uncertainites are considered in the computation, but only the major sources of error (with a contribution of at least the 1%) are listed in the lower part of the Tables. The first Table refers to the SF regions: SF-loose is affected by a systematic error of 16%, while SF-tight by a 30% error. Large contributions come from the MC statistic and the VV-SF normalization factor uncertainties. Concerning the theoretical systematics, the dominant diboson uncertainties are the CKKW variation and the resummation and renormalization scale. The $t\bar{t}$ and Z+jets theoretical uncertainties are significant only in the SF-loose region, since these background contributions become negligible in the SF-tight selection. The E_{T}^{miss} soft term, the jet energy scale and resolution and the b-tagging efficiency are the major sources of experimental systematics. Small contributions also come from the Matrix Method used to estimate the fake and non-prompt leptons and from the integrated luminosity uncertainties.

In the case of the DF inclusive signal regions (Table 6.14), the total systematic uncertainty ranges from 10% to 99%. The dominant systematics are similar to the SF regions case, but with variations that reflect the different background composition. The region DF-100 has a large $t\bar{t}$ components, so the uncertainties due to the $t\bar{t}$ normalization factor and on the b-tagging efficiency have a larger contribution. The Z+jets theoretical systematics are not present, since this background is now negligible.

The comparison between the observed data and the SM expectation in the case of the exclusive SRs with SF leptons is reported in Tables 6.15, 6.16 and 6.17 and, as in the case of the inclusive region, the significance of the fluctuation is reported in the last row. A good agreement between the data and the SM prediction is generally observed, SR-e (1.6σ), SR-f (1.9σ) and SR-m (2.0σ) being the regions with the larger excesses. Table 6.18 reports the observed data and the SM prediction in the exclusive region with DF leptons: the larger excesses are present in DF-c (1.2σ) and DF-d (1.3σ).

In order to group together the results obtained in the various inclusive and exclusive SRs, Figure 6.24 summarizes each SR considered in the search in one bin. The histogram corresponds to the SM prediction, showing also the background composition, and the observed data are overlayed. The lower pad reports the significance of the observed fluctuation. All the sources of uncertainties are considered. No significant excess above the SM estimated background is observed in any of the SRs considered.

Control regions yields			
	CR2-Top	CR2-VV-DF	CR2-VV-SF
Observed	6973	9412	332
Total SM	6970 ± 80	9410 ± 100	332 ± 18
$t\bar{t}$	6300 ± 100	3400 ± 800	$0.05^{+0.09}_{-0.05}$
Wt	640 ± 40	1040 ± 90	–
VV	18 ± 6	4500 ± 800	293 ± 33
FNP	–	320 ± 60	–
Z+jets	0.36 ± 0.08	5^{+19}_{-5}	34 ± 27
Other	6^{+9}_{-6}	109 ± 23	4.5 ± 0.6
$m(\tilde{\ell}, \tilde{\chi}_1^0)$ = (400,1) GeV	–	–	1.34 [0.4%]
$m(\tilde{\ell}, \tilde{\chi}_1^0)$ = (500,1) GeV	–	–	0.39 [0.1%]
$m(\tilde{\chi}_1^{\pm}, \tilde{\chi}_1^0)$ = (300,150) GeV	5.98 [0.1%]	131.35 [1.4%]	3.81 [1.1%]
$m(\tilde{\chi}_1^{\pm}, \tilde{\chi}_1^0)$ = (750,150) GeV	0.05 [0.001%]	0.72 [0.01%]	0.41 [0.1%]

Table 6.10: Background-only likelihood fit results for the control regions, including all the systematic and statistical uncertainties. The MC normalization factors extracted from the control regions are applied to the yields of the MC simulations, for $t\bar{t}$ and diboson processes. The second part of the Table shows the number of expected signal events from different samples and the signal contamination, expressed as percentage of the total SM background in the region. The uncertainties can be correlated and do not necessarily add up quadratically to the total SM uncertainty.

6.10.2 Model-dependent fit and exclusion limits

The results obtained performing the model-dependent likelihood fit, as described in Section 5.7.4, are now presented.

Since no significant excess was observed in the SRs, limits on the free parameters of the SUSY models considered are set. The likelihood fit is performed considering the data observed in the CRs and SRs as constrain and using $\mu_{sig} = 1$. The fit is repeated for each point of the signal grid in order to compute the CL_s value. As illustrated in Section 5.7.3, the hypothesis of the presence of new physics phenomena is rejected at the 95% CL if the CL_s is less then 0.05. In this way it is possible to place exclusion limits on the SUSY model parameters and a contour of exclusion in the masses space is built.

As addressed in Sections 5.7.5 and 5.7.6, the exclusive SRs are optimized to maximize to coverage of the exclusion contour and therefore they are the only SRs used in the model-dependent fit. Only the exclusive SRs with SF leptons are used the likelihood fit for the direct sleptons production signal, since no signal events are expected in the DF case, while the likelihood fit for the charginos via sleptons signal model used both the SF and the DF regions combined together.

Concerning the direct sleptons production, the exclusion limits obtained are reported in Figure 6.25, represented in the slepton-neutralino masses plane. As in the case of the

Validation regions yields

	VR2-Top	VR2-VV-DF	VR2-VV-SF
Observed	285	1848	1962
Total SM	270 ± 50	1830 ± 120	1840 ± 230
$t\bar{t}$	240 ± 50	900 ± 180	730 ± 180
Wt	26 ± 7	259 ± 22	209 ± 20
VV	2.0 ± 0.8	640 ± 130	520 ± 80
FNP	–	26 ± 9	13^{+22}_{-13}
Z+jets	0.18 ± 0.03	–	360 ± 110
Other	$1.5^{+2.6}_{-1.5}$	10 ± 5	12.7 ± 3.0
$m(\tilde{\ell},\tilde{\chi}_1^0)$ = (400,1) GeV	–	–	3.73 [0.2%]
$m(\tilde{\ell},\tilde{\chi}_1^0)$ = (500,1) GeV	–	–	0.91 [0.05%]
$m(\tilde{\chi}_1^{\pm},\tilde{\chi}_1^0)$ = (300,150) GeV	1.39 [0.5%]	118 [6%]	96 [5%]
$m(\tilde{\chi}_1^{\pm},\tilde{\chi}_1^0)$ = (750,150) GeV	0.23 [0.1%]	0.69 [0.04%]	0.85 [0.05%]

Table 6.11: Background-only likelihood fit results for the validation regions, including all the systematic and statistical uncertainties. The MC normalization factors extracted from the control regions are applied to the yields of the MC simulations, for $t\bar{t}$ and diboson processes. The second part of the Table shows the number of expected signal events from different samples and the signal contamination, expressed as percentage of the total SM background in the region. The uncertainties can be correlated and do not necessarily add up quadratically to the total SM uncertainty.

ATLAS result obtained using the LHC Run 1 data, the exclusion limit computed with the observed data (red continuous line) contains all the uncertainties, excepted the one from the SUSY signal cross sections, that are included in the contour represented by the red dotted lines. The contour that would be obtained in the case of data matching exactly the SM prediction is also shown (blue dashed line), with the $\pm 1\sigma$ variation (yellow band).

Three different exclusion limits are presented:

- to produce the exclusion limit in Figure 6.25(a), only signal events coming from LH sleptons were considered. Sleptons with a mass up to 470 GeV are excluded, in the case of neutralino with a 1 GeV mass;

- the plot in Figure 6.25(b) is obtained selecting signal events originated from RH sleptons. Due to the smaller production cross section the limit is weaker in this case, the exclusion contour reaches a slepton mass of 380 GeV;

- events from LH and RH sleptons are considered together in the result shown in Figure 6.25(c): the coverage of the exclusion limits reaches a slepton mass of 500 GeV in the case of neutralino with a 1 GeV mass. Looking at the region with slepton mass between 500 and 570 GeV, it can be noticed that the observed exclusion limits is weaker compared to the expected one. This is due to the fact that for large

Inclusive signal regions yields						
SR2-	SF-loose	SF-tight	DF-100	DF-150	DF-200	DF-300
Observed	153	9	78	11	6	2
Total SM	133 ± 22	9.8 ± 2.9	68 ± 7	11.5 ± 3.1	2.1 ± 1.9	0.6 ± 0.6
$t\bar{t}$	27 ± 11	–	24 ± 8	–	–	–
Wt	5.0 ± 2.2	–	4.5 ± 1.0	–	–	–
VV	70 ± 11	9.6 ± 3.0	37 ± 8	10.8 ± 3.0	2.0 ± 1.9	0.6 ± 0.6
FNP	6 ± 4	0.0 ± 0.0	2.17 ± 0.29	0.42 ± 0.23	$0.00^{+0.01}_{-0.00}$	$0.00^{+0.01}_{-0.00}$
Z+jets	23 ± 14	$0.09^{+0.34}_{-0.09}$	–	–	–	–
Other	0.79 ± 0.23	0.09 ± 0.01	0.67 ± 0.16	0.26 ± 0.08	0.09 ± 0.07	0.02 ± 0.02
Significance	1.0	–	0.77	–	1.5	1.3

Table 6.12: Background-only likelihood fit results for the inclusive signal regions, including all the systematic and statistical uncertainties. The MC normalization factors extracted from the control regions are applied to the yields of the MC simulations, for $t\bar{t}$ and diboson processes. The second part of the Table shows the significance of the data fluctuation compared to the SM prediction. The uncertainties can be correlated and do not necessarily add up quadratically to the total SM uncertainty.

sleptons mass, the regions providing the best signal discrimination are the ones with a large m_{T2} selection. The region SF-m is then one with the tighter m_{T2} selection ($m_{\mathrm{T2}} > 300$ GeV) and it shows an excess of 2.0σ, as consequence the observed exclusion limit is not strong as the expected one.

The results of the analogous search performed by the ATLAS Collaboration at the LHC Run 1 are reported for comparison (gray area). A large improvement of the past results was obtained due to the search here presented.

The exclusion limit obtained considering the chargino pair production with slepton mediated decay model is presented in Figure 6.26. The result are presented using the same graphic convention of the direct sleptons production model result. Chargino with a mass up to 740 GeV is excluded at 95% CL in the case of a neutralino with a 1 GeV mass. A large difference between the observed and the expected exclusion limits is observed in the region with the charginos mass between 750 and 850 GeV. As in the case of the slepton exclusion limit, this is due to the fact that for large charginos mass the best signal discrimination is provided by region with with a large m_{T2} selection. The region DF-c ($m_{\mathrm{T2}} > 200$ GeV), DF-d ($m_{\mathrm{T2}} > 300$ GeV) and SF-m ($m_{\mathrm{T2}} > 300$ GeV) all show an excess in the observed data compared to the SM prediction (1.2σ, 1.3σ and 2.0σ respectively), causing the observed exclusion limit to be weaker then the expected one.

6.10.3 Model-independent fit and upper limits

In this Section the model-independent upper limits are reported. The result is obtained with the model-independent fit configuration described in Section 5.7.4.

Systematic uncertainties in the SF signal regions		
Region	SR2-SF-loose	SR2-SF-tight
Background expectation	133	9.8
Total systematic	16%	30%
Monte Carlo statistic	8%	14%
VV SF normalization	6%	12%
VV MC CKKW	2%	23%
VV MC renormalization	2%	7%
VV MC resummation	–	1%
$t\bar{t}$ MC generator	6%	–
$t\bar{t}$ MC parton shower	5%	–
Z+jets MC renormalization	5%	3%
E_{T}^{miss} soft term resolution	7%	2%
E_{T}^{miss} soft term energy scale	3%	–
Jets energy scale	4%	2%
Jets energy resolution	–	1%
b-tagging efficiency	3%	–
FNP	2%	–
Luminosity	1%	–

Table 6.13: Considering the inclusive signal regions with SF leptons, the expected background and the total systematic uncertainties are reported. The breakdown of the dominant systematic uncertainties is shown in the second part of the Table, expressed as the percentages relative to the total expected background. Uncertainties lower of the 1% are included in the fit but are not reported in the Table. The uncertainties can be correlated and do not necessarily add up quadratically to the total background uncertainty.

The data observed in the CRs and in the SRs are both used as constrain. No signal contamination is considered in the CRs, but a dummy signal sample is considered in the SR (the number of expected signal events is set to one). The fit is performed independently for each of the inclusive signal regions, that were optimized for the signal discovery.

The results for all the regions are summarized in Table 6.19. The columns labeled as N_{obs} and N_{exp} reports the observed data and the expected SM background as estimated in the background-only likelihood fit. The upper limits on the visible cross section ($\langle\epsilon\sigma\rangle^{95}_{\mathrm{obs}}$) are then reported. This value represent the maximum possible cross section for a beyond the SM process, compatible with the observed data. The cross section is labeled as *visible* since the acceptance of the SR selection and the efficiency due to the objects reconstruction (acceptance × efficiency = ϵ) need to be considered.

The Table then shows the S^{95}_{obs} and S^{95}_{exp} values, that are the observed and expected upper limits on the number of possible signal events in the SR, at 95% CL. The $\pm 1\sigma$ variation on the expected value, computed using all the uncertainties considered in the

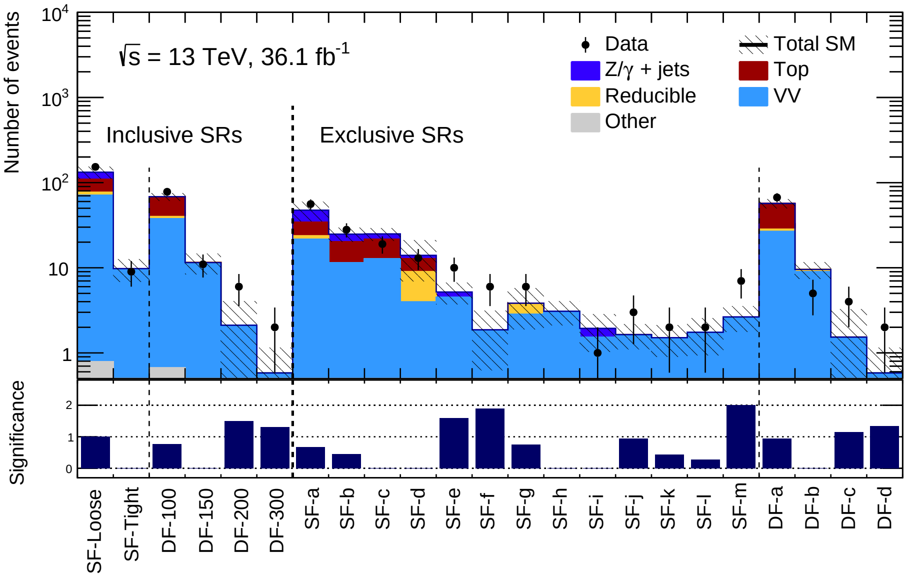

Figure 6.24: Summary of the inclusive and exclusive SRs considered in the search. Each bin in the plot represents one SR, after performing the background-only likelihood fit. The uncertainty bands include all systematic and statistical contributions. The lower pad reports the significance of the fluctuation observed, that is set to zero in case of an under-fluctuation of the data compared to the SM prediction

search, is reported for the expected value.

Finally the p-value and the significance, computed assuming the null hypothesis of background-only events, are shown in the last two columns. In the regions where the number of observed events is less then the SM prediction, the p-value is set to 0.5 and the significance to zero.

The information provided by the model-independent upper limits is important since it allows for a simple reinterpretation of the result obtained in a specific search. Given a new theoretical model for the production of beyond the SM particles with two leptons and missing transverse energy signature, it is possible to compare the number of events predicted by the new model to the upper limits obtained in this search. In this way it can be investigated if the new model is allowed or excluded by the result of the search.

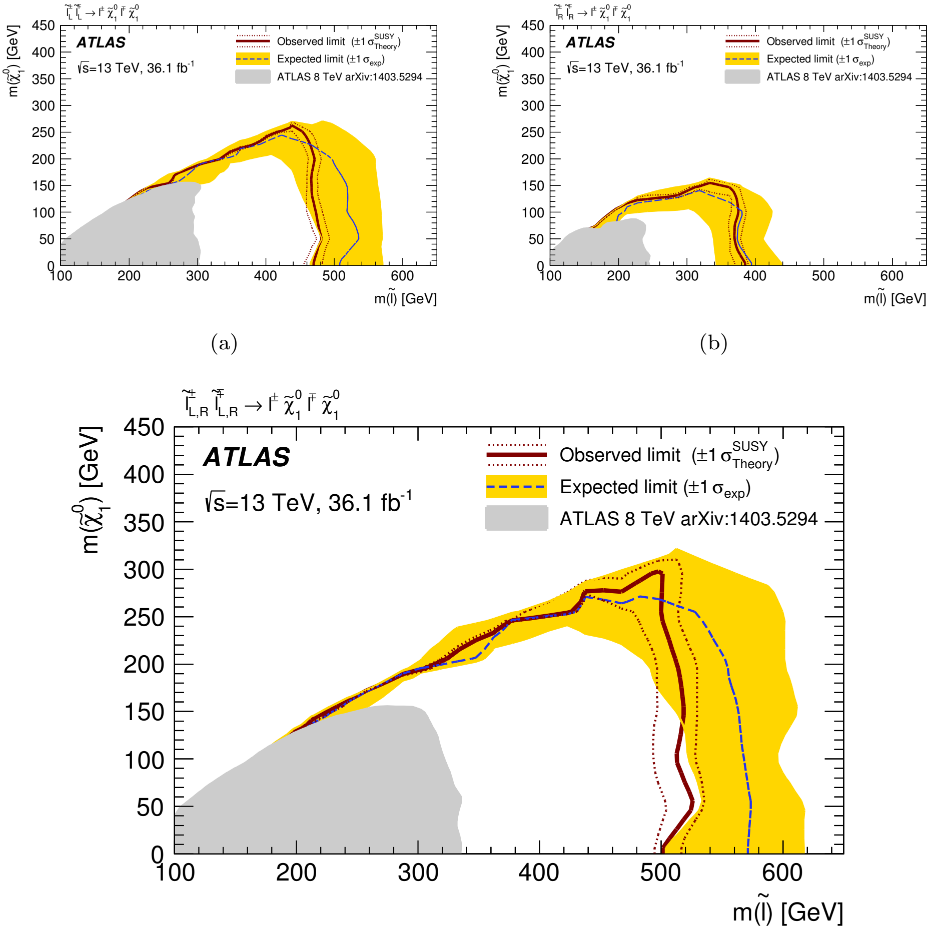

(a) (b)

(c)

Figure 6.25: Exclusion limits at the 95% confidence level in the slepton-neutralino masses plane, in the case of (a) RH, (b) LH and (c) both RH and LH sleptons. The blue dashed line represents the expected exclusion limit, with the yellow band corresponding to the $\pm1\sigma$ variation due to all the uncertainties sources except the one on the the signal cross-section. The red line correspond to the observed exclusion limit, with a $\pm1\sigma$ variation due to the signal cross-section uncertainty (red dotted lines). The observed limits obtained from ATLAS in the Run 1 search (discussed in Section 6.1) are also shown [125].

Systematic uncertainties in the DF signal regions				
Region	SR2-DF-100	SR2-DF-150	SR2-DF-200	SR2-DF-300
Background expectation	68	12	2.1	0.6
Total systematic	10%	27%	92%	99%
Monte Carlo statistic	5%	8%	72%	70%
VV DF normalization	10%	17%	17%	17%
$t\bar{t}$ normalization	1%	–	–	–
$t\bar{t}$ MC generator	8%	–	–	–
$t\bar{t}$ MC parton shower	6%	–	–	–
VV MC CKKW	1%	9%	46%	20%
VV MC resummation	–	7%	27%	61%
VV MC renormalization	–	1%	8%	2%
VV MC factorization	–	1%	3%	1%
E_{T}^{miss} soft term energy scale	3%	–	1%	–
E_{T}^{miss} soft term resolution	2%	–	4%	1%
Jets energy resolution	4%	2%	9%	14%
Jets energy scale	2%	–	1%	7%
b-tagging efficiency	5%	–	–	–
Electron isolation efficiency	–	–	1%	1%
Muon isolation efficiency	–	–	1%	–
FNP	–	2%	–	–
Luminosity	1%	–	–	–

Table 6.14: Considering the inclusive signal regions with DF leptons, the expected background and the total systematic uncertainties are reported. The breakdown of the dominant systematic uncertainties is shown in the second part of the Table, expressed as the percentages relative to the total expected background. Uncertainties lower of the 1% are included in the fit but are not reported in the Table. The uncertainties can be correlated and do not necessarily add up quadratically to the total background uncertainty.

Exclusive SF signal regions yields

SR2-	SF-a	SF-b	SF-c	SF-d	SF-e
Observed	56	28	19	13	10
Total SM	47 ± 12	25 ± 5	25 ± 4	14 ± 7	5.2 ± 1.4
$t\bar{t}$	10 ± 4	7.4 ± 3.5	7.3 ± 3.0	2.7 ± 1.7	–
Wt	1.0 ± 1.0	1.3 ± 0.7	1.6 ± 0.6	1.1 ± 1.1	–
VV	21 ± 4	11.3 ± 2.9	12.6 ± 2.4	3.9 ± 2.4	4.4 ± 1.3
FNP	$2.1^{+2.9}_{-2.1}$	$0.0^{+0.4}_{-0.0}$	$0.0^{+0.5}_{-0.0}$	5 ± 4	$0.0^{+0.1}_{-0.0}$
Z+jets	13 ± 9	4.7 ± 2.6	3.3 ± 3.2	$1.2^{+1.7}_{-1.2}$	0.7 ± 0.6
Other	0.18 ± 0.08	0.12 ± 0.05	0.11 ± 0.04	0.09 ± 0.05	0.05 ± 0.03
Significance	0.68	0.45	–	–	1.6

Table 6.15: Background-only fit results for the exclusive SF signal regions (from SF-a to SF-e), including all the systematic and statistical uncertainties. The MC normalization factors extracted from the control regions are applied to the yields of the MC simulations, for $t\bar{t}$ and diboson processes. The last row of the Table shows the significance of the data fluctuation compared to the SM prediction.

Exclusive SF signal regions yields

SR2-	SF-f	SF-g	SF-h	SF-i	SF-j
Observed	6	6	0	1	3
Total SM	1.9 ± 1.2	3.8 ± 1.9	3.1 ± 1.0	1.9 ± 0.9	1.6 ± 0.5
$t\bar{t}$	–	$0.11^{+0.21}_{-0.11}$	–	–	–
Wt	–	–	–	–	–
VV	1.8 ± 1.2	2.8 ± 1.6	3.0 ± 1.0	1.5 ± 0.8	1.6 ± 0.5
FNP	$0.00^{+0.01}_{-0.00}$	0.9 ± 0.4	$0.00^{+0.02}_{-0.00}$	$0.0^{+0.1}_{-0.0}$	$0.00^{+0.01}_{-0.00}$
Z+jets	$0.02^{+0.21}_{-0.02}$	–	$0.02^{+0.11}_{-0.02}$	0.42 ± 0.20	–
Other	0.03 ± 0.01	0.05 ± 0.02	0.03 ± 0.01	0.03 ± 0.02	–
Significance	1.9	0.76	–	–	0.94

Table 6.16: Background-only fit results for the exclusive SF signal regions (from SF-f to SF-j), including all the systematic and statistical uncertainties. The MC normalization factors extracted from the control regions are applied to the yields of the MC simulations, for $t\bar{t}$ and diboson processes. The last row of the Table shows the significance of the data fluctuation compared to the SM prediction.

Exclusive SF signal regions yields			
SR2-	SF-k	SF-l	SF-m
Observed	2	2	7
Total SM	1.5 ± 0.6	1.8 ± 0.8	2.6 ± 0.9
$t\bar{t}$	–	–	–
Wt	–	–	–
VV	1.4 ± 0.6	1.7 ± 0.8	2.6 ± 0.9
FNP	$0.00^{+0.01}_{-0.00}$	$0.00^{+0.02}_{-0.00}$	$0.00^{+0.01}_{-0.00}$
Z+jets	$0.02^{+0.20}_{-0.02}$	–	$0.02^{+0.06}_{-0.02}$
Other	0.04 ± 0.02	0.02 ± 0.01	0.02 ± 0.02
Significance	0.44	0.28	2.0

Table 6.17: Background-only fit results for the exclusive SF signal regions (from SF-k to SF-m), including all the systematic and statistical uncertainties. The MC normalization factors extracted from the control regions are applied to the yields of the MC simulations, for $t\bar{t}$ and diboson processes. The last row of the Table shows the significance of the data fluctuation compared to the SM prediction.

Exclusive DF signal regions yields				
SR2-	DF-a	DF-b	DF-c	DF-d
Observed	67	5	4	2
Total SM	57 ± 7	9.6 ± 1.9	$1.5^{+1.7}_{-1.5}$	0.6 ± 0.6
$t\bar{t}$	24 ± 8	–	–	–
Wt	4.5 ± 1.0	–	–	–
VV	26 ± 6	8.8 ± 1.8	$1.5^{+1.7}_{-1.5}$	0.6 ± 0.6
FNP	1.75 ± 0.18	0.57 ± 0.23	$0.00^{+0.01}_{-0.00}$	$0.00^{+0.01}_{-0.00}$
Z+jets	–	–	–	–
Other	0.40 ± 0.09	0.17 ± 0.07	0.07 ± 0.07	0.02 ± 0.02
Significance	0.95	–	1.2	1.3

Table 6.18: Background-only fit results for the exclusive DF signal regions, including all the systematic and statistical uncertainties. The MC normalization factors extracted from the control regions are applied to the yields of the MC simulations, for $t\bar{t}$ and diboson processes. The last row of the Table shows the significance of the data fluctuation compared to the SM prediction.

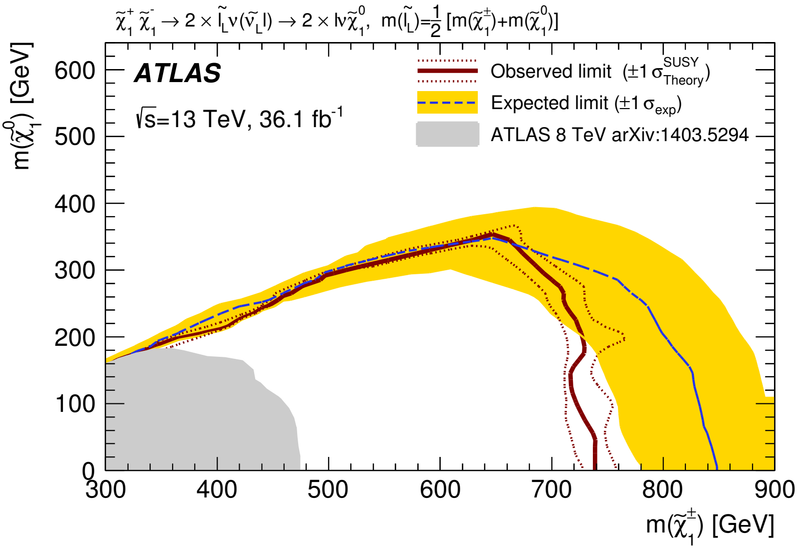

Figure 6.26: Exclusion limits at the 95% confidence level in the chargino-neutralino masses plane for the chargino pair production with slepton mediated decay model. The blue dashed line represents the expected exclusion limit, with the yellow band corresponding to the $\pm 1\sigma$ variation due to all the uncertainties sources except the one on the the signal cross-section. The red line correspond to the observed exclusion limit, with a $\pm 1\sigma$ variation due to the signal cross-section uncertainty (red dotted lines). The observed limits obtained from ATLAS in the Run 1 search (discussed in Section 6.1) are also shown [125].

Model independent limits							
Signal region	N_{obs}	N_{exp}	$\langle\epsilon\sigma\rangle_{\mathrm{obs}}^{95}$[fb]	S_{obs}^{95}	S_{exp}^{95}	p-value	Z
DF-100	78	68 ± 7	0.88	32	27^{+11}_{-8}	0.22	0.77
DF-150	11	11.5 ± 3.1	0.32	11.4	12^{+5}_{-4}	0.5	0
DF-200	6	2.1 ± 1.9	0.33	12.0	$10.3^{+2.9}_{-1.9}$	0.06	1.5
DF-300	2	0.6 ± 0.6	0.18	6.6	$5.6^{+1.1}_{-0.9}$	0.10	1.3
SF-loose	153	133 ± 22	2.02	73	53^{+21}_{-16}	0.16	1.0
SF-tight	9	9.8 ± 2.9	0.29	10.5	12^{+4}_{-3}	0.5	0

Table 6.19: Summary of results obtained from the model-independent likelihood fit in the inclusive SRs. The observed number of events (N_{obs}) and expected SM background (N_{exp}) in the SRs are reported. Signal model-independent upper limits at 95% confidence level on the the visible signal cross-section ($\langle\epsilon\sigma\rangle_{\mathrm{obs}}^{95}$) is then shown. S_{obs}^{95} and S_{exp}^{95} are respectively the observed and expected upper limit on the number of beyond the SM events, where the $\pm 1\sigma$ variations on the expected limit originate from the statistical and systematic uncertainties in the background prediction. The p-value and the corresponding significance for the background-only hypothesis are reported in the last two columns. In the region where the observed data are less then the SM background prediction the p-value is truncated at 0.5 and the significance is set to 0.

6.11 Comparison with the CMS Collaboration results

The results obtained by the CMS Collaboration [9] for the same models considered in this Chapter are briefly summarized in the following. The CMS data collected at the LHC Run 2 between 2015 and 2016 are considered, with a total amount of 35.9 fb^{-1}.

Concerning the search for direct slepton pair production [152], the analysis performed by the CMS Collaboration considers events with exactly two leptons, with opposite sign and same flavor, and no hadron activity (jets with $p_{\mathrm{T}} > 25$ GeV are vetoed). The signal regions are selected using $m_{\mathrm{T2}} > 90$ GeV and different E_{T}^{miss} selections: [100-150], [150-225], [225-300], and [300,∞] GeV. No excess over the SM prediction was observed, the exclusion contour at 95% CL for the slepton and the neutralino masses is reported in Figure 6.27, considering both LH and RH sleptons. Slepton with a mass up to 440 GeV is excluded at 95% CL in the case of a neutralino with a 1 GeV mass. Upper limits on the direct slepton pair production cross section are also displayed, assuming branching ratios of 100%.

A different strategy was adopted in the search for chargino pair production with slepton mediated decay [153]. Events with exactly two opposite sign leptons and no b-tagged jets are considered and signal regions with $E_{\mathrm{T}}^{miss} \in$ [140-200], [200-300], or [300,∞] GeV are defined. The m_{T2} variable full range is then binned in order to perform a shape fit. The obtained exclusion limit is shown in Figure 6.28: in the case of a neutralino with mass 1 GeV, the chargino is excluded up to 810 GeV. The upper limits on the production cross section are also reported.

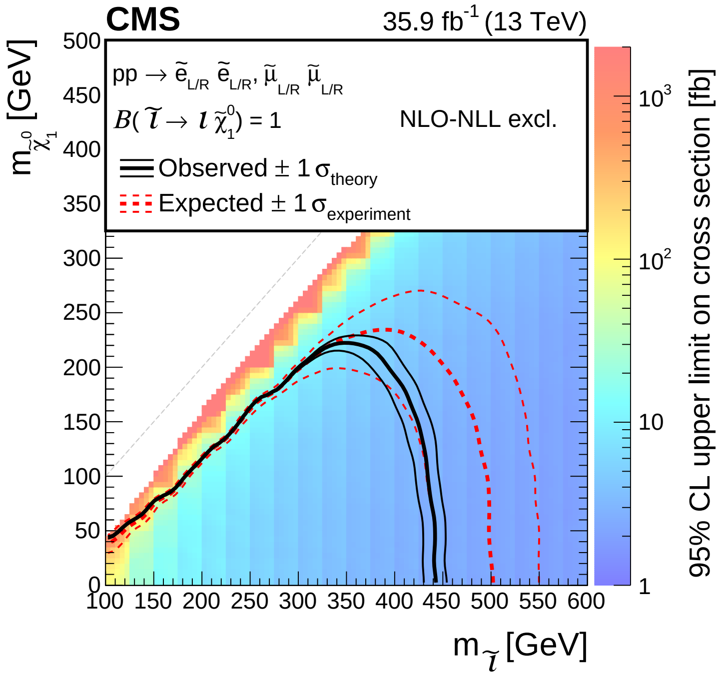

Figure 6.27: Exclusion limits at the 95% confidence level in the slepton-neutralino masses plane, considering both RH and LH sleptons, obtained by the CMS Collaboration using 35.9 fb^{-1} of LHC Run 2 data. The red line represents the expected exclusion limit, while the black one correspond to the observed exclusion limit, with a $\pm 1\sigma$ variation due to the signal cross-section uncertainty. Cross section upper limits are also reported [152].

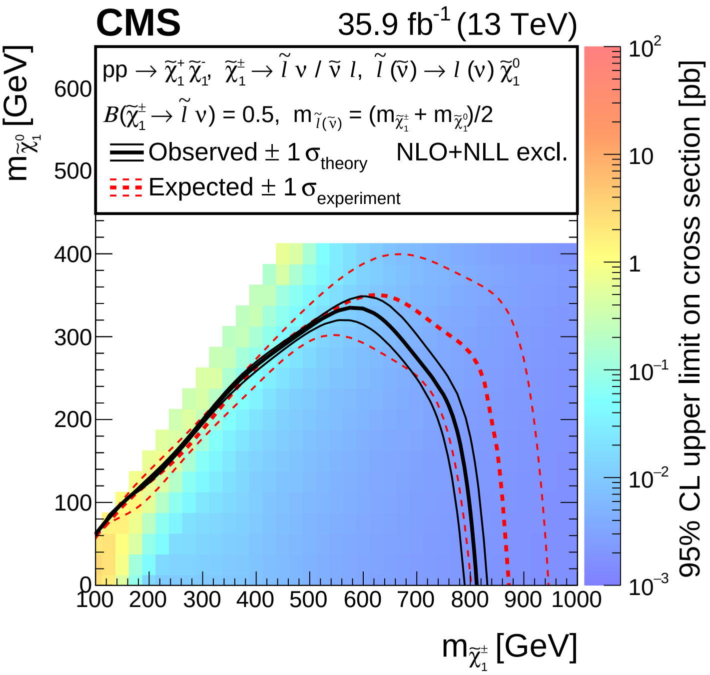

Figure 6.28: Exclusion limits at the 95% confidence level in the charginos-neutralino masses plane, obtained by the CMS Collaboration using 35.9 fb^{-1} of LHC Run 2 data. The red line represents the expected exclusion limit, while the black one correspond to the observed exclusion limit, with a $\pm 1\sigma$ variation due to the signal cross-section uncertainty. Cross section upper limits are also reported [153]

CHAPTER 7

Search for charginos direct production with W boson mediated decay

The search for the direct production of chargino pairs with W boson mediated decay will be presented in this Chapter. The analysis uses proton-proton collision data collected by ATLAS in 2015, 2016 and 2017, with a total integrated luminosity of 80.5 fb^{-1}. The release 21.0 of the ATLAS software `ATHENA` is used in this search, allowing the use of more sophisticated tools for the missing transverse energy reconstruction [59].

The Chapter is structured as follows: the model is described in Section 7.1; Sections 7.3, 7.4 and 7.5 present the trigger selection, the objects definitions and the preliminary selection; signal region are described in Section 7.6; the background estimate and the validation procedure are reported in Section 7.7 and 7.8 respectively; the uncertainties are described in Section 7.9; the results of the search are shown in Section 7.10; finally, the the results obtained by the CMS Collaboration for the signal model are briefly reported in Section 7.11.

7.1 Model and signature

The model of direct production of chargino pairs with W boson mediated decay is illustrated in Section 1.4.1. The process has a signature that is similar to the one already illustrated in the previous chapter for the chargino pair production with sleptons mediated decay: the final state consists of two leptons of opposite sign (electron or muon), no hadronic activity and missing transverse energy from neutrinos and neutralinos. A large mass splitting between the chargino and the neutralino is considered (Figure 7.1) and leptons with large momentum are selected for the search.

The charginos production cross sections are the same considered in the previous Chapter, but due to the branching ratio of the W boson decaying only leptonically the acceptance of the signal is reduced, making the process observation more difficult. The SUSY signal is also very similar to the Standard Model WW production. Despite the similarities between the SUSY processes, it is not possible to use the analysis illustrated in the previous Chapter for the search of chargino pairs with W boson mediated decay, since the sensitivity to the SUSY signal is very low.

For this reason, the search for chargino pair production with W mediated decay was performed later. In this way it was possible to include also the data collected by ATLAS during 2017, reaching an integrated luminosity of 80.5 fb^{-1}. The larger luminosity allows to re-optimize the analysis and the use of a new software release gives more advanced tools to perform the search.

A search aiming to observe the SUSY process was performed also with the data collected by the ATLAS detector during LHC Run 1, with $\sqrt{s} = 8$ TeV [125]. The exclusion limit obtained is reported in Figure 7.2, in the plane chargino-neutralino masses: charginos with mass up to 180 GeV is excluded at 95% CL, with a neutralino mass between 1 and 20 GeV. Since the excluded phase space is quite limited, data collected by ATLAS at the LHC Run 2 provided a great occasion for a discovery or a large improvement of the exclusion limits.

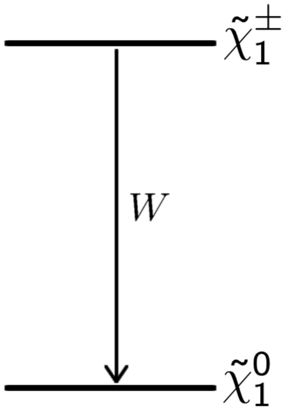

Figure 7.1: Mass spectrum in the case of the charginos direct production, where the chargino decays in W boson.

7.2 Monte Carlo samples

The Monte Carlo samples used in the search for charginos direct production with W boson mediated decay, both for signal and background processes, are described in this section. Some samples coincide with the ones used in the analysis described in Chapter 6, in other cases the samples have been updated and the motivations behind the changes will be illustrated.

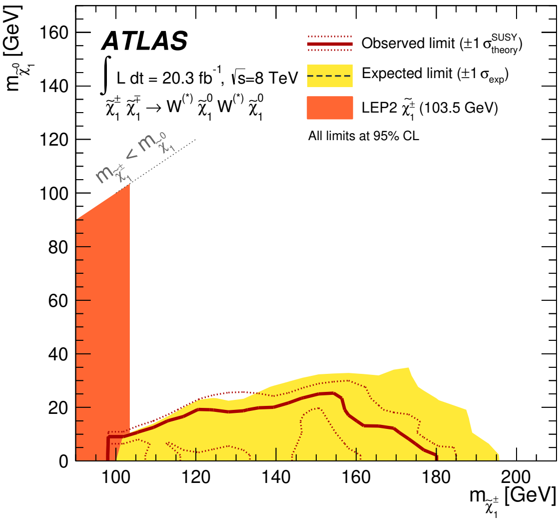

Figure 7.2: Exclusion limits at the 95% confidence level in the chargino-neutralino masses plane for the chargino pair production with W boson mediated decay model. The yellow band corresponds to the $\pm 1\sigma$ variation, due to all the uncertainties sources except the one on the the signal cross-section, around the expected exclusion limit central value. The red line correspond to the observed exclusion limit, with a $\pm 1\sigma$ variation due to the signal cross-section uncertainty (red dotted lines). The result is obtained using the data collected by ATLAS at the LHC Run 1, with $\sqrt{s} = 8$ TeV and an integrated luminosity of 20.3 fb^{-1} [125].

7.2.1 Pile-up condition

As addressed in Section 2.2.2, the number of interactions per bunch crossing is increasing each year. The average pile-up was 13.4 in 2015, 25.1 during 2016 and then 37.8 in 2017 data taking. In order to ensure a good description of the data, two sets of Monte Carlo with different pile-up distributions are used: the first one matches the 2015-2016 pile-up, while the second one is meant to follow the 2017 pile-up distribution. The two Monte Carlo simulation sets are combined together in the final result.

7.2.2 Signal samples

The Monte Carlo signal samples are generated using MadGraph5_aMC@NLO [127], that provides leading-order matrix elements with up to two extra partons. The SUSY particles decay chain is simulated using MadSpin [154] and Pythia8 [128], the A14 tune is used for parton showering and hadronization. The PDF used are the NNPDF2.3 LO set.

The cross sections are calculated at the next-to-leading-order, with soft gluon emission effects added at next-to-leading-logarithm accuracy, and the uncertainty is taken from an envelope of predictions that use different PDF sets and different factorization and renormalization scales.

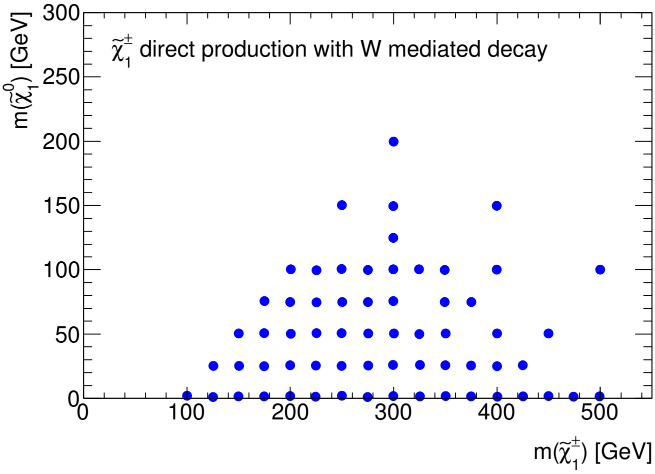

Figure 7.3: Points of the Monte Carlo simulation of the signal grid used in the search for charginos direct production with W boson mediated decay.

The grid of signal samples is shown in Figure 7.3: chargino mass between 100 and 500 GeV is considered, with 25 GeV step; neutralino mass ranges from 1 to 200 GeV, with 25 GeV step; the grid steps are larger in the region with larger mass since a lower sensitivity is expected in this phase space.

7.2.3 Background samples

The background samples used and the changes compared to the analysis illustrated in Chapter 6 are reported in the following:

- the most relevant difference is the change of the diboson process MC sample [155]. The Sherpa v2.2.1 generator [130] was used in search for direct sleptons production and charginos direct production with sleptons mediated decay. Sherpa generates together all the processes giving the same final state and the parent particles information is not available in the MC sample. As consequence it is not possible to classify an event as WW or ZZ. Due the similarity between the SUSY signal and the WW process, a MC sample providing the diboson processes separately was needed to better understand the background composition and to have a solid SM estimate. Samples generated with Powheg [156] were used, with Pythia8 [128] as parton shower and AZNLO [157] for the tuning. CTEQ6L1 [158] is used as PDF set and the cross sections are computed at NLO. It should also be noticed that a 20% difference between the Powheg and Sherpa cross sections is observed in those MC samples [155]. The effect is due to the choice of the electroweak parameters used in the simulation, but also to the inclusion of loop-induced diboson processes in the Sherpa MC, while they are not included in Powheg. Anyway the different cross section does not affect the final result, since the Powheg (Sherpa) simulation is normalized in dedicated CRs in the search considered in this (the previous) Chapter;

Monte Carlo samples				
Sample	Generator	Parton shower	PDF	Cross section
SUSY signal	MadGraph5-MadSpin	Pythia8	NNPDF30NNLO	NLO+NNLL
Diboson	Powheg	Pythia8	CTEQ6L	NLO
$t\bar{t}$	Powheg	Pythia8	CT10	NNLO+NNLL
Wt	Powheg	Pythia6	CT10	NLO
Z/γ^*+jets	Sherpa	Sherpa	CT10	NNLO
Triboson	Sherpa	Sherpa	NNPDF30NNLO	NLO
$t\bar{t}V$	MadGraph5	Pythia8	NNPDF30NNLO	NLO
Higgs	Pythia8	Pythia8	NNPDF30NNLO	NNLO+NNLL

Table 7.1: Signal and background samples used in the analysis illustrated in this Chapter. For each process the generator, the parton shower, the PDF set and the order of the cross section are reported.

- concerning the $t\bar{t}$ sample [134, 135], the events generator is Powheg [136], with the CT10 PDF set [138] and Perugia 2012 tune [140] for the underlying event. Pythia8 was used for the parton shower instead of Pythia6;
- all the other background samples were kept unchanged compared to the search illustrated in Chapter 6 and the detailed description can be found in Section 6.2.2. The summary of the MC samples is reported in Table 7.1.

7.3 Trigger and events quality

The trigger selection is similar to the one illustrated in Section 6.3.1. Triggers requiring two leptons (two electrons, two muons, or one electron and one muon) are used. In order to consider the higher luminosity and pile-up condition in the 2017 data, the online threshold for the particles momentum were changed in 2017. Depending on the trigger, the thresholds range from 12 to 24 GeV, as illustrated in Table 7.2. A cut of 25 GeV on the leptons momentum is applied to ensure a good trigger efficiency.

The data quality requirements applied to the data are unchanged compared to the previous Chapter, and they are summarized in Section 6.3.2.

7.4 Physics objects definition and selection

The objects used for the search are described in this Section and a summary is reported in Table 7.3.

The electron object definition is unchanged compared to the analysis reported in Chapter 6, the momentum selection is $p_{\mathrm{T}} > 25$ GeV and the acceptance is $|\eta| < 2.47$. The identification working point is Medium and GradientLoose isolation is required. Requirements on the impact parameters are also used, in order to ensure a good compatibility with the primary vertex.

Trigger online selection			
Trigger type	2015 data	2016 data	2017 data
ee	$p_{\mathrm{T}}^{e} > 12$ GeV	$p_{\mathrm{T}}^{e} > 17$ GeV	$p_{\mathrm{T}}^{e} > 24$ GeV
$\mu\mu$	$p_{\mathrm{T}}^{\mu} > 18$ GeV	$p_{\mathrm{T}}^{\mu} > 22$ GeV	$p_{\mathrm{T}}^{\mu} > 22$ GeV
$e\mu$	$p_{\mathrm{T}}^{e} > 17$ GeV,	$p_{\mathrm{T}}^{e} > 17$ GeV	$p_{\mathrm{T}}^{e} > 17$ GeV
	$p_{\mathrm{T}}^{\mu} > 14$ GeV	$p_{\mathrm{T}}^{\mu} > 14$ GeV	$p_{\mathrm{T}}^{\mu} > 14$ GeV

Table 7.2: Online selection on the leptons transverse momentum performed by the dileptonic triggers used in the search. The p_{T} thresholds are different in the case of di-electron, di-muon or electron-muon pairs. The thresholds of the triggers were progressively increased, in order to account for the higher integrated luminosity and pile-up condition.

In the case of muons, the Medium identification requirement and GradientLoose isolation are used. The momentum is required to be larger then 25 GeV and the geometric acceptance is $|\eta| < 2.7$.

Jets with $|\eta| < 2.4$ and $p_{\mathrm{T}} > 20$ GeV are selected. The b-tagging working point tagging efficiency was changed from 77% to 85% in order to improve the rejection of the $t\bar{t}$ background.

Concerning the missing transverse energy, with the ATLAS software `ATHENA` release 21.0, more sophisticated tools are available, in order to ensure a good performance also with the increasing pile-up. Different working points for the missing transverse energy are present, depending on the requirement on the jets entering in the E_{T}^{miss} computation [159]:

- *Loose* working point: all the jets with $p_{\mathrm{T}} > 20$ GeV are included and the JVT selection is applied to jets with $p_{\mathrm{T}} < 60$ GeV and $|\eta| < 2.4$. This working point correspond to the E_{T}^{miss} definition used in Chapter 6;

- *Tight* working point, designed to reduce the E_{T}^{miss} pile-up dependency. Forward jets with $|\eta| > 2.4$ and $20 < p_{\mathrm{T}} < 30$ GeV are not included in the E_{T}^{miss} computation, since in this region most of the jets come from the pile-up and not from a hard interaction. This working point is the one used for the analysis illustrated in this Chapter.

7.5 Preliminary selection

The preliminary selection that will be applied to all the regions used in the analysis is reported in Table 7.4. Since the final state is the same considered in the previous Chapter, the selection is similar. Events with exactly two opposite sign leptons, with same flavor or different flavor, are used. The cut on the leptons invariant mass is looser in this case ($m_{\ell\ell} > 25$ GeV instead of 40 GeV). Due to the lower signal event acceptance, the selection removes the low mass resonance without loosing too much statistic.

Objects definition		
Object	Quantity	Value
Electrons	Acceptance	$\|\eta\| < 2.47$
	Momentum	$p_{\mathrm{T}} > 25$ GeV
	Identification	Medium
	Isolation	GradientLoose
	Impact parameter	$\|z_0 \sin\theta\| < 0.5$ mm
		$\|d_0/\sigma_{d_0}\| < 5$
Muons	Acceptance	$\|\eta\| < 2.7$
	Momentum	$p_{\mathrm{T}} > 25$ GeV
	Identification	Medium
	Isolation	GradientLoose
	Impact parameter	$\|z_0 \sin\theta\| < 0.5$ mm
		$\|d_0/\sigma_{d_0}\| < 3$
Jets	Acceptance	$\|\eta\| < 2.4$
	Momentum	$p_{\mathrm{T}} > 20$ GeV
	Jet vertex tagger	JVT> 0.59 if $p_{\mathrm{T}} < 60$ GeV.
	b-tagging	85 % working point
E_{T}^{miss}	Working point	Tight

Table 7.3: Requirement for the objects used in the analysis: electrons, muons, jets and E_{T}^{miss}.

7.6 Signal regions

The strategy developed for the signal regions definition is similar to the one used in Section 6.6, but due to the larger statistic available a new optimization of region selection was performed and new kinematic variables are used. The stransverse mass is again one of the most effective selections, but also an explicit selection on E_{T}^{miss} is used. A lower cut on missing transverse energy significance $\mathcal{S}(E_{\mathrm{T}}^{miss})$ was also proved to be an effective way to reject background.

Two sets of signal regions are used: inclusive signal regions, optimized for the discovery of the new SUSY particles, and exclusive signal regions used to perform the shape fit and to maximize the exclusion limits, following the strategy described in Section 5.7.5 and 5.7.6.

The kinematic variables selections common to all the regions are:

- *jets multiplicity*: no hadronic activity is expected to originate directly from the SUSY decay chain. Jets are classified as b-tagged and non-b-tagged jets, the momentum threshold being $p_{\mathrm{T}} > 20$ GeV in both the cases. A zero b-tagged jets requirement is applied, while non-b-tagged jets are require to be ≤ 1, since it is possible to have initial state radiation;

Preliminary selection	
Quantity	Selection
Quality requirement	✓
Trigger	✓
Leptons number	exactly 2
Leptons sign	opposite sign
Leptons flavor	SF or DF
Leptons momentum	$p_{\mathrm{T}} > 25$ GeV
Leptons invariant mass	$m_{\ell\ell} > 25$ GeV

Table 7.4: Preliminary selection in common to all the regions considered in the analysis.

Signal regions common selection	
Quantity	Selection
non-b-tagged jets multiplicity	≤ 1 ($p_{\mathrm{T}} > 20$ GeV)
b-tagged jets multiplicity	0 ($p_{\mathrm{T}} > 20$ GeV)
Z peak veto in SF leptons events	$\lvert m_{\ell\ell} - m_Z \rvert > 30$ GeV
Stransverse mass	$m_{\mathrm{T2}} > 100$ GeV
Missing transverse energy	E_{T}^{miss} >110 GeV
Missing transverse energy significance	$\mathcal{S}(E_{\mathrm{T}}^{miss})$ >10

Table 7.5: Selection common to all the SRs.

- *Z veto*: in order to remove Z+jets events, a veto on the SF leptons with invariant mass close to the Z is applied, $\lvert m_{\ell\ell} - m_Z \rvert > 30$ GeV;
- *stansverse mass*: also in these search, the m_{T2} variable is a powerful tool to remove most of the $t\bar{t}$ and diboson backgrounds. The $m_{\mathrm{T2}} > 100$ GeV cut is used;
- *missing transverse energy*: since a larger E_{T}^{miss} is expected in the signal events due to the presence of the neutralinos, E_{T}^{miss} >110 GeV is required. In order to remove events where the E_{T}^{miss} arise from wrong object reconstruction or mis-measurement, such as in the Z+jets process, a cut on the $\mathcal{S}(E_{\mathrm{T}}^{miss})$ variable is used. Figure 7.4 reports the $\mathcal{S}(E_{\mathrm{T}}^{miss})$ distribution for the main background process ($t\bar{t}$, diboson and Z+jets) and two signal samples, after performing the preliminary selection. As it can be appreciated from the comparison of the plots, the signal over background ratio increases at large value of $\mathcal{S}(E_{\mathrm{T}}^{miss})$. A $\mathcal{S}(E_{\mathrm{T}}^{miss}) > 10$ selection is applied to all the SRs.

The selections common to all the SRs are summarized in Table 7.5.

7.6.1 Inclusive signal regions

The inclusive SRs are built classifying the events using the leptons flavor and the number of non-b-tagged-jets, and then performing different selections on the m_{T2} variable, as illustrated in Table 7.6.

Inclusive signal regions definitions				
Region	SR-DF-0J	SR-DF-1J	SR-SF-0J	SR-SR-1J
Leptons flavor	DF	DF	SF	SF
non-b-tagged jets multiplicity	0	1	0	1
m_{T2} [GeV]	$\in [100, \infty]$ $\in [160, \infty]$ $\in [100, 120]$ $\in [120, 160]$			

Table 7.6: Definitions of the inclusive signal regions. Labels "DF" and "SF" refers respectively to signal regions with different flavor or same flavor lepton pairs, labels "0J" and "1J" to the number of non-b-tagged jets.

The background composition is different selecting DF or SF leptons pairs: in the first case the dominant process are $t\bar{t}$ and WW, while in the latter also WZ and ZZ are significant. The number of non-b-tagged jets can be zero or one, in order to account for possible initial state radiation. The ISR jets can be useful to boost the SUSY particles system and to give larger E_{T}^{miss} and this compensates for the larger background in regions with one non-b-tagged jet.

The four regions obtained (SR-DF-0J, SR-DF-1J, SR-SF-0J and SR-SF-1J) are then split using m_{T2}, as reported in Table 7.6:

- two regions only have a lower cut on the m_{T2} variable, the first one being $m_{\mathrm{T2}} >$ 100 GeV and the second one, optimized for large charginos masses, defined with $m_{\mathrm{T2}} >$ 160 GeV;
- two regions also have an upper limit: since the m_{T2} variable is upper limited by the chargino and neutralino mass (Eq. (5.10)), in the case of small SUSY particle masses this kind of selection allows to remove the diboson background, that still presents a tail at large m_{T2} values. The selected intervals are $m_{\mathrm{T2}} \in [100, 120]$ GeV and $m_{\mathrm{T2}} \in [120, 160]$ GeV

7.6.2 Exclusive signal regions

In order to define the exclusive SRs used in the exclusion fit, the events classification using the leptons flavor and the number of non-b-tagged jet is performed as in the inclusive SRs case. The SR-DF-0J, SR-DF-1J, SR-SF-0J and SR-SR-1J regions are then divided into bins using the m_{T2} variables: from 100 GeV to infinity, the regions are delimited by 105, 110, 120, 140, 160, 180 and 220 GeV. The binning is not uniform, the initial 5 GeV steps are important in the case of signals with small chargino mass, where the m_{T2} distribution has a sharp edge around 100 GeV (as it can be observed from Figure 5.3). To account for the decreasing number of events in the m_{T2} tail, the steps are larger in this region. The binned SRs definition is reported in Table 7.7.

Exclusive signal regions definitions				
Region	SR-DF-0J	SR-DF-1J	SR-SF-0J	SR-SR-1J
Leptons flavor	DF	DF	SF	SF
non-b-tagged jets multiplicity	0	1	0	1
m_{T2} [GeV]	$\in$[100,105] $\in$[105,110] $\in$[110,120] $\in$[120,140] $\in$[140,160] $\in$[160,180] $\in$[180,220] $\in [220, \infty]$			

Table 7.7: Definitions of the inclusive signal regions. Labels "DF" and "SF" refers respectively to signal regions with different flavor or same flavor lepton pairs, labels "0J" and "1J" to the number of non-b-tagged jets.

The m_{T2} distribution for the data and the SM prediction in SR-SF-0J and SR-SR-1J are reported in Figure 7.5, while SR-DF-0J and SR-DF-1J are shown in Figure 7.6. The binning of the histograms corresponds to the division used in the exclusive SRs definition. Three signal samples, with masses $m(\tilde{\chi}_1^{\pm}, \tilde{\chi}_1^0)$ = (200,1) GeV, $m(\tilde{\chi}_1^{\pm}, \tilde{\chi}_1^0)$ = (250,1) GeV, and $m(\tilde{\chi}_1^{\pm}, \tilde{\chi}_1^0)$ = (300,1) GeV, are overlayed to the background distribution. All the sources of uncertainties (that will be described in Section 7.9) are included in the plots.

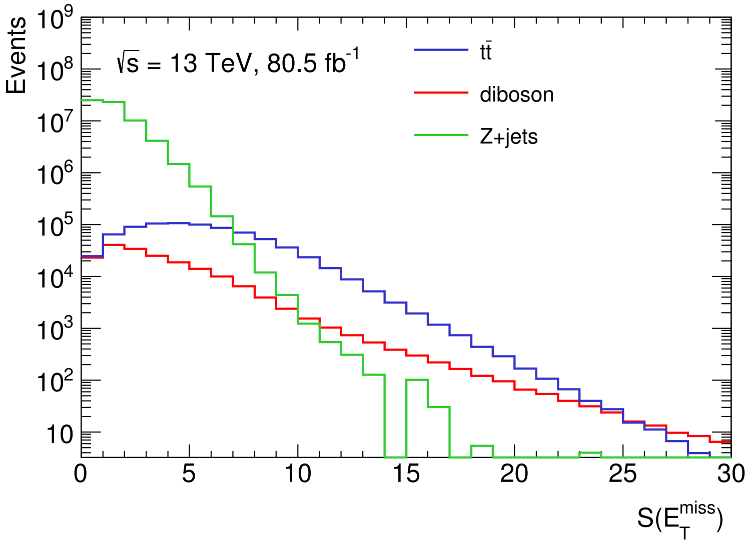

(a)

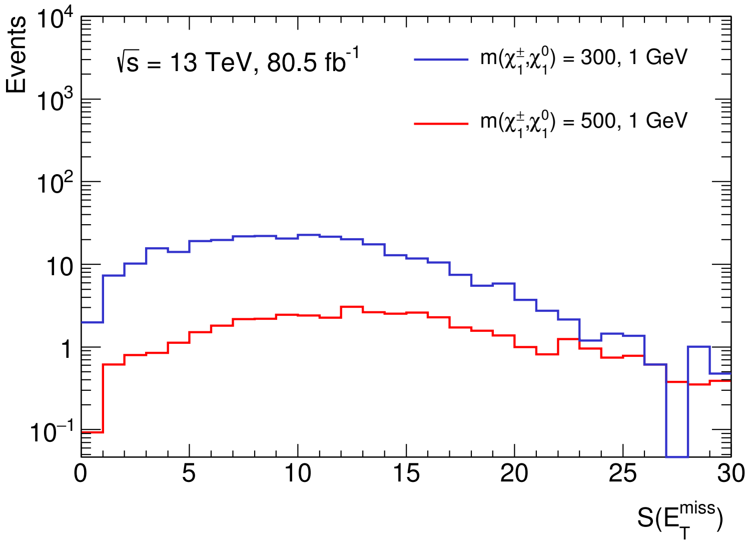

(b)

Figure 7.4: Distribution of the missing transverse energy significance, after performing the preliminary selection, for the $t\bar{t}$, diboson and Z+jets background (a) and for two signal samples (b), with masses $m(\tilde{\chi}_1^\pm, \tilde{\chi}_1^0)$ = (300,1) GeV and $m(\tilde{\chi}_1^\pm, \tilde{\chi}_1^0)$ = (500,1) GeV.

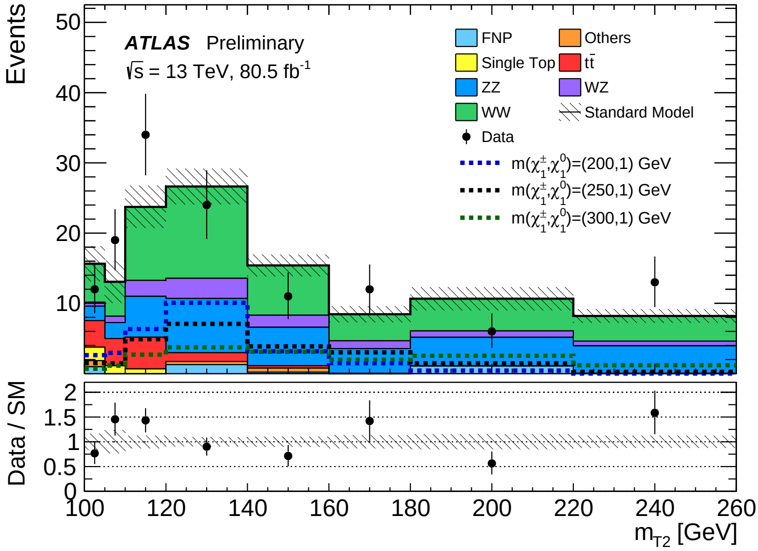

(a) m_{T2} distribution in SR-SF-0J

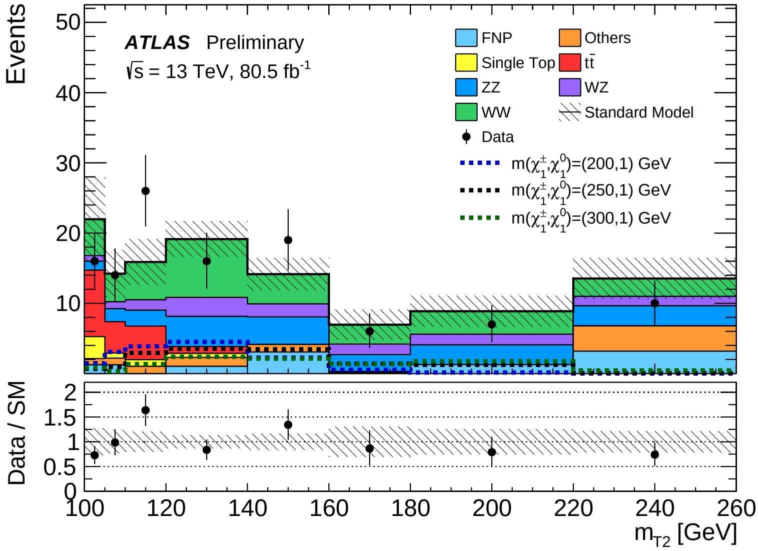

(b) m_{T2} distribution in SR-SF-1J

Figure 7.5: The m_{T2} distribution for the data and the estimated SM backgrounds in (a) SR-SF-0J and (b) SR-SF-1J, after performing the background-only likelihood fit. The binning of the histograms is the division used in the exclusive SRs selection. The intervals $[100, \infty]$, $[160, \infty]$, $[100, 120]$ and $[120, 160]$ correspond to the inclusive SRs. The uncertainty bands include all systematic and statistical contributions. Simulated signal samples are overlayed for comparison: chargino with mass of 200, 250 or 300 GeV and neutralino mass of 1 GeV are considered.

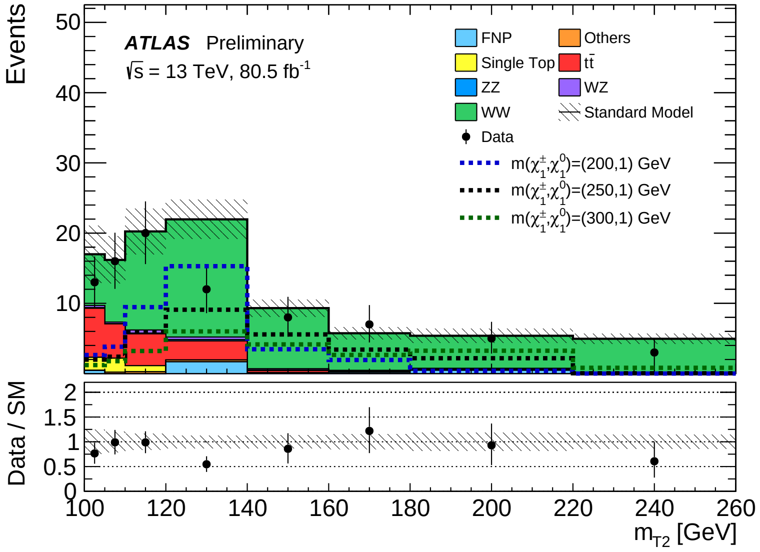

(a) m_{T2} distribution in SR-DF-0J

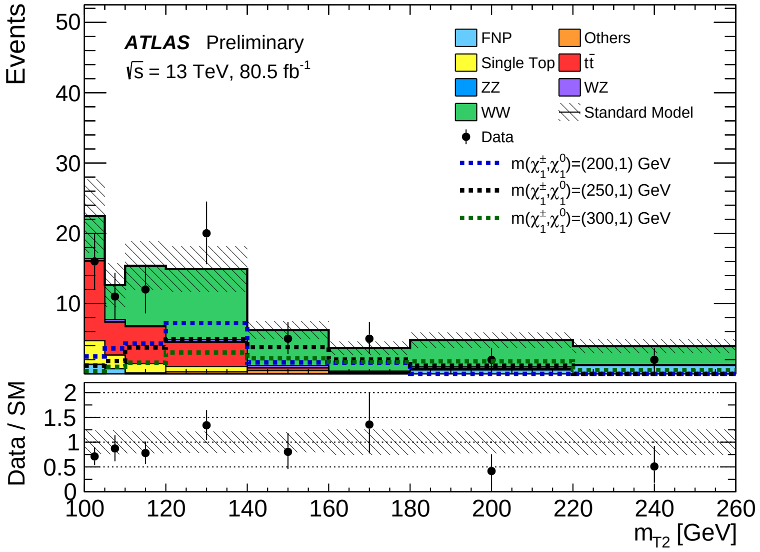

(b) m_{T2} distribution in SR-DF-1J

Figure 7.6: The m_{T2} distribution for the data and the estimated SM backgrounds in (a) SR-DF-0J and (b) SR-DF-1J (b), after performing the background-only likelihood fit. The binning of the histograms is the division used in the exclusive SRs selection. The intervals $[100, \infty]$, $[160, \infty]$, $[100, 120]$ and $[120, 160]$ correspond to the inclusive SRs. The uncertainty bands include all systematic and statistical contributions. Simulated signal samples are overlayed for comparison: chargino with mass of 200, 250 or 300 GeV and neutralino mass of 1 GeV are considered.

7.7 Background estimation

Due to the similarity of the signal regions selection and the background composition, the strategy to estimate the Standard Model background is similar to the one illustrated in Section 6.7. The WW and $t\bar{t}$ processes are dominant in the selection with DF leptons pair, while WZ and ZZ become significant in the SF leptons selections.

Since the diboson background is evaluated using Powheg MC simulation (as explained in Section 7.2.3), it is possible to separate the different processes and perform the MC normalization in the control regions independently for each component. The CRs used in the search are the following:

- CR-VZ is dedicated to the normalization of WZ and ZZ processes, with a single parameter in the likelihood fit. Events with SF leptons are used and the zero b-tagged and non-b-tagged jets requirement, with threshold $p_T > 20$ GeV, is applied to avoid Z+jets and $t\bar{t}$ contaminations. Leptons invariant mass close to the Z peak is required ($|m_{\ell\ell} - m_Z| < 30$ GeV), in order to be orthogonal to the SRs. Large stransverse mass, $m_{\mathrm{T2}} > 120$ GeV, is considered. Selection on the missing transverse energy and its significance are used both to remove the Z+jets contamination and to have a selection close to the SRs: $E_{\mathrm{T}}^{miss} > 110$ GeV and $\mathcal{S}(E_{\mathrm{T}}^{miss}) > 10$ are required;

- CR-WW is used for the WW Monte Carlo normalization, selecting events with DF leptons and vetoing b-tagged and non-b-tagged jets. Intermediate value of m_{T2} are used ($60 < m_{\mathrm{T2}} < 65$ GeV), in order to allow for a validation region between the CR and SRs. $E_{\mathrm{T}}^{miss} > 60$ GeV and $\mathcal{S}(E_{\mathrm{T}}^{miss}) > 5$ selections are applied to have a selection close to the SRs.

- CR-top is the region where the $t\bar{t}$ and single top background are normalized to data, using a single parameter in the likelihood fit. Events with DF leptons and zero non-b-tagged jets are used. At least one b-tagged jets and large stransverse mass ($m_{\mathrm{T2}} > 100$ GeV) are required to select the $t\bar{t}$ and single top processes.

The definition of the CRs is summarized in Table 7.8.

Minor contributions come from Z+jets, triboson, Higgs and $t\bar{t}$ associated to boson (Z, W or H) processes and they are evaluated using the Monte Carlo simulation. The minor backgrounds will be grouped together under the “Other” label in the following. Fake and non-prompt leptons are estimated using the Matrix Method, as in the analysis described in Chapter 6, as reported in Section 6.7.3.

The kinematic distributions for the data and expected SM background in the CRs are reported in Figure 7.7, that show the m_{T2} distribution in CR-VZ and CR-top, and 7.8, that reports E_{T}^{miss} in CR-WW. The plots show the estimation of the SM background obtained performing background-only likelihood fit and all the sources of uncertainties are included in the error bands.

Control regions definitions			
Region	CR-VZ	CR-WW	CR-top
Lepton flavor	SF	DF	DF
b-tagged jets multiplicity	0	0	1
non-b-tagged jets multiplicity	0	0	0
m_{T2} [GeV]	> 120	$\in [60, 65]$	> 100
E_{T}^{miss} [GeV]	> 110	> 60	> 110
$\mathcal{S}(E_{\mathrm{T}}^{miss})$	> 10	> 5	> 5
$\|m_{\ell\ell} - m_Z\|$ [GeV]	< 30	–	–

Table 7.8: Definition of the control regions for WZ and ZZ (CR-VZ), WW (CR-WW) and $t\bar{t}$ (CR-top) processes. The b-tagged and non-b-tagged jets momentum threshold is $p_T > 20$ GeV, as in the SRs.

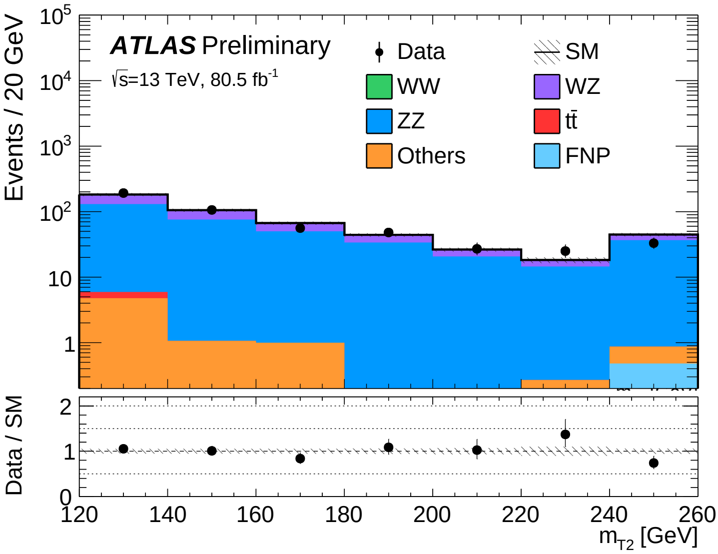

(a) m_{T2} in CR-VZ

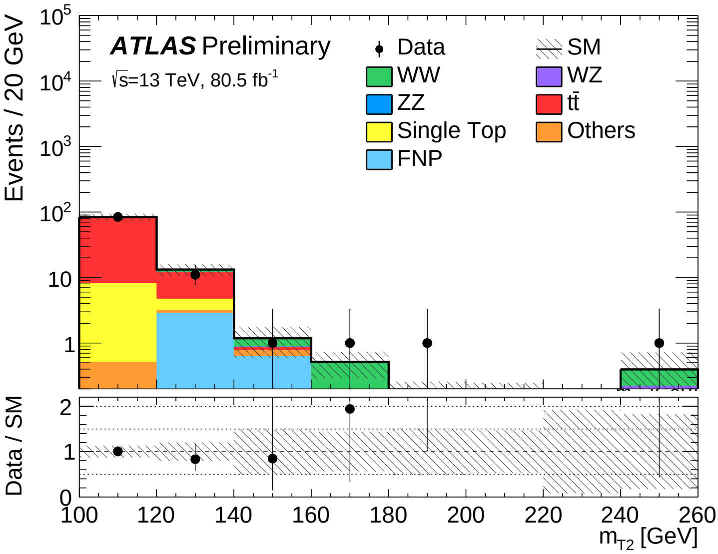

(b) m_{T2} in CR-top

Figure 7.7: The m_{T2} distribution for the data and the estimated SM backgrounds in (a) CR-VZ and (b) CR-top, after performing the background-only likelihood fit. The uncertainty bands include all systematic and statistical contributions.

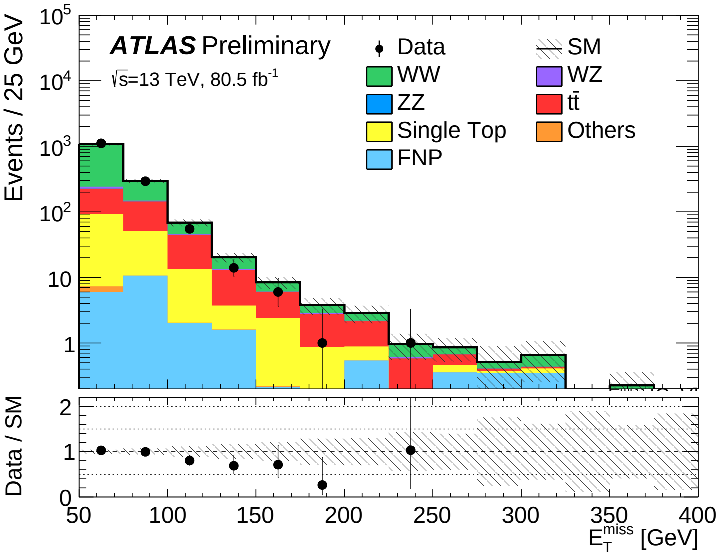

Figure 7.8: The E_{T}^{miss} distribution for the data and the estimated SM backgrounds in CR-WW, after performing the background-only likelihood fit. The uncertainty bands include all systematic and statistical contributions.

7.8 Validation

Validation regions are built in order to ensure the correct estimation of the SM background. Section 7.8.1 reports the VRs defined using a selection with a two leptons final state, while Section 7.8.2 illustrates the validation of the diboson tail at large m_{T2} using events with 3 leptons.

7.8.1 Validation regions using 2 leptons selection

Five validation regions based on the selection of events with two leptons are defined, with the aim of validating the estimate of the diboson and $t\bar{t}$ backgrounds. The regions definitions are summarized in Table 7.9.

The regions VR-WW-0J and VR-WW-1J are dedicated to the validation of the WW background estimation. The kinematic cuts are close to the corresponding CR, with DF leptons, zero b-tagged jets, $E_{\mathrm{T}}^{miss} > 60$ GeV and $\mathcal{S}(E_{\mathrm{T}}^{miss}) > 5$, but stransverse mass is larger ($65 < m_{\mathrm{T2}} < 100$ GeV). The number of non-b-tagged jets is zero for VR-WW-0J and one for VR-WW-1J, in order to reflect the SRs selection.

The WZ and ZZ backgrounds are validated in the region VR-VZ, with a selection similar to CR-VZ: events with SF leptons are used, b-tagged and non-b-tagged jets have to be zero, the requirement on the lepton invariant mass is $|m_{\ell\ell} - m_Z| < 30$ GeV, the missing energy cuts are $E_{\mathrm{T}}^{miss} > 110$ GeV and $\mathcal{S}(E_{\mathrm{T}}^{miss}) > 10$. The region is orthogonal to the CR due to the stransverse mass selection, $100 < m_{\mathrm{T2}} < 120$ GeV.

The estimation of the $t\bar{t}$ background is validated in two regions. The common requirement are DF leptons, one b-tagged-jets to have a large amount of $t\bar{t}$ events, large missing energy $E_{\mathrm{T}}^{miss} > 110$ GeV with $\mathcal{S}(E_{\mathrm{T}}^{miss}) > 5$. VR-top-low uses the lower stransverse mass selection ($80 < m_{\mathrm{T2}} < 100$ GeV) and zero non-b-tagged jets. VR-top-high require one non-b-tagged jets, so $m_{\mathrm{T2}} > 100$ GeV is used to remove Z+jets contamination.

In order to better understand the motivation behind the validation regions definition, Figure 7.9 reports the VRs together with the corresponding CRs using planes corresponding to two kinematic variables. The SRs are also reported. In particular:

- Figure 7.9(a) shows the m_{T2}-$m_{\ell\ell}$ plane, in the case of zero b-tagged jets and considering only SF leptons. The horizontal band corresponding to the Z boson peak ($|m_{\ell\ell} - m_Z| < 30$ GeV) contains CR-VZ and VR-VZ. SR-SF-0J is defined outside the Z boson peak region;

- Figure 7.9(b) considers the m_{T2}-[non-b-tagged jets multiplicity] plane, for zero b-tagged jets and DF leptons events. CR-WW is located in the low m_{T2} space, VR-WW-0J and VR-WW-1J occupy the intermediate region, SR-DF-0J and SR-DF-1J have $m_{\mathrm{T2}} > 100$ GeV;

- In the case of Figure 7.9(c), the selection is one b-tagged jets and DF leptons. In the m_{T2}-[non-b-tagged jets multiplicity] plane, CR-top is in the large m_{T2} region, while VR-top-low and VR-top-high are at low and high m_{T2} respectively, with different non-b-tagged jets multiplicity;

Validation regions definitions			
Region	VR-WW-0J	VR-WW-1J	VR-VZ
Lepton flavor	DF	DF	SF
b-tagged jets multiplicity	0	0	0
non-b-tagged jets multiplicity	0	1	0
m_{T2} [GeV]	$\in [65, 100]$	$\in [65, 100]$	$\in [100, 120]$
E_{T}^{miss} [GeV]	> 60	> 60	> 110
$\mathcal{S}(E_{\mathrm{T}}^{miss})$	> 5	> 5	> 10
$\lvert m_{\ell\ell} - m_Z \rvert$ [GeV]	–	–	< 30
Region	VR-top-low		VR-top-high
Lepton flavor	DF		DF
b-tagged jets multiplicity	1		1
non-b-tagged jets multiplicity	0		1
m_{T2} [GeV]	$\in [80, 100]$		> 100
E_{T}^{miss} [GeV]	> 110		> 110
$\mathcal{S}(E_{\mathrm{T}}^{miss})$	> 5		> 5
$\lvert m_{\ell\ell} - m_Z \rvert$ [GeV]	–		–

Table 7.9: The first part of the Table report the definition of the validation regions for WW (VR-WW-0J and VR-WW-1J) and WZ-ZZ (VR-VZ) processes, while in the second part the definition of the validation regions for the $t\bar{t}$ process is shown. The b-tagged and non-b-tagged jets momentum threshold is $p_T > 20$ GeV, as in the SRs.

The m_{T2} distributions in the VRs dedicated to $t\bar{t}$ and WW background validation are reported in Figure 7.10 and 7.11, while Figure 7.12 shows the E_{T}^{miss} and $\mathcal{S}(E_{\mathrm{T}}^{miss})$ distribution in VR-VZ. In all the Figures, the expected SM background obtained in the background-only likelihood fit is reported and all the statistical and systematics uncertainties are included. A good modeling of the data is observed in all the validation regions considered.

7.8.2 Validation of the m_{T2} tail

In regions with large stransverse mass, the dominant background is the WW process. The VR designed to validate the estimation of this background is at $m_{\mathrm{T2}} < 100$ GeV, since it is difficult to find a region orthogonal to the SRs and with low SUSY signal contamination, using only events with a two leptons final state. In order to solve the issue, a selection that requires 3 leptons in the final state is used. The WZ background is validated in the regions with the 3 leptons selection, and if the data are well modeled by the process, this is taken as an indication of good modeling of the WW process.

The validation procedure is performed as follows:

- in order to have a region dominated by the WZ background, events with exactly three leptons, as defined in Table 7.3, are selected. Two of the leptons are assumed to come from the Z decay, so a leptons pair with SF, opposite sign (SFOS) and invariant mass close to the Z peak ($\lvert m_{\ell\ell} - m_Z \rvert < 10$ GeV) is selected. In the case where more then one SFOS pair is possible, the pair with the invariant mass closer to the the Z boson mass is selected;

- WZ events enter in the two leptons selection of the analysis due to the loss of a leptons (acceptance or mis-reconstruction). In order to have a selection with two opposite sign leptons, the lepton assigned to the Z boson, with the same sign of the lepton assigned to the W boson, is added to the the missing transverse energy, as if it was a neutrino. These events are called *pseudo-2lep*;
- the WZ MC is normalized to the data in a control region (CR-3lep) where the original missing transverse energy is $40 < E_{\mathrm{T}}^{miss} < 120$ GeV and the number of b-tagged and non-b-tagged jets is zero. The E_{T}^{miss} upper cut is needed to reduce contamination from other SUSY signals. Considering the associated production of chargino $\tilde{\chi}_1^{\pm}$ and neutralino $\tilde{\chi}_2^0$ (Figure 1.6), the chargino can decay in a W boson and a neutralino $\tilde{\chi}_1^0$, while the $\tilde{\chi}_2^0$ decays in a Z boson and a $\tilde{\chi}_1^0$. In the case of a leptonic decay of the W and Z bosons, the signature consists of 3 leptons and missing transverse energy and the $E_{\mathrm{T}}^{miss} < 120$ GeV selection allows to reduce potential signal contribution [58];
- the data and Monte Carlo simulation, after applying the WZ normalization factor, are compared for the pseudo-2lep events to validate the diboson modeling.

The E_{T}^{miss} and m_{T2} distributions for the pseudo-2lep selection after the normalization of the WZ in CR-3lep are reported in Figure 7.13, a good modeling is observed and thus the WW estimation at large m_{T2} is considered reliable.

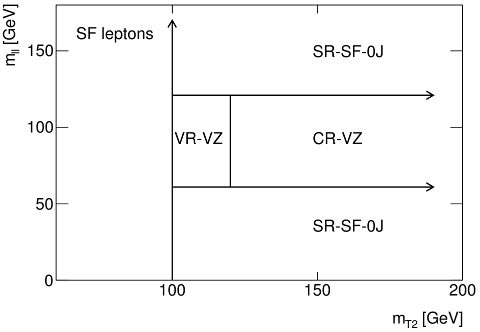

(a)

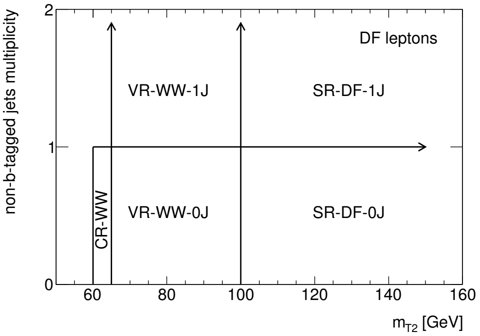

(b)

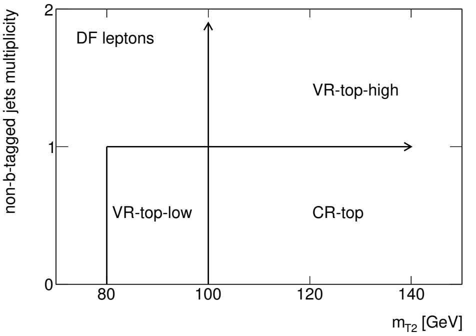

(c)

Figure 7.9: Schematic representation of the regions used in the search presented in this Chapter. Figure (a) shows CR-VZ, VR-VZ and SR-SF-0J in the m_{T2}-$m_{\ell\ell}$ plane, considering only SF leptons. Figure (b) represents CR-WW, the corresponding validation regions VR-WW-0J and VR-WW-1J, and the two signal regions SR-DF-0J and SR-DF-1J, in the m_{T2}-[non-b-tagged jets multiplicity] plane and considering DF leptons. Finally, Figure (c) shows the m_{T2}-[non-b-tagged jets multiplicity] in the case of one b-tagged jets and DF leptons, CR-top, VR-top-low and VR-top-high are reported.

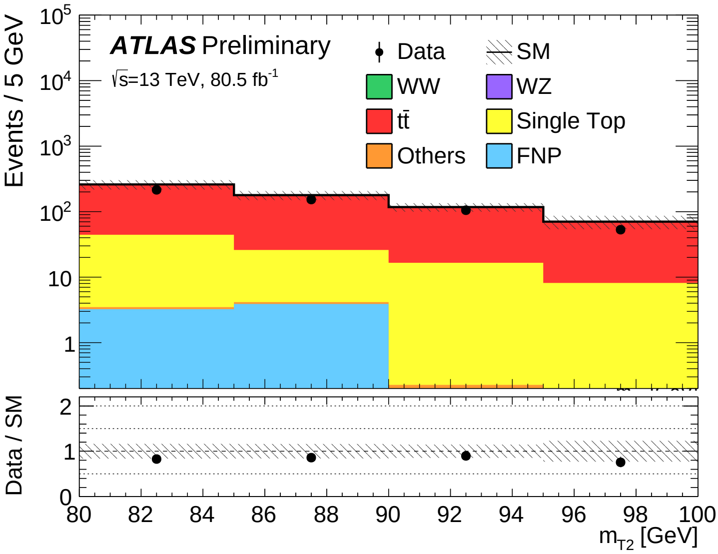

(a) m_{T2} in VR-top-low

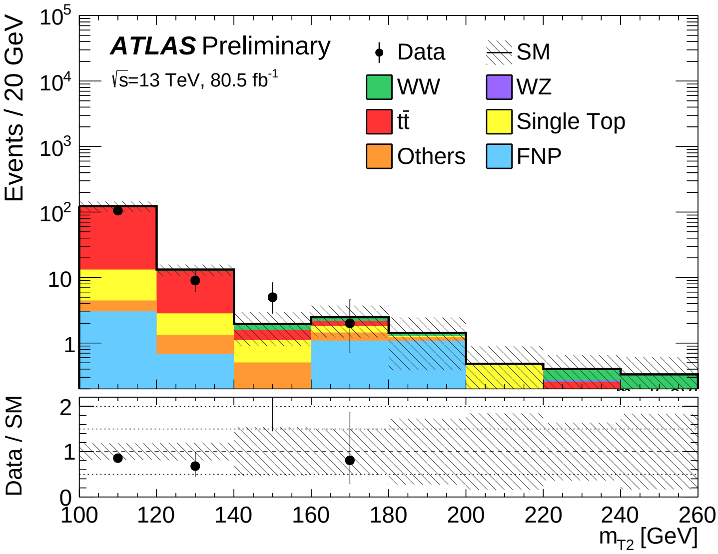

(b) m_{T2} in VR-top-high

Figure 7.10: The m_{T2} distribution for the data and the estimated SM backgrounds in (a) VR-top-low and (b) VR-top-high, after performing the background-only likelihood fit. The uncertainty bands include all systematic and statistical contributions.

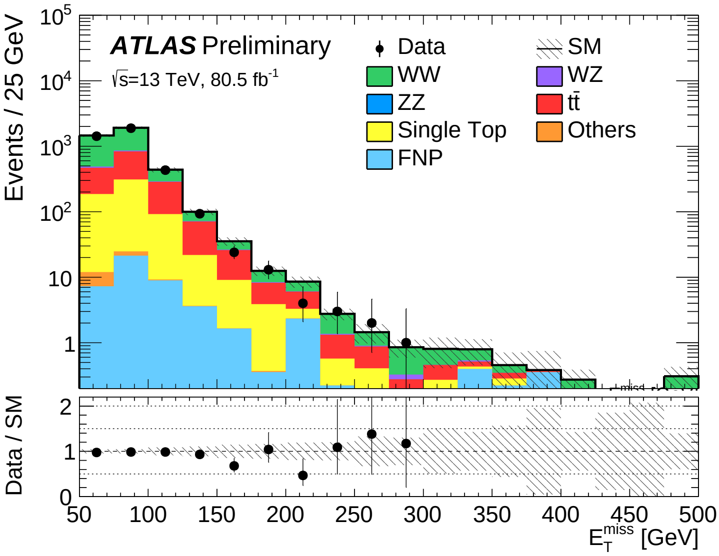

(a) E_{T}^{miss} in VR-WW-0J

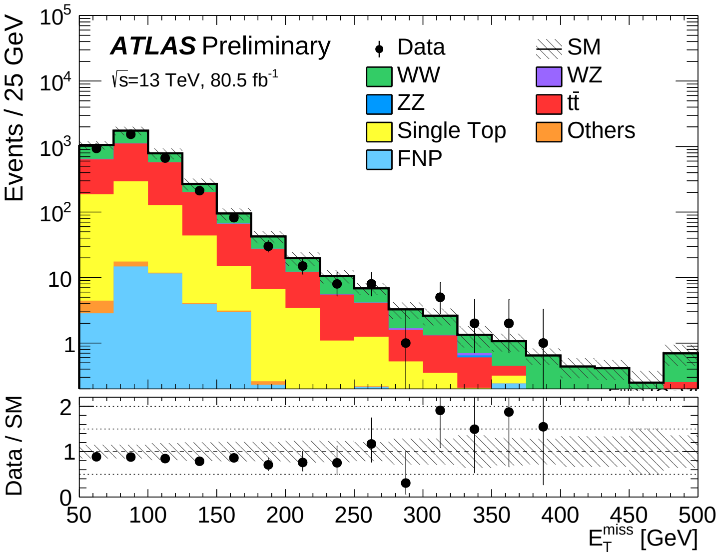

(b) E_{T}^{miss} in VR-WW-1J

Figure 7.11: The E_{T}^{miss} distribution for the data and the estimated SM backgrounds in (a) VR-WW-0J and (b) VR-WW-1J, after performing the background-only likelihood fit. The uncertainty bands include all systematic and statistical contributions.

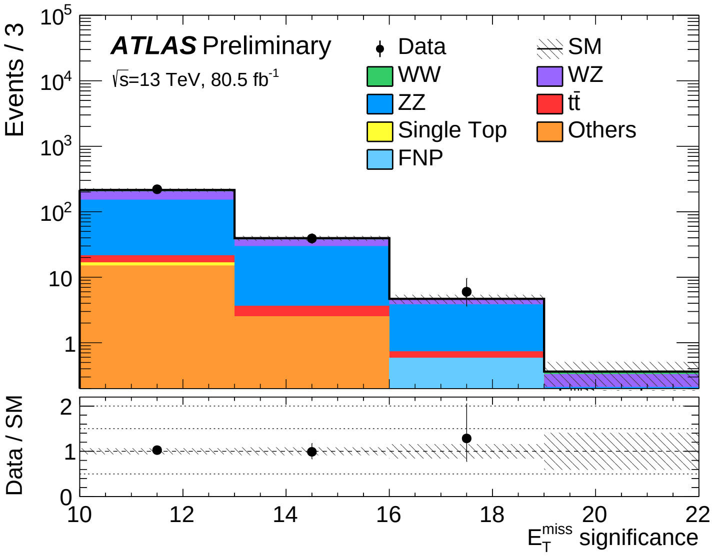

(a) $\mathcal{S}(E_{\mathrm{T}}^{miss})$ in VR-VZ

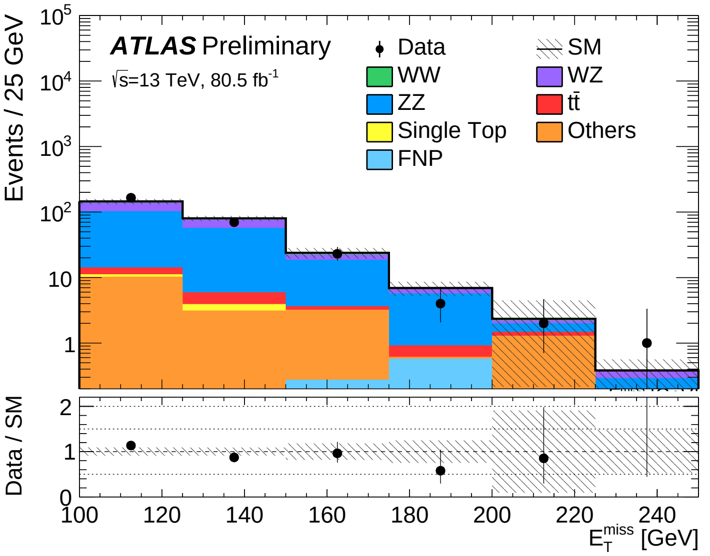

(b) E_{T}^{miss} in VR-VZ

Figure 7.12: The (a)$\mathcal{S}(E_{\mathrm{T}}^{miss})$ and (b) E_{T}^{miss} distribution for the data and the estimated SM backgrounds in VR-VZ, after performing the background-only likelihood fit. The uncertainty bands include all systematic and statistical contributions.

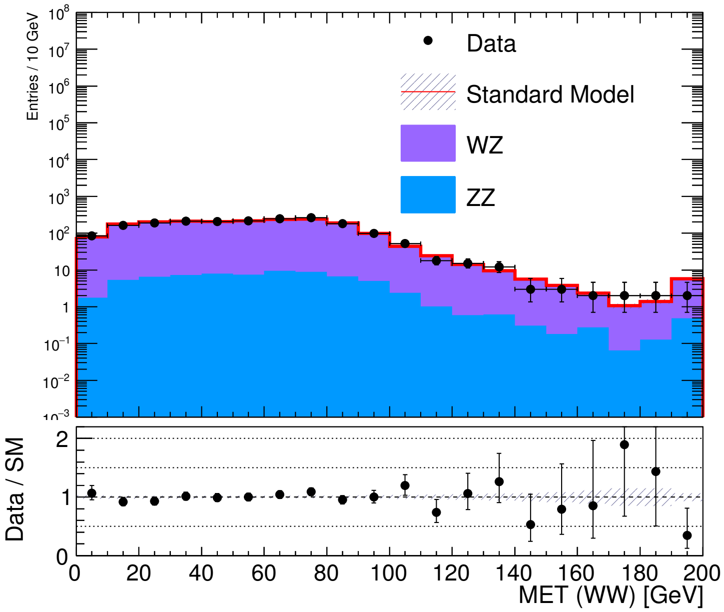

(a) E_{T}^{miss} distribution for the pseudo-2lep selection

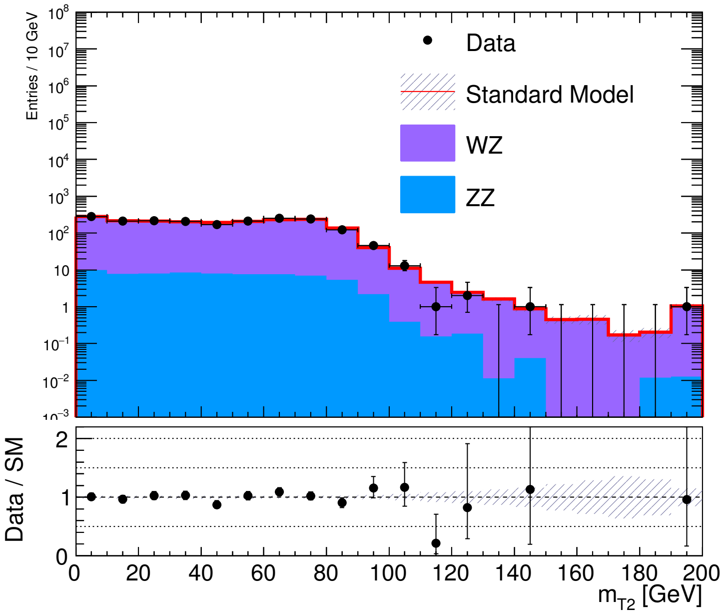

(b) m_{T2} distribution for the pseudo-2lep selection

Figure 7.13: E_{T}^{miss} and m_{T2} distribution for data and the diboson backgrounds, after normalizing the WZ sample in CR-3lep, for the pseudo-2lep selection used for the validation of diboson estimation. The errors shown are statistical only.

7.9 Systematic uncertainties

The theoretical and experimental systematic uncertainties considered in the analysis are now described.

Concerning the experimental systematic effects, all the uncertainties described in Section 5.6 are included in the likelihood fit. The complete fit result will be illustrated in Section 7.10, showing that the dominant experimental uncertainties are the ones coming from energy scale and resolution of the E_{T}^{miss} soft term and of the jets. The m_{T2} distribution obtained using the nominal E_{T}^{miss} soft term and the systematic variations is reported in Figure 7.14, for two main backgrounds, the $t\bar{t}$ and diboson processes. Figure 7.15 shows the comparison between the m_{T2} distribution in the case of the nominal jets resolution and scale, and considering their systematic variations, in the case of the $t\bar{t}$ and diboson MC simulations. The diboson samples show a small variation between the nominal MC simulation and the systematics variation. The difference is larger for the $t\bar{t}$ process, especially in the region with $m_{\mathrm{T2}} > 100$ GeV.

The theoretical uncertainties are now illustrated. Concerning the diboson samples, the following systematic effects are considered:

- *QCD scale*: the factorization and renormalization scale are varied up and down by factors 2.0 and 0.5 with respect to the nominal values used in the MC generation. These uncertainties are evaluated using the same Powheg samples considered as nominal MC. Figure 7.16 reports the m_{T2} distribution for the nominal WW, WZ and ZZ processes and their factorization and renormalization scale variations, after the preliminary selection. The uncertainties are computed at the Truth level and a variation of about the 5% is observed between the nominal samples and the systematics variations;

- *PDF uncertainty*: the PDF CTEQ6L set used for the diboson samples contains multiple different PDFs, one is used as nominal, while the 52 variations are used in the uncertainty computation. The varied PDFs are combined together in order to built the uncertainty band. For each events the PDF variations, compared to the nominal value, are classified as up or down variation. All the up (down) variation are then added in quadrature in order to built the upper (lower) band. The result is shown in Figure 7.17: the m_{T2} distribution for the nominal sample and the PDF uncertainty band are reported for the WW, WZ and ZZ processes, an up and down variation of about 10% is observed.

- *CKKW and resummation scale*: these uncertainties are computed using Sherpa diboson samples, and then they are applied to the Powheg MC simulation used as nominal samples in the search. As illustrated in Section 7.2.3, Powheg MC simulator allows to separate the WW, WZ and ZZ processes, while Sherpa does not. For this reason, Sherpa events with DF leptons are used to compute the uncertainties for the WW process, while events with SF leptons are used for the WZ and ZZ processes. The uncertainty associated to the matching between the matrix elements and parton shower, performed following the CKKW recommendation with a scale of 20 GeV, is computed with variation samples using a matching scale of 15 GeV and

30 GeV. The resummation scale systematic uncertainty is evaluated using samples where the scale is varied by factors 2.0 and 0.5. Figure 7.18 represents the CKKW and resummation systematic variations compared to the nominal sample, in the case of DF and SF leptons events, after performing the preliminary selection.

Theoretical systematic uncertainties for $t\bar{t}$ and Wt are also considered. The nominal $t\bar{t}$ PowhegPythia8 MC sample is compared to a variation sample produced with PowhegHerwig7, in order to account for the systematic effect due to the choice of a specific parton shower. In order to account for the different possible tuning of the initial state and final state radiation, samples with lower and higher amount of radiation are used to compute the associated uncertainty. The comparison between the nominal sample and the variation is shown in Figure 7.19, after performing the preliminary selection.

Concerning the Wt background, the nominal sample is obtained using the diagram removal method to delete the $t\bar{t}$-Wt interference contribution. To account for the systematic effects due to the method, the sample is compared to a Monte Carlo simulation that uses the diagram subtraction technique instead.

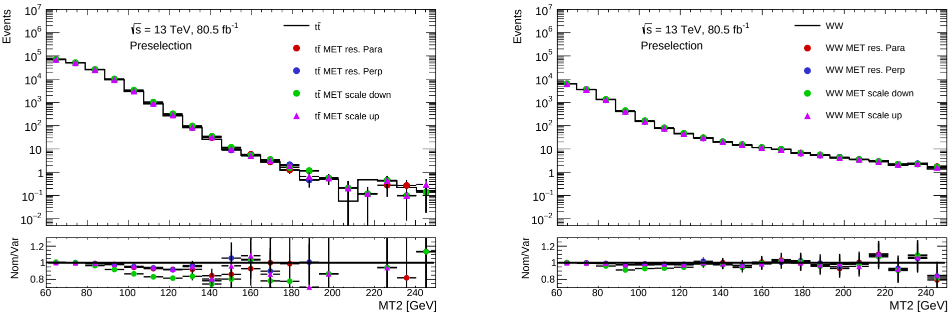

(a) $t\bar{t}$ process (b) WW process

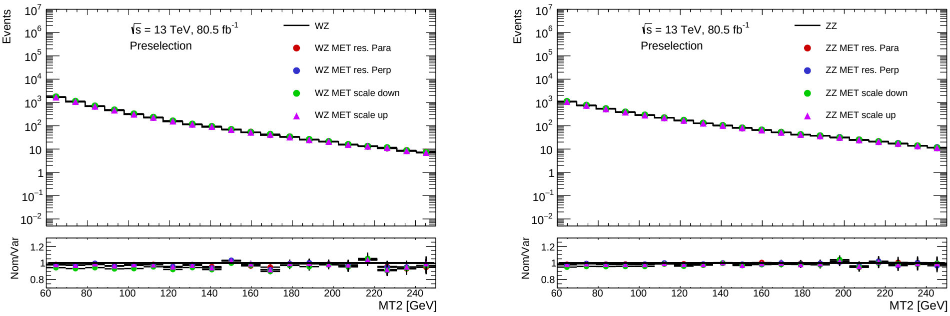

(c) WZ process (d) ZZ process

Figure 7.14: The m_{T2} distribution for the nominal sample and the experimental systematics variation due to the energy resolution and scale of the E_{T}^{miss} soft term, for $t\bar{t}$ (a), WW (b), WZ (c) and ZZ (d) processes. The preliminary selection is considered.

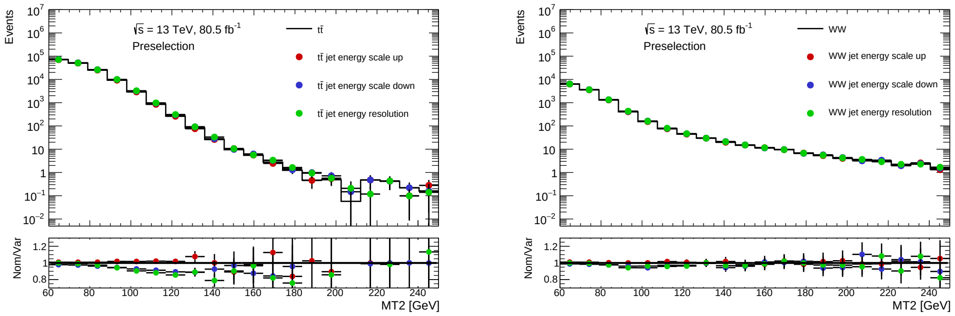

(a) $t\bar{t}$ process (b) WW process

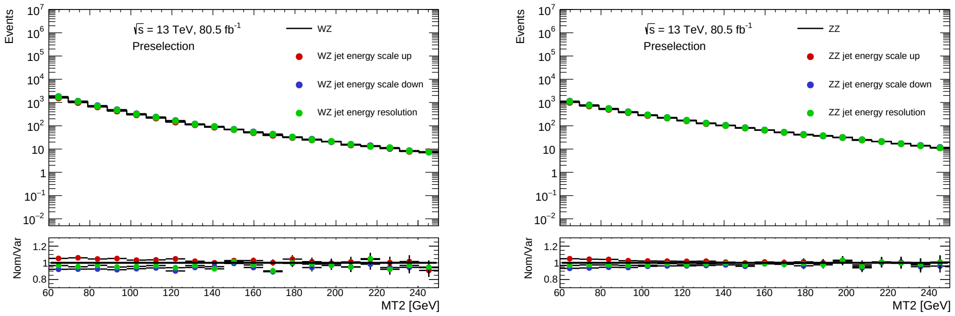

(c) WZ process (d) ZZ process

Figure 7.15: The m_{T2} distribution for the nominal sample and the experimental systematics variation due to the jet energy resolution and scale, for $t\bar{t}$ (a), WW (b), WZ (c) and ZZ (d) processes. The preliminary selection is considered.

7.9.1 Low statistic effects

As already mentioned in Section 5.6.3, the Monte Carlo simulations are produced with a large number of events, in order to have an equivalent integrated luminosity that is larger compared to the luminosity of the data. But in extreme regions of the phase space, such as the signal regions, the Monte Carlo simulation can be affected by low statistic, especially in the case of the binned SRs.

The issue can affect not only the nominal MC samples, but also the systematic variations. The theoretical uncertainties can be computed comparing different MC samples (that can have different statistic), but the systematic variations can also be contained in the nominal samples, implemented as multiple event weights. The low statistic problem is usually stronger in the case where different MC samples are used, since the variation sample can have lower statistic compared to the nominal one. Instead in the case of MC simulations with multiple event weights, the number of events is the same using the nominal weight and using the variations.

In the search illustrated in this Chapter, different variation samples are used in the estimate of the diboson resummation and CKKW systematic effect and the MC simulations present low statistic in regions with large m_{T2} requirement, in particular in the exclusive bins designed for the signal region. The number of events in the exclusive SRs for the nominal samples and the systematic variations, at Truth level, are reported in Table 7.10. The yields are subject to many fluctuations, that are due to the limited number of events and not to physical effects.

In order to have a reliable uncertainties estimation, the diboson resummation and CKKW systematic are evaluated in the signal regions with $m_{\mathrm{T2}} \in [100,\infty]$ GeV instead of the bins. The procedure is justified by the fact that the difference between the nominal samples and the systematic variations lies in the normalization and not in the shape of the kinematic variables. From Figures 7.18 and 7.19, it can be appreciated that the systematic variations do not affect the m_{T2} shape, so using a more inclusive selection based on this kinematic variable is appropriated.

Table 7.11 report the yields for the nominal and the variation samples for the integrated SRs. These numbers are used to compute the uncertainties reported in Table 7.11, applying the formula reported in the Eq. (5.13). The resulting uncertainties, expressed as percentage of the diboson background, are reported in Table 7.12.

As stated in Section 5.6, the input to the likelihood fit for the uncertainties are usually the yields computed for the nominal and the variation samples, but it is also possible to use directly the relative error on a specific background, so the number reported in Table 7.12 can be added to the fit.

A similar procedure is applied in the case of the $t\bar{t}$ uncertainties. In this case the low statistic in the large m_{T2} region is not only due to the limited number of events in the MC simulation, but also to the intrinsic characteristic of the m_{T2} variable. As addressed in Section 5.2, the m_{T2} distribution end-point is limited by the W boson mass, but the long tail of the distribution is due to events with off-shell W boson mass and to the detector resolution. Since the theoretical systematics are estimated using Truth level samples, the m_{T2} tail is significantly shorter. As consequence a low number of events is present in the SRs. Table 7.13 shows the number of events for the $t\bar{t}$ nominal and variation samples, in the exclusive SRs: the yields are zero in the regions with $m_{\mathrm{T2}} > 140$ GeV.

As in the diboson case, the number of events used in the uncertainties estimation is computed in the regions with $m_{\mathrm{T2}} \in [100,\infty]$ GeV instead of the exclusive SRs, obtaining the yields reported in Table 7.13. These number are used to compute the uncertainties, to be applied to the exclusive SRs. The radiation and showering systematics expressed as percentage of the $t\bar{t}$ background are reported in Table 7.15. As discussed in the diboson case, the procedure is suitable since the $t\bar{t}$ nominal sample and its systematic variations have the same m_{T2} shape, as it can be observed from Figure 7.15.

Exclusive signal regions Truth yields for diboson								
SR-DF-0J - $m_{T2} \in$	[100,105]	[105,110]	[110,120]	[120,140]	[140,160]	[160,180]	[180,220]	[220,∞]
Nominal	2.66	1.88	4.38	6.47	3.98	4.04	4.15	3.22
QSF down	1.48	2.14	4.00	4.75	3.52	2.39	2.30	2.56
QSF up	1.00	1.64	2.42	4.55	3.03	3.88	2.40	2.87
CKKW down	1.50	0.54	1.43	4.84	4.45	2.10	1.03	4.38
CKKW up	0.45	1.33	2.28	5.83	3.02	2.56	2.49	2.71
SR-DF-1J - $m_{T2} \in$	[100,105]	[105,110]	[110,120]	[120,140]	[140,160]	[160,180]	[180,220]	[220,∞]
Nominal	0.25	0.58	2.11	2.70	1.83	1.59	2.05	1.68
QSF down	0.43	0.49	2.31	1.39	4.36	2.71	0.59	1.56
QSF up	0.63	0.23	1.77	1.67	1.06	1.32	1.65	2.60
CKKW down	0.44	0.25	1.88	0.82	1.52	1.18	0.58	3.30
CKKW up	-0.04	0.95	1.00	3.46	1.89	1.76	1.89	0.30
SR-SF-0J - $m_{T2} \in$	[100,105]	[105,110]	[110,120]	[120,140]	[140,160]	[160,180]	[180,220]	[220,∞]
Nominal	1.60	1.91	5.26	7.54	5.90	2.46	5.82	5.71
QSF down	0.60	1.09	3.22	4.96	2.68	1.58	3.43	4.96
QSF up	1.40	1.68	4.01	4.27	2.86	0.67	4.12	4.93
CKKW down	1.42	0.68	1.98	3.59	4.09	1.43	2.80	4.94
CKKW up	0.41	0.71	2.86	3.59	4.34	1.05	3.60	3.31
SR-SF-1J - $m_{T2} \in$	[100,105]	[105,110]	[110,120]	[120,140]	[140,160]	[160,180]	[180,220]	[220,∞]
Nominal	0.71	1.40	1.99	4.18	1.39	3.36	2.65	3.43
QSF down	0.79	1.24	1.37	1.92	2.81	2.81	1.33	3.20
QSF up	0.62	1.17	1.01	3.43	2.43	3.95	1.34	2.47
CKKW down	1.24	1.67	1.34	4.40	2.39	3.49	1.56	4.26
CKKW up	0.72	0.79	2.55	1.55	3.47	2.56	2.46	3.56

Table 7.10: Number of events in the exclusive SRs for the nominal samples and the systematic variations for the Sherpa diboson MC samples, at Truth level.

Integrated signal regions Truth yields for diboson				
m_{T2}	SR-DF-0J $\in [100, \infty]$	SR-DF-1J $\in [100, \infty]$	SR-SF-0J $\in [100, \infty]$	SR-SF-1J $\in [100, \infty]$
Nominal	30.77	12.79	37.10	18.20
QSF down	23.13	13.83	23.74	14.22
QSF up	21.78	10.94	27.21	13.14
CKKW down	20.26	9.96	22.10	18.29
CKKW up	20.68	11.20	21.38	16.14

Table 7.11: Number of events in the SRs, considering $m_{T2} > 100$ GeV, for the nominal samples and the systematic variations for the Sherpa diboson MC samples, at Truth level.

Diboson resummation and CKKW unceratinties in SRs				
	SR-DF-0J	SR-DF-1J	SR-SF-0J	SR-SF-1J
m_{T2}	$\in [100, \infty]$	$\in [100, \infty]$	$\in [100, \infty]$	$\in [100, \infty]$
QSF down	-23.0%	-76.8%	+17.3%	-0.9
QSF up	-19.8%	-44.7%	+15.2%	+16.5
CKKW down	-8.1%	-27.7%	+28.5%	-16.0
CKKW up	-15.2%	-50.1%	+30.2%	-7.5

Table 7.12: Resummation and CKKW uncertainties expressed as percentage of the diboson background. The uncertainties are computed using the SRs with integrated m_{T2}.

Exclusive signal regions Truth yields for $t\bar{t}$								
SR-DF-0J - $m_{\mathrm{T2}} \in$	[100,105]	[105,110]	[110,120]	[120,140]	[140,160]	[160,180]	[180,220]	[220,∞]
Nominal	0.14	–	0.21	–	–	–	–	–
Rad. down	0.13	–	0.21	–	–	–	–	–
Rad. up	–	–	0.36	–	–	–	–	–
Showering	0.37	–	–	0.37	–	–	–	–
SR-DF-1J - $m_{\mathrm{T2}} \in$	[100,105]	[105,110]	[110,120]	[120,140]	[140,160]	[160,180]	[180,220]	[220,∞]
Nominal	0.14	0.07	0.14	0.14	–	–	–	–
Rad. down	0.14	0.06	0.14	0.11	–	–	–	–
Rad. up	0.32	–	0.23	0.16	–	–	–	–
Showering	–	–	0.37	–	–	–	–	–
SR-SF-0J - $m_{\mathrm{T2}} \in$	[100,105]	[105,110]	[110,120]	[120,140]	[140,160]	[160,180]	[180,220]	[220,∞]
Nominal	0.14	0.07	0.14	0.07	–	–	–	–
Rad. down	0.11	0.05	0.13	0.11	–	–	–	–
Rad. up	0.20	0.11	0.16	–	–	–	–	–
Showering	–	–	0.37	–	–	–	–	–
SR-SF-1J - $m_{\mathrm{T2}} \in$	[100,105]	[105,110]	[110,120]	[120,140]	[140,160]	[160,180]	[180,220]	[220,∞]
Nominal	0.07	0.07	0.36	0.07	–	–	–	–
Rad. down	0.08	0.07	0.33	0.05	–	–	–	–
Rad. up	–	0.24	–	0.09	–	–	–	–
Showering	0.37	–	0.37	–	–	–	–	–

Table 7.13: Number of events in the exclusive SRs for the nominal samples and the systematic variations for the $t\bar{t}$ MC simulation, at Truth level. The "-" indicates that the yield is zero.

Integrated signal regions Truth yields for $t\bar{t}$				
m_{T2}	SR-DF-0J $\in [100, \infty]$	SR-DF-1J $\in [100, \infty]$	SR-SF-0J $\in [100, \infty]$	SR-SF-1J $\in [100, \infty]$
Nominal	0.36	0.50	0.43	0.57
Radiation down	0.34	0.44	0.39	0.54
Radiation up	0.36	0.71	0.46	0.34
Showering	0.74	0.37	0.37	0.74

Table 7.14: Number of events in the SRs, considering $m_{\mathrm{T2}} > 100$ GeV, for the nominal samples and the systematic variations for the $t\bar{t}$ simulation, at Truth level.

$t\bar{t}$ unceratinties in SRs				
m_{T2}	SR-DF-0J $\in [100, \infty]$	SR-DF-1J $\in [100, \infty]$	SR-SF-0J $\in [100, \infty]$	SR-SF-1J $\in [100, \infty]$
Radiation down	-6.3%	+0.1%	-3.0%	-5.8%
Radiation up	+9.7%	-27.3%	+2.8%	+47.6%
Showering	+87.9%	+32.8%	+21.7%	-17.3%

Table 7.15: Radiation and showering uncertainties expressed as percentage of the $t\bar{t}$ background. The uncertainties are computed using the SRs with integrated m_{T2}.

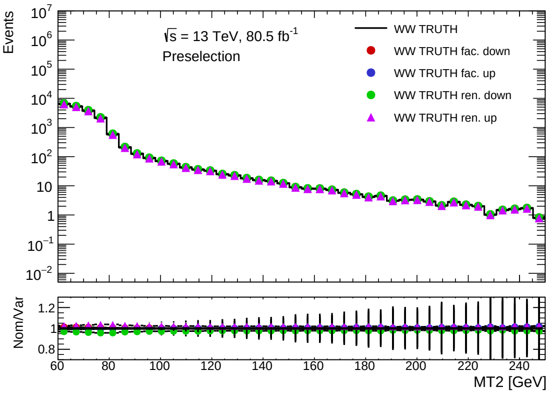

(a) WW process, preliminary selection

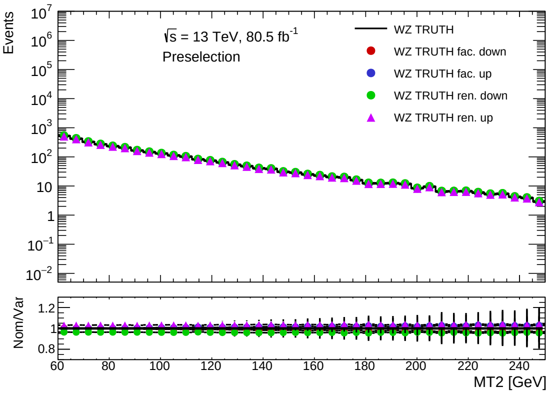

(b) WZ process, preliminary selection

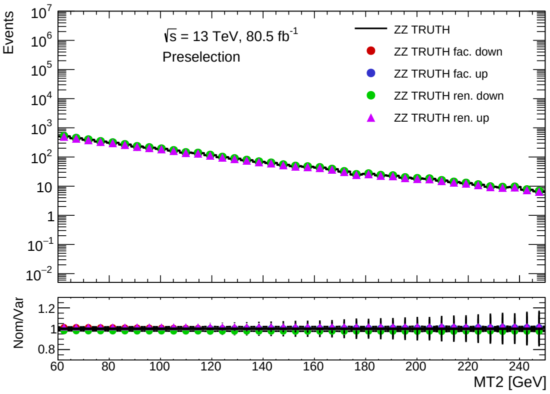

(c) ZZ process, preliminary selection

Figure 7.16: The m_{T2} distribution for the nominal WW, WZ and WW samples and the factorization and renormalization scale systematics variation, at the Truth level. The preliminary selection is considered.

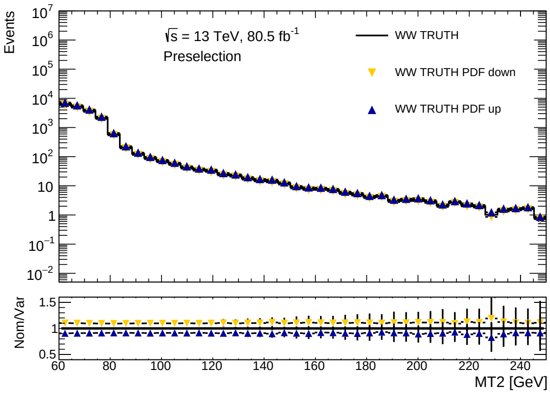

(a) WW process, preliminary selection

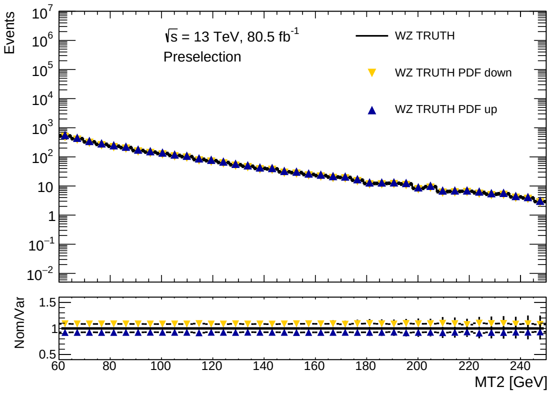

(b) WZ process, preliminary selection

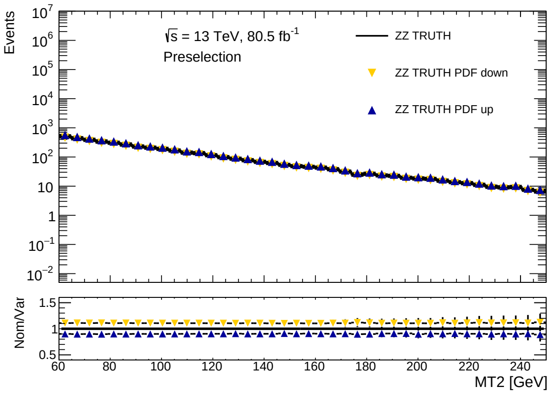

(c) ZZ process, preliminary selection

Figure 7.17: The m_{T2} distribution for the nominal WW, WZ and WW samples and the PDF systematics variation band, at the Truth level. The preliminary selection is considered.

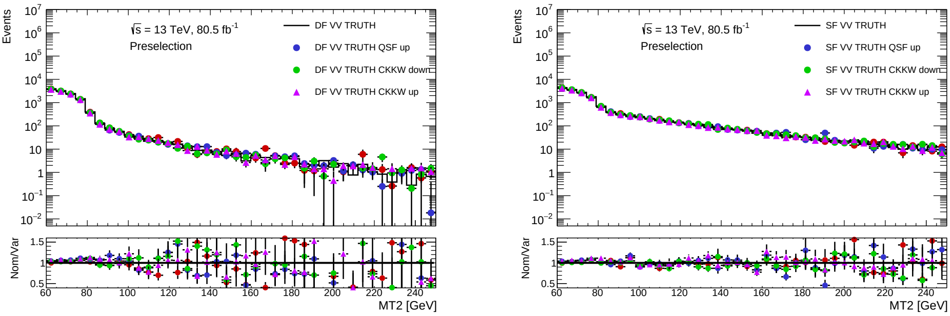

(a) DF diboson, preliminary selection

(b) SF diboson, preliminary selection

Figure 7.18: The m_{T2} distribution for the nominal Sherpa diboson samples and the theoretical systematics variation, for events with DF leptons (a) or SF leptons (b), at the Truth level. The preliminary selection is considered.

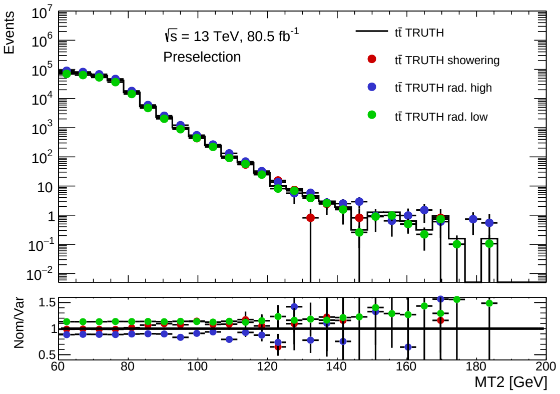

Figure 7.19: The m_{T2} distribution for the nominal $t\bar{t}$ sample and the theoretical systematics variation, at the Truth level. The preliminary selection is considered.

7.10 Result and interpretation

This Section reports the result obtained for the search of the direct production of chargino pair with W boson mediated decay. As in the analysis illustrated in the previous Chapter, three likelihood fits are performed, following the definition reported in Section 5.7.4. Section 7.10.1 illustrated the background-only fit, Section 7.10.2 reports the model-dependent fit result with the exclusion limit, finally Section 7.10.3 is dedicated to the model-independent fit and the upper limits.

7.10.1 Background-only likelihood fit

The result of the background-only likelihood fit, used to estimate the total SM background in the SRs, is now reported. The fit is performed normalizing the MC simulation for diboson and $t\bar{t}$ to the data in the CRs, as described in Section 5.7.4, without any assumption on the signal model. Three normalization factors are used: one for the WW process, one for WZ and ZZ samples, and one for the $t\bar{t}$. The factors obtained from the fit are:

- $\mu_{NF}^{\mathrm{WW}} = 1.36 \pm 0.11$
- $\mu_{NF}^{\mathrm{VZ}} = 1.26 \pm 0.06$
- $\mu_{NF}^{t\bar{t}} = 1.07 \pm 0.17$

The factors are then transfered to the VRs and SRs.

The yields of the observed data in the CRs, compared to the total Standard Model background prediction, are shown in Table 7.16. The numbers are obtained from the background-only likelihood fit and all the systematic and statistical uncertainties are included. The breakdown of the SM background composition, after applying the MC normalization factors, is reported. The lower part of the Table reports the expected yields for three signal samples and the contamination in the region expressed as percentage of the total SM expected background. Signals with $m(\tilde{\chi}_1^{\pm}, \tilde{\chi}_1^0) =$ (200,1) GeV, $m(\tilde{\chi}_1^{\pm}, \tilde{\chi}_1^0) =$ (250,1) GeV and $m(\tilde{\chi}_1^{\pm}, \tilde{\chi}_1^0) =$ (300,1) GeV are considered. The signal contamination is very small in all the cases, the maximum being of the 2%.

The yields obtained in the VRs after applying the normalization factors and including all the uncertainties are shown in Table 7.17. Comparing the observed data to the SM expected background, it can be observed that the data are compatible with the prediction within the uncertainties. The signal contaminations for different signal hypothesis are reported in the second part of the Table, they are generally negligible and the maximum contamination is of the 3%.

The comparison between the observed data and the expected SM events in the inclusive SRs is reported in Tables 7.18, 7.19, 7.20 and 7.21, for the regions DF-0J, DF-1J, SF-0J and SF-1J respectively. In order to quantify the excess of the data compared to the SM prediction, the statistical significance is reported in the last row of each Table. The significance is set to zero in case of observed data less then the SM prediction.

Considering Table 7.18, it can be observed that the WW process is the dominant background in the DF-0J selection and that the data are well modeled by the SM prediction. In the case of the DF-1J selection (Table 7.19), the $t\bar{t}$ process also gives a significant contribution to the SM background. The data are in good agreement with the SM prediction, the only region showing a small excess (0.74σ) being SR-DF-1J with $m_{\mathrm{T2}} \in$ [120,160] GeV.

The SRs using the zero non-b-tagged jets and SF leptons selection are illustrated in Table 7.20, the background is dominated by the WW, ZZ and $t\bar{t}$ events. An excess of 1.64σ is present in the region with $m_{\mathrm{T2}} \in$ [100,160] GeV. In the SF-1J case, reported in Table 7.21, the $t\bar{t}$ contribution is larger and the data are well modelled by the SM background prediction.

Despite the 1.64σ excess in SR-SF-0J $m_{\mathrm{T2}} \in$ [100,160] GeV and other minor excesses, the fluctuations are not significant enough to claim the evidence of any new physics phenomena.

Table 7.22 illustrates the composition of the uncertainties in the SRs. Only the inclusive SRs case with $m_{\mathrm{T2}} \in [100,\infty]$ GeV is presented, since the other regions are a sub-selection of this one. The first row of the Table shows the expected SM background, followed by the total systematic uncertainty in the regions, expressed as per cents of the total SM expectation. The uncertainty values range from 7.4 to 11.8%.

A significant source of systematic effects for all the regions are the MC statistic and the uncertainties on MC normalization factor, in particular from the WW and $t\bar{t}$ processes. Another important component is given by the theoretical systematics, that can reach the 10%: diboson are dominated by the resummation and CKKW variation uncertainties, while in the $t\bar{t}$ case the parton showering gives the larger contribution. The experimental sources of uncertainties are then reported and errors of few percentage come from the E_{T}^{miss} modelling, the pile-up reweighting procedure and the leptons modelling. The uncertainties associated to the jet energy resolution and scale and to the b-tagging efficiency are mainly due to the $t\bar{t}$ background and for this reason they are larger in the regions with the one non-b-tagged jets selection, where the $t\bar{t}$ events are an important component. The last contribution to the uncertainty is the systematic effects associated to the evaluation of the fake and non-prompt leptons evaluated with the Matrix Method. As it can be observed by the last row of Table 7.22, this contribution is almost negligible.

Concerning the exclusive signal regions, the result of the background-only fit is summarized in Figure 7.20, that reports the comparison between the observed data and the expected SM background. Each bin of the histogram corresponds to one of the inclusive SRs, with the m_{T2} selection reported on the x axis, and all the sources of uncertainties are considered. In the lower pad of the Figure, the significance of the observed fluctuation is shown. The significance is set to zero for the regions where the data are less than the expected background. Few regions show excesses between 1σ and 2σ, but in general a good agreement between the data and the SM prediction is observed and none of the excesses is significant enough to claim for the presence of new phenomena.

Control regions yields			
	CR-VZ	CR-WW	CR-top
Observed events	487	1480	99
Total SM	486 ± 22	1480 ± 40	99 ± 10
WW	11.3 ± 1.6	1020 ± 80	3.5 ± 1.9
WZ	114 ± 6	21.6 ± 1.8	0.23 ± 0.09
ZZ	353 ± 17	0.8 ± 0.1	–
$t\bar{t}$	$1.2^{+1.3}_{-1.2}$	270 ± 50	81 ± 9
Single top	–	144 ± 23	9.2 ± 1.8
FNP	–	22.0 ± 2.5	3.34 ± 0.32
Other	7.4 ± 3.4	1.4 ± 1.1	1.28 ± 0.15
$m(\tilde{\chi}_1^{\pm}, \tilde{\chi}_1^0)$ = (200,1) GeV	8.5 [2%]	13 [0.9%]	1.5 [2%]
$m(\tilde{\chi}_1^{\pm}, \tilde{\chi}_1^0)$ = (250,1) GeV	7.6 [2%]	4.6 [0.3%]	1.7 [2%]
$m(\tilde{\chi}_1^{\pm}, \tilde{\chi}_1^0)$ = (300,1) GeV	4.1 [0.8%]	1.6 [0.1%]	0.9 [1%]

Table 7.16: Background-only likelihood fit results for the control regions, including all the systematic and statistical uncertainties. The MC normalization factors extracted from the control regions are applied to the yields of the MC simulations, for $t\bar{t}$ and diboson processes. The second part of the Table shows the number of expected signal events from different samples and the signal contamination, expressed as percentage of the total SM background in the region. The uncertainties can be correlated and do not necessarily add up quadratically to the total SM uncertainty.

7.10.2 Model-dependent fit and exclusion limits

As observed from the background-only fit result, no significant excesses are present in the SRs considered in the search. The model-dependent likelihood fit can be used to compute the exclusion limits on the masses of the SUSY particles considered in the model.

The fit is performed as described in Section 5.7.4. The observed data in the CRs and SRs are used as constrain and the signal strength μ_{sig} is set to one, both for the CRs and SRs. The CL_s value (defined in Section 5.7.3) is computed for each sample, with specific mass parameters, of the signal grid. The signal points with $CL_s < 0.05$ are excluded at the 95% CL and an exclusion contour in the mass parameter space is built.

Applying the strategy illustrated in Section 5.7.6, the exclusive SRs defined in Section 7.6.2 are optimized to maximize the extension of the exclusion limits and therefore they are the only SRs used in the model-dependent fit.

Figure 7.21 shows the exclusion contours obtained in the search, represented in the chargino-neutralino masses plane. The usual graphic conventions, common to all the ATLAS results, are followed. The observed exclusion limit containing all the uncertainties (except the SUSY cross sections) is reported with a red continuous line, while the SUSY signal cross sections uncertainties are considered only for the limits represented with the red dotted lines. The contour computed with the expected SM prediction is shown with

Validation regions yields

	VR-WW-0J	VR-WW-1J	VR-VZ
Observed events	3873	3509	265
Total SM	3970 ± 170	4000 ± 700	260 ± 21
WW	2210 ± 190	1360 ± 150	11.0 ± 1.3
WZ	49 ± 4	36 ± 4	61 ± 5
ZZ	2.97 ± 0.28	1.28 ± 0.21	161 ± 14
$t\bar{t}$	1076 ± 200	2000 ± 600	6 ± 4
Single top	570 ± 100	640 ± 160	1.7 ± 1.3
FNP	47 ± 6	36 ± 6	–
Other	9 ± 3	5 ± 2	17.7 ± 6.6
$m(\tilde{\chi}_1^{\pm}, \tilde{\chi}_1^0)$ = (200,1) GeV	67 [2%]	34 [1%]	8.0 [3%]
$m(\tilde{\chi}_1^{\pm}, \tilde{\chi}_1^0)$ = (250,1) GeV	30 [0.8%]	17 [0.4%]	2.9 [1%]
$m(\tilde{\chi}_1^{\pm}, \tilde{\chi}_1^0)$ = (300,1) GeV	15 [0.4%]	9.1 [0.2%]	1.9 [0.7%]

	VR-top-low	VR-top-high
Observed events	526	121
Total SM	620 ± 100	143 ± 29
WW	6 ± 5	$2.9^{+3.0}_{-2.9}$
WZ	0.17 ± 0.13	$0.18^{+0.22}_{-0.18}$
ZZ	–	–
$t\bar{t}$	520 ± 90	118 ± 26
Single top	87 ± 13	11.5 ± 2.9
FNP	6.9 ± 0.7	5.8 ± 0.5
Other	–	3.4 ± 0.4
$m(\tilde{\chi}_1^{\pm}, \tilde{\chi}_1^0)$ = (200,1) GeV	–	0.80 [0.6%]
$m(\tilde{\chi}_1^{\pm}, \tilde{\chi}_1^0)$ = (250,1) GeV	0.33 [0.05%]	0.76 [0.5%]
$m(\tilde{\chi}_1^{\pm}, \tilde{\chi}_1^0)$ = (300,1) GeV	0.14 [0.02%]	0.47 [0.3%]

Table 7.17: Background-only likelihood fit results for the validation regions, including all the systematic and statistical uncertainties. The MC normalization factors extracted from the control regions are applied to the yields of the MC simulations, for $t\bar{t}$ and diboson processes. The second part of the Table shows the number of expected signal events from different samples and the signal contamination, expressed as percentage of the total SM background in the region. The uncertainties can be correlated and do not necessarily add up quadratically to the total SM uncertainty.

a blue dashed line, with the yellow band corresponding to its $\pm 1\sigma$ variation.

The chargino with a mass up to 410 GeV is excluded at 95% CL in the case of a neutralino with a 1 GeV mass. The limit also covers a large mass range for the neutralino: for a 300 GeV chargino, the neutralino is excluded up to 120 GeV. The observed limit

Inclusive signal regions yields - DF 0J				
Region	SR-DF-0J $[100, \infty]$	SR-DF-0J $[160, \infty]$	SR-DF-0J $[100, 120]$	SR-DF-0J $[120, 160]$
Observed events	84	15	49	20
Total SM	100.8 ± 11.9	16.1 ± 2.0	53.4 ± 9.0	31.5 ± 3.5
WW	70.7 ± 7.5	14.8 ± 1.9	30.3 ± 3.5	25.6 ± 3.0
WZ	2.02 ± 0.25	0.47 ± 0.07	0.98 ± 0.21	0.58 ± 0.10
ZZ	0.66 ± 0.08	0.17 ± 0.04	$0.25^{+0.25}_{-0.25}$	0.23 ± 0.04
$t\bar{t}$	19.6 ± 9.3	–	16.6 ± 7.9	3.1 ± 1.5
Single top	4.8 ± 2.6	–	4.8 ± 2.6	$0.00^{+0.14}_{-0.00}$
FNP	2.19 ± 0.33	0.53 ± 0.15	$0.00^{+0.05}_{-0.00}$	1.75 ± 0.17
Other	0.81 ± 0.18	0.05 ± 0.01	0.47 ± 0.17	0.28 ± 0.07
Significance	–	–	–	–

Table 7.18: Background-only likelihood fit results for the inclusive signal regions defined using zero non-b-tagged jets and DF leptons, including all the systematic and statistical uncertainties. The MC normalization factors extracted from the control regions are applied to the yields of the MC simulations, for $t\bar{t}$ and diboson processes. The row of the Table shows the significance of the data fluctuation compared to the SM prediction. The uncertainties can be correlated and do not necessarily add up quadratically to the total SM uncertainty.

performs better than the expected one in the region with a chargino mass between 370 and 410 GeV. This is due to the fact that, the regions with large m_{T2} are the ones providing the best signal over background discrimination for large chargino masses. As it can be observed from Figure 7.20, in some of the bins with a large m_{T2} selection the data are under-fluctuating compared to the background, giving an observed exclusion limit that performs better than the expected one.

The result of the search performed by the ATLAS Collaboration at the LHC Run 1 for the same signal model is reported in the plot as a gray area. A large improvement of exclusion limits was obtained compared to the Run 1 result.

7.10.3 Model-independent fit and upper limits

The result of the model-independent upper limits are now illustrated. The fit configuration is described in Section 5.7.4: the observed data in the CRs and SRs are used as constrain, no signal contamination is considered in the CRs and a dummy signal sample is injected in the SR (the number of expected signal events is set to one). The inclusive signal regions, optimized for the signal discovery, are considered and the likelihood fit is repeated for each SR.

The result for each region is shown in Table 7.23. The number of observed data (N_{obs}) and the expected SM background (N_{exp}), as estimated in the background-only likelihood fit, are reported. The upper limits on the visible cross section ($\langle\epsilon\sigma\rangle^{95}_{\mathrm{obs}}$), the observed

Inclusive signal regions yields - DF 1J				
Region	SR-DF-1J $[100, \infty]$	SR-DF-1J $[160, \infty]$	SR-DF-1J $[100, 120]$	SR-DF-1J $[120, 160]$
Observed events	73	9	39	25
Total SM	83.5 ± 14.6	12.2 ± 2.5	50.6 ± 10.7	21.2 ± 4.0
WW	45 ± 10	9.8 ± 2.3	19.6 ± 4.8	15.2 ± 3.5
WZ	1.83 ± 0.45	0.50 ± 0.15	0.77 ± 0.24	0.56 ± 0.17
ZZ	0.60 ± 0.15	0.29 ± 0.09	0.14 ± 0.04	0.17 ± 0.05
$t\bar{t}$	25.2 ± 8.4	–	21.4 ± 7.3	3.8 ± 1.6
Single top	7.4 ± 4.1	–	6.6 ± 3.7	0.78 ± 0.46
FNP	2.77 ± 0.27	1.48 ± 0.20	1.90 ± 0.16	$0.00^{+0.01}_{-0.00}$
Other	1.11 ± 0.18	0.15 ± 0.04	0.21 ± 0.07	0.75 ± 0.10
Significance	–	–	–	0.74

Table 7.19: Background-only likelihood fit results for the inclusive signal regions defined using one non-b-tagged jets and DF leptons, including all the systematic and statistical uncertainties. The MC normalization factors extracted from the control regions are applied to the yields of the MC simulations, for $t\bar{t}$ and diboson processes. The row of the Table shows the significance of the data fluctuation compared to the SM prediction. The uncertainties can be correlated and do not necessarily add up quadratically to the total SM uncertainty.

(S^{95}_{obs}) and expected (S^{95}_{exp}) upper limits on the number of possible signal events in the SR, at 95% CL, are then showed.

In the last two columns the p-value and the significance, computed assuming the null hypothesis of background-only events, are reported. In the regions where the number of observed events is less then the SM prediction, the p-value is set to 0.5 and the significance to zero.

Inclusive signal regions yields - SF 0J				
Region	SR-SF-0J $[100, \infty]$	SR-SF-0J $[160, \infty]$	SR-SF-0J $[100, 120]$	SR-SF-0J $[120, 160]$
Observed events	131	31	65	35
Total SM	119.67 ± 9.0	27.1 ± 2.7	50.9 ± 5.7	42.3 ± 3.4
WW	53.2 ± 7.7	12.0 ± 2.0	21.0 ± 3.3	20.3 ± 2.9
WZ	11.09 ± 0.74	2.72 ± 0.26	3.75 ± 0.44	4.62 ± 0.35
ZZ	35.1 ± 2.4	11.6 ± 1.0	10.2 ± 1.0	13.28 ± 0.95
$t\bar{t}$	13.9 ± 3.2	$0.02^{+0.04}_{-0.02}$	12.3 ± 2.9	1.61 ± 0.66
Single top	3.7 ± 2.2	–	3.7 ± 2.2	$0.00^{+0.15}_{-0.00}$
FNP	2.03 ± 0.21	0.82 ± 0.11	$0.00^{+0.01}_{-0.00}$	1.51 ± 0.12
Other	$0.6^{+1.7}_{-0.6}$	$0.00^{+0.30}_{-0.00}$	$0.00^{+1.5}_{-0.00}$	1.02 ± 0.19
Significance	0.95	0.74	1.64	–

Table 7.20: Background-only likelihood fit results for the inclusive signal regions defined using zero non-b-tagged jets and SF leptons, including all the systematic and statistical uncertainties. The MC normalization factors extracted from the control regions are applied to the yields of the MC simulations, for $t\bar{t}$ and diboson processes. The row of the Table shows the significance of the data fluctuation compared to the SM prediction. The uncertainties can be correlated and do not necessarily add up quadratically to the total SM uncertainty.

Inclusive signal regions yields - SF 1J				
Region	SR-SF-1J $[100, \infty]$	SR-SF-1J $[160, \infty]$	SR-SF-1J $[100, 120]$	SR-SF-1J $[120, 160]$
Observed events	114	23	56	35
Total SM	114 ± 13	29 ± 5	51.7 ± 10.0	33 ± 4
WW	36 ± 5	8.6 ± 1.7	14.6 ± 2.4	12.6 ± 1.9
WZ	12.2 ± 1.7	4.38 ± 0.80	3.28 ± 0.47	4.59 ± 0.75
ZZ	21.8 ± 3.0	8.1 ± 1.5	5.43 ± 0.95	8.3 ± 1.3
$t\bar{t}$	20.0 ± 7.5	$0.15^{+0.17}_{-0.15}$	19 ± 7	0.99 ± 0.95
Single top	5.4 ± 3.5	–	4.9 ± 3.2	0.59 ± 0.41
FNP	10.44 ± 0.83	4.58 ± 0.68	1.79 ± 0.16	4.07 ± 0.45
Other	8.0 ± 2.7	2.8 ± 1.5	2.9 ± 1.8	2.34 ± 0.89
Significance	0.08	–	0.39	0.28

Table 7.21: Background-only likelihood fit results for the inclusive signal regions defined using one non-b-tagged jets and SF leptons, including all the systematic and statistical uncertainties. The MC normalization factors extracted from the control regions are applied to the yields of the MC simulations, for $t\bar{t}$ and diboson processes. The row of the Table shows the significance of the data fluctuation compared to the SM prediction. The uncertainties can be correlated and do not necessarily add up quadratically to the total SM uncertainty.

Systematic uncertainties in the inclusive signal regions				
m_{T2}	SR-DF-0J $\in [100, \infty]$	SR-DF-1J $\in [100, \infty]$	SR-SF-0J $\in [100, \infty]$	SR-SF-1J $\in [100, \infty]$
Total background expectation	101	83	120	113
Total background systematic	11.8%	17.7%	7.4%	11.0%
MC statistical uncertainties	4%	5%	4%	5%
WW normalization	6%	5%	4%	3%
VZ normalization	$< 1\%$	$< 1\%$	2%	2%
$t\bar{t}$ normalization	4%	6%	2%	4%
Diboson theoretical uncertainties	3%	10%	5%	4%
Top theoretical uncertainties	9%	8%	2%	5%
E_{T}^{miss} soft term modelling	2%	2%	2%	2%
Jet energy scale	1%	8%	1%	5%
Jet energy resolution	1%	4%	1%	3%
Pile-up reweighting	1%	1%	1%	2%
b-tagging	$< 1\%$	6%	$< 1\%$	4%
Lepton modelling	1%	$< 1\%$	$< 1\%$	1%
FNP	$< 1\%$	$< 1\%$	$< 1\%$	$< 1\%$

Table 7.22: Considering the inclusive signal regions with DF leptons, the expected background and the total systematic uncertainties are reported. The breakdown of the dominant systematic uncertainties is shown in the second part of the Table, expressed as the percentages relative to the total expected background. The uncertainties can be correlated and do not necessarily add up quadratically to the total background uncertainty.

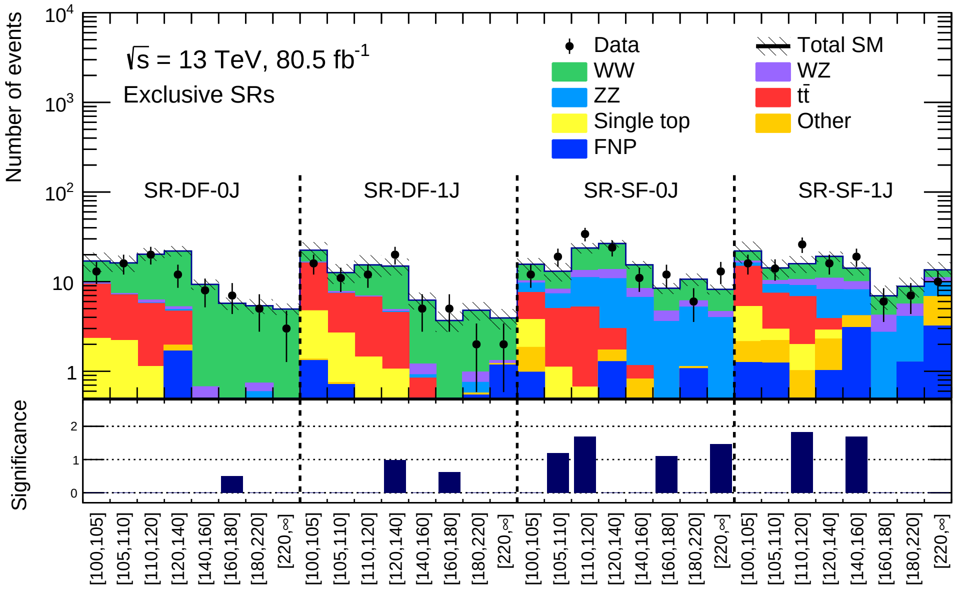

Figure 7.20: Summary of the exclusive SRs considered in the search. Each bin in the plot represents one SR, after performing the background-only likelihood fit. The uncertainty bands include all systematic and statistical contributions. The lower pad reports the significance of the fluctuation observed, that is set to zero in case of an under-fluctuation of the data compared to the SM prediction.

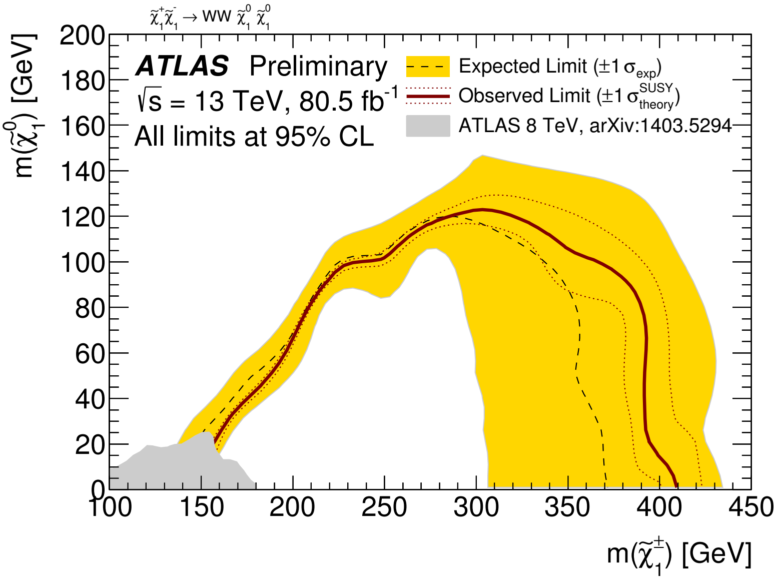

Figure 7.21: Exclusion limits at the 95% confidence level in the chargino-neutralino masses plane for the chargino pair production with W boson mediated decay model. The blue dashed line represents the expected exclusion limit, with the yellow band corresponding to the $\pm1\sigma$ variation due to all the uncertainties sources except the one on the the signal cross-section. The red line correspond to the observed exclusion limit, with a $\pm1\sigma$ variation due to the signal cross-section uncertainty (red dotted lines). The observed limits obtained from ATLAS in the Run 1 search (discussed in Section 7.1) are also shown.

Model independent limits

Signal region		N_{obs}	N_{exp}	$\langle\epsilon\sigma\rangle^{95}_{\text{obs}}$[fb]	S^{95}_{obs}	S^{95}_{exp}	p-value	Z
SR-DF-0J								
$m_{\text{T2}} \in$	$[100, \infty]$	84	100.8 ± 11.9	0.29	23.1	$33.1^{+11.1}_{-8.7}$	0.5	0
	$[160, \infty]$	15	16.1 ± 2.0	0.12	9.2	$9.7^{+4.0}_{-2.8}$	0.48	0.05
	$[100, 120]$	49	53.4 ± 9.0	0.26	20.9	$23.4^{+9.1}_{-6.4}$	0.5	0
	$[120, 160]$	20	31.5 ± 3.5	0.09	7.4	$13.6^{+5.1}_{-3.7}$	0.5	0
SR-DF-1J								
$m_{\text{T2}} \in$	$[100, \infty]$	73	83.5 ± 14.6	0.30	24.0	$29.2^{+11.5}_{-8.0}$	0.5	0
	$[160, \infty]$	9	12.2 ± 2.5	0.09	6.8	$8.4^{+4.2}_{-2.6}$	0.5	0
	$[100, 120]$	39	50.6 ± 10.7	0.22	17.8	$25.8^{+9.3}_{-8.3}$	0.5	0
	$[120, 160]$	25	21.2 ± 4.0	0.18	14.4	$13.4^{+4.3}_{-2.1}$	0.23	0.74
SR-SF-0J								
$m_{\text{T2}} \in$	$[100, \infty]$	131	119.67 ± 9.0	0.52	42.0	$31.1^{+12.5}_{-8.1}$	0.17	0.95
	$[160, \infty]$	31	27.1 ± 2.7	0.21	16.4	$14.7^{+4.0}_{-5.4}$	0.23	0.74
	$[100, 120]$	65	50.9 ± 5.7	0.43	34.2	$22.0^{+6.6}_{-8.0}$	0.05	1.6
	$[120, 160]$	35	42.3 ± 3.4	0.14	11.5	$15.8^{+5.8}_{-4.1}$	0.5	0
SR-SF-1J								
$m_{\text{T2}} \in$	$[100, \infty]$	114	114 ± 13	0.40	32.3	$30.9^{+13.2}_{-7.4}$	0.47	0.08
	$[160, \infty]$	23	29 ± 5	0.15	11.6	$14.1^{+5.9}_{-3.2}$	0.50	0
	$[100, 120]$	56	51.7 ± 10.0	0.36	29.0	$27.5^{+9.1}_{-8.3}$	0.35	0.39
	$[120, 160]$	35	33 ± 4	0.23	18.4	$17.2^{+3.5}_{-6.9}$	0.39	0.28

Table 7.23: Summary of results obtained from the model-independent likelihood fit in the inclusive SRs. The observed number of events (N_{obs}) and expected SM background (N_{exp}) in the SRs are reported. Signal model-independent upper limits at 95% confidence level on the the visible signal cross-section ($\langle\epsilon\sigma\rangle^{95}_{\text{obs}}$) is then shown. S^{95}_{obs} and S^{95}_{exp} are respectively the observed and expected upper limit on the number of beyond the SM events, where the $\pm 1\sigma$ variations on the expected limit originate from the statistical and systematic uncertainties in the background prediction. The p-value and the corresponding significance for the background-only hypothesis are reported in the last two columns. In the region where the observed data are less then the SM background prediction the p-value is truncated at 0.5 and the significance is set to 0.

7.11 Comparison with the CMS Collaboration result

The result obtained by the CMS Collaboration [9] in the case of chargino pair production with W boson mediated decay [153] is reported in this Section. The analysis uses the CMS data collected between 2015 and 2016, with a total amount of 35.9 fb^{-1}. It is not possible to have a direct comparison with the ATLAS result, since in the ATLAS search described in this manuscript also the 2017 data were included.

The analysis strategy used is the same illustrated in Section 6.11 for the chargino pair with sleptons mediated decay search. The sensitivity of the analysis to the chargino pair with W boson mediated decay is limited. Only the case with neutralino mass equal to 1 GeV is considered. The expected and observed upper limits on the chargino pair production cross section, as a function of the chargino mass, are reported in Figure 7.22, and compared to theoretical cross sections.

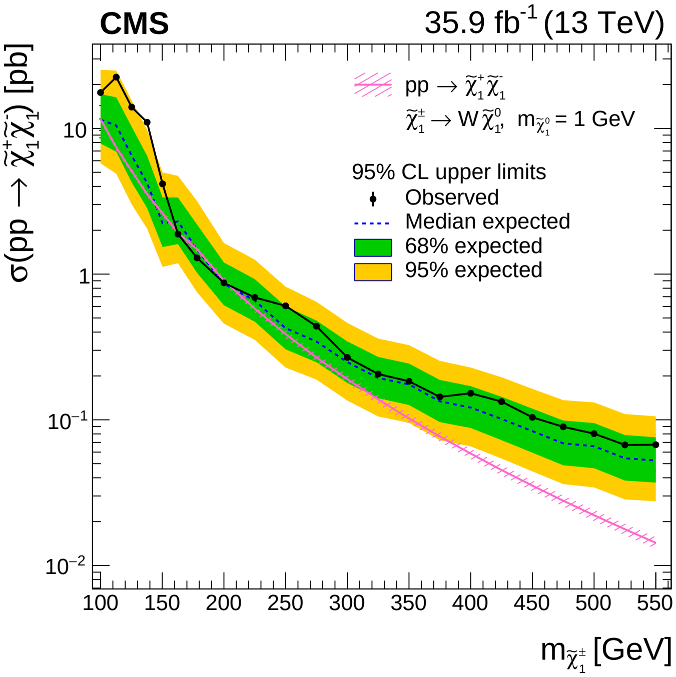

Figure 7.22: Observed and expected upper limits on the chargino pair production cross section at 95% CL, considering a neutralino mass equal to 1 GeV, obtained by the CMS Collaboration using 35.9 fb^{-1} of LHC Run 2 data. [153]

Conclusion

This Thesis presents two closely related searches for the electroweak production of Supersymmetric particles, that use the proton-proton collision data collected by the ATLAS experiment at the LHC Run2. The searches presented in this manuscript consider the same signature, a final state with two leptons (electrons or muons) and missing transverse energy. As consequence similar analysis strategies are developed.

The first search is presented in Chapter 6. The SUSY models considered are the slepton pair production, decaying in charged leptons and neutralinos, and the chargino pair production with sleptons mediated decay, with the slepton decaying in lepton and neutralino. The data collected by ATLAS between 2015 and 2016 are used, with an integrated luminosity of 36.1 fb^{-1}. Inclusive signal regions defined to optimize the discovery probability and orthogonal regions optimized to maximize the exclusion limits are both exploited in the search. The regions are defined using the leptons invariant mass and the stransverse mass m_{T2}. The background is dominated by the $t\bar{t}$ and diboson processes, both estimated with Monte Carlo simulation normalized to data in dedicated control regions.

In the inclusive signal regions, no significant excess above the Standard Model prediction is present, the largest fluctuation being of 1.5σ. Tight exclusion limits, computed using the orthogonal signal regions, are placed on the free parameters of the models. Concerning the slepton pair production, in the case of a massless neutralino a slepton with a mass up to 500 GeV is excluded at 95% CL. The neutralino is excluded up to 300 GeV in the case of a slepton with mass equal to 500 GeV. In the case of the chargino pair production with slepton mediated decay, the upper limit on the chargino mass is 720 GeV, considering a massless neutralino. The neutralino is excluded up to 350 GeV in the case of a chargino with mass equal to 650 GeV.

The search presented in Chapter 7 seeks the observation of the chargino pair production decaying in a neutralino and a W boson. Only the leptonic decay of the W boson is considered, leading to a signature with two leptons and missing transverse energy. The search is more challenging compared to the previous one, since the branching ratio of the W boson decay reduces the acceptance of the process and the SUSY model is very similar to the WW Standard Model process. The search uses the data collected by ATLAS between 2015 and 2017, the integrated luminosity being 80.5 fb^{-1}.

Two sets of signal regions are considered, optimized to maximize the discovery probability or to maximize the exclusion limits. The kinematic variables used for the regions definition are m_{T2}, the missing transverse energy and its significance. Also in this search, $t\bar{t}$ and diboson are the main background processes and their Monte Carlo simulation are normalized in dedicated control regions.

The fluctuations observed in the inclusive signal regions are not significant enough to claim evidence of new phenomena, since the largest excess is 1.6σ. The orthogonal signal regions are therefore used to set the exclusion limits on the SUSY particles masses. The chargino is excluded up to 410 GeV, considering a massless neutralino. The upper limit on the neutralino is 120 GeV, in the case of a chargino mass of 300 GeV.

The searches presented in this document are an important part of the Supersymmetric model investigation. The exclusion limits on the Supersymmetric particles masses illustrated have largely surpassed the previous results. The limits obtained in the case of the slepton pair production and the chargino pair production with the W boson mediated decay are the first available results on such model obtained using data collected at LHC Run 2. The Run 1 results are largely improved: in the slepton case the excluded mass is enlarged by a factor 1.5, in the chargino with W boson mediated decay by a factor 2.3.

After four years of successful operation, the LHC is about to start a 2 years *Long Shutdown* phase, necessary to the machine maintenance and upgrade. The full dataset collected by the ATLAS experiment during the LHC Run 2 will soon be available to the analysis teams. A new paper that will consider all the Supersymmetric models presented in this manuscript is under preparation. The increased luminosity and the constant improvement of the analysis technique will allow to investigate phase spaces not yet explored, providing a great occasion for the discovery of beyond the Standard Model physics.

Bibliography

[1] S. L. Glashow, *Partial-symmetries of weak interactions*, Nuclear Physics **22** no. 4, (1961) 579 – 588. `http://www.sciencedirect.com/science/article/pii/0029558261904692`.

[2] S. Weinberg, *A Model of Leptons*, Phys. Rev. Lett. **19** (1967) 1264–1266.

[3] S. F. Novaes, *Standard model: An Introduction*, `arXiv:hep-ph/0001283 [hep-ph]`.

[4] A. Salam, *Gauge Unification of Fundamental Forces*, Rev. Mod. Phys. **52** (1980) 525–538. [,306(1980)].

[5] *LEP design report*. CERN, Geneva, 1984. `https://cds.cern.ch/record/102083`.

[6] O. S. Brüning, P. Collier, P. Lebrun, S. Myers, R. Ostojic, J. Poole, and P. Proudlock, *LHC Design Report*. CERN Yellow Reports: Monographs. CERN, Geneva, 2004. `https://cds.cern.ch/record/782076`.

[7] *Design Report Tevatron 1 project*, Tech. Rep. FERMILAB-DESIGN-1984-01, 1984. `https://cds.cern.ch/record/1478620`.

[8] ATLAS Collaboration, *The ATLAS Experiment at the CERN Large Hadron Collider*, Journal of Instrumentation **3** no. 08, (2008) S08003. `http://stacks.iop.org/1748-0221/3/i=08/a=S08003`.

[9] CMS Collaboration, *The CMS Experiment at the CERN LHC*, JINST **3** (2008) S08004.

[10] ATLAS Collaboration, *Observation of a new particle in the search for the Standard Model Higgs boson with the ATLAS detector at the LHC*, Phys. Lett. **B716** (2012) 1–29, `arXiv:1207.7214 [hep-ex]`.

[11] CMS Collaboration, *Observation of a new boson at a mass of 125 GeV with the CMS experiment at the LHC*, Phys. Lett. **B716** (2012) 30–61, `arXiv:1207.7235 [hep-ex]`.

[12] D. Volkov and V. Akulov, *Is the neutrino a goldstone particle?*, Physics Letters B **46** no. 1, (1973) 109 – 110. `http://www.sciencedirect.com/science/article/pii/0370269373904905`.

[13] C. R. Nappi and B. A. Ovrut, *Supersymmetric extension of the* $SU(3) \times SU(2) \times U(1)$ *model*, Physics Letters B **113** no. 2, (1982) 175 – 179. `http://www.sciencedirect.com/science/article/pii/037026938290418X`.

[14] J. Wess and B. Zumino, *Supergauge transformations in four dimensions*, Nuclear Physics B **70** no. 1, (1974) 39 – 50. `http://www.sciencedirect.com/science/article/pii/0550321374903551`.

[15] J. Wess and B. Zumino, *Supergauge invariant extension of quantum electrodynamics*, Nuclear Physics B **78** no. 1, (1974) 1 – 13. `http://www.sciencedirect.com/science/article/pii/0550321374901126`.

[16] S. Ferrara and B. Zumino, *Supergauge invariant Yang-Mills theories*, Nuclear Physics B **79** no. 3, (1974) 413 – 421. `http://www.sciencedirect.com/science/article/pii/0550321374905598`.

[17] A. Salam and J. Strathdee, *Super-symmetry and non-Abelian gauges*, Physics Letters B **51** no. 4, (1974) 353 – 355. `http://www.sciencedirect.com/science/article/pii/0370269374902263`.

[18] ATLAS Collaboration, *Search for squarks and gluinos in final states with jets and missing transverse momentum using 36 fb*$^{-1}$ *of* $\sqrt{s} = 13$ *TeV pp collision data with the ATLAS detector*, Phys. Rev. **D97** no. 11, (2018) 112001, `arXiv:1712.02332 [hep-ex]`.

[19] CMS Collaboration, *Search for supersymmetry in multijet events with missing transverse momentum in proton-proton collisions at 13 TeV*, Phys. Rev. **D96** no. 3, (2017) 032003, `arXiv:1704.07781 [hep-ex]`.

[20] CMS Collaboration, *Search for new phenomena with the* M_{T2} *variable in the all-hadronic final state produced in proton–proton collisions at* $\sqrt{s} = 13$ *TeV*, Eur. Phys. J. **C77** no. 10, (2017) 710, `arXiv:1705.04650 [hep-ex]`.

[21] A. Purcell, *Standard Model*,. `https://cds.cern.ch/record/1473657`.

[22] M. E. Peskin and D. V. Schroeder, *An Introduction to quantum field theory.* Addison-Wesley, Reading, USA, 1995. `http://www.slac.stanford.edu/~mpeskin/QFT.html`.

[23] P. W. Higgs, *Broken Symmetries and the Masses of Gauge Bosons*, Phys. Rev. Lett. **13** (1964) 508–509. `https://link.aps.org/doi/10.1103/PhysRevLett.13.508`.

[24] F. Englert and R. Brout, *Broken Symmetry and the Mass of Gauge Vector Mesons*, Phys. Rev. Lett. **13** (1964) 321–323. `https://link.aps.org/doi/10.1103/PhysRevLett.13.321`.

[25] V. C. Rubin and W. K. Ford, Jr., *Rotation of the Andromeda Nebula from a Spectroscopic Survey of Emission Regions*, Astrophys. J. **159** (1970) 379–403.

[26] K. G. Begeman, A. H. Broeils, and R. H. Sanders, *Extended rotation curves of spiral galaxies: Dark haloes and modified dynamics*, Mon. Not. Roy. Astron. Soc. **249** (1991) 523.

[27] Planck Collaboration, P. A. R. Ade et al., *Planck 2015 results. XIII. Cosmological parameters*, Astron. Astrophys. **594** (2016) A13, `arXiv:1502.01589 [astro-ph.CO]`.

[28] B. D. Fields, K. Freese, and D. S. Graff, *Massive compact halo objects viewed from a cosmological perspective: Contribution to the baryonic mass density of the universe*, New Astron. **3** (1998) 347–361, `arXiv:astro-ph/9804232 [astro-ph]`.

[29] K. Freese, B. Fields, and D. Graff, *What are MACHOs? Limits on stellar objects as the dark matter of our halo*, `arXiv:astro-ph/9901178 [astro-ph]`.

[30] M. Kamionkowski, *WIMP and axion dark matter*, `arXiv:hep-ph/9710467 [hep-ph]`.

[31] K. Saikawa, *Axion as a non-WIMP dark matter candidate*, PoS **EPS-HEP2017** (2017) 083, `arXiv:1709.07091 [hep-ph]`.

[32] G. Bertone, *Particle Dark Matter: Observations, Models and Searches.* Cambridge University Press, 2010.

[33] G. Bertone, D. Hooper, and J. Silk, *Particle dark matter: Evidence, candidates and constraints*, Phys. Rept. **405** (2005) 279–390, `arXiv:hep-ph/0404175 [hep-ph]`.

[34] Z.-Z. Xing and S. Zhou, *Cosmological Matter-antimatter Asymmetry.* Springer Berlin Heidelberg, Berlin, Heidelberg, 2011. `https://doi.org/10.1007/978-3-642-17560-2_11`.

[35] S. P. Martin, *A Supersymmetry primer*, `arXiv:hep-ph/9709356 [hep-ph]`. [Adv. Ser. Direct. High Energy Phys.18,1(1998)].

[36] E. Gildener, *Gauge-symmetry hierarchies*, Phys. Rev. D **14** (1976) 1667–1672. `https://link.aps.org/doi/10.1103/PhysRevD.14.1667`.

[37] L. Susskind, *Dynamics of spontaneous symmetry breaking in the Weinberg-Salam theory*, Phys. Rev. D **20** (1979) 2619–2625. `https://link.aps.org/doi/10.1103/PhysRevD.20.2619`.

[38] P. Fayet, *Spontaneously broken supersymmetric theories of weak, electromagnetic and strong interactions*, Physics Letters B **69** no. 4, (1977) 489 – 494. `http://www.sciencedirect.com/science/article/pii/0370269377908528`.

[39] S. Dimopoulos, S. Raby, and F. Wilczek, *Supersymmetry and the scale of unification*, Phys. Rev. D **24** (1981) 1681–1683. `https://link.aps.org/doi/10.1103/PhysRevD.24.1681`.

[40] M. Dine and A. E. Nelson, *Dynamical supersymmetry breaking at low energies*, Phys. Rev. D **48** (1993) 1277–1287. `https://link.aps.org/doi/10.1103/PhysRevD.48.1277`.

[41] M. Dine, A. E. Nelson, Y. Nir, and Y. Shirman, *New tools for low-energy dynamical supersymmetry breaking*, Phys. Rev. **D53** (1996) 2658–2669, `arXiv:hep-ph/9507378 [hep-ph]`.

[42] M. Dine, A. E. Nelson, and Y. Shirman, *Low-energy dynamical supersymmetry breaking simplified*, Phys. Rev. **D51** (1995) 1362–1370, `arXiv:hep-ph/9408384 [hep-ph]`.

[43] R. Barbieri and L. J. Hall, *Signals for supersymmetric unification*, Phys. Lett. **B338** (1994) 212–218, `arXiv:hep-ph/9408406 [hep-ph]`.

[44] R. Barbieri and G. F. Giudice, *$b \to s\gamma$ decay and supersymmetry*, Phys. Lett. **B309** (1993) 86–90, `arXiv:hep-ph/9303270 [hep-ph]`.

[45] J. Hisano, T. Moroi, K. Tobe, M. Yamaguchi, and T. Yanagida, *Lepton flavor violation in the supersymmetric standard model with seesaw induced neutrino masses*, Phys. Lett. **B357** (1995) 579–587, `arXiv:hep-ph/9501407 [hep-ph]`.

[46] F. Gabbiani, E. Gabrielli, A. Masiero, and L. Silvestrini, *A Complete analysis of FCNC and CP constraints in general SUSY extensions of the standard model*, Nucl. Phys. **B477** (1996) 321–352, `arXiv:hep-ph/9604387 [hep-ph]`.

[47] S. Abel, S. Khalil, and O. Lebedev, *EDM constraints in supersymmetric theories*, Nucl. Phys. **B606** (2001) 151–182, `arXiv:hep-ph/0103320 [hep-ph]`.

[48] G. Burdman, E. Golowich, J. L. Hewett, and S. Pakvasa, *Rare charm decays in the standard model and beyond*, Phys. Rev. **D66** (2002) 014009, `arXiv:hep-ph/0112235 [hep-ph]`.

[49] J. L. Hewett and J. D. Wells, *Searching for supersymmetry in rare B decays*, Phys. Rev. **D55** (1997) 5549–5560, `arXiv:hep-ph/9610323 [hep-ph]`.

[50] Y. Grossman, Y. Nir, and R. Rattazzi, *CP violation beyond the standard model*, Adv. Ser. Direct. High Energy Phys. **15** (1998) 755–794, `arXiv:hep-ph/9701231 [hep-ph]`. [,755(1997)].

[51] P. Draper and H. Rzehak, *A Review of Higgs Mass Calculations in Supersymmetric Models*, Phys. Rept. **619** (2016) 1–24, `arXiv:1601.01890 [hep-ph]`.

[52] R. M. Godbole, P. Roy, and X. Tata, *Tau signals of R-parity breaking at LEP-200*, Nucl. Phys. **B401** (1993) 67–92, `arXiv:hep-ph/9209251 [hep-ph]`.

[53] G. Bhattacharyya and D. Choudhury, *D and tau decays: Placing new bounds on R-parity violating supersymmetric coupling*, Mod. Phys. Lett. **A10** (1995) 1699–1704, `arXiv:hep-ph/9503263 [hep-ph]`.

[54] G. Bhattacharyya, *R-parity violating supersymmetric Yukawa couplings: A Minireview*, Nucl. Phys. Proc. Suppl. **52A** (1997) 83–88, `arXiv:hep-ph/9608415 [hep-ph]`.

[55] G. R. Farrar and P. Fayet, *Phenomenology of the production, decay, and detection of new hadronic states associated with supersymmetry*, Physics Letters B **76** no. 5, (1978) 575 – 579. `http://www.sciencedirect.com/science/article/pii/0370269378908584`.

[56] C. Borschensky, M. Kramer, A. Kulesza, M. Mangano, S. Padhi, T. Plehn, and X. Portell, *Squark and gluino production cross sections in pp collisions at* $\sqrt{s} =$ *13, 14, 33 and 100 TeV*, Eur. Phys. J. **C74** no. 12, (2014) 3174, `arXiv:1407.5066 [hep-ph]`.

[57] J. Alwall, P. Schuster, and N. Toro, *Simplified Models for a First Characterization of New Physics at the LHC*, Phys. Rev. **D79** (2009) 075020, `arXiv:0810.3921 [hep-ph]`.

[58] ATLAS Collaboration, *Search for electroweak production of supersymmetric particles in final states with two or three leptons at* $\sqrt{s} = 13$ *TeV with the ATLAS detector*, Eur. Phys. J. **C78** no. 12, (2018) 995, `arXiv:1803.02762 [hep-ex]`.

[59] ATLAS Collaboration, *Search for direct chargino pair production with W-boson mediated decays in events with two leptons and missing transverse momentum at* $\sqrt{s} = 13$ *TeV with the ATLAS detector*,. `https://cds.cern.ch/record/2632578`.

[60] B. Fuks, M. Klasen, D. R. Lamprea, and M. Rothering, *Precision predictions for electroweak superpartner production at hadron colliders with* RESUMMINO, Eur. Phys. J. C **73** (2013) 2480, `arXiv:1304.0790 [hep-ph]`.

[61] B. Fuks, M. Klasen, D. R. Lamprea, and M. Rothering, *Revisiting slepton pair production at the Large Hadron Collider*, JHEP **01** (2014) 168, `arXiv:1310.2621 [hep-ph]`.

[62] B. Fuks, M. Klasen, D. R. Lamprea, and M. Rothering, *Gaugino production in proton-proton collisions at a center-of-mass energy of 8 TeV*, JHEP **10** (2012) 081, `arXiv:1207.2159 [hep-ph]`.

[63] A. V. Gladyshev, D. I. Kazakov, and M. G. Paucar, *Long-lived next-to-lightest supersymmetric particles*,. `http://quarks.inr.ac.ru/2008/proceedings/p2_SM/gladyshev.pdf`.

[64] M. Fairbairn, A. C. Kraan, D. A. Milstead, T. Sjostrand, P. Z. Skands, and T. Sloan, *Stable massive particles at colliders*, Phys. Rept. **438** (2007) 1–63, `arXiv:hep-ph/0611040 [hep-ph]`.

[65] A. Djouadi, M. M. Muhlleitner, and M. Spira, *Decays of supersymmetric particles: The Program SUSY-HIT (SUspect-SdecaY-Hdecay-InTerface)*, Acta Phys. Polon. **B38** (2007) 635–644, `arXiv:hep-ph/0609292 [hep-ph]`.

[66] H. Wiedemann, *Particle accelerator physics; 3rd ed.* Springer, Berlin, 2007. `https://cds.cern.ch/record/1083415`.

[67] J. M. Butterworth, G. Dissertori, and G. P. Salam, *Hard Processes in Proton-Proton Collisions at the Large Hadron Collider*, Ann. Rev. Nucl. Part. Sci. **62** (2012) 387–405, `arXiv:1202.0583 [hep-ex]`.

[68] J. C. Collins and D. E. Soper, *The Theorems of Perturbative QCD*, Ann. Rev. Nucl. Part. Sci. **37** (1987) 383–409.

[69] A. D. Martin, W. J. Stirling, R. S. Thorne, and G. Watt, *Parton distributions for the LHC*, Eur. Phys. J. **C63** (2009) 189–285, `arXiv:0901.0002 [hep-ph]`.

[70] LHCb Collaboration, *The LHCb Detector at the LHC*, Journal of Instrumentation **3** no. 08, (2008) S08005. `http://stacks.iop.org/1748-0221/3/i=08/a=S08005`.

[71] ALICE Collaboration, *The ALICE experiment at the CERN LHC*, Journal of Instrumentation **3** no. 08, (2008) S08002. `http://stacks.iop.org/1748-0221/3/i=08/a=S08002`.

[72] F. Marcastel, *CERN's Accelerator Complex. La chaîne des accélérateurs du CERN*,. `https://cds.cern.ch/record/1621583`.

[73] ATLAS Collaboration, *ATLAS luminosity public results - Run 2*,. `https://twiki.cern.ch/twiki/bin/view/AtlasPublic/LuminosityPublicResultsRun2`.

[74] ATLAS Collaboration, *ATLAS central solenoid: Technical Design Report.* Technical Design Report ATLAS. CERN, Geneva, 1997. `https://cds.cern.ch/record/331067`.

[75] ATLAS Collaboration, J. P. Badiou, J. Beltramelli, J. M. Baze, and J. Belorgey, *ATLAS barrel toroid: Technical Design Report.* Technical Design Report ATLAS. CERN, Geneva, 1997. `https://cds.cern.ch/record/331065`.

[76] ATLAS Collaboration, *ATLAS end-cap toroids: Technical Design Report.* Technical Design Report ATLAS. CERN, Geneva, 1997. `https://cds.cern.ch/record/331066`.

[77] ATLAS Collaboration, *ATLAS inner detector: Technical design report. Vol. 1*,.

[78] ATLAS Collaboration, *ATLAS inner detector: Technical design report. Vol. 2*,.

[79] ATLAS Collaboration, *Technical Design Report for the ATLAS Inner Tracker Pixel Detector*, Tech. Rep. CERN-LHCC-2017-021. ATLAS-TDR-030, CERN, Geneva, Sep, 2017. `https://cds.cern.ch/record/2285585`.

[80] ATLAS Collaboration, M. Capeans, G. Darbo, K. Einsweiller, M. Elsing, T. Flick, M. Garcia-Sciveres, C. Gemme, H. Pernegger, O. Rohne, and R. Vuillermet, *ATLAS Insertable B-Layer Technical Design Report*, Tech. Rep. CERN-LHCC-2010-013. ATLAS-TDR-19, Sep, 2010. `https://cds.cern.ch/record/1291633`.

[81] A. Abdesselam and F. Anghinolfi, *The ATLAS semiconductor tracker end-cap module*, Nucl. Instrum. Methods Phys. Res., A **575** no. 3, (2007) 353–389. `http://cds.cern.ch/record/1063618`.

[82] A. Abdesselam and T. Akimoto, *The Barrel Modules of the ATLAS SemiConductor Tracker*, Tech. Rep. ATL-INDET-PUB-2006-005. ATL-COM-INDET-2006-009. CERN-ATL-COM-INDET-2006-009, CERN, Geneva, Jul, 2006. `http://cds.cern.ch/record/974073`.

[83] ATLAS TRT Collaboration, E. e. a. Abat, *The ATLAS TRT Barrel Detector*, JINST **3** (2008) P02014. `http://cds.cern.ch/record/1094548`.

[84] ATLAS TRT Collaboration, E. e. a. Abat, *The ATLAS TRT end-cap detectors*, JINST **3** (2008) P10003. `https://cds.cern.ch/record/1151338`.

[85] ATLAS Collaboration, A. Airapetian et al., *ATLAS: Detector and physics performance technical design report. Volume 1,*.

[86] ATLAS Collaboration, *ATLAS liquid-argon calorimeter: Technical Design Report.* Technical Design Report ATLAS. CERN, Geneva, 1996. `https://cds.cern.ch/record/331061`.

[87] ATLAS Collaboration, *ATLAS tile calorimeter: Technical Design Report.* Technical Design Report ATLAS. CERN, Geneva, 1996. `https://cds.cern.ch/record/331062`.

[88] ATLAS Collaboration, *The ATLAS Forward Calorimeter*, Journal of Instrumentation **3** no. 02, (2008) P02010. `http://stacks.iop.org/1748-0221/3/i=02/a=P02010`.

[89] ATLAS Collaboration, *ATLAS muon spectrometer: Technical Design Report.* Technical Design Report ATLAS. CERN, Geneva, 1997. `https://cds.cern.ch/record/331068`.

[90] ATLAS Collaboration, P. Jenni, M. Nessi, M. Nordberg, and K. Smith, *ATLAS high-level trigger, data-acquisition and controls: Technical Design Report.* Technical Design Report ATLAS. CERN, Geneva, 2003. `https://cds.cern.ch/record/616089`.

[91] ATLAS Collaboration, *Performance of the ATLAS Trigger System in 2015*, Eur. Phys. J. **C77** no. 5, (2017) 317, `arXiv:1611.09661 [hep-ex]`.

[92] ATLAS Collaboration, *Luminosity determination in pp collisions at $\sqrt{s} = 8$ TeV using the ATLAS detector at the LHC*, Eur. Phys. J. **C76** no. 12, (2016) 653, `arXiv:1608.03953 [hep-ex]`.

[93] ATLAS Collaboration, P. Laycock, M. A. Chelstowska, T. Cuhadar Donszelmann, J. Guenther, A. M. Nairz, R. Nicolaidou, E. Shabalina, J. Strandberg, A. Taffard, and S.-M. Wang, *ATLAS data preparation in run 2*, Tech. Rep. ATL-DAPR-PROC-2017-001. 4, CERN, Geneva, Feb, 2017. `https://cds.cern.ch/record/2253427`.

[94] ATLAS TDAQ Collaboration, M. Abolins et al., *The ATLAS Data Acquisition and High Level Trigger system*, JINST **11** no. 06, (2016) P06008.

[95] ATLAS Collaboration, *ATLAS data quality public results - Run 2*,. `https://twiki.cern.ch/twiki/bin/view/AtlasPublic/RunStatsPublicResults2010`.

[96] ATLAS Collaboration, *The ATLAS Simulation Infrastructure*, Eur. Phys. J. **C70** (2010) 823–874, `arXiv:1005.4568 [physics.ins-det]`.

[97] R. Frühwirth, *Application of Kalman filtering to track and vertex fitting*, Nuclear Instruments and Methods in Physics Research Section A: Accelerators, Spectrometers, Detectors and Associated Equipment **262** no. 2, (1987) 444 – 450. `http://www.sciencedirect.com/science/article/pii/0168900287908874`.

[98] R. Fruhwirth, W. Waltenberger, and P. Vanlaer, *Adaptive vertex fitting*, J. Phys. **G34** (2007) N343.

[99] ATLAS Collaboration, *Topological cell clustering in the ATLAS calorimeters and its performance in LHC Run 1*, Eur. Phys. J. **C77** (2017) 490, `arXiv:1603.02934 [hep-ex]`.

[100] ATLAS Collaboration, *Electron efficiency measurements with the ATLAS detector using the 2015 LHC proton-proton collision data*, Tech. Rep. ATLAS-CONF-2016-024, CERN, Geneva, Jun, 2016. `https://cds.cern.ch/record/2157687`.

[101] ATLAS Collaboration, A. Collaboration, *Muon reconstruction performance of the ATLAS detector in proton–proton collision data at $\sqrt{s}$=13 TeV. Muon reconstruction performance of the ATLAS detector in proton–proton collision data at $\sqrt{s}$=13 TeV*, Eur. Phys. J. C **76** no. CERN-EP-2016-033. CERN-EP-2016-033, (2016) 292. 45 p. `http://cds.cern.ch/record/2139897`.

[102] M. Cacciari, G. P. Salam, and G. Soyez, *The Anti-k(t) jet clustering algorithm*, JHEP **04** (2008) 063, `arXiv:0802.1189 [hep-ph]`.

[103] ATLAS Collaboration, M. Aaboud et al., *Jet energy scale measurements and their systematic uncertainties in proton-proton collisions at $\sqrt{s} = 13$ TeV with the ATLAS detector*, Phys. Rev. **D96** no. 7, (2017) 072002, `arXiv:1703.09665 [hep-ex]`.

[104] ATLAS Collaboration, *Performance of pile-up mitigation techniques for jets in pp collisions at $\sqrt{s} = 8$ TeV using the ATLAS detector*, Eur. Phys. J. **C76** no. 11, (2016) 581, `arXiv:1510.03823 [hep-ex]`.

[105] *Tagging and suppression of pileup jets with the ATLAS detector*, Tech. Rep. ATLAS-CONF-2014-018, CERN, Geneva, May, 2014. `https://cds.cern.ch/record/1700870`.

[106] ATLAS Collaboration, *Optimisation and performance studies of the ATLAS b-tagging algorithms for the 2017-18 LHC run*, Tech. Rep. ATL-PHYS-PUB-2017-013, CERN, Geneva, Jul, 2017. `https://cds.cern.ch/record/2273281`.

[107] ATLAS Collaboration, *Measurements of b-jet tagging efficiency with the ATLAS detector using $t\bar{t}$ events at $\sqrt{s} = 13$ TeV*, `arXiv:1805.01845 [hep-ex]`.

[108] ATLAS Collaboration, *Calibration of light-flavour jet b-tagging rates on ATLAS proton-proton collision data at $\sqrt{s} = 13$ TeV*, Tech. Rep. ATLAS-CONF-2018-006, CERN, Geneva, Apr, 2018. `https://cds.cern.ch/record/2314418`.

[109] ATLAS Collaboration, *Performance of missing transverse momentum reconstruction with the ATLAS detector using proton-proton collisions at $\sqrt{s}$ = 13 TeV*, `arXiv:1802.08168 [hep-ex]`.

[110] ATLAS Collaboration, *Object-based missing transverse momentum significance in the ATLAS detector*, Tech. Rep. ATLAS-CONF-2018-038, CERN, Geneva, Jul, 2018. `https://cds.cern.ch/record/2630948`.

[111] G. Cowan, *Statistical data analysis.* Oxford University Press, USA, 1998.

[112] C. G. Lester and D. J. Summers, *Measuring masses of semiinvisibly decaying particles pair produced at hadron colliders*, Phys. Lett. **B463** (1999) 99–103, `arXiv:hep-ph/9906349 [hep-ph]`.

[113] A. Barr, C. Lester, and P. Stephens, *m(T2): The Truth behind the glamour*, J. Phys. **G29** (2003) 2343–2363, `arXiv:hep-ph/0304226 [hep-ph]`.

[114] B. C. Allanach, A. J. Barr, A. Dafinca, and C. Gwenlan, *Discovery reach for generic supersymmetry at the LHC: MT2 versus missing transverse momentum selections for pMSSM searches*, JHEP **07** (2011) 104, `arXiv:1105.1024 [hep-ph]`.

[115] P. Z. Skands, *QCD for Collider Physics*, `arXiv:1104.2863 [hep-ph]`.

[116] GEANT4 Collaboration, *GEANT4: A Simulation toolkit*, Nucl. Instrum. Meth. **A506** (2003) 250–303.

[117] ATLAS Collaboration, *Jet Calibration and Systematic Uncertainties for Jets Reconstructed in the ATLAS Detector at $\sqrt{s} = 13$ TeV*, Tech. Rep. ATL-PHYS-PUB-2015-015, CERN, Geneva, Jul, 2015. `https://cds.cern.ch/record/2037613`.

[118] ATLAS Collaboration, *Expected performance of missing transverse momentum reconstruction for the ATLAS detector at $\sqrt{s} = 13$ TeV*, Tech. Rep. ATL-PHYS-PUB-2015-023, CERN, Geneva, Jul, 2015. `https://cds.cern.ch/record/2037700`.

[119] M. Baak, G. J. Besjes, D. Côte, A. Koutsman, J. Lorenz, and D. Short, *HistFitter software framework for statistical data analysis*, Eur. Phys. J. **C75** (2015) 153, `arXiv:1410.1280 [hep-ex]`.

[120] E. S. Neyman, J.and Pearson, *On the Problem of the Most Efficient Tests of Statistical Hypotheses.* Springer New York, New York, NY, 1992. `https://doi.org/10.1007/978-1-4612-0919-5_6`.

[121] G. Cowan, K. Cranmer, E. Gross, and O. Vitells, *Asymptotic formulae for likelihood-based tests of new physics*, Eur. Phys. J. **C71** (2011) 1554, `arXiv:1007.1727 [physics.data-an]`. [Erratum: Eur. Phys. J.C73,2501(2013)].

[122] A. L. Read, *Presentation of search results: The CL(s) technique*, J. Phys. **G28** (2002) 2693–2704. [,11(2002)].

[123] G. Zech, *Upper limits in experiments with background or measurement errors*, Nucl. Instrum. Methods Phys. Res., A **277** no. CERN-EP-88-164, (1988) 608. 6 p. `https://cds.cern.ch/record/193135`.

[124] T. Junk, *Confidence level computation for combining searches with small statistics*, Nucl. Instrum. Meth. **A434** (1999) 435–443, `arXiv:hep-ex/9902006 [hep-ex]`.

[125] ATLAS Collaboration, *Search for direct production of charginos, neutralinos and sleptons in final states with two leptons and missing transverse momentum in pp collisions at $\sqrt{s} = 8$ TeV with the ATLAS detector*, JHEP **05** (2014) 071, `arXiv:1403.5294 [hep-ex]`.

[126] ATLAS Collaboration, *Search for supersymmetry with two and three leptons and missing transverse momentum in the final state at $\sqrt{s}$=13 TeV with the ATLAS detector*, Tech. Rep. ATLAS-CONF-2016-096, CERN, Geneva, Sep, 2016. `http://cds.cern.ch/record/2212162`.

[127] J. Alwall, P. Demin, S. de Visscher, R. Frederix, M. Herquet, F. Maltoni, T. Plehn, D. L. Rainwater, and T. Stelzer, *MadGraph/MadEvent v4: The New Web Generation*, JHEP **09** (2007) 028, `arXiv:0706.2334 [hep-ph]`.

[128] T. Sjostrand, S. Mrenna, and P. Z. Skands, *A Brief Introduction to PYTHIA 8.1*, Comput. Phys. Commun. **178** (2008) 852–867, `arXiv:0710.3820 [hep-ph]`.

[129] ATLAS Collaboration, *Multi-Boson Simulation for 13 TeV ATLAS Analyses*, Tech. Rep. ATL-PHYS-PUB-2016-002, CERN, Geneva, Jan, 2016. `https://cds.cern.ch/record/2119986`.

[130] T. Gleisberg, S. Hoeche, F. Krauss, M. Schonherr, S. Schumann, F. Siegert, and J. Winter, *Event generation with SHERPA 1.1*, JHEP **02** (2009) 007, `arXiv:0811.4622 [hep-ph]`.

[131] T. Gleisberg and S. Hoeche, *Comix, a new matrix element generator*, JHEP **12** (2008) 039, `arXiv:0808.3674 [hep-ph]`.

[132] F. Cascioli, P. Maierhofer, and S. Pozzorini, *Scattering Amplitudes with Open Loops*, Phys. Rev. Lett. **108** (2012) 111601, `arXiv:1111.5206 [hep-ph]`.

[133] NNPDF Collaboration, R. D. Ball et al., *Parton distributions for the LHC Run II*, JHEP **04** (2015) 040, `arXiv:1410.8849 [hep-ph]`.

[134] ATLAS Collaboration, *Simulation of top quark production for the ATLAS experiment at sqrt(s) = 13 TeV*, Tech. Rep. ATL-PHYS-PUB-2016-004, CERN, Geneva, Jan, 2016. `https://cds.cern.ch/record/2120417`.

[135] ATLAS Collaboration, *Improvements in $t\bar{t}$ modelling using NLO+PS Monte Carlo generators for Run2*, Tech. Rep. ATL-PHYS-PUB-2018-009, CERN, Geneva, Jul, 2018. `https://cds.cern.ch/record/2630327`.

[136] S. Frixione, P. Nason, and G. Ridolfi, *A Positive-weight next-to-leading-order Monte Carlo for heavy flavour hadroproduction*, JHEP **09** (2007) 126, `arXiv:0707.3088 [hep-ph]`.

[137] E. Re, *Single-top Wt-channel production matched with parton showers using the POWHEG method*, Eur. Phys. J. **C71** (2011) 1547, `arXiv:1009.2450 [hep-ph]`.

[138] H.-L. Lai, M. Guzzi, J. Huston, Z. Li, P. M. Nadolsky, J. Pumplin, and C. P. Yuan, *New parton distributions for collider physics*, Phys. Rev. **D82** (2010) 074024, `arXiv:1007.2241 [hep-ph]`.

[139] T. Sjostrand, S. Mrenna, and P. Z. Skands, *PYTHIA 6.4 Physics and Manual*, JHEP **05** (2006) 026, `arXiv:hep-ph/0603175 [hep-ph]`.

[140] P. Z. Skands, *Tuning Monte Carlo Generators: The Perugia Tunes*, Phys. Rev. **D82** (2010) 074018, `arXiv:1005.3457 [hep-ph]`.

[141] M. Czakon and A. Mitov, *Top++: A Program for the Calculation of the Top-Pair Cross-Section at Hadron Colliders*, Comput. Phys. Commun. **185** (2014) 2930, `arXiv:1112.5675 [hep-ph]`.

[142] ATLAS Collaboration, *Monte Carlo Generators for the Production of a W or Z/γ^* Boson in Association with Jets at ATLAS in Run 2*, Tech. Rep. ATL-PHYS-PUB-2016-003, CERN, Geneva, Jan, 2016. `https://cds.cern.ch/record/2120133`.

[143] ATLAS Collaboration, *ATLAS simulation of boson plus jets processes in Run 2*, Tech. Rep. ATL-PHYS-PUB-2017-006, CERN, Geneva, May, 2017. `https://cds.cern.ch/record/2261937`.

[144] R. Gavin, Y. Li, F. Petriello, and S. Quackenbush, *FEWZ 2.0: A code for hadronic Z production at next-to-next-to-leading order*, Comput. Phys. Commun. **182** (2011) 2388–2403, `arXiv:1011.3540 [hep-ph]`.

[145] ATLAS Collaboration, *Modelling of the $t\bar{t}H$ and $t\bar{t}V$ $(V = W, Z)$ processes for $\sqrt{s} = 13$ TeV ATLAS analyses*, Tech. Rep. ATL-PHYS-PUB-2016-005, CERN, Geneva, Jan, 2016. `https://cds.cern.ch/record/2120826`.

[146] ATLAS Collaboration, *Studies of Monte Carlo generators in Higgs boson production for ATLAS Run 2*, Tech. Rep. ATL-PHYS-PUB-2014-022, CERN, Geneva, Dec, 2014. `https://cds.cern.ch/record/1978192`.

[147] ATLAS Collaboration, *2015 start-up trigger menu and initial performance assessment of the ATLAS trigger using Run-2 data*, Tech. Rep. ATL-DAQ-PUB-2016-001, CERN, Geneva, Mar, 2016. `https://cds.cern.ch/record/2136007`.

[148] ATLAS Collaboration, *Non-collision backgrounds as measured by the ATLAS detector during the 2010 proton-proton run*, Tech. Rep. ATLAS-CONF-2011-137, CERN, Geneva, Sep, 2011. `https://cds.cern.ch/record/1383840`.

[149] ATLAS Collaboration, *Selection of jets produced in 13TeV proton-proton collisions with the ATLAS detector*, Tech. Rep. ATLAS-CONF-2015-029, CERN, Geneva, Jul, 2015. `https://cds.cern.ch/record/2037702`.

[150] D. Adams et al., *Recommendations of the Physics Objects and Analysis Harmonisation Study Groups 2014*, Tech. Rep. ATL-PHYS-INT-2014-018, CERN, Geneva, Jul, 2014. `https://cds.cern.ch/record/1743654`.

[151] ATLAS Collaboration, *Measurement of the top quark-pair production cross section with ATLAS in pp collisions at $\sqrt{s} = 7$ TeV*, Eur. Phys. J. **C71** (2011) 1577, `arXiv:1012.1792 [hep-ex]`.

[152] CMS Collaboration, *Search for supersymmetric partners of electrons and muons in proton-proton collisions at $\sqrt{s} = 13$ TeV*, Submitted to: Phys. Lett. (2018), `arXiv:1806.05264 [hep-ex]`.

[153] CMS Collaboration, *Searches for pair production of charginos and top squarks in final states with two oppositely charged leptons in proton-proton collisions at $\sqrt{s} = 13$ TeV*, JHEP **11** (2018) 079, `arXiv:1807.07799 [hep-ex]`.

[154] P. Artoisenet, R. Frederix, O. Mattelaer, and R. Rietkerk, *Automatic spin-entangled decays of heavy resonances in Monte Carlo simulations*, Journal of High Energy Physics **2013** no. 3, (2013) 15. `https://doi.org/10.1007/JHEP03(2013)015`.

[155] ATLAS Collaboration, *Multi-Boson Simulation for 13 TeV ATLAS Analyses*, Tech. Rep. ATL-PHYS-PUB-2017-005, CERN, Geneva, May, 2017. `https://cds.cern.ch/record/2261933`.

[156] S. Alioli, P. Nason, C. Oleari, and E. Re, *A general framework for implementing NLO calculations in shower Monte Carlo programs: the POWHEG BOX*, JHEP **06** (2010) 043, `arXiv:1002.2581 [hep-ph]`.

[157] ATLAS Collaboration, *Measurement of the Z/γ^* boson transverse momentum distribution in pp collisions at $\sqrt{s} = 7$ TeV with the ATLAS detector*, JHEP **09** (2014) 145, `arXiv:1406.3660 [hep-ex]`.

[158] J. Pumplin, D. R. Stump, J. Huston, H. L. Lai, P. M. Nadolsky, and W. K. Tung, *New generation of parton distributions with uncertainties from global QCD analysis*, JHEP **07** (2002) 012, `arXiv:hep-ph/0201195 [hep-ph]`.

[159] ATLAS Collaboration, *E_T^{miss} performance in the ATLAS detector using 2015-2016 LHC p-p collisions*, Tech. Rep. ATLAS-CONF-2018-023, CERN, Geneva, Jun, 2018. `https://cds.cern.ch/record/2625233`.

Acknowledgments

At the end of this journey, there are many people I would like to thank, without them this work would not have been possible.

First of all, I would like to express my sincere gratitude to my supervisor Tommaso Lari, for his immense physics knowledge, for his constant guidance and for all the precious advices. Thank you for your patience and motivation and for being really a great example of what a physicist should be.

I would like to thank all the brilliant people that are or were part of the Milano ATLAS group during my PhD. Thanks for your support, your advices and the stimulating discussions, and also for all the coffee breaks together.

During these three years I had the chance to work with many talented people from the ATLAS Collaboration. I would like to thank the Supersymmetry group and its conveners, Iacopo Vivarelli, Till Eifert and Zach Marshall, for the precious review of my work and for their guidance. My thanks to the Third Generation and to the Electroweak sub-groups and all their sub-conveners.

I had the opportunity to be part of great analysis teams: first the Stop2l, then the EWK2/3lep group and finally the C1C1WW team. I want to thank all the members of the analysis teams for all the hard work done together, by day and by night, and for their dedication. I'm especially grateful to Federico Meloni, Sarah Williams and Margherita Primavera, thanks for your guidance and for always being supportive.

I would like to thank Claudia and Lorenzo, not only for their help in Supersymmetry related issues, but also for their support and friendship. Thank you for hearing all of my (many) complains. Thanks to the whole Milano crew at CERN, because they were always ready to give me good advices and to encourage me, but also thanks for your friendship and for the awesome time together.

Thanks to my parents, they always supported my choices and encourage me to follow my inclination, since I was a little girl. Thanks for the immense trust you have placed in me and for always being proud of me. Thanks to my sister Erika, for being an important part of my life. Thanks again to Alice, for always supporting me in a very special way.

Finally thanks to Michele, the love of my life, for always being there for me. You supported me throughout these years and you forgave me if I alway have to "*answer this mail*" or "*run the fit*". Thank you for encouraging me to follow my aspiration and for always believing in me.